# Tropical-Extratropical Teleconnections And Atmospheric Drivers Of European Drought Events




Ronald Li
Jesus College
University of Oxford

A thesis submitted for the degree of
*Doctor of Philosophy*

Trinity 2018

This thesis is dedicated to

my parents

for their love and support

# Acknowledgements

I wish to thank my supervisors Tim Woollings, Michael Blackburn, Brian Hoskins and Adam Scaife, for their support throughout.

I am indebted to the people in my research group, including Chris O'Reilly, Tess Parker, Cheikh Mbengue, Regina Rodrigues, Peter Watson, Marie Drouard, Hugh Baker and Matthew Patterson, for their feedback on my work at group meetings.

I am grateful to my D.Phil. examiners Antje Weisheimer and Adrian Matthews for their careful reading of this thesis. I am also grateful to Lesley Gray and Anu Dudhia for examining my transfer and confirmation reports.

I would like to thank Len Shaffrey and the NERC IMPETUS project for providing this D.Phil. opportunity, and Jesus College for supporting me to various conferences.

Finally, thanks go to my parents, Victor and Teresa, for giving me all the support I need. None of this would have been possible without the continuing support of my family.

# Abstract

Atmospheric dynamics are important in tropical-extratropical teleconnections. Using maximum covariance analysis (MCA), we investigate the leading modes of covariability between the tropical outgoing longwave radiation and the extratropical geopotential height. Using observed data, the leading mode of covariability on the seasonal timescale is associated with the El-Niño Southern Oscillation. Using a Met Office climate model (GC3) control run, although the leading tropical mode is still ENSO, the extratropical pattern shows large differences in the North Pacific-American region.

GC3 has a large North Pacific jet bias, which according to ray tracing can affect wave propagations from the tropics. Using a barotropic model with the same ENSO tropical forcing but linearized upon the different basic states of reanalysis and GC3, the largest differences in the response are in the North Pacific-American region and agree with the MCA differences. The result is also supported by baroclinic experiments. Our finding may contribute to resolving the signal-to-noise paradox in some climate predictions.

Next, we test the mechanism of influence from the tropics to European droughts, to find potential tropical drivers of Rossby waves that are consistent between observations and the idealized models. We identify a northward shift in the tropical Atlantic precipitation and a weakening of the tropical eastern Pacific precipitation, which significantly influence about 60% of European drought events.

# Glossary of acronyms

| | |
|---|---|
| CMIP | Coupled model intercomparison project |
| CRU | Climate Research Unit |
| DJF | December-January-February |
| EA | East Atlantic pattern |
| EAJS | East Asian jet stream |
| ECMWF | European Centre for Medium-Range Weather Forecasts |
| ENSO | El-Niño Southern Oscillation |
| EOF | Empirical orthogonal function |
| ERA-I | ECMWF Reanalysis Interim |
| GBE | Greenland blocking event |
| GCM | General circulation model |
| GPCP | Global Precipitation Climatology Project |
| IPCC | Intergovernmental Panel on Climate Change |
| ITCZ | Inter Tropical Convergence Zone |
| JJA | June-July-August |
| MCA | Maximum covariance analysis |
| MJO | Madden-Julian oscillation |
| MOGC3 | Met Office HadGEM-GC3.0 |
| NAO | North Atlantic Oscillation |
| NCAR | National Center for Atmospheric Research |
| NCEP | National Centers for Environmental Prediction |
| OLR | Outgoing longwave radiation |
| PNA | Pacific-North American teleconnection pattern |
| PV | Potential vorticity |
| QBO | Quasi-Biennial Oscillation |
| QGPV | Quasi-geostrophic potential vorticity |
| RWAF | Rossby wave activity flux |
| RWS | Rossby wave source |
| SCF | Squared covariance fraction |
| SST | Sea surface temperature |
| SSW | Sudden stratospheric warming |
| Z250 | 250 hPa geopotential height |
| Z500 | 500 hPa geopotential height |

# Contents


**1 Introduction** **1**

1.1 Motivation . . . . . 1

1.2 Extratropical atmospheric variability . . . . . 6

1.3 Rossby wave theory . . . . . 13

1.4 Tropical-extratropical teleconnection . . . . . 16

1.5 Thesis outline . . . . . 20

**2 Methods** **22**

2.1 Maximum covariance analysis . . . . . 22

2.2 Ray tracing . . . . . 24

2.3 Barotropic model . . . . . 27

2.3.1 Patch method . . . . . 29

2.3.2 Rossby wave activity flux . . . . . 33

2.3.3 Barotropic instability of basic state . . . . . 34

2.4 Baroclinic model . . . . . 36

2.4.1 Model equations . . . . . 36

2.4.2 Model set up . . . . . 38

2.4.3 Reproduction of literature . . . . . 42

2.5 Blocking index . . . . . 44

**3 Tropical-extratropical teleconnections** **47**

3.1 Reanalysis MCA . . . . . 47

3.1.1 Seasonal analysis . . . . . 48

3.1.2 Various sensitivities . . . . . 54

3.1.3 ENSO intraseasonal responses . . . 56
3.1.4 Daily analysis . . . 58
3.1.4.1 All years . . . 58
3.1.4.2 ENSO-neutral years . . . 63
3.2 MOGC3 MCA . . . 67
3.2.1 Seasonal analysis . . . 68
3.2.2 Daily analysis . . . 69
3.2.2.1 All years . . . 69
3.2.2.2 ENSO-neutral years . . . 74
3.3 Chapter summary . . . 77

**4 ENSO Experiments** **80**
4.1 Jet and waveguide biases . . . 81
4.2 Ray tracing . . . 84
4.3 Barotropic experiments . . . 90
4.3.1 Circumglobal tropical forcing . . . 92
4.3.1.1 Sensitivity to MOGC3 forcing . . . 102
4.3.2 Regional tropical forcing . . . 103
4.3.3 RWS mean bias and jet bias . . . 108
4.4 Baroclinic model experiments . . . 113
4.4.1 On the reanalysis basic state . . . 115
4.4.2 On the MOGC3 basic state . . . 122
4.4.3 Difference between the two basic states . . . 124
4.5 Chapter discussion and summary . . . 127

**5 Atmospheric drivers of European drought events** **130**
5.1 Observational analysis . . . 131
5.2 Barotropic model experiments . . . 140
5.2.1 Circumglobal patch forcings . . . 140
5.2.2 Individual patch forcings . . . 145
5.2.3 Barotropic results discussion . . . 148

5.3 Ray tracing . . . 150
5.4 Baroclinic model experiments . . . 151
5.4.1 Tropical Atlantic forcings . . . 151
5.4.2 Forcings in other basins . . . 159
5.5 Chapter discussion and summary . . . 162

**6 Conclusion** **172**
6.1 Chapter summaries . . . 172
6.1.1 Ch1: Motivation . . . 172
6.1.2 Ch2: Methods . . . 172
6.1.3 Ch3: Tropical-extratropical teleconnections . . . 173
6.1.4 Ch4: ENSO experiments . . . 174
6.1.5 Ch5: Atmospheric drivers of European drought events . . . 175
6.2 On the usefulness of our methods . . . 176
6.3 Implications and future work . . . 177

**A Additional figures** **180**

**Bibliography** **195**

# Chapter 1

# Introduction

## 1.1 Motivation

Atmospheric dynamics are important in the seasonal timescale. For example, the recent winters of 2010 and 2012 exhibited extreme displacements in the North Atlantic eddy-driven jet latitude (Santos et al., 2013). Woollings et al. (2010) showed that this jet latitude, together with its speed, described the large-scale circulation over the North Atlantic and European region well. They also showed that there were three preferred regimes for the jet latitude. In 2010, this jet was predominantly in the southern position regime, which resulted in anomalous precipitation in southern Europe and anomalous cold outbreaks in northern Europe. In 2012, this jet was predominantly in the northern position regime, which resulted in anomalously dry southern Europe and anomalously warm northern Europe. In both winters, the jet posed drought risks in some parts of Europe. This was one of the motivations behind the NERC project on Improving Predictions of Drought for User Decision Making (IMPETUS), under which this study was funded. The aim of IMPETUS was to improve UK drought forecasts on monthly to decadal timescales, by improving meteorological, hydrological and water demand forecasts and how they were combined to produce drought forecasts. According to the National Oceanic and Atmospheric Administration (NOAA), there are four types of droughts. Meteorological drought is based on the degree of rainfall deficit and the length of the dry period. Hydrological drought is based on the impact of rainfall deficits on the water supply. Agricultural drought refers to the impacts on

agriculture by the rainfall deficits. Socioeconomic drought considers the impact of drought conditions on supply and demand of economic goods. In this study, we focus on meteorological drought referring to rainfall deficit only, and consider droughts that are on the seasonal timescale.

Seasonal forecasts provide estimates of the seasonal statistics. One of the major skills originates from the ocean, which has a predictable signal with a timescale often longer than the atmosphere. Of particular importance is the El-Niño Southern Oscillation (ENSO), an ocean-atmosphere coupled phenomenon originating from the tropical Pacific. ENSO has global teleconnections in both the ocean and the atmosphere. For example, it affects global ocean basins through surface heat fluxes from atmospheric bridges (Alexander et al., 2002). The rearrangement of the convections in the Walker circulation also causes anomalous precipitation in other ocean basins globally (Dai and Wigley, 2000). And the anomalous tropospheric divergences in the tropics drive planetary scale Rossby waves into the extratropics to cause global atmospheric teleconnections (Trenberth et al., 1998). The importance of ENSO in seasonal forecasts is its predictability. For example, in a study of ENSO hindcasts using a suite of coupled general circulation models (GCMs), Jin et al. (2008) showed that ENSO could be predicted with an anomaly correlation coefficient of 0.86 six months ahead.

Seasonal forecasts are still challenging, particularly for precipitation and away from the El-Niño region (Weisheimer and Palmer, 2014). One region that is particularly challenging is Europe. Europe is affected by several large-scale atmospheric dynamical processes that are still not well-represented in current models (Woollings, 2010). These include the aforementioned jet stream, storm tracks, Rossby waves and the North Atlantic Oscillation (NAO). The NAO is described by the anti-correlated patterns in sea level pressure between Iceland and the Azores. Together with ENSO, NAO is a major source of seasonal variability in the global atmosphere (Wanner et al., 2001).

Until recently, forecast models struggled to predict the NAO at seasonal lead times (Smith et al., 2012). Some observations and modelling studies have sug-

gested potential sources of skill in NAO prediction, such as ENSO, North Atlantic sea surface temperatures (SSTs), Arctic sea ice, Eurasian snow cover, the Quasi-Biennial Oscillation (QBO) and solar variability. Using an atmosphere-only dry model, Derome et al. (2005) showed statistically significant skill in forecasting the Arctic Oscillation (AO), which is a pattern highly correlated with the NAO (Ambaum et al., 2001). Even in the absence of a strong ENSO-like forcing, their model still showed significant skill in predicting the AO, indicating the skill was not related to ENSO. As Lin et al. (2002) and Greatbatch et al. (2003) had shown that part of the winter AO variability was related to anomalous tropical atmospheric forcings, the skill might have come from the tropics outside of the ENSO region. Using fully coupled atmosphere-ocean models, Müller et al. (2005) found a small but statistically significant skill in predicting the seasonal NAO, for the period 1987 to 2001. Although the multi-model yielded an enhancement of the NAO skill related to the improved representation of uncertainty, the skill was still occasional as the skill became statistically insignificant for the period 1959 to 2001.

Scaife et al. (2014) also showed skilful seasonal prediction of the wintertime NAO, for the hindcast period of 1993 to 2012. The model they used, the Met Office seasonal forecasting system Global Seasonal forecast system version 5 (GloSea5), had been specifically designed to capture the potential sources of predictability mentioned above (Smith et al., 2016). Their GloSea5 hindcasts showed correlations greater than 0.6 between observations of the wintertime NAO and the ensemble mean, with members initiated around the the beginning of November each year. Although the NAO seasonal forecast skill was later shown to be dependent on the state of the NAO in a study spanning a longer period from 1900 to 2009 with a different model which has generally lower NAO skill (Weisheimer et al., 2017), with the positive phase having higher predictability than the negative phase, it was still worth investigating where the skill in forecasting the recent decades of the positive NAO originated. In the follow up study by Scaife et al. (2017), they showed that tropical rainfall explained 40 percent of the variance in the seasonal forecast of the NAO. Through ray tracing, they suggested the mechanism to be

stationary, linear, barotropic Rossby wave propagation from the tropics.

Apart from seasonal forecasts, there are also large uncertainties in climate projections with important consequences. One of the atmospheric variables that shows large uncertainty in projections is precipitation, which is affected by both dynamical and thermodynamical changes. For projections into the end of the $21^{st}$ century, the IPCC AR5 report (Collins et al., 2013, figure 12.22) highlighted the need to reduce regional precipitation projection uncertainty. In an earlier study using CMIP3 multi-model ensemble, Hawkins and Sutton (2011) decomposed the climate projection uncertainty in regional precipitation into three factors, namely internal variability, emission (RCP) scenario uncertainty and model uncertainty. Scenario uncertainty was found to be small; internal variability was found to be dominant for up to three decades in the projection; model uncertainty, regarding different model responses to the same forcing, was found to be dominant for longer lead times. This showed that in order to reduce regional precipitation projection uncertainty, it was important to reduce model uncertainty.

Using CMIP5 projections, Fereday et al. (2018) investigated the precipitation uncertainties over Europe. They isolated the dynamical component of European precipitation based on mean sea level pressure, with the other component being the thermodynamical component related to water vapour changes. By comparing the intermodel variance in European precipitation trends in future projections before and after the removal of the dynamical component, they showed that more than half of this variance was related to the uncertainty in future atmospheric circulation projection. Looking into the mechanism related to the dynamical component, Fereday et al. (2018) suggested the importance of tropical rainfall in driving Rossby waves into Europe. To reduce this intermodel variance in European precipitation trends, in addition to reducing the uncertainty in tropical rainfall projections, another solution might be by improving the forced dynamical response in these models. Zappa et al. (2015) also used CMIP5 projections to investigate the wintertime Mediterranean precipitation change. They found that a large fraction of intermodel variance was related to atmospheric circulation

changes in North Africa, whereas the thermodynamical contribution was little. This agreed with Fereday et al. (2018), although the regions were not exactly the same but still very close to each other. This showed that at least for some regions like the Mediterranean, atmospheric circulation contributed more than thermodynamics towards the model uncertainty in precipitation.

The reason that atmospheric dynamics is more uncertain than thermodynamics in future projections is because the former responds indirectly to radiative forcing, while the latter responds directly. Changes in radiative forcing perturbs the climate thermodynamic system directly, with a response typically distinct from the internal variability (Stott et al., 2000). In the extratropics, radiative forcing can perturb the circulation indirectly for example through eddy feedbacks, which then perturbs the dynamical balance between eddy momentum fluxes in the free atmosphere and friction in the boundary layer. It has been suggested that the mean response of the climate system to forcing should resemble the dominant patterns of natural variability, which should themselves remain unchanged (Palmer, 1999). This has been investigated in some studies. For example, Deser et al. (2004) looked at the wintertime atmospheric circulation response to the observed North Atlantic sea surface temperature and sea ice anomalies in recent decades in a GCM. They found that the part of the response which projected onto the leading mode of internal variability, dominated the total geopotential height response and resembled the NAO or the northern hemisphere annular mode. As this projection of future climate response onto the modes of natural variability can be strong, Shepherd (2014) suggested that there was hope that further understanding of the errors in present-day model dynamics could reduce the dynamical uncertainty in future projections, in agreement with the suggestion in Fereday et al. (2018). This is another motivation for us to look at present-day dynamics, in addition to the aforementioned motivation from seasonal forecasting.

## 1.2 Extratropical atmospheric variability

Apart from the tropical rainfall mentioned in Scaife et al. (2017), extratropical atmospheric variability is also important in driving the NAO at seasonal timescale. Feldstein (2003) looked at the NAO life cycle on a much shorter timescale of around 10 days. By a composite analysis of each term in the streamfunction tendency equation, they showed that transient eddy vorticity fluxes were important for the growth, maintenance and decay of both phases of persistent NAO episodes. This could have implications at a longer timescale, as some of the variability on seasonal timescale can be noise from shorter timescale.

Rossby wave breaking is an important mechanism in extratropical atmospheric variability. Such wave breaking at upper levels can cause mid-latitude blocking (Pelly and Hoskins, 2003). Yao and Luo (2015) gave observational evidence between blocking and the NAO. They showed that northern European blocking led NAO- and southern European blocking lagged NAO+. Woollings et al. (2008) found that high-latitude blocking events in the North Atlantic, which they termed Greenland blocking events (GBEs), were dominated by cyclonic wave breaking. Before GBE onsets, both a northern Europe blocking, and a quasi-stationary equivalent barotropic Rossby wave across North America with transient waves passing through it at group velocity, were identified. The northern European blocking imposed a diffluent flow over the Atlantic, leading to meridionally elongated transient eddies, which favored wave breaking. The transients strengthened the wave up until onset, when the wave amplitude was strong enough for wave breaking. In the onset of the GBEs, anomalous transient eddies across southern North America advected the anomalous warm subtropical air up to the poleward side of the jet, forming the block. The middle tropospheric heating associated with cyclones in the storm track to the south could also have amplified the upper troposphere negative potential vorticity (PV) anomaly from the anomalous subtropical air. During the GBEs, NAO- happened. The GBEs and NAO- time series correlation was strong both interannually and interdecadally. The GBEs in-

creased the likelihood of subsequent wave breaking, which maintained the blocking through feedbacks.

This was in agreement with Benedict et al. (2004), which suggested that cyclonic breaking of upper-level Rossby waves led to NAO-. Although Benedict et al. (2004) also suggested that anticyclonic breaking led to NAO+, the absence of such anticyclonic wave breaking in Woollings et al. (2008) could be due to their time and spatial scales applied, which prevented transient identifications. In the viewpoint of Woollings et al. (2008), NAO+ could be considered as the unblocked state of the atmosphere, while NAO- could be considered as the occurrence of high latitude Greenland blockings.

Looking further upstream, Drouard et al. (2013) used reanalysis to identify an anomalous ridge in the northeastern Pacific associated with NAO+, and an anomalous trough in the same region associated with NAO-. Using a three-level quasigeostrophic model, they showed that the ridge anomaly induced more equatorward propagation of synoptic-scale wave downstream, which favoured anticyclonic wave breaking in the North Atlantic and NAO+. Similarly, they showed that the trough anomaly induced more poleward propagation of these waves, which favoured cyclonic wave breaking and NAO-. In a follow-up study using reanalysis, Drouard et al. (2015) confirmed this mechanism of the planetary-scale ridge or trough anomaly affecting the downstream propagation of synoptic wave. These studies are in line with Woollings et al. (2008) and Benedict et al. (2004), and shows that the extratropical atmospheric variability in different regions can be closely connected.

Extratropical atmospheric variability also has many different timescales. In the monthly timescale, Wallace and Gutzler (1981) identified recurrent patterns like the NAO and the Pacific-North American pattern (PNA). The PNA consists of a north-south seesaw in geopotential heights in the central Pacific, with the positive phase having higher height in the subtropical Pacific and lower height in the North Pacific, together with higher height in western Canada and lower height in southeastern USA. In a study with more detailed separation in timescale,

Blackmon et al. (1984a) identified extratropical variability patterns associated with short (2 to 6 days), intermediate (10 to 30 days) and long (above 30 days) timescales. Their long timescale patterns agreed with Wallace and Gutzler (1981), and their intermediate and short timescale results showed wave patterns of lower and higher zonal wavenumber respectively.

Rennert and Wallace (2009) further investigated the interactions between these timescales by looking at the cross-frequency couplings. For the coupling between the long and intermediate timescales, they found that in the North Atlantic, long timescale NAO- was associated with enhanced intermediate timescale variance over Greenland. This was due to enhanced GBEs and cyclonic wave breaking in this region, in agreement with Woollings et al. (2008); whereas in the NAO+ state, GBEs were infrequent and the flow was unblocked, resulting in lower variance. For the coupling between the long and short timescales, they found that the baroclinic waves reinforced the background flow. In another study that looked at the interaction between the longer and shorter timescales, Branstator (2002) showed that the waveguiding effect of the time-averaged tropospheric jets on shorter timescale disturbances matched well between observations and theory.

Combining the studies of Branstator (2002) and Rennert and Wallace (2009), we investigate the effect of the longer timescale NAO on the propagation of shorter timescale disturbances using observations. We apply temporal filtering onto daily geopotential height on 500 hPa from the NCEP-NCAR reanalysis 1 (Kalnay et al., 1996), and perform empirical orthogonal function (EOF) analysis (Hannachi et al., 2007) on the filtered data. The period we focus on is the northern hemisphere winter (DJF) 1949 to 2014. Using similar timescales as Rennert and Wallace (2009), after removing the seasonal cycle by computing the climatology of each calendar day, we filter the anomaly into three timescales, namely short (less than 6 days), intermediate (6 to 30 days) and long (more than 30 days). To minimize the Gibbs phenomenon with a sharper cutoff than the filtering used in Rennert and Wallace (2009), we use a Lanczos filter (Duchon, 1979), with 1.5 months as the Lanczos filtering window on either side of the concerned day (Kallberg et al.,

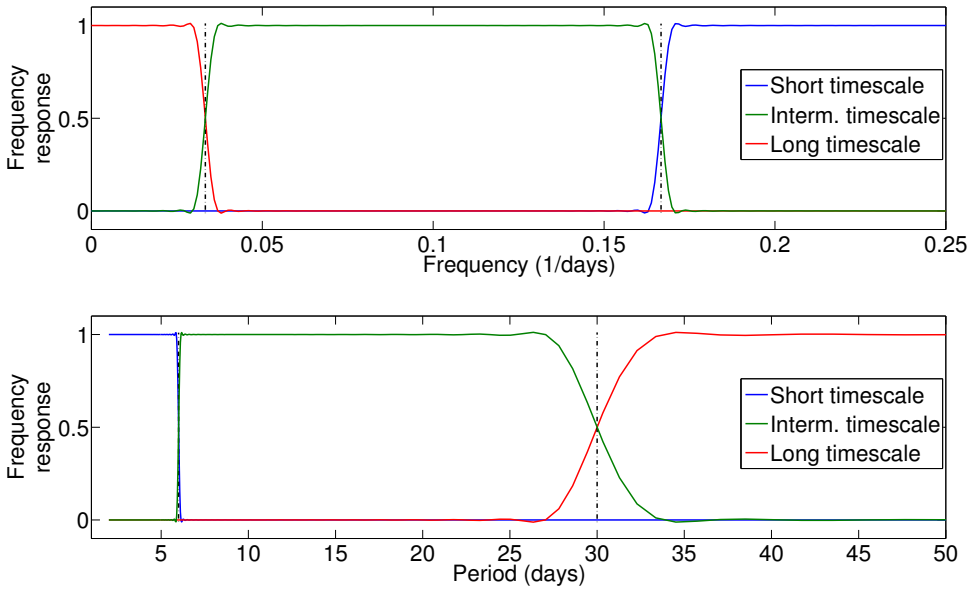
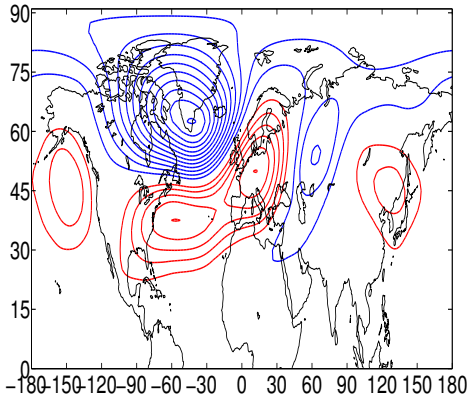



Figure 1.1: Frequency response for the filters used to isolate low, intermediate and long timescales.

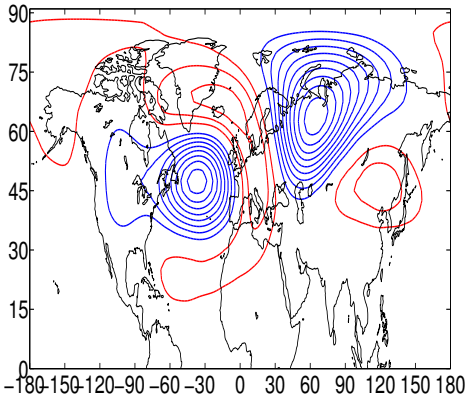
2005). The filter response is shown in figure 1.1.

We reproduce the EOF analysis of Rennert and Wallace (2009) over the Atlantic region (20°-90°N, 90°W-90°E) in figure 1.2. The leading mode for the long timescale is the NAO (figure 1.2a) in agreement with Wallace and Gutzler (1981) and Blackmon et al. (1984a), followed by the East Atlantic (EA) pattern (figure 1.2b). The two leading modes for the intermediate timescale (figures 1.2c and 1.2d) are zonally-orientated and eastward-propagating waves originating from the North Atlantic jet entrance and propagating along the jet, in agreement with Blackmon et al. (1984a). Finally, the leading modes for the short timescale (figures 1.2e and 1.2f) are zonally-orientated waves with a higher wavenumber of 6 to 7, propagating along the climatological storm tracks, in agreement with Blackmon et al. (1984a). In a follow up study to Blackmon et al. (1984a) looking at the time variations of these patterns, Blackmon et al. (1984b) showed that the short and intermediate timescale waves were baroclinic waves and Rossby waves respectively, and the long timescale patterns resembled the fastest growing barotropic instability normal modes of the climatological flow.

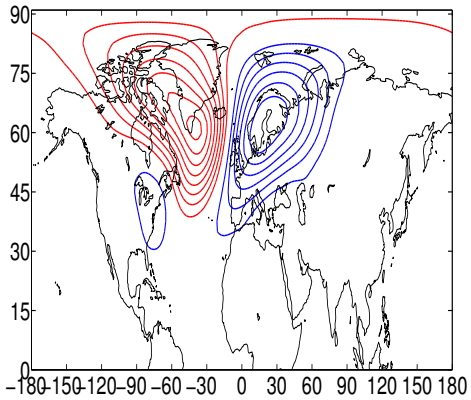
(a) 22%.



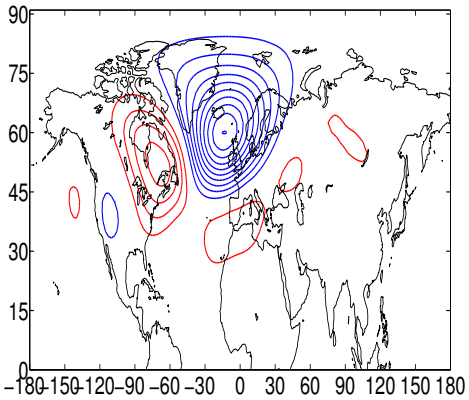

(b) 15%.



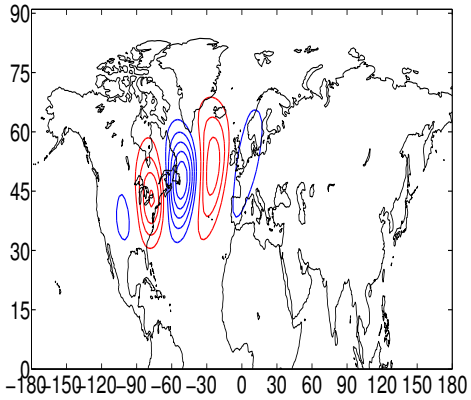

(c) 13%.




(d) 11%.




(e) 11%.




(f) 11%.

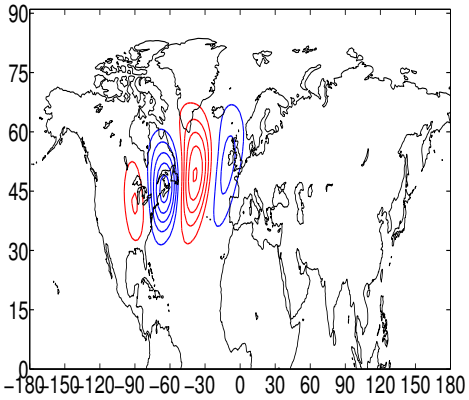



Figure 1.2: EOFs for Atlantic DJF daily 500 hPa geopotential height filtered with the frequency response shown in Figure 1.1. The rows are long, intermediate and short timescales from top to bottom. Left column is EOF1 and right column is EOF2. Percentage of variance explained is indicated with each figure.

From the theory of Rossby wave propagation on a basic state, because of this separation in timescales, the longer timescale modes can affect the basic state on which the waves propagate and can lead to different propagations. We aim to test this propagation sensitivity to the basic state by using observations only. Using the EOF-based NAO seasonal indices from Hurrell et al. (2013), we define our positive and negative NAO periods to be the top and bottom sixth of the data (11 years each, from the 66-year period) of the index. Figures 1.3a and 1.3b show the unfiltered zonal wind composites. In positive NAO, the North Atlantic jet is more tilted, whereas it is more zonal in negative NAO.

We use lag correlations to investigate wave propagation under these two basic states. We choose the base point to be at the centre of the North Atlantic (43°N 300°E), and perform correlations on the intermediate timescale meridional wind at 300 hPa. A correlation map is done by calculating the correlation coefficients of the time series at the base point with the corresponding time series at all the grid points. For a correlation map with a lag of -2 days, the DJF time series of the base point is correlated with the time series of DJF minus 2 days (i.e. $29^{th}$ November to $26^{th}$ February) for each year, and these 11 values of correlations are averaged to give the correlation at each grid point. By construction, the correlation at the base point at zero lag is always 1, and slightly less than 1 for non-zero lag because of autocorrelation.

At lag -2 days (figures 1.3c and 1.3d), the correlations show similar waves for both phases of the NAO, propagating from the west coast of the USA across North America into central North Atlantic. At lag 0 days (figures 1.3e and 1.3f), both waves reach eastern North Atlantic. At lag 2 days (figures 1.3g and 1.3h), the waves are very different. In the positive phase of the NAO, the wave propagates strongly at higher latitudes into Scandinavia and only weakly into the equatorial Atlantic. In the negative phase, the wave propagates strongly into northwestern Africa, with no propagation over Scandinavia. These findings are consistent with the different North Atlantic jet orientations and with the waveguide theory from Hoskins and Ambrizzi (1993), which showed that a strong jet could act as a

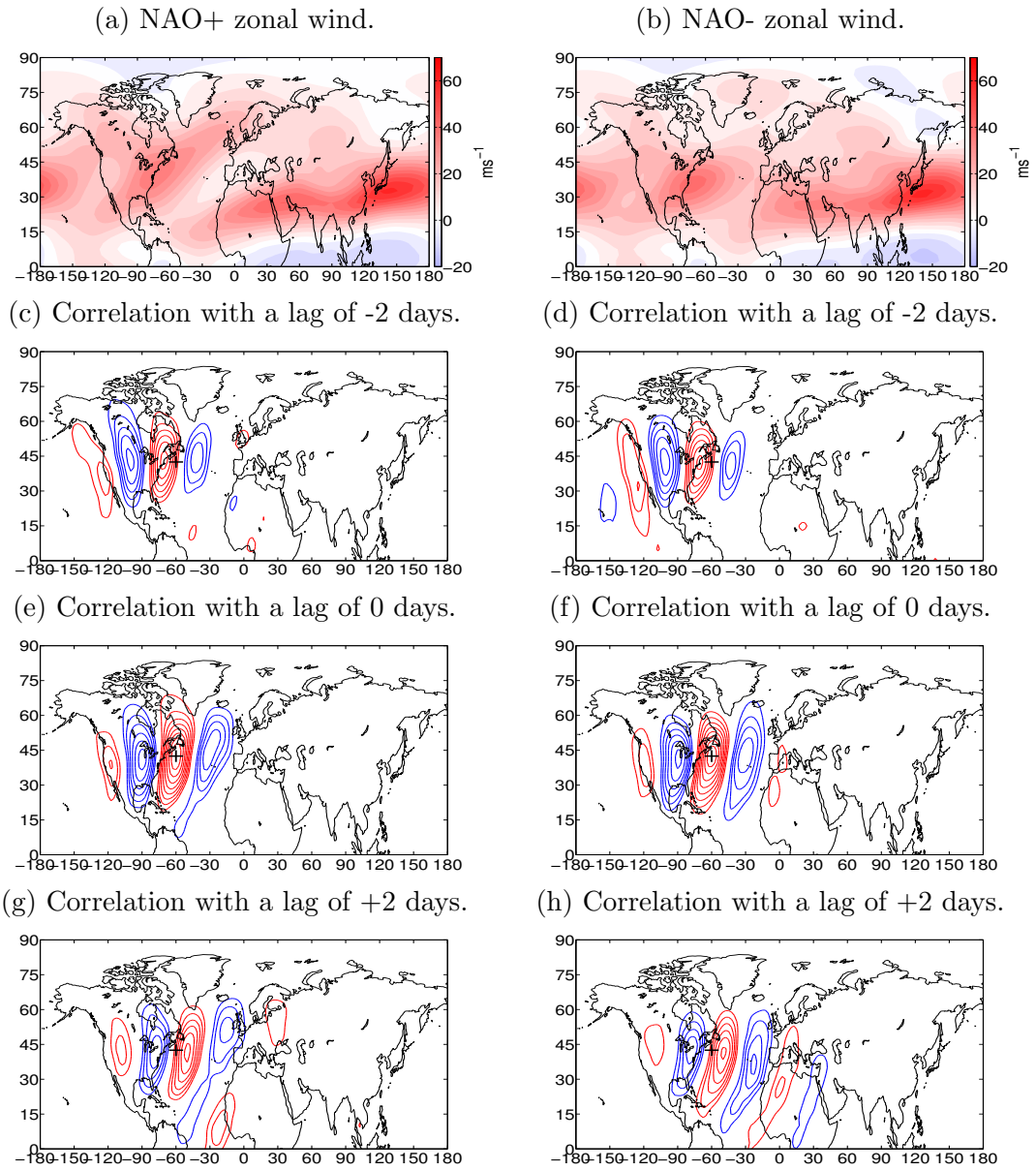



Figure 1.3: Unfiltered 300 hPa zonal wind for DJF NAO+ (left column) and NAO- (right) composites, and lag correlation maps of intermediate timescale 300 hPa meridional wind at base point 43°N 300°E (marked by a "+"). Contour interval 0.1 with red (blue) for positive (negative). Contours at 0, -0.1 and +0.1 are not shown.

waveguide for Rossby waves.

To illustrate wave propagation and waveguide, we use the schematic diagram from Hoskins and Ambrizzi (1993, figure 2). The propagation depends on the latitudinal variation of the stationary wavenumber $K_s$, which we will further discuss in section 2.2. The stationary wavenumber depends on the zonal wind in the flow, and determines the latitude at which poleward propagating waves reflect equatorward. Figure 1.4b illustrates a wave reflecting at the latitude where the stationary wavenumber equals the zonal wavenumber of the wave. If the stationary wavenumber shows a maximum between two minima (figure 1.4e), which is particularly likely to occur in a strong westerly jet, reflection also occurs on the equatorward side and results in a waveguide effect.

To summarize, the dynamics of the longer timescale planetary teleconnection patterns can affect the intermediate timescale wave dynamics through perturbing the basic state. This highlights the importance of the basic state in Rossby wave propagation, which we will investigate more in the thesis.

## 1.3 Rossby wave theory

Mathematically, Rossby waves can be derived by considering small amplitude perturbations to a basic flow. Here, we follow the derivation in Andrews (2010). For example, consider a uniform zonal basic flow (U,0,0) where U is a constant. This flow corresponds to a geostrophic streamfunction $\psi = -Uy$, and including the perturbation this becomes $\psi = -Uy + \psi'$. Since Rossby waves have large horizontal wavelengths, they have low Rossby number $Ro \equiv \frac{U}{fL}$, where $f$ is the Coriolis parameter and $L$ is the horizontal length scale. Therefore, they satisfy the quasi-geostrophic potential vorticity (QGPV) equation (equation 1.1), which required the Rossby number to be small.

$$D_g q = 0 \tag{1.1}$$

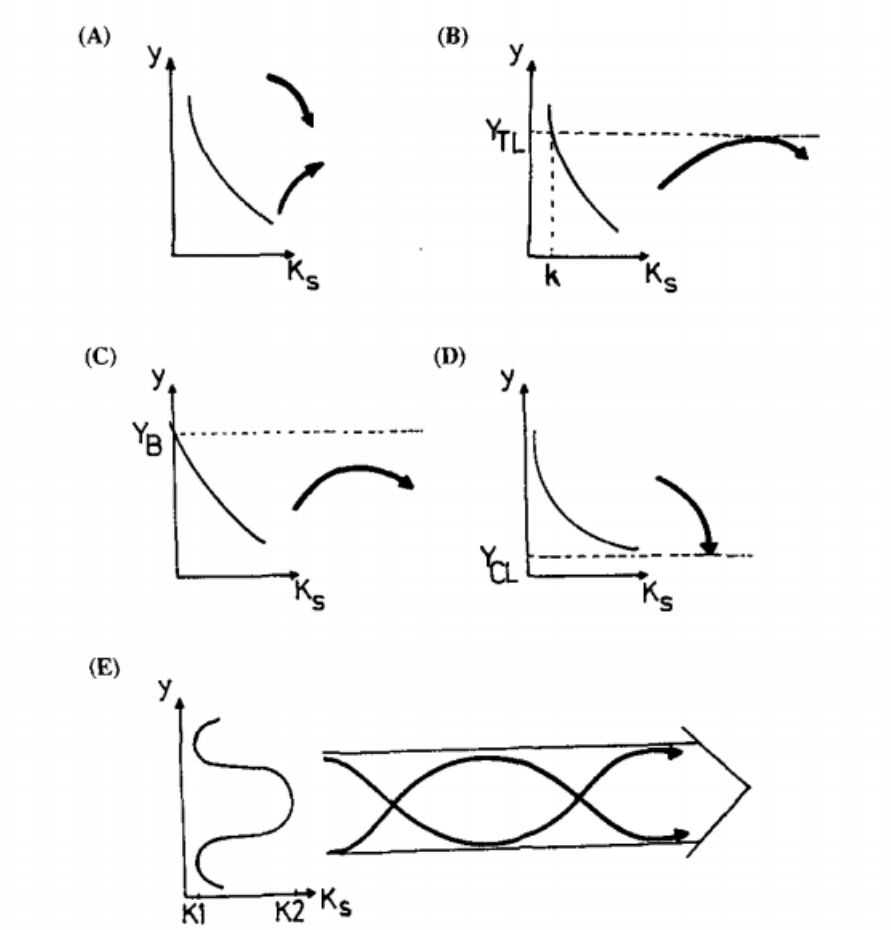



FIG. 2. Schematic stationary Rossby wavenumber ($K_s$) profiles and ray path refraction. In each panel, $K_s$ is shown as a function of $y$ and schematic ray paths are shown by heavy lines with arrowheads. (a) simple refraction; (b) reflection from a turning latitude $Y_{TL}$ at which $K_s = k$; (c) reflection of all wavenumbers before a latitude $Y_B$ at which $\beta_* = 0$; (d) refraction into a critical latitude $Y_{CL}$ at which $\bar{U} = 0$; (e) waveguide effect of a $K_s$ maximum. For more discussion see text.

Figure 1.4: Schematic diagram explaining Rossby wave propagation on a flow with varying stationary wavenumber. Figure is from Hoskins and Ambrizzi (1993, figure 2).

where the material or advective derivative in time following the geostrophic flow is defined as

$$D_g \equiv \frac{\partial}{\partial t} + u_g \frac{\partial}{\partial x} + v_g \frac{\partial}{\partial y} \tag{1.2}$$

and the QGPV is

$$q \equiv f_0 + \beta y + \frac{\partial^2 \psi}{\partial x^2} + \frac{\partial^2 \psi}{\partial y^2} + \frac{\partial}{\partial z}\left(\frac{f_0^2}{N_B^2}\frac{\partial \psi}{\partial z}\right) \tag{1.3}$$

where $f_0 = 2\omega \sin \phi_0$ is the f-plane approximation at the tangent plane at latitude $\phi_0$ and $\omega$ is the rotation rate of the Earth; $\beta = \frac{2\omega \cos \phi_0}{a}$ is the $\beta$-plane approximation and $a$ is the radius of the Earth; $N_B^2 \equiv -\frac{g}{\rho_0}\frac{d\overline{\rho}}{dz}$ is the square of the buoyancy frequency for the stratified incompressible flow, $g$ is the gravitational constant, $\overline{\rho}(z)$ is the background density and $\rho_0$ is a reference value of the background density. The first two terms on the right-hand side of equation 1.3 combine to give the planetary vorticity, and the remaining three terms combine to give the relative vorticity. This equation shows that the QGPV is conserved following the geostrophic flow, when friction and diabatic heating and mass sources are neglected. Substituting a plane-wave solution of the perturbed streamfunction into the QGPV equation, the dispersion relation for Rossby waves can be derived.

$$\omega = kU - \frac{\beta k}{k^2 + l^2 + \frac{f_0^2 m^2}{N_B^2}} \tag{1.4}$$

where $\omega$ is the frequency, $k$ is the zonal wavenumber, $l$ is the meridional wavenumber and $m$ is the vertical wavenumber. The zonal phase speed ($c_p$) and the zonal component of the group velocity ($c_g^{(x)}$) are given by

$$c_p = \frac{\omega}{k} \qquad , \qquad c_g^{(x)} = \frac{\partial \omega}{\partial k} \tag{1.5}$$

An important property is that the $\beta$ effect is crucial to the existence of these waves. Also, according to the Charney-Drazin criterion (Charney and Drazin, 1961), stationary waves can only propagate vertically in westerly basic flows that are not too strong, and that long waves can propagate vertically under a wider range of westerly flows than short waves. This has consequences in the stratosphere, for example long waves are observed only in the northern hemisphere

winter stratosphere where the basic flow is westerly, and are not observed in the summer stratosphere where the basic flow is easterly.

Physically, Rossby wave describes large masses of air moving horizontally, with the masses being displaced mostly northward and southward. For the rotating Earth, planetary vorticity increases with the latitude. Under the conservation of QGPV, a northward-moving air mass must lose some of its relative vorticity, and so it must develop anomalous anticyclonic circulation around itself; whereas a southward-moving air mass must gain some relative vorticity and develop anomalous cyclonic circulation around itself. These anomalous relative vorticities influence neighbouring air masses in such a way as to propagate the original disturbance towards the west, upstream of the background flow. The reason behind the often observed eastward propagation of Rossby waves is that in addition to propagating upstream in the background flow, the wave is also carried along with the background flow which is often westerly.

In this thesis, we focus on stationary Rossby waves, which propagate at the group velocity but with zero phase velocity, because they can cause persistent anomalies and have larger regional impact than non-stationary waves.

## 1.4 Tropical-extratropical teleconnection

This thesis focuses on the tropical-extratropical teleconnections. Here, we provide an overview on this topic. As demonstrated in the seasonal hindcasts in Scaife et al. (2017), on a seasonal timescale a significant fraction of extratropical atmospheric variability could be explained by the tropics through tropical rainfall triggering Rossby waves. Early studies have demonstrated the extratropical Rossby wave response to tropical diabatic heating, using simple barotropic and baroclinic models (e.g. Hoskins and Karoly, 1981; Simmons, 1982). The wave responses were not only sensitive to the longitude of the tropical heating, but also sensitive to the basic state in the extratropics. For example, Ting and Sardeshmukh (1993) reported differences in the extratropical wave responses when running the heating experiment with the same source but with two climatologies of different periods.

Two major drivers of tropical variability are the ENSO and the Madden-Julian oscillation (MJO). The MJO is a coupled ocean-atmosphere phenomenon, described by packets of alternating wet and dry periods that propagate eastward from the western Indian Ocean to the central Pacific Ocean with a period between 30 and 60 days (Madden and Julian, 1972). The extratropical pattern associated with the MJO extends over the North Pacific, North America, the Atlantic, the Southern Ocean and South America. Using a GCM linearized about the climatological basic state, Matthews et al. (2004) showed that this pattern was consistent with Rossby waves propagation from the tropics. MJO has also been shown to affect mid-latitude Rossby wave breaking and high latitude blockings (Henderson et al., 2016), and subsequently the NAO (Cassou, 2008).

In the ENSO review by Brönnimann (2007), apart from tropospheric horizontal Rossby wave propagation, ENSO in the tropics could affect European weather through modifying the Walker circulation over the Pacific and the Atlantic, which in turn could modify the Atlantic Hadley cell. The stratosphere could also play a role, where vertically propagating tropospheric Rossby waves could weaken the polar vortex and cause sudden stratospheric warming (SSW), which then could have a downward propagating signal over Europe (Bell et al., 2009).

The ENSO extratropical response also has a notable non-linear aspect. Hoerling et al. (1997) discovered a phase shift of around 35° in the extratropical teleconnection pattern between warm and cold events. In addition, the maximum tropical rainfall anomalies were located east of the Date Line during warm events, but west of the Date Line during cold events. Using models, they explained the extratropical phase shift by the nonlinearity of the tropical rainfall. Another aspect of nonlinearity in ENSO teleconnection is from the stratosphere (Toniazzo and Scaife, 2006). In intermediate El-Niño events, the stratospheric pathway dominated the tropospheric pathway for European winter climate. But for strong El-Niño events, the tropospheric forcing dominated the European response. This was later confirmed using GCMs by Bell et al. (2009). The North Atlantic response was also shown to be not symmetric for large El-Niños and large

La-Niñas (Hardiman et al., 2019). They showed that while the tropospheric teleconnection grew linearly with ENSO, the stratospheric response was asymmetric. The dominant pathway was tropospheric for large El-Niños, in agreement with Toniazzo and Scaife (2006) and Bell et al. (2009), while the dominate pathway was stratospheric for large La-Niñas.

Regarding the relative importance of the tropics and the stratosphere, Newman and Sardeshmukh (2008) found that in general, the tropics had a larger influence on the extratropical tropospheric variability than from the stratosphere. However, the conclusion can be different depending on the type of events and the regions studied. For example, in a study looking at the impact of strong ENSO events on the North Atlantic, Hardiman et al. (2019) found that the dominant pathway is stratospheric for strong La-Niña events and tropospheric for strong El-Niño events.

The teleconnection is not necessarily always from the tropics into the extratropics. Using five-day averages of observed mid-latitude geopotential heights and tropical outgoing longwave radiation (OLR), Liebmann and Hartmann (1984) found that while the dominant teleconnection in the western Pacific was the tropics forcing the extratropics, it was dominated by the other direction in the eastern Pacific. The mechanism suggested for the latter was also Rossby waves, although they were propagating equatorward from the extratropics instead of poleward into the extratropics. In addition to the eastern Pacific, Kiladis and Weickmann (1992) also found similar conclusion for the Atlantic Inter Tropical Convergence Zone (ITCZ) using observations, as well as with GCMs (Kiladis and Feldstein, 1994).

The MJO also seems to be a two-way tropical-extratropical interaction. Matthews and Kiladis (1999) showed that the structure of the Asian-Pacific jet that acted as a Rossby waveguide changed according to the phase of the MJO. When the MJO was in the phase with enhanced convection over the east Indian Ocean and Indonesia, the climatological waveguide weakened. High frequency (6 to 25 days) transient Rossby waves could leak into the tropics, which could induce enhanced

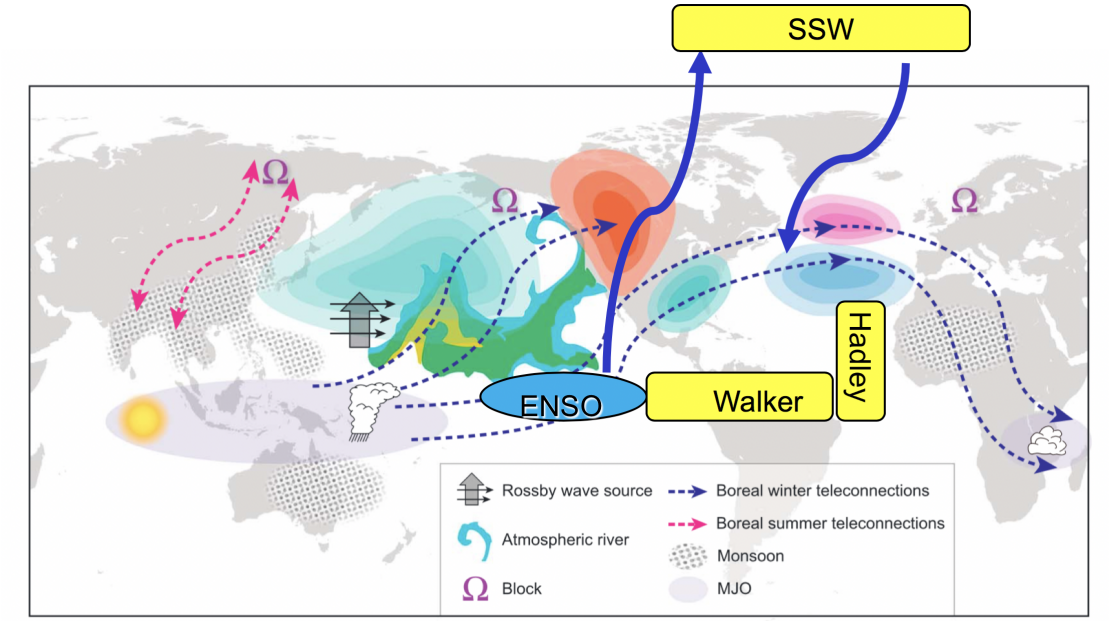



Figure 1.5: Summary schematic indicating the main features of tropical-extratropical interactions. Adapted and modified from Stan et al. (2017, figure 6).

convective variability near the Date Line in the tropics. This could project back onto the intraseasonal timescale of the MJO and affect its associated diabatic heating.

While ENSO has the strongest impact on the climate in the central and eastern Pacific, Yang et al. (2002) identified an East Asian jet stream pattern (EAJS) with strongest impact in east Asia and western Pacific which was not strongly linked to ENSO. A strong EAJS was associated with a decrease in the extratropical North Pacific sea surface temperature (SST). A strong EAJS was also related to a strong east-southeastward propagation of stationary waves, and was related to enhanced convections over the equatorial Asian-Australian region. This might suggest a possible link from extratropical SST to tropical convection.

Figure 1.5 shows the main features of the tropical-extratropical interactions. The tropical convections of the MJO (grey shading with cloud symbol) creates upper level divergence (grey block arrow), which acts across the vorticity gradients (thin black arrows) to create Rossby wave sources. Poleward propagating Rossby waves are triggered from the tropics, and affect the dominant modes of variability

in mid-latitudes, including the NAO (pink and blue shading) and the PNA (light green and orange shading). Blocking frequencies are also affected (indicated by $\Omega$). Atmospheric rivers (dark green and the yellow shading), which are highly focused streams of precipitable water important for extratropical vapor transport, are also affected by Rossby wave propagations especially in the eastern Pacific. The global monsoon systems (dotted pattern) also interact with the mid-latitudes. For example, mid-latitude circulation anomalies can feed back onto the subsequent evolution of tropical convection and can feed back onto new MJO phases. The other major driver of tropical variability, the ENSO, can trigger Rossby wave propagation into North America. ENSO can affect Europe through the Walker circulation and the Atlantic Hadley cell, and it can also affect Europe through the stratosphere by causing SSWs.

In this thesis, we aim to understand the contributions of the linear propagation of stationary tropospheric Rossby waves from the tropics into the extratropics to the seasonal tropical-extratropical teleconnection for some events, and their representations in a climate model.

## 1.5 Thesis outline

In chapter 2, we explain the methods in our investigations, and reproduce some literature results to justify our model settings.

In chapter 3, we begin by investigating the leading patterns of covariability between the tropics and the extratropics in the whole of the northern hemisphere in reanalysis data, at both seasonal and daily timescales. We then compare these teleconnections with those identified in a free-running present-day climate model control simulation, to identify the tropical-extratropical covariance bias in the climate model.

In chapter 4, we investigate to what extent does the model climatological jet bias contribute to the identified covariance bias identified in chapter 3, through linear stationary Rossby wave propagation. We make use of ray tracing, barotropic

model and also baroclinic model to test the sensitivity of Rossby wave propagation to the basic state bias.

In chapter 5, we continue with the tropical-extratropical teleconnection theme but focus on European precipitation and drought events. Using similar methods as in chapter 4, we investigate to what extent does Rossby wave propagation from the tropics contribute to the extratropical large-scale anomalies associated with these European events. Whereas we focus on the effect of basic state on wave propagation in chapter 4, in this chapter we focus on the contributions from different tropical sources on the same basic state.

In chapter 6, we conclude our findings, comment on the usefulness of our methods, and suggest future work. Finally, plots that are useful but not essential are included in the appendix.

# Chapter 2

# Methods

## 2.1 Maximum covariance analysis

Maximum covariance analysis (MCA) looks for patterns in two space-time datasets which explain a maximum fraction of the covariance between them (Wilks, 2011b). Let $S$ be the tropical outgoing longwave radiation (OLR), measured n times at p locations ($S$ is n by p), and $P$ be the extratropical 500 hPa geopotential height (Z500), measured n times at q locations ($P$ is n by q). Each column of $S$ contains a time series for a particular location, and each row contains a map for a given time, and similarly for $P$. After removing the time mean of each field, we form the cross-covariance matrix $C$,

$$C = S^t P \tag{2.1}$$

It is also possible to scale the variability in $S$ and $P$ by dividing each time series by its standard deviation, to obtain the cross-correlation matrix. The reasoning is that if one set of variables has much higher amplitude variability than the other, the variability in that field may dominate the covariance structure between the matrices. We then perform a singular value decomposition (SVD) on the cross-covariance matrix, such that we find matrices $U$ and $V$ and a diagonal matrix $L$ that satisfy

$$C = ULV^t \tag{2.2}$$

The singular vectors for $S$ are the columns of $U$, and the singular vectors for $P$ are the columns of $V$. Each pair of singular vectors is a mode of covariability between

the fields $S$ and $P$. The columns of $U$ and $V$ are called the left and right patterns respectively. Similar to the EOFs, these patterns represent standing oscillation in the data fields. Succeeding SVD modes maximize the covariance, subject to the constraint that the singular vectors be spatially orthogonal to the previous modes.

To find the time series describing how each mode of variability oscillates in time (the expansion coefficients), we project the data matrices onto these modes,

$$A = SU \qquad , \qquad B = PV \tag{2.3}$$

where the columns of the matrices $A$ and $B$ contain the expansion coefficients of each mode. For example, because $U$ and $V$ are both orthogonal, the original data matrices $S$ and $P$ can be recovered by

$$S = AU^t \qquad , \qquad P = BV^t \tag{2.4}$$

The correlation between the expansion coefficients of the two fields for one mode indicates how strongly related the couple patterns of this mode are. The expansion coefficients associated with different modes are not guaranteed to be uncorrelated however (Bretherton et al., 1992), a property different to the EOF.

The singular values are given by the diagonal of $L$. The total squared covariance in $C$ is given by the sum of the squared diagonal values of $L$. Each mode explains an amount of the overall squared covariance in the covariance matrix given by the square of the singular value. The squared covariance fraction (SCF) assesses the relative importance of each mode. If $l_i = L(i,i)$ is the $i^{th}$ singular value, the SCF explained by the corresponding singular vectors $\overrightarrow{u_i}$ and $\overrightarrow{v_i}$ is

$$SCF_i = \frac{l_i^2}{\sum l_i^2} \tag{2.5}$$

North et al. (1982) defined the typical errors between two neighbouring eigenvalues $\lambda$ and between two neighbouring eigenvalues $\psi$ by

$$\Delta\lambda_k \approx \sqrt{\frac{2}{n}}\lambda_k \tag{2.6}$$

$$\Delta\psi_k \approx \frac{\Delta\lambda_k}{\lambda_j - \lambda_k}\psi_j \tag{2.7}$$

where $\lambda_j$ is the eigenvalue closest to $\lambda_k$ and $n$ is the number of independent samples. The estimation of the EOF $\psi_k$, associated with eigenvalue $\lambda_k$, is mainly contaminated by the pattern of the closest neighbouring EOF $\psi_j$, associated with eigenvalue $\lambda_j$. The closer the eigenvalues, the smaller the difference $\lambda_j - \lambda_k$ and the more severe the contamination. To assess the significance of the MCA modes, we compute the typical errors between two neighbouring singular values using this rule of thumb by North et al. (1982). If the typical error $\Delta\lambda$ of a particular singular value is comparable or larger than the difference between the singular value and its closest neighbour, then the typical error $\Delta\psi$ of the singular vector will be comparable to the size of the neighbouring eigenvector.

This rule of thumb assumes independent samples, which is possibly not valid for atmospheric data due to autocorrelations. To account for this, we replace the number of independent samples $n$ by the effective sample size $n_e$.

$$n_e = n\frac{1 - \rho_1\rho_2}{1 + \rho_1\rho_2} \tag{2.8}$$

where $\rho_1$ and $\rho_2$ are the lag-1 autocorrelation coefficients of the two expansion coefficients in $A$ and $B$. This expression is based on the similar expression used in Woollings et al. (2008), generalized from Bretherton et al. (1999) and Wilks (2011a).

## 2.2 Ray tracing

The theory of barotropic Rossby wave ray tracing applied to a linearized non-divergent barotropic vorticity equation on a sphere was first developed by Hoskins and Karoly (1981). They apply it to a zonally symmetric basic state with slow meridional variation. The group velocity of the ray could be solved from a plane wave solution. Because the dispersion equation has no explicit dependence on x and t, kinematic wave theory gives that $k$ and $\omega$ are constant along a ray. To satisfy the dispersion equation everywhere on the sphere, the meridional wavenumber has to vary along the ray. It is this variation that changes the propagation direction.

To solve for the amplitude and phase, the slow meridional variation is required for the WKBJ theory to theoretically hold strictly.

As an example in Hoskins and Karoly (1981), they consider a stationary wave propagating polewards and eastwards. For their zonally averaged zonal flow, the stationary wavenumber $K_s$ decreases with latitude. To satisfy the dispersion equation along the ray, since the zonal wavenumber is constant along the ray, the meridional wavenumber $l$ varies along the ray. $l$ decreases with increasing latitude, which means the ray becomes more zonal gradually, until the ray reaches the latitude where $l$ equals zero and $K_s$ equals $k$. At this instant the ray is completely zonal. At this turning latitude, the WKBJ theory is no longer valid but it can be shown that the latitudinal behaviour of the amplitude is that of an Airy function. Just above the turning latitude, the amplitude decreases exponentially. Just below the turning latitude, the solution becomes wavelike again but equatorwards. Therefore the wave is reflected at the turning latitude and now propagates equatorward. The meridional wavenumber again continues to adjust along the ray to satisfy the dispersion equation. If a ray approaches a latitude with zero zonal wind, the ray tends to become meridional and the group velocity tends to zero. At this critical latitude, the WKBJ theory is no longer valid. In a linear dissipative model, the wave energy is absorbed. So the ray is terminated at the critical latitude.

Karoly (1983) modifies the ray tracing to some idealized zonally varying basic states. The group velocities now contain further terms including advection by the meridional flow and derivatives in the zonal direction. Furthermore, both $k$ and $l$ now vary along the ray. Hoskins and Ambrizzi (1993) notes that this treatment, although more rigorous, gives little direct insight compared to the original more simple ray tracing theory. Also given the dominance in large scale flow fields of zonal over meridional wind, and the dominance in meridional over longitudinal gradients of the basic flow, to first order approximation the changes in $k$ along a ray path could be neglected compared with the changes in $l$. They apply the original ray tracing theory locally to an observed basic flow with both meridional

and zonal variations, and conclude that the result may still be qualitatively useful.

Here we follow the approach in Scaife et al. (2017) to use 60° sectoral zonal averaging on the climatological $250\,hPa$ zonal wind. We then calculate $K_s$ at every grid point from this smoothed climatological wind, using the equation in Hoskins and Karoly (1981)

$$\begin{aligned} K_s &= \left(\frac{\beta_M}{\overline{u}_M}\right)^{\frac{1}{2}} \\ &= \left(\frac{\frac{2\Omega}{a}cos^2\phi - \frac{\partial}{\partial y}\frac{1}{cos^2\phi}\frac{\partial}{\partial y}\left(\frac{\overline{u}}{cos\phi}cos^2\phi\right)}{\frac{\overline{u}}{cos\phi}}\right)^{\frac{1}{2}} \end{aligned} \tag{2.9}$$

where $\beta_M$ is $cos\phi$ times the meridional gradient of the absolute vorticity on the sphere, and $\overline{u}_M$ is the basic zonal velocity on the Mercator projection on the sphere, proportional to the angular velocity. For a given zonal wavenumber of the ray to be traced, we calculate the group velocities $u_g$ and $v_g$ at every grid point, using the equations in Hoskins and Karoly (1981)

$$u_g = \frac{2\overline{u}_M^2 k^2}{\beta_M} \tag{2.10}$$

$$v_g = \frac{2\overline{u}_M^2 k\left(K_s^2 - k^2\right)^{\frac{1}{2}}}{\beta_M} \tag{2.11}$$

$$c_g = 2\frac{k}{K_s}\overline{u}_M \tag{2.12}$$

From the starting position of a ray, we step forward in time by 30 minutes to calculate the new location of the ray in Mercator projection of the sphere, which is the coordinate system used in the derivation of the equations in Hoskins and Karoly (1981). The equations relating the coordinates in this projection and in spherical coordinates are

$$x = a\lambda \qquad , \qquad \partial\lambda = \frac{\partial x}{a} \tag{2.13}$$

$$y = a\ln\frac{1+sin\phi}{cos\phi} \qquad , \qquad \partial\phi = cos\phi\frac{\partial y}{a} \tag{2.14}$$

where $a$ is the radius of the Earth and $\lambda$ is the longitude. We then step forward again from the new position and this is repeated for the number of days needed.

To sample the sensitivity to the starting position of a ray, we also plot an ensemble of eight other rays located around a square of 5° in both longitude and latitude centered on the first ray.

A technical note. Although theoretically the ray should reflect exactly at the turning latitude, this cannot always be achieved in our numerical integration with discrete timesteps. For example, at one particular timestep where the ray is very close to the turning latitude, a timestep forward would bring the ray across the turning latitude into a region where propagation is not allowed. The ray would incorrectly terminate instead of reflecting meridionally. To solve this issue, we use a short timestep of 30 minutes. We also introduce a turning latitude threshold of 0.5 in stationary wavenumber on both side of the turning latitude. For example when a k=3 ray approaches a turning latitude, although it should strictly only reflect when it arrives the $K_s$=3 boundary, we allow it to reflect already when it reaches $K_s$=2.5 boundary. This value of 0.5 is also consistent with Hoskins and Karoly (1981) , where it is noted that for strict application of the wave theory, the integer values of the zonal wavenumber should be taken as characteristic of zonal wavenumbers in a band centered on that value.

Finally, we check our ray tracing by reproducing the ray paths initiated from the east Pacific in Scaife et al. (2017) (c.f. figure 2.1 with their figure 10 a). Due to the different $K_s$ contours for zonal wavenumber 2 and 4, the k2 ray propagates out of the tropics and across North America and reaching Hudson Bay, whereas the k4 ray undergoes total internal reflection already at around 30° in the southwest of USA and propagates back into the tropics.

## 2.3 Barotropic model

The barotropic model used is from O'Reilly et al. (2018), and is based on the model in Hoskins and Ambrizzi (1993). The damped barotropic vorticity equation is

$$\left(\frac{\partial}{\partial t} + \mathbf{V}_\Psi \cdot \nabla\right)\zeta = F - \lambda\zeta - \mu\nabla^4\zeta \tag{2.15}$$

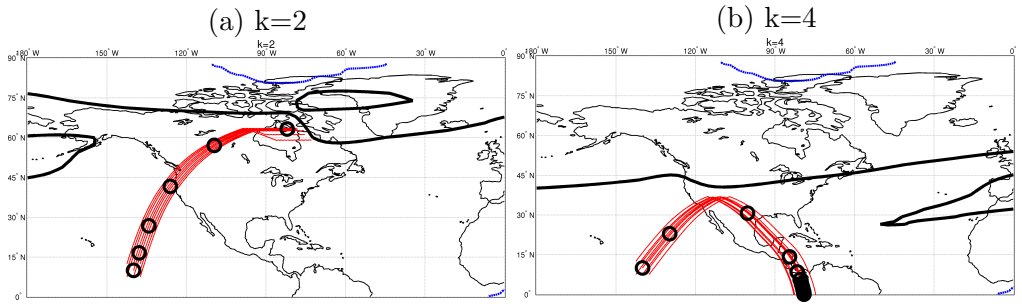



Figure 2.1: Ray tracing initiated from the east Pacific (140°W, 10°N), for rays with zonal wavenumber (a) k=2 and (b) k=4. NCEP2 DJF 250 hPa zonal wind with 60° zonal smoothing is used as the basic state. For each zonal wavenumber ray traced, the corresponding stationary wavenumber contour is plotted in black. Each ensemble ray is plotted in red, and black circles are superimposed daily on the central ray. Easterlies are contoured in blue every $5ms^{-1}$ with the zero contour included.

where $\mathbf{V}_\Psi$ is the rotational velocity, $\zeta$ is the absolute vorticity on the sphere, $F$ is a constant forcing, and $\lambda$ is a linear damping with a time scale of around 10 days.

$\mu$ is the biharmonic diffusion coefficient. We use a value of $5 \times 10^{16}\,\mathrm{m^4\,s^{-1}}$, which is slightly different to the $2.338 \times 10^{16}\,\mathrm{m^4\,s^{-1}}$ in Hoskins and Ambrizzi (1993). They used a spectral transform technique with a triangular truncation at wavenumber 21 (T21). This is equivalent to 64 grid points along a latitude circle, giving a zonal grid resolution of 625 km at the equator. Assuming the smallest length scale to be half the grid resolution, because any quantities spanning less than half the grid resolution cannot be rounded up to the grid resolution, the time scale of which the biharmonic diffusion is acting on the smallest length scale is given by $\frac{(312.5\times10^3\,\mathrm{m})^4}{2.338\times10^{16}\,\mathrm{m^4\,s^{-1}}}$ through dimensional analysis, which is around 4 days and agreeing with the quoted value in Hoskins and Ambrizzi (1993). Our model uses a triangular truncation at wavenumber 42 (T42). This doubles the number of grid points along a latitude circle, and halves the smallest length scale. Because it is not clear whether the biharmonic diffusion time scale on our new smallest length scale should still be 4 days, we perturb the value of $\mu$ around until we can reproduce the experimental results reported in Hoskins and Ambrizzi (1993). The value we finally settle down with corresponds to a time scale of about 3 hours acting on our smallest length scale.

$F$ is a constant forcing, and is expressed as $\overline{F} + S'$ where $\overline{F}$ is determined such that the basic state used is an exact solution of equation (2.15), and $S'$ is the linearized Rossby wave source (RWS). We use the calculation of the RWS from Dawson et al. (2011), which is based on the expression from Sardeshmukh and Hoskins (1988)

$$\begin{aligned} \text{RWS} &= -\nabla \cdot \left(\mathbf{V}_\chi \zeta\right) \\ &= -\mathbf{V}_\chi \cdot \nabla\zeta - \zeta \nabla \cdot \mathbf{V}_\chi \end{aligned} \tag{2.16}$$

where the first term is vorticity advection by the divergent wind, and the second term is vortex stretching. When linearized about a climatological flow,

$$\begin{aligned} \text{S}' &= -\nabla \cdot \left(\mathbf{V}'_\chi \overline{\zeta}\right) - \nabla \cdot \left(\overline{\mathbf{V}}_\chi \zeta'\right) \\ &= -\left(\mathbf{V}'_\chi \cdot \nabla\overline{\zeta} + \overline{\mathbf{V}}_\chi \cdot \nabla\zeta'\right) - \left(\zeta'\nabla \cdot \overline{\mathbf{V}}_\chi + \overline{\zeta}\nabla \cdot \mathbf{V}'_\chi\right) \end{aligned} \tag{2.17}$$

where the overbars denote the climatology and the primes denote the perturbations. For linear Rossby wave propagation, we multiply the RWS by $10^{-6}$ to make the calculation effectively linear by making the non-linear terms almost negligible, and the model responses are scaled back up by $10^6$. Our RWS is also stationary in time, allowing us to investigate the propagation of stationary Rossby waves. We also run one of the experiments without scaling down the RWS, and the conclusions are similar to the linear version. We integrate the equation for 45 days with time steps of 15 minutes. We present the quasi-stationary responses by averaging between days 7 and 10.

### 2.3.1 Patch method

In the patch forcing method, we run the experiment multiple times, with each forced by an idealized RWS resembling a Green's function. Following Barsugli and Sardeshmukh (2002), each forcing is a 2D cosine-square patch of the form

$$P_k(\lambda, \phi) = B cos^2\big(\frac{\pi}{2}\frac{\lambda - \lambda_k}{\lambda_w}\big) cos^2\big(\frac{\pi}{2}\frac{\phi - \phi_k}{\phi_w}\big) \tag{2.18}$$

within the rectangle spanned by $\lambda_k \pm \lambda_w$ in longitude and $\phi_k \pm \phi_w$ in latitude, where $\lambda_k$ and $\phi_k$ specify the centre of each forcing, and $\lambda_w$ and $\phi_w$ are the half widths in longitude and latitude respectively. Outside the rectangle, $P_k$ is set to zero

everywhere. The advantage of this form of forcing is that the distance between the centres of neighbouring forcings equal the half-width of the cosine-square, so that a uniform plateau of forcing can be achieved upon addition of neighbouring forcings. Each patch forcing is around 11° wide zonally ($2 \times \lambda_w$) and 5° wide meridionally ($2 \times \phi_w$). Together they cover all longitudes with 32 patch forcings, and cover latitudes from 45° S to 45° N with 17 patch forcings. We do not include more poleward forcings because we are interested in waves forced from the tropics and the subtropics into the extratropics. And unlike in Barsugli and Sardeshmukh (2002, figure 1a), we only use one subgrid of forcings to cover our area instead of their two overlapping subgrids.

For each patch, we use a magnitude B of $2 \times 10^{-11} s^{-2}$ at the centre. We remove the zonal mean of each forcing before putting into the barotropic model, because we find that in another set of patch experiments without removing the zonal mean, the responses have a large zonal mean component. But it is also found that if we remove the zonal mean from that set of patch experiment, the results resemble the current zonal-mean-removed-forcing experiment responses. We again further scale down the forcing by $10^{-6}$. For each patch forcing we again average the response between days 7 and 10.

To test our model settings, we reproduce some key Rossby wave propagation results from Hoskins and Ambrizzi (1993). Our vorticity forcing patches are much smaller spatially than theirs, which were around 30° in radius. We are still able to reproduce their key findings. Figure 2.2b shows the relative vorticity response from a forcing placed at the North African-Asian jet entrance. It captures well the Rossby wave pattern across Africa and Asia, for example the positive vorticities over north-western Africa, Pakistan, southern Japan and the tropical eastern Pacific. However, in our model the positive vorticities over southern Japan and over western North Pacific join together, and the negative vorticity at the central North Pacific over the Date Line is missing. Branstator (1983) has suggested that the large positive vorticity response over southern Japan, which coincides with the maximum $\overline{u}_M$ and $\beta_M$ with negative $\beta_M$ to the north and south, is due to

wave over-reflection by the zero $\beta_M$ lines. This dependence on the fine detail of the basic state may explain why our response is different to Hoskins and Ambrizzi (1993) near this region, because we use different years when averaging the DJF climatological basic state. Nonetheless, our response reproduces the split in propagation path in the North Pacific, with a wave curving south-eastward into the equatorial east Pacific, and another wave passing through North America.

Figure 2.2e shows the response from a forcing placed to the west of the North Atlantic jet. It reproduces the Eurasian wave pattern guided by the North Atlantic jet waveguide, and the Middle East wave pattern resulting from the leak of wave activity from the locally weaker Mediterranean flank of the waveguide. Figure 2.2h shows the response from a forcing placed near the North Atlantic jet maximum. It shows the Eurasian and Middle East wave patterns again, but with a different phase due to the shift in the forcing. Figure 2.2k shows the response from a forcing placed near the Maritime Continent. It reproduces the large amplitude centres at 150°E related to the barotropic growth suggested by Simmons et al. (1983), and the subsequent propagation across North Pacific into North America and also wave activity leaking into the tropical east Pacific.

There are small scale ripple patterns directing radially outwards from the source regions in all of the above vorticity responses. These are not seen in the corresponding streamfunction responses because according to the Poisson equation

$$\xi = \nabla^2 \psi \tag{2.19}$$

the streamfunction $\psi$ is a smoothed version of the relative vorticity $\xi$. So for our settings, expressing our model responses in streamfunction is preferred to relative vorticity.

In subsequent chapters, we often use geopotential height to display extratropical responses because it is more readily available than streamfunction. The geopotential height response $\phi'$ is approximated from the streamfunction response $\psi'$ by

$$\phi' = \frac{f}{g}\psi' \tag{2.20}$$

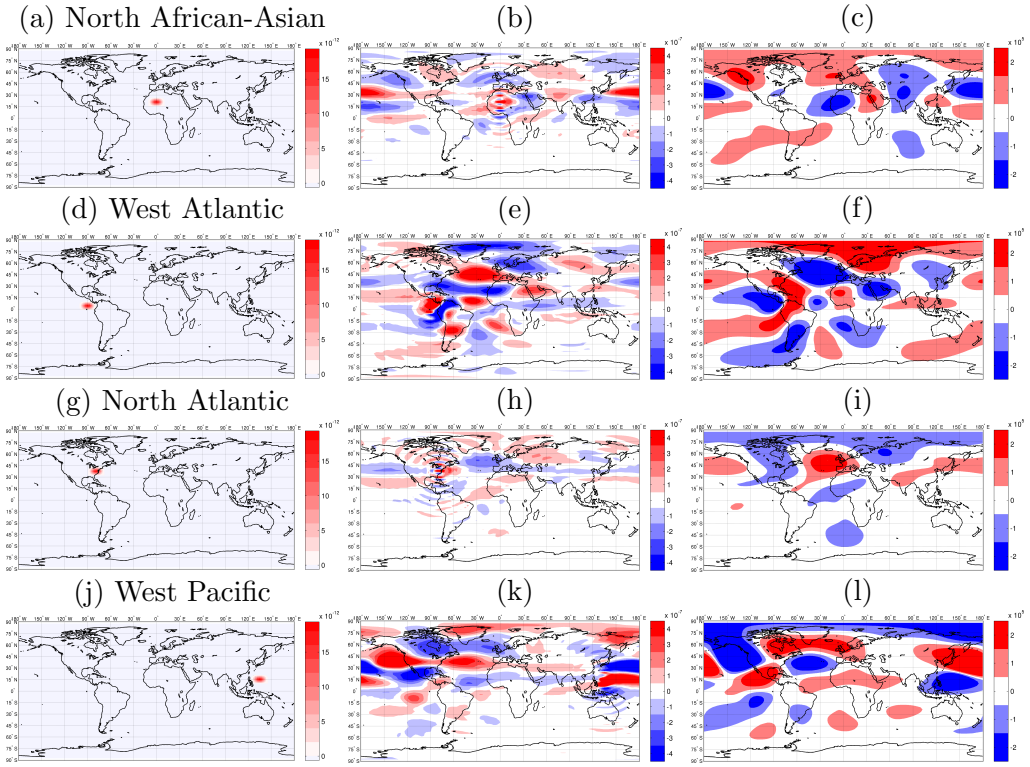



Figure 2.2: (First column) Vorticity forcing ($s^{-2}$) used in the barotropic model. Responses in (second column) relativity vorticity ($s^{-1}$) and (third column) streamfunction ($m^2 s^{-1}$) from these forcings, averaged between days 7 and 10, using the NCEP2 DJF climatological basic state.

where $f$ is the Coriolis parameter and $g$ is the gravitational constant. This approximation has been traditionally used in the derivation of the quasi-geostrophic potential vorticity equation, a framework that supports Rossby wave propagation. Finally, from the Poisson equation solution, streamfunction and vorticity are anti-correlated, which is clearly seen in our model responses in figure 2.2.

To conclude, our barotropic model setting successfully reproduces the stationary Rossby wave propagations along the major northern hemisphere waveguides, namely the North African-Asian jet and the North Atlantic jet, and from the Maritime Continent into the North Pacific. This justifies our use of this model in investigating wave propagation.

In later chapters, we will match specific observed extratropical patterns onto our patch responses. We project the target extratropical pattern onto each of these responses, by doing a dot product in the extratropics (40° N to 75° N) be-

tween these two patterns with cosine latitude weighting, and normalize by the magnitude of the target pattern. We choose to do a projection rather than a spatial correlation because we want to take into account the amplitude of the patch responses. We then weigh the patch forcings and patch responses accordingly when we sum them, to get the combined pattern of forcings that can generate the most similar combined response to the target pattern.

### 2.3.2 Rossby wave activity flux

In cases where the vorticity forcing is applied at more than one longitude, it is sometimes not very clear where the wave is propagating. We make use of the Rossby wave activity flux (RWAF), used in for example the study by Rodrigues et al. (2015) for looking at the impact of ENSO in the southern hemisphere. Based on Takaya and Nakamura (2001) equation (38), the two components of the flux on the sphere are given by:

$$W_\lambda = \frac{\cos\phi}{2 \mid \mathbf{U} \mid}\left[\frac{U}{a^2\cos^2\phi}\left(\left(\frac{\partial\psi'}{\partial\lambda}\right)^2 - \psi'\frac{\partial^2\psi'}{\partial\lambda^2}\right) + \frac{V}{a^2\cos\phi}\left(\frac{\partial\psi'}{\partial\lambda}\frac{\partial\psi'}{\partial\phi} - \psi'\frac{\partial^2\psi'}{\partial\lambda\partial\phi}\right)\right] \tag{2.21}$$

$$W_\phi = \frac{\cos\phi}{2 \mid \mathbf{U} \mid}\left[\frac{U}{a^2\cos\phi}\left(\frac{\partial\psi'}{\partial\lambda}\frac{\partial\psi'}{\partial\phi} - \psi'\frac{\partial^2\psi'}{\partial\lambda\partial\phi}\right) + \frac{V}{a^2}\left(\left(\frac{\partial\psi'}{\partial\phi}\right)^2 - \psi'\frac{\partial^2\psi'}{\partial\phi^2}\right)\right] \tag{2.22}$$

where $\mathbf{U}$ is the basic state winds with zonal component $U$ and meridional component $V$, $a$ is the radius of the Earth, $\lambda$ is the longitude, $\phi$ is the latitude, and $\psi'$ is the streamfunction anomaly from the basic state. Because our data is on pressure level, we adapt their equation accordingly to not include the multiplicative factor of pressure in both equations. This is justified by comparing to their equation (C5), which is derived for data on pressure level but in Cartesian coordinates. This flux is a generalization of the Eliassen-Palm flux (Andrews and McIntyre, 1976) from a zonally symmetric basic state to include zonal asymmetries. It is also a generalization of the flux in Takaya and Nakamura (1997), from stationary Rossby waves to include also migratory Rossby waves. Because we are looking at

quasi-stationary waves, We have also set the second term in their equation (38) to zero. Because the RWAF is parallel to the local group velocity, it provides a snapshot diagnosis of stationary waves on a zonally varying basic state. Finally, this flux also has the advantage of being phase-independent.

### 2.3.3 Barotropic instability of basic state

We address whether our barotropic model results are indeed forced stationary wave responses, or whether they could arise from the barotropic instability modes of the basic state. Simmons et al. (1983) showed that the barotropic instability of the northern hemisphere DJF basic state has a large contribution to the low frequency variability. For example, in one of their experiments where they force in southeast Asia (their fig 13), they observe a standing-wave model response that is oscillating with a period of 45 days. This oscillating instability mode, despite already having its exponential growth rate damped exactly by the model linear drag, still has a magnitude comparable to the forced stationary-wave component.

We first try to reproduce the experiment in their figure 13. We use their drag coefficient of 6.8 days, which corresponds to exactly cancelling the exponential growth of the fastest growing mode they have identified for their basic state. We use the same cosine squared patch RWS forcing centered at (10° N, 120° E) with half-widths of 15° in latitude and 45° in longitude, and same amplitude as theirs and without any scaling down by $10^{-6}$. However there are some differences between ours and theirs. Their model has a lower spatial resolution of T21, whereas ours is T42. Their timestep is 1 hour while ours is 15 minutes. Their fourth order hyperdiffusion coefficient is $2 \times 10^{16} m^4 s^{-1}$ but this is not numerically stable for our model with high frequency waves developing within a couple of days into the integration. So we continue to use our previous coefficient of $5 \times 10^{16} m^4 s^{-1}$. Their basic state is the 300 hPa January climatology, whereas we continue to use the same 250 hPa DJF basic state from NCEP2.

Given that their identified mode has a period of 45 days, we run our model for 90 days to allow sufficient time for any such modes to develop. We do not observe

any oscillation in wave magnitude within our 90 days. Roughly halfway through our integration, a k=1 wave with positive streamfunction ($\psi$) at 60° W and negative $\psi$ at 120° E starts to develop with fast growing amplitude, and dominates by day 90. The negative $\psi$ at 120°E is related to the positive RWS at 120°E, because $\psi$ and vorticity are anti-correlated. However, as noted in other experiments in Simmons et al. (1983), modes with no oscillation in time are not uncommon.

To further test if this is our fastest growing barotropically unstable mode, we test the sensitivity of this k=1 mode to the forcing. When we shrink the longitudinal half-width of the original forcing at 120° E to 22.5° in longitude, the wave remains k=1 and in the same position as the 120° E forcing case, suggesting that the zonal wavenumber of this mode is not sensitive to the zonal extent of the forcing. When we shift the forcing to 30° E to make it out of phase to the original forcing by $\frac{\pi}{2}$, the k=1 wave has positive $\psi$ at 150° W and negative $\psi$ at 30° E. This shift is inconsistent with the instability theory. The unstable mode should be an intrinsic property of the basic state, and should not change with the forcing position.

Returning to the question of whether our model responses are some barotropically unstable modes, although we cannot identify the fastest growing unstable mode from our basic state, there are two additional reasons that may give us confidence that our responses are the forced stationary-wave component instead of the barotropic instability modes of the basic state. Firstly, in all of our experiments, quasi-stationary wavelike geopotential height responses develop within the first 10 days in the extratropics. These responses only grow into the aforementioned k1 patterns beyond day 30, by then the magnitude is almost doubled that of the initial wavelike response, suggesting some kind of instability. By averaging the responses between days 7 and 10, which is relatively early for barotropic instability to develop and dominate, we are focusing on the forced stationary-wave component. We also note that the instability that developed beyond day 30 is also seen in the streamfunction, indicating it is not coming from the geopotential height conversion approximation. Secondly, as we will show later on, our responses

agree with ray tracing, which is a theory for Rossby wave rather than barotropic instability.

## 2.4 Baroclinic model

We use the Reading Intermediate Global Circulation Model version 1 (IGCM1). It was developed by Hoskins and Simmons (1975) as a computationally fast atmospheric GCM. Since then, newer versions have been developed. For example, IGCM2 includes a simplified moisture parameterization, and IGCM3 includes a more sophisticated radiation scheme. We choose the original dry version because it captures the basic physics of Rossby wave propagation that we are investigating, without unnecessary complications from other physical processes.

### 2.4.1 Model equations

The model contains four prognostic variables, namely the vertical component of absolute vorticity ($\zeta$), horizontal divergence ($D$), temperature ($T$) and surface pressure ($p_s$). Temperature is divided into a reference part $T_R(\sigma)$ and an anomaly $T_A$. The horizontal coordinates used are $\lambda$ for longitude and $\mu = \sin(\phi)$ where $\phi$ is the latitude. In the vertical, terrain-following $\sigma$ coordinates are used, where $\sigma = \frac{p}{p_s}$.

It is convenient to replace the zonal and meridional velocity components $u$ and $v$ by:

$$U = u\cos(\phi) = u\sqrt{1-\mu^2}$$
$$V = v\cos(\phi) = v\sqrt{1-\mu^2}$$

After rendering the variables dimensionless, the four model prognostic equations are:

$$\frac{\partial \zeta}{\partial t} = \frac{1}{1-\mu^2}\frac{\partial}{\partial \lambda}F_v - \frac{\partial}{\partial \mu}F_u - \frac{\zeta - \mu}{\tau_F} + K(-1)^{\frac{p}{2}}\nabla^p(\zeta - \mu) \qquad (2.23)$$

$$\frac{\partial D}{\partial t} = \frac{1}{1-\mu^2}\frac{\partial}{\partial \lambda}F_u + \frac{\partial}{\partial \mu}F_v - \nabla^2\left[\frac{U^2+V^2}{2(1-\mu^2)} + \Phi + T_R \ln P_s\right] - \frac{D}{\tau_F} + K(-1)^{\frac{p}{2}}\nabla^p D \tag{2.24}$$

$$\frac{\partial T_a}{\partial t} = -\frac{1}{1-\mu^2}\frac{\partial}{\partial \lambda}(UT_A) - \frac{\partial}{\partial \mu}(VT_A) + DT_A - \dot{\sigma}\frac{\partial T}{\partial \sigma} + \kappa\frac{T\omega}{p} + \frac{T_R - T}{\tau_E} + K(-1)^{\frac{p}{2}}\nabla^p T_A \tag{2.25}$$

$$\frac{\partial(\ln p_s)}{\partial t} = -\frac{U}{1-\mu^2}\frac{\partial}{\partial \lambda}(\ln p_s) - V\frac{\partial}{\partial \mu}(\ln p_s) - D - \frac{\partial \dot{\sigma}}{\partial \sigma} \tag{2.26}$$

where

$$F_U = V\zeta - \dot{\sigma}\frac{\partial U}{\partial \sigma} - T_A\frac{\partial(\ln p_s)}{\partial \lambda}$$
$$F_V = -U\zeta - \dot{\sigma}\frac{\partial V}{\partial \sigma} - T_A(1-\mu^2)\frac{\partial(\ln p_s)}{\partial \mu}$$

In these equations, $\tau_F$ is the Rayleigh friction timescale corresponding to 1 day, applied only on the lowest model sigma level; $K$ is the artificial hyperdiffusion timescale corresponding to 6 hours and is applied at the smallest resolved horizontal scale; $p$ is the order of the hyperdiffusion which has a value of 6; $\Phi$ is the geopotential; $\kappa$ is the ratio of the gas constant to the specific heat capacity of dry air at constant pressure, and has a value of 0.286; $\omega$ is the vertical velocity; $\tau_E$ is the radiative equilibrium timescale corresponding to 15 days and is applied at all model sigma levels. There is also a non-prognostic hydrostatic equation for the geopotential.

$$\frac{\partial \Phi}{\partial(\ln \sigma)} = -T \tag{2.27}$$

Together with the mass conservation relationship (Hoskins and James, 2016),

$$\frac{D(\ln p_s)}{Dt} + \nabla \cdot \mathbf{u} = 0 \tag{2.28}$$

where $\mathbf{u}$ is the velocity vector, these six equations can be solved for the six variables.

The method of solution is based on the spectral transform technique in the horizontal, finite differences in sigma coordinates in the vertical, and a semi-implicit time scheme. Under this method of solution, the total energy and total mass are formally conserved, but angular momentum is not formally conserved (Hoskins and Simmons, 1975). In this thesis, all the experiments with this model have a horizontal spectral truncation of T42, and have 15 levels in the vertical. The integration timestep used is 30 minutes. We find that the Newtonian cooling term is important in our experiments, without it the diabatic heating can initiate baroclinic instability which dominates from around day 8, and does not allow enough time for our model wave response to reach quasi-stationary state. To delay the onset of such instability, we use Newtonian cooling in all our experiments. And we choose the radiative equilibrium temperature structure $T_R$ to be the temperature structure of the basic state.

### 2.4.2 Model set up

Unlike in the barotropic model, the set up of the basic state in the baroclinic model is not as straightforward, because of more equations and also because some of the prognostic variables, for example the divergence and vorticity, are not always readily available on pressure levels. We use a routine from Mike Blackburn that reads in the horizontal winds and temperature on 37 pressure levels from 1 hpa to 1000 hPa, and the surface pressure, from the ERA-Interim (ERA-I) reanalysis (Dee et al., 2011) with a horizontal spectral truncation of T85. Together with the input of the surface geopotential, the routine computes the model prognostic variables on sigma levels accordingly. In all our experiments with the ERA-I basic state, we use the DJF climatology from 1980 to 2017.

The Met Office HadGEM3-GC3.0 (MOGC3, to be introduced in chapter 3) climate control run data has 17 pressure levels from 10 hPa to 1000 hPa, and we also apply a horizontal spectral truncation of T85 as with ERA-I. The set up of this basic state is not as straightforward as with ERA-I. The complication arises because it does not provide model data below orography or sea level. For example,

there are missing data as high up as the 600 hPa level. Although the aforementioned routine from Mike Blackburn includes vertical extrapolations, we find that the resulting basic state is not stable for our experiments. The reason is that in the climate model there are large monthly variability in the intersection between the sea level and the 1000 hPa level. This results in large areas of the 1000 hPa data missing, especially near the Antarctica. The aforementioned extrapolation routine does not handle these well. Our solution is to first remove the MOGC3 1000 hPa level. In addition to the vertical linear extrapolation, we also find it necessary to apply a horizontal Gaussian filter on pressure levels to smooth out the sharp discontinuities from the vertical extrapolation. To assess the importance of the 1000 hPa data for setting up the model basic state, we remove all the 1000 hPa level data from ERA-I and compare the resulting basic state with the basic state where the 1000 hPa data is included. We find that the difference between these two basic states is negligible. Also, the difference in the wave response from identical diabatic heating on these two basic states is negligible. In all our experiments, the ERA-I basic state is computed with the inclusion of the 1000 hPa level data, but the MOGC3 basic state is not.

Whereas in the barotropic model the inverse initial tendency has been incorporated into the code, our version of the baroclinic model does not. Without the inverse initial tendency, the basic state is not maintained for two reasons. Firstly, the climatological flow is not exactly balanced. Secondly, the model does not have orography, so for example the surface pressure around orographic features will drift in time. The time-stepping scheme of the model evaluates the diabatic and the adiabatic tendencies separately. The equations are also complicated by the application of a Robert time filter intended to give smoother solutions. In the first timestep when the heating is not turned on, we apply the inverse initial tendencies in all four variables in both the diabatic and the adiabatic timesteps, as well as in the Robert time filter equations. We then run the model for two days to confirm that the initial state is indeed exactly maintained, before turning on the diabatic heating as forcing in our experiments. In our analysis, we only refer to the day

the heating is turned on as day 0. A caveat is that our approach is not compatible with the conservation of mass in the model. We therefore have to comment out the model routine on mass conservation. Instead, in all of our experiments we first plot the total atmospheric mass evolution to check that each experiment is running stably.

The diabatic heating routine we use is originally from Hoskins and Karoly (1981) and modified by Liu et al. (2007). It is an elliptical heating on the horizontal tangent plane, with a sine-squared half-wave vertical structure between surface and tropopause, to give upper tropospheric peak. With the heating top set at the 0.15 sigma level, the heating peaks vertically at around 400 hPa. In our experiments, we alter the horizontal position, the zonal wavenumber of the ellipse, the eccentricity of the ellipse, and the amplitude and sign of the heating, while keeping the heating top fixed at the 0.15 sigma level. And to prevent unrealistically adding net heat to the system, we remove the zonal average of the diabatic heating at each latitude, so outside the heating ellipse there is zonally uniform cooling. Finally, similar to our barotropic experiments, all our heatings are stationary in time and are scaled down linearly by $10^{-6}$ to focus on linear stationary Rossby wave propagation, with the responses scaled back up by $10^6$ during analysis.

The observed monthly vertically integrated diabatic heating (Q) is based on the index used in Li and Wettstein (2012) and is calculated by Matthew Patterson,

$$Q = R_T + F_S + LP = R_T + (-R_S + H_S + H_L) + LP \tag{2.29}$$

where $R_T$ is the net downward radiation at the top of the atmosphere, $F_S$ is the net upward surface flux, $L$ is the latent heat of evaporation $P$ is the precipitation rate, $R_S$ is the net downward radiation at the surface, and $H_S$ and $H_L$ are the upward sensible and latent heat fluxes at the surface respectively. To convert between the diabatic heating units of the observation ($\mathrm{Wm}^{-2}$) and of the baroclinic model ($\mathrm{K\,day}^{-1}$), $1\,\mathrm{K\,day}^{-1}$ net radiative cooling through the depth of the atmosphere is equivalent to around $120\,\mathrm{Wm}^{-2}$ radiative flux divergence in the column under

radiative-convective equilibrium.

$$\begin{aligned}
&1\,\mathrm{K\,day^{-1}} \times C \times M \\
=&\,1\,\mathrm{K\,day^{-1}} \times C \times \frac{p_0}{g} \\
=&\,1\,\mathrm{K\,day^{-1}} \times 10^3\,\mathrm{J\,K^{-1}\,kg^{-1}} \times \frac{10^5\,\mathrm{kg\,m^{-1}\,s^{-2}}}{9.81\,\mathrm{m\,s^{-2}}} \\
=&\,120\,\mathrm{W\,m^{-2}}
\end{aligned}$$

where $C$ is the specific heat capacity of dry air, $M$ is the mass of the atmosphere in a column, $p_0$ is the surface pressure and $g$ is the gravitational constant. This can be completely balanced by around $120\,\mathrm{Wm^{-2}}$ surface turbulent flux, or completely by around $4\,\mathrm{mm\,day^{-1}}$ precipitation, or a combination of both.

$$\begin{aligned}
&\frac{120\,\mathrm{W\,m^{-2}}}{L \times \rho} \\
=&\,\frac{120\,\mathrm{W\,m^{-2}}}{2.26\,\mathrm{J\,kg^{-1}} \times 1000\,\mathrm{kg\,m^{-3}}} \\
=&\,4\,\mathrm{mm\,day^{-1}}
\end{aligned}$$

where $L$ is the latent heat of vaporization and $\rho$ is the density of water. Climatologically, about 80% of the $120\,\mathrm{Wm^{-2}}$ net radiative cooling is balanced by latent heating in the atmosphere (Zhang and Rossow, 1997, figure 3). This is consistent with an analysis of the individual terms in equation 2.29, where $R_T$ and $R_S$ mostly cancel out, and $LP$ dominates over the sum of $H_S$ and $H_L$.

It is found that at least around 10 days is needed to allow sufficient time for the extratropical response to develop into a quasi-stationary pattern, in agreement with timescale of around 2 weeks reported by other studies using similar versions of the same model (Jin and Hoskins (1995), Matthews et al. (2004)). This is longer than the time of around 7 days for the wave to develop in the barotropic model. This is possibly because whereas the RWS is specified from day 0 in the barotropic model, it takes time for the baroclinic model to set up the RWS from the specified diabatic heating. It is also found that baroclinic unstable waves, identified by eastward phase propagation consistent with movement with the basic flow at a steering level at which the feature has significant amplitude (Ambrizzi

and Hoskins (1997), Jin and Hoskins (1995)), sometimes start to develop beyond around 20 days. Therefore, we average the responses between days 10 to 14 after the heating is turned on.

### 2.4.3 Reproduction of literature

To test our model settings, we reproduce some of the Rossby wave propagation results from Ambrizzi and Hoskins (1997). Figure 2.3a shows our diabatic heating horizontal structure. It is of a smaller spatial size than their heating used. It is found that using the spatial size of their heating results in too large amplitude in our model response, and with unphysical behaviour developing in southeast Asia. This may be because their model is smoother, with a spectral triangular horizontal truncation at total wavenumber 31 (T31). Another reason may be our omission of vertical diffusion. Also using IGCM, Liu et al. (2007) reported that without vertical diffusion, the flow near the south side of the Tibetan Plateau tends to develop grid-scale structures, whose origin may be inertial instability in the near equatorial region. Ambrizzi and Hoskins (1997) also reported that without vertical diffusion, the upper-level equatorial meridional wind field tends to show grid-scale structure. Although we have omitted vertical diffusion due to unavailability of the codes, by using our spatially smaller forcings, this omission is found to only affect our wave propagation across the Asian jet waveguide at later days. Figure 2.3b shows the time evolution of the total atmospheric mass in our experiment, calculated from integrating the model surface pressure over the whole globe. It shows that despite turning off the mass conservation routine in the model, atmospheric mass is still mostly conserved until around day 20.

Figure 2.4 shows the model response to the heating, averaged between days 10 and 14. Comparable to Ambrizzi and Hoskins (1997, figure 1a), our model shows similar wave propagation along the Asian jet, with northerly winds in northeastern Africa, northeastern India, central North Pacific just west of the International Date Line, and the west coast of Canada. Because Ambrizzi and Hoskins (1997, figure 1a) only shows the day 10 response, our result further indicate the con-

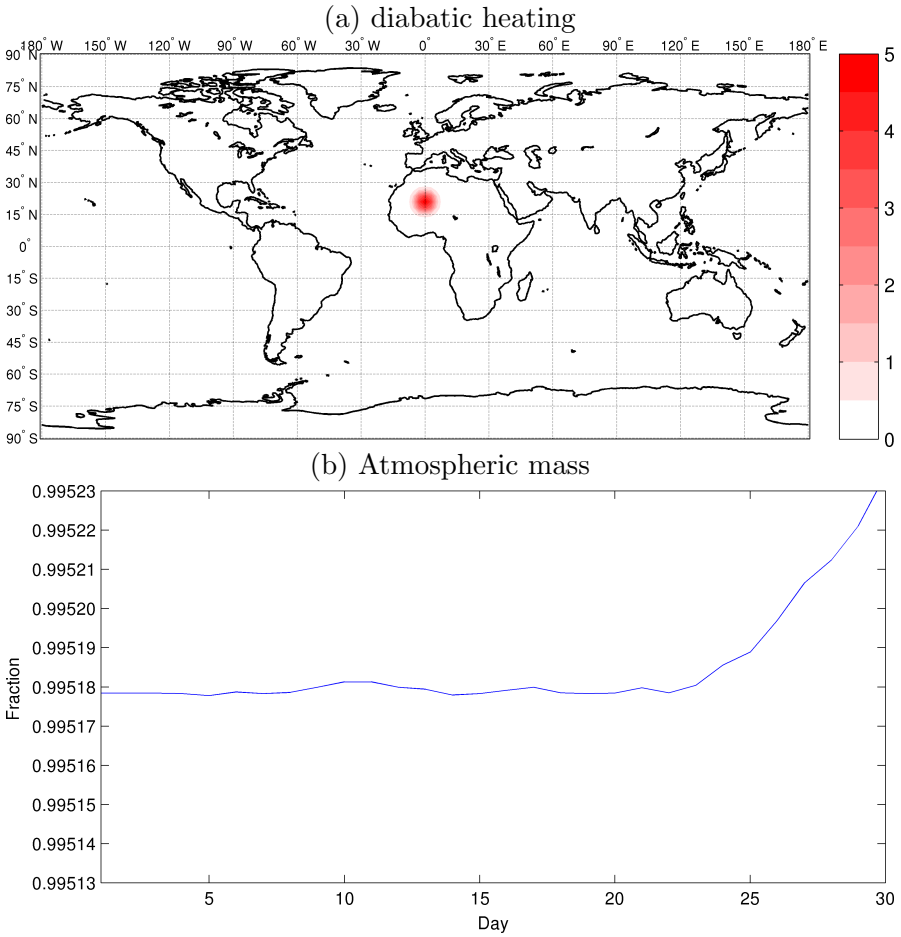



Figure 2.3: (a) Diabatic heating at 0°E 20°N ($\mathrm{K\,day^{-1}}$). (b) The evolution of the total atmospheric mass in our model as a fraction of the observed mass.

tinued propagation across North America and turning into the tropical Atlantic. Figures 2.4b and 2.4c show the vertical cross section and the Hovmöller diagram of the geopotential height response, which is stronger and clearer than the meridional wind response when averaged between 45°N and 60°N. The vertical cross section shows an equivalent barotropic structure, and also a slight westward tilt in the lowest levels due to the drag (Jin and Hoskins, 1995). In the Hovmöller diagram, the first 16 days are dominated by a quasi-stationary Rossby wave pattern, with almost zero phase speed and eastward group velocity propagating from the International Date Line from day 4 and reaching North America by day 8. By day 16, the amplitude over the North Pacific starts to markedly increase. This together with the eastward phase propagation of the high near the Aleutian Islands, suggest the increasing domination of baroclinic instability.

To conclude, our model set up can successfully reproduce a Rossby wave propagation from the literature, justifying our settings.

## 2.5 Blocking index

The blocking index we use is the absolute geopotential height index from Scherrer et al. (2006). It is a two-dimensional generalization of the blocking index in Tibaldi and Molteni (1990). The geopotential height gradient to the south (GHGS) and to the north (GHGN) are computed at every grid point between 35°N and 75°N,

$$\mathrm{GHGS}\,(\lambda, \phi_0) = \frac{Z(\lambda, \phi_0) - Z(\lambda, \phi_0 - 15^\circ)}{15^\circ} \tag{2.30}$$

$$\mathrm{GHGN}\,(\lambda, \phi_0) = \frac{Z(\lambda, \phi_0 + 15^\circ) - Z(\lambda, \phi_0)}{15^\circ} \tag{2.31}$$

where $Z$ is the geopotential height on 500 hPa, $\lambda$ is the longitude, and $\phi_0$ is the latitude within the above range. A grid point is classified as blocked if three criteria are satisfied. Firstly, the gradient to the south should be reversed compared to the climatology,

$$\mathrm{GHGS} > 0 \tag{2.32}$$

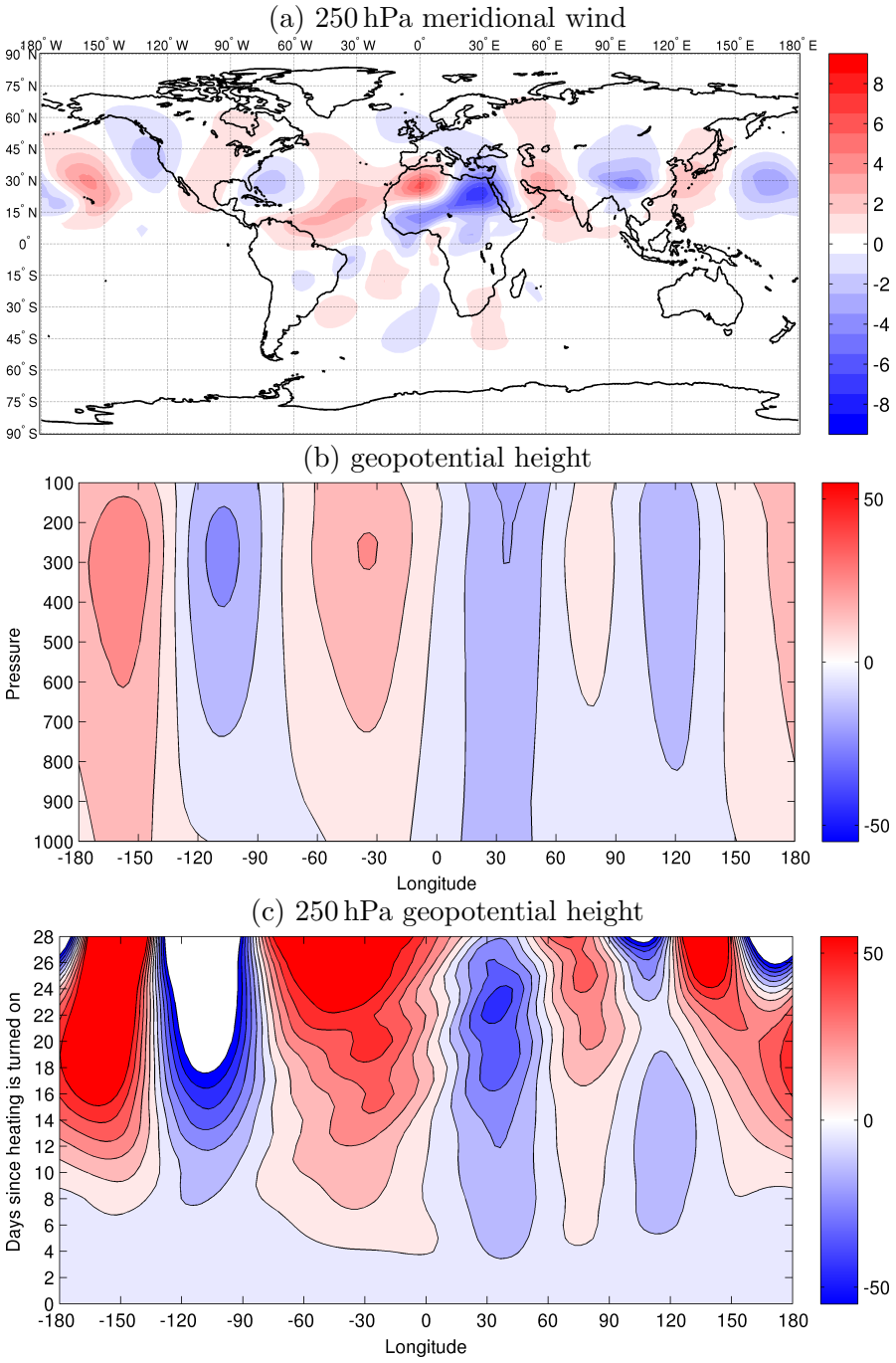



Figure 2.4: Model responses to the heating in figure 2.3a averaged between days 10 and 14. (a) 250 hPa meridional wind ($ms^{-1}$). (b) Vertical cross section of geopotential height (m). (c) Hovmöller diagram of 250 hPa geopotential height (m). Both (b) and (c) are averaged meridionally from 45°N to 60°N.

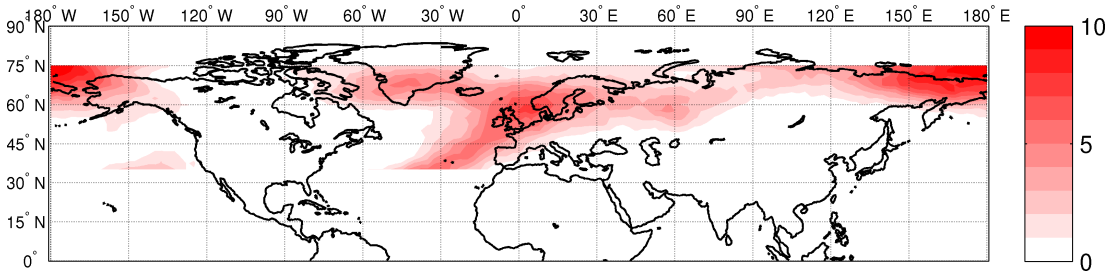



Figure 2.5: DJF 1949-2010 climatological blocking frequency. Unit is percentage of blocked days to the total number of days per season.

Secondly, the gradient to the north should be the same sign as the climatology but stronger in amplitude,

$$\text{GHGN} < -10\,\text{m per}\,^\circ\,\text{latitude} \tag{2.33}$$

Thirdly, a grid point is only considered blocked when the two criteria above are satisfied for five or more consecutive days. The result is a daily binary two-dimensional map of grid points classified as either blocked or unblocked.

We use NCEP1 daily 500 hPa geopotential height from 1948 to 2010. We compute the daily bocking index on all days from all seasons, to ensure the blocking indices at the beginning and end of the DJF seasons are computed correctly due to the consecutive days criterion. We then extract the DJF days and averaged over the season, to reproduce the DJF climatological blocking frequency in figure 2.5. Blockings are concentrated over the northern North Pacific, southern Greenland, and eastern North Atlantic including the UK.

# Chapter 3

# Tropical-extratropical teleconnections

## 3.1 Reanalysis MCA

Bretherton et al. (1992) compared the ability of several statistical methods, including maximum covariance analysis (MCA), to detect a coupled signal in a simple but geophysically relevant model system they have constructed. They concluded that MCA was one of the most preferable for general use because of its lack of systematic bias and good general performance. Wallace et al. (1992) compared these different methods when applied to real and collocated sea surface temperature and geopotential height data, and concluded that SVD could clearly isolate the two most important modes of variability. MCA has been traditionally applied onto collocated data, for example Wallace et al. (1992) looked at the covariability between the two fields over the same region in the North Pacific. More recently, MCA has been applied to fields in regions not necessarily collocated, to investigate teleconnections. For example, Ding et al. (2011) applied MCA onto boreal summer circumglobal tropical rainfall and circumglobal extratropical geopotential height, and identified the two leading modes of covariability to be a circumglobal teleconnection pattern and a more regional western Pacific-North America pattern. Rodrigues and Woollings (2017) applied MCA onto austral summer tropical outgoing longwave radiation and geopotential height over South America, to identify potential tropically-forced variability related to South Atlantic blockings. O'Reilly et al. (2018) applied MCA onto boreal summer tropical precipitation and

geopotential height over the Euro-Atlantic sector, and identified that the tropical rainfall could affect the extratropical circulation across Europe via a circumglobal wave.

### 3.1.1 Seasonal analysis

We investigate the teleconnection patterns between the tropical (15°S to 15°N) outgoing longwave radiation (OLR) from top of atmosphere and the northern hemisphere extratropical (40°N to 90°N) geopotential height at 500 hPa (Z500). The motivation for choosing OLR is because these are often associated with tropical deep convections, which can cause upper level divergence and has been considered a substantial Rossby wave source (Sardeshmukh and Hoskins, 1988). The OLR is from the National Oceanic and Atmospheric Administration (NOAA), with any gaps filled with temporal and spatial interpolation. The advantage is that it is satellite observation and not a model product, which may subject to model bias. But the disadvantage is its relatively short period of data availability. The Z500 is from the United States National Centers for Environmental Prediction 2 (NCEP2) reanalysis. The input data to the MCA, with dimensions in longitude and latitude and time, are weighted by the square-root of the cosine in latitude to compensate for the higher concentration of grid points at higher latitudes. The time series we use is the DJF seasonal mean of each year from 1980 to 2013.

Figures 3.1, 3.2 and 3.3 show the MCA results between hemispheric tropical OLR and northern hemispheric extratropical Z500. We first focus on the regression patterns. As explained in section 2.1, MCA gives two expansion coefficients, one for the OLR and one for the Z500. Homogeneous regression refers to when a field is regressed onto the expansion coefficient of the same field, for example the OLR regressing onto the OLR expansion coefficient. Heterogeneous regression refers to when a field is regressed onto the expansion coefficient of the other field, for example the Z500 regressing onto the OLR expansion coefficient. When regressed onto the expansion coefficient of the leading MCA mode in OLR, the homogeneously regressed OLR pattern in figure 3.1a shows reduced OLR over the

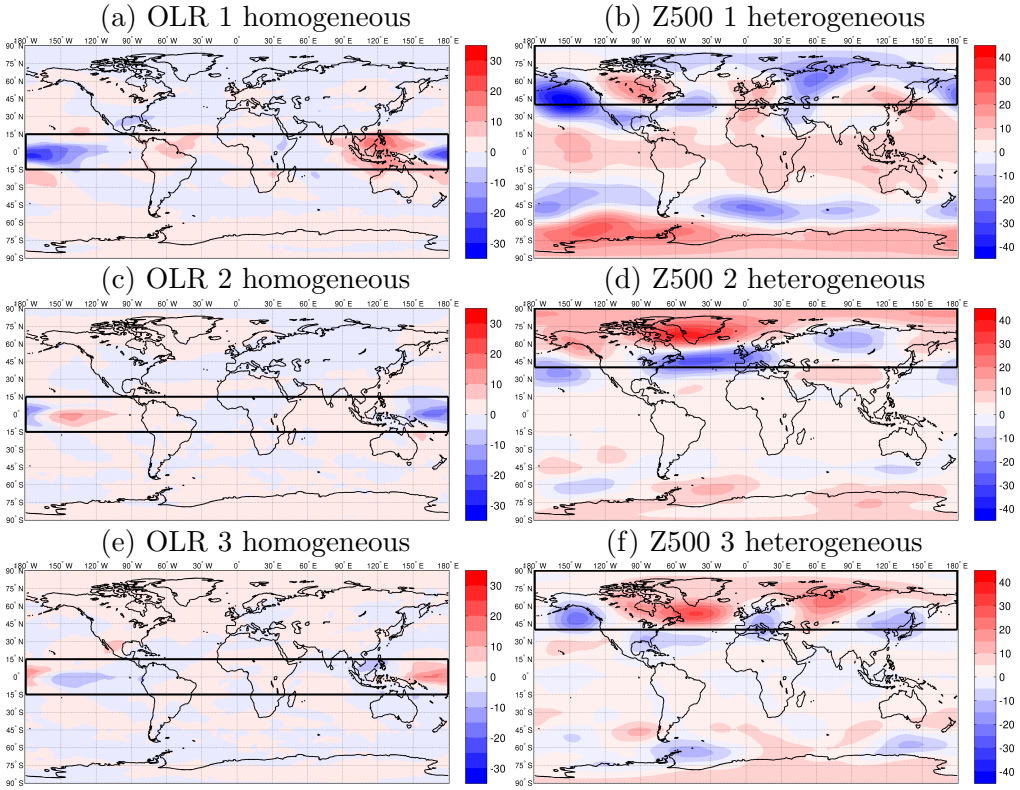
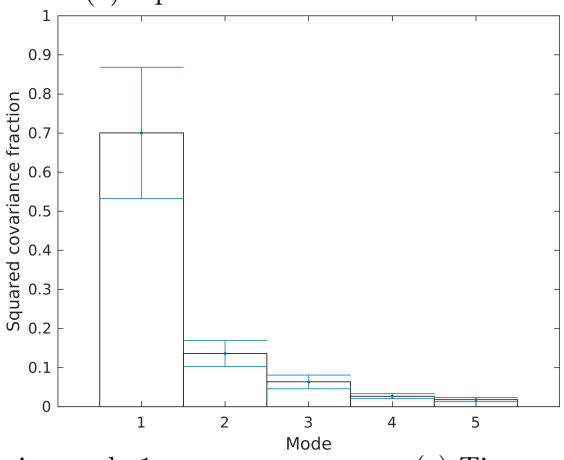
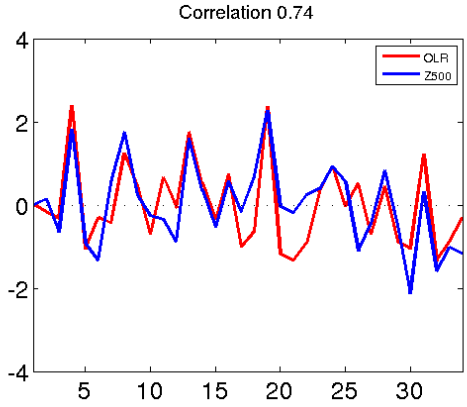



Figure 3.1: First three MCA modes, with hemispheric tropical NOAA OLR homogeneously regressed ($Wm^{-2}$), and northern hemispheric extratropical NCEP2 Z500 heterogeneously regressed (m). The black boxes mark the MCA regions.

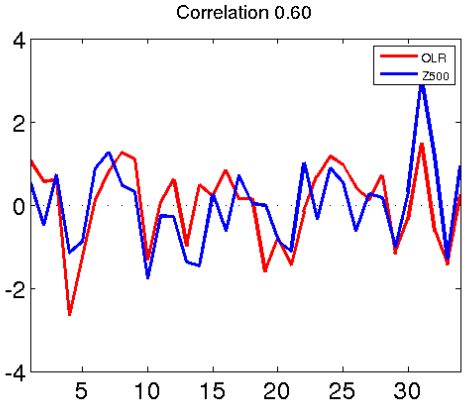
(a) Squared covariance fraction




(b) Time series mode 1




(c) Time series mode 2




(d) Time series mode 3

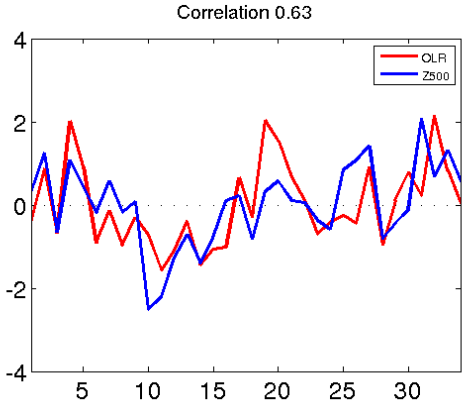



Figure 3.2: Squared covariance fraction and the time series from the MCA between hemispheric tropical NOAA OLR and northern hemispheric extratropical NCEP2 Z500.

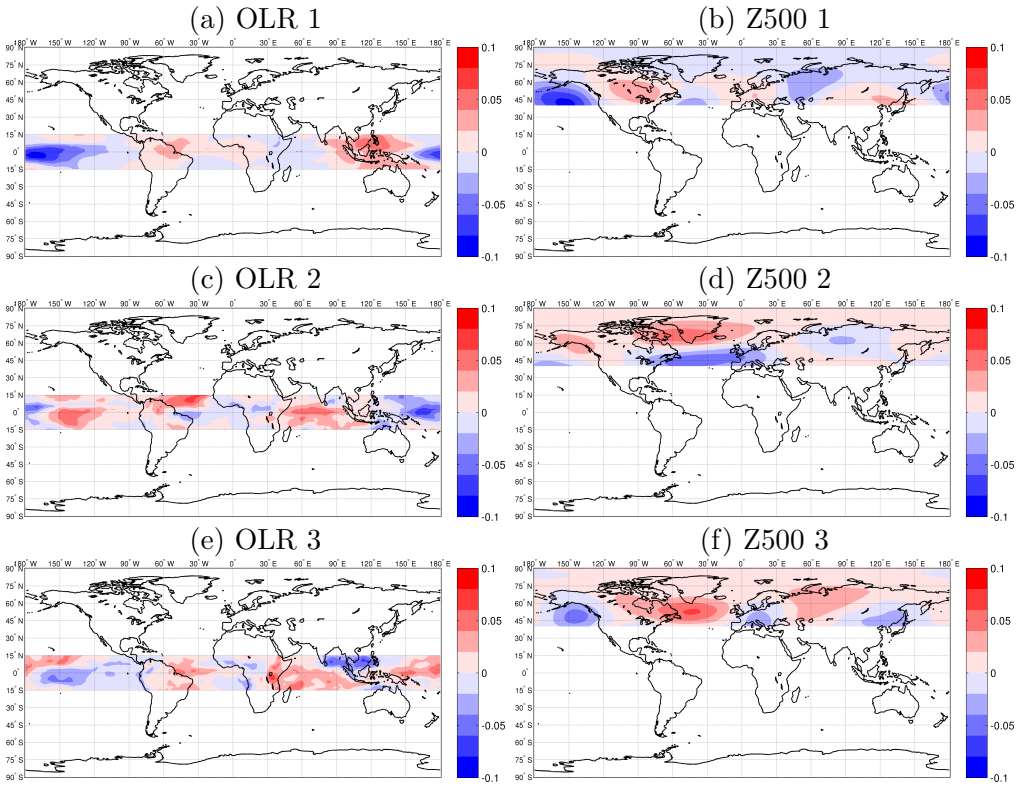



Figure 3.3: The singular vectors of OLR and Z500 of the first three MCA modes, between hemispheric tropical NOAA OLR and northern hemispheric extratropical NCEP2 Z500.

tropical central Pacific and increased OLR over the Maritime Continent. Reduced OLR in the tropics is associated with increased deep convections, pushing the cloud tops higher where they emit less infra-red to space because higher level is colder. This zonal dipole of OLR anomalies resembles closely the positive phase of ENSO (El-Niño). It is very similar to the OLR anomaly in the winter of 1986-87 during one of the strong El-Niño events (Trenberth et al., 1998, figure 3b). The heterogeneous regression of Z500 (figure 3.1b) shows a strong wave-like anomaly over the North Pacific and North America. The signal is weaker in the North Atlantic and European region. This pattern again resembles Trenberth et al. (1998, figure 3e), with the low heights near the Aleutian Islands, high heights over Canada, low heights over the US east coast, and high heights over southeast Asia with low heights to the north. This suggests that the leading mode of seasonal tropical-extratropical covariability is the ENSO.

This leading mode explains up to 70% of the squared covariance between these two tropical and extratropical fields (figure 3.2a). Figure 3.2b shows the expansion coefficients of the tropics and the extratropics for this leading mode. The temporal correlation is high (0.74), showing a strong coupling between these patterns. This high correlation also is the reason why the homogeneously regressed Z500 (figure A.1a) is so similar to the heterogeneously regressed pattern. As mentioned in section 2.1, the expansion coefficients of different modes are not guaranteed to be uncorrelated in MCA, unlike in EOF analysis. It is desirable to check the regressed patterns to see if they match the singular vectors, which are spatially orthogonal to each other. Comparison of the regressed mode 1 patterns in OLR and Z500 to the corresponding singular vectors (figure 3.3a and 3.3b) shows that the patterns are similar, suggesting there is not much contamination in this leading mode regression pattern from other modes. Finally, the mode 1 Z500 pattern seems to have a projection onto the Pacific-North-American pattern (PNA), although it is shifted to the east and also more hemispherical than the PNA.

Next, we discuss the mode 2 patterns. Although the mode 2 homogeneously regressed OLR (figure 3.1c) has similar negative anomaly as the mode 1 regressed

OLR over the central Pacific near the Date Line, the mode 2 pattern differs in the eastern tropical Pacific with a positive anomaly. This is also seen in the singular vector (figure 3.3c). The heterogeneously regressed Z500 (figure 3.1d) shows a very annular anomaly from the North Pacific across to the North Atlantic and Europe. This is similar to the North Atlantic Oscillation (NAO) in the Euro-Atlantic region. This is in sharp contrast to the mode 1 wave-like anomaly. This can be understood by considering that the singular vector of Z500 mode 2 (figure 3.3d) is constrained to be spatially orthogonal to the singular vector of Z500 mode 1. The temporal correlations between the mode 2 expansion coefficients are still strong (figure 3.2c), although is weaker than that of mode 1. The squared covariance fraction explained by this second mode however, is only around 0.15 (figure 3.2a). This shows that the ENSO mode dominates in the tropical-extratropical covariances over the NAO mode.

To estimate the typical errors between these two modes, we apply North's rule of thumb (section 2.1). In figure 3.2a, because the lower end of the mode 1 error bar (around 0.5) does not cover the SCF value of mode 2 (around 0.15), and because the upper end of the mode 2 error bar (around 0.2) does not cover the SCF value of mode 1 (around 0.7), we conclude that the typical error in the singular vectors in these two modes are small and not comparable to the size of the neighbouring singular vector. Therefore, we have high confidence in the significance of these two modes, and we refer to them as well-separated in SCF.

We also show the mode 3 patterns. However, given that mode 3 explains less than 0.1 in SCF (figure 3.2a), and also given that it has been subjected to the strong constraints of being orthogonal to modes 1 and 2, the physical significance in this mode may be small, and so we do not investigate mode 3 further.

After comparing the spatial patterns qualitatively to other well-known teleconnection patterns, we quantify the link between them. Table 3.1 shows that the OLR mode 1 is correlated with the Oceanic Niño index (Huang et al., 2015, Niño-3.4), and the Z500 mode 2 is anti-correlated with the Hurrell NAO index. Both correlations are statistically significant at the 95% level, and are in agreement

| | Niño-3.4 | NAO |
|---|---|---|
| OLR mode 1 | **0.94** | 0.02 |
| Z500 mode 1 | **0.67** | 0.08 |
| OLR mode 2 | 0.20 | **-0.50** |
| Z500 mode 2 | 0.14 | **-0.96** |

Table 3.1: Correlations of the mode 1 and 2 OLR and Z500 time series in figure 3.2, with the Niño-3.4 and NAO indices. Correlations that are significant at 95% confidence are in bold.

with the spatial patterns. Niño-3.4 is the primary indicator of NOAA for monitoring ENSO. The NAO index is based on the principle components of the NCAR reanalysis sea level pressure (Hurrell et al., 2013). According to a two-sided resampling test, none of the six expansion coefficients show significant trends, with all p-values larger than 0.1. To show the impact of these variabilities, figure 3.4 shows the GPCP version 2.3 combined precipitation dataset regressed onto the expansion coefficients of the MCAs. Extratropical precipitation anomalies associated with mode 1 are confined to the North Pacific and US east coast, while those associated with mode 2 are confined to the North Atlantic. Tropical precipitations are omitted because although they have larger magnitudes, they are simply anti-correlated with the tropical OLR due to the strong convections.

### 3.1.2 Various sensitivities

We test the sensitivity of modes 1 and 2 to the MCA regions chosen. We restrict the Z500 to the band 45° N to 75° N to have the same number of grid points as the tropical OLR. All SCFs, expansion coefficient couplings and regressed patterns are similar. Next, we restrict the extratropical region to over the North Atlantic. A key motivation is to investigate links to the Atlantic sector, as the links are less clear in the literature. The spatial patterns stay similar (figure A.2). We then further restrict the tropical region to over the East Pacific. The spatial patterns again stay similar (figure A.3). Therefore, the patterns we are capturing are hemispheric large scale patterns with little sensitivity to the regions chosen. But using these smaller regions decrease the expansion coefficient couplings to

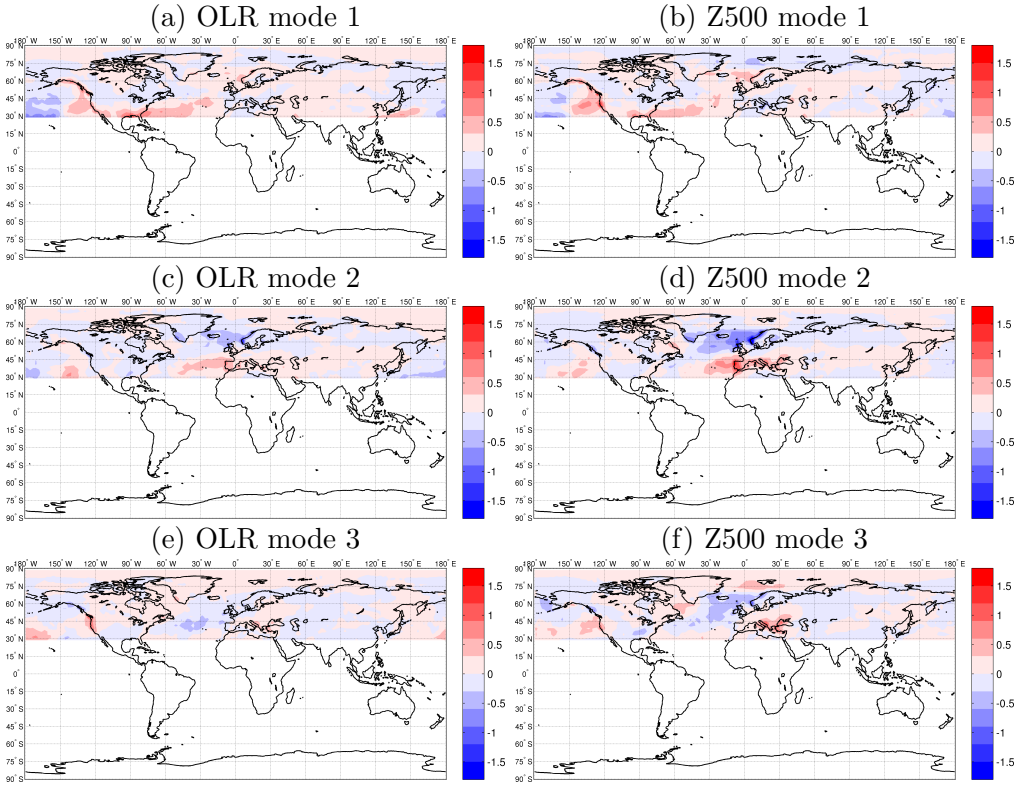



Figure 3.4: GPCP precipitation rate (mm day$^{-1}$) regressed onto the expansion coefficients of the MCA modes in figure 3.2. Note the color bar direction.

| | Niño-3.4 | NAO |
|---|---|---|
| OLR mode 1 | **0.88** | 0.12 |
| Z500 mode 1 | **0.41** | **0.55** |
| OLR mode 2 | **0.70** | **-0.61** |
| Z500 mode 2 | 0.26 | **-0.92** |

Table 3.2: Correlations of the mode 1 and 2 OLR and Z500 expansion coefficients using NCEP2 seasonal standardized data, with the Niño-3.4 and NAO indices, with 95% significances in bold.

around 0.4-0.5. Based on these tests, we continue with using the hemispheric boxes in figure 3.1.

All our MCA results are not sensitive to using geopotential heights on 250 hPa instead of 500 hPa, suggesting that our patterns have an equivalent barotropic structure. When separated into odd and even years to test the robustness to sampling, the couplings in all modes are stronger. The ENSO mode remains the leading mode but the NAO mode is sometimes interchanged with the third mode. The SCF of the ENSO mode remains well separated from the next mode, but the second and third modes are not separated. This shows that although the leading mode is robust, the second and third modes are susceptible to sub-sampling uncertainty given we only have 34 years of data.

While unstandardized data have been used in Bretherton et al. (1992), Wallace et al. (1992) has reported sensitivities to this. In a separate test, we standardize the Z500 and OLR time series before computing the MCAs, to weigh the OLR and Z500 equally. The SCFs show more sensitivity, with mode 1 decreasing to 0.45 and mode 2 increasing to 0.25. But the spatial patterns and couplings are all similar. The expansion coefficient correlations with the Niño-3.4 and NAO indices are also similar to before, with both fields in mode 1 correlating significantly with ENSO and both fields in mode 2 correlating significantly with the NAO (table 3.2).

### 3.1.3 ENSO intraseasonal responses

Given the close connection of our MCA leading mode with ENSO, we test the sensitivity to different months. King et al. (2018) showed that the ENSO teleconnection pattern exhibits intraseasonal changes between November and the next

February. In November, the teleconnection is strong over the North Atlantic and Europe, resembling the positive East Atlantic (EA) teleconnection pattern. Ayarzagüena et al. (2018) suggested that this pattern originates from a tropical Atlantic RWS, associated with ENSO-related precipitation anomalies over the Gulf of Mexico and Caribbean Sea. Although the tropical Pacific SST anomalies are already strong in autumn, the Rossby wave forced by ENSO over the North Pacific and North America is not fully established until January. In December, the EA weakens and anomalies in the North Pacific and America strengthen. In January and February, a Rossby wave develops fully over the North Pacific and North America, while the signal over the North Atlantic-Europe region becomes weak and indistinct. When we perform the MCA on the individual months using reanalysis, for November (figure A.4b) the Z500 leading mode pattern is similar to the EA pattern in the North Atlantic, with weak amplitudes in the North Pacific, in agreement with King et al. (2018). For December, anomalies in the extratropical Pacific strengthens and the EA weakens, and a zonal wavenumber (k) 3 wave pattern emerges (figure A.4d). In January (figure A.4f), it resembles our DJF pattern in figure 3.1b. Therefore, our DJF seasonal pattern captures mostly the January ENSO teleconnection in both the North Pacific and the North Atlantic.

Secondly, the ENSO teleconnection over the North Atlantic is not linear in ENSO amplitude. Focusing on the North Atlantic and Europe in January and February, Toniazzo and Scaife (2006) found a non-linear response to El-Niño that changed pattern over the eastern North Atlantic as the amplitude of the El-Niño anomaly increases. They showed that the transition happens at around $+1.5^{\circ}$ C in the Niño-3 amplitude. It is worth noting that the Niño-3 index captures more eastward sea surface temperature anomalies in the tropical Pacific than our Niño-3.4 index. While the response of moderate El-Niño cases project onto the negative phase of the NAO, the strong cases do not. Instead, the response in the strong cases is high pressure over the East Atlantic and western Europe similar to a negative EA, but it also extends into the northwestern North Atlantic where the EA should have no signal. Toniazzo and Scaife (2006) suggested that the strong

case response can be due to tropospheric Rossby wave propagation from a tropical Atlantic RWS. That in turn may be part of the Walker circulation response of the tropical atmosphere to El-Niño. Ineson and Scaife (2008) explained the observed intraseasonal transition of moderate El-Niño over the Euro-Atlantic region through stratospheric processes, from the positive EA in November and December to the negative NAO in January and February. In the North Pacific, the El-Niño response consists of a deeper Aleutian Low shifted towards the west coast of North America. In November, it destructively interferes with the climatological stationary wave. It reduces the stratospheric wave activity, and strengthens the stratospheric westerlies. This reduces the number of sudden stratospheric warming (SSW) events, and a smaller downward propagation of the stratospheric signal into the troposphere, resulting in almost no change to the EA. From December onwards into January and February, it constructively interferes with the climatological stationary wave, and the opposite happens, with a stronger downward propagation of the stratospheric signal into the troposphere, resulting in negative NAO in January and February. Our February reanalysis MCA shows a negative NAO pattern (figure A.4h), in agreement with this late winter NAO response in moderate El-Niño. Our DJF reanalysis MCA pattern (figure 3.1b) has the moderate El-Niño feature of lower heights in the central North Atlantic. But it also has the strong El-Niño feature of higher heights in western Europe and lower heights in Greenland. Therefore, our pattern over the North Atlantic-European region is a mixture of the moderate and strong El-Niño events as studied in the literature.

### 3.1.4 Daily analysis

#### 3.1.4.1 All years

We use daily data to further investigate the timescale of our MCA patterns. We first removed the daily climatology, by removing the climatological mean of each calendar day, which is otherwise the leading mode in the daily MCAs. We remove all leap days for more straightforward manipulation. We detrend all time series because we are after the shorter-term teleconnection. To relate the daily expansion

coefficients to the seasonal mean Niño-3.4 and NAO indices, we compute the seasonal mean of the expansion coefficients and then calculate the correlations.

We perform MCA on both concurrent data and on data where a lead has been introduced between OLR and Z500. We introduce the lead because one mechanism of tropical-extratropical teleconnection is Rossby wave propagation. As the typical timescale to propagate from the tropics into the extratropics is around 10 to 14 days, we lead the OLR ahead of Z500 by 14 days. For each year, Z500 runs from $1^{st}$ December to $28^{th}$ February and OLR runs from $17^{th}$ November to $14^{th}$ February. Table 3.3a shows the correlations with concurrent data, and table 3.3b shows the correlations with the lead data.

ENSO correlates strongly with the leading mode using concurrent data (table 3.3a), and the strong correlations remain almost the same when using lead data (table 3.3b). ENSO has larger interannual variability than intraseasonal variability, and the MCA does not require the lead time to capture the maximum covariance. To confirm this, for each MCA expansion coefficient we take the ratio of the interannual mean of the intraseasonal standard deviations, over the interannual standard deviation of the intraseasonal means (table 3.4). The smaller the ratio, the larger is the interannual variability compared to the intraseasonal variability. The ratios for the leading mode OLR using concurrent and lead data are both smaller than 1 (0.88 and 0.74 respectively), confirming that ENSO has larger interannual variability than intraseasonal variability.

Using lead data, while mode 1 correlates strongly with ENSO, mode 2 correlates strongly with the NAO (table 3.3b). Figure 3.5 shows the regressions for the 14-days-lead MCA. Within each mode, the expansion coefficient correlations (figures 3.6b and 3.6c) are lower than in the seasonal MCAs (figures 3.2b and 3.2c). This is because the extratropical transient cyclones and anticyclones are not expected to correlate well with the tropical OLR. The SCFs of modes 1 and 2 are not well separated (figure 3.6a).

To test the robustness of our daily MCAs, we apply sub-sampling because we have enough daily data. We subsample odd and even years rather than odd

| (a) | Niño-3.4 | NAO |
|---|---|---|
| OLR mode 1 | **-0.92** | 0.13 |
| Z500 mode 1 | **-0.60** | **0.51** |
| OLR mode 2 | **-0.69** | -0.22 |
| Z500 mode 2 | -0.30 | **-0.51** |
| (b) | | |
| OLR mode 1 | **0.88** | 0.06 |
| Z500 mode 1 | **0.56** | 0.19 |
| OLR mode 2 | **0.67** | **-0.40** |
| Z500 mode 2 | 0.32 | **-0.91** |
| (c) | | |
| OLR mode 1 | **0.43** | **0.51** |
| Z500 mode 1 | 0.18 | **0.86** |
| OLR mode 2 | **-0.79** | -0.32 |
| Z500 mode 2 | **-0.41** | -0.02 |

Table 3.3: Correlations of the mode 1 and 2 OLR and Z500 expansion coefficients using the Niño-3.4 and NAO indices, with NCEP2 (a) concurrent daily data, (b) daily data with OLR leading Z500 by 14 days, and (c) same as (b) but with ENSO years removed. Correlations that are significant at 95% confidence are in bold.

| (a) Concurrent | Mode 1 | Mode 2 |
|---|---|---|
| OLR | 0.88 | 1.50 |
| Z500 | 1.94 | 2.60 |
| (b) OLR 14-days lead | | |
| OLR | 0.74 | 1.81 |
| Z500 | 1.97 | 1.74 |

Table 3.4: Ratios of the interannual mean of the intraseasonal standard deviations, over the interannual standard deviation of the intraseasonal means, of each of the expansion coefficients from MCAs using NCEP2 (a) concurrent daily data and (b) daily data with OLR leading Z500 by 14 days.

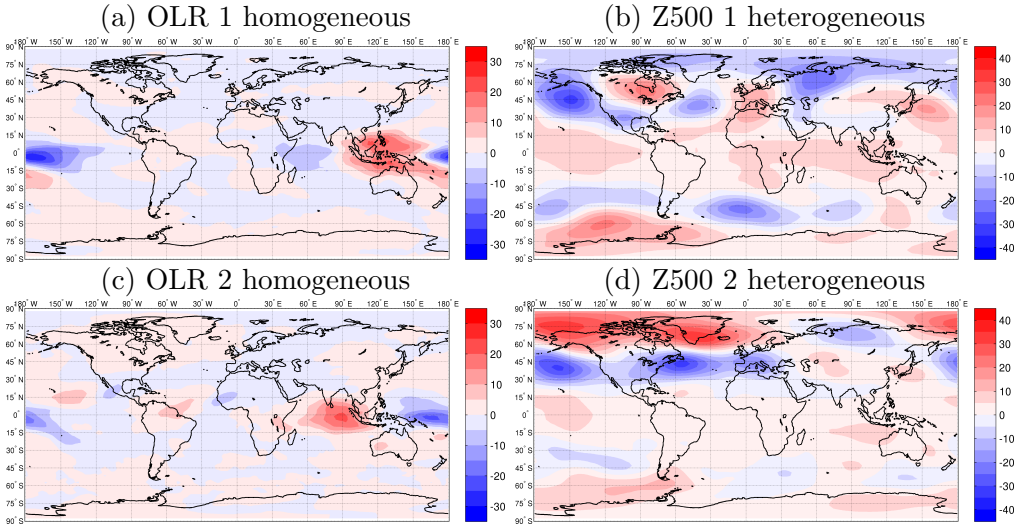
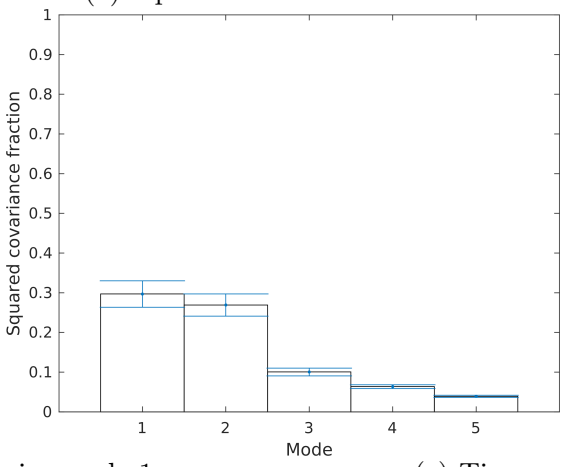



Figure 3.5: Calculated from daily data with OLR leading Z500 by 14 days, with all years used. First two MCA modes, with hemispheric tropical NOAA OLR homogeneously regressed ($Wm^{-2}$), and northern hemispheric extratropical NCEP2 Z500 heterogeneously regressed (m).

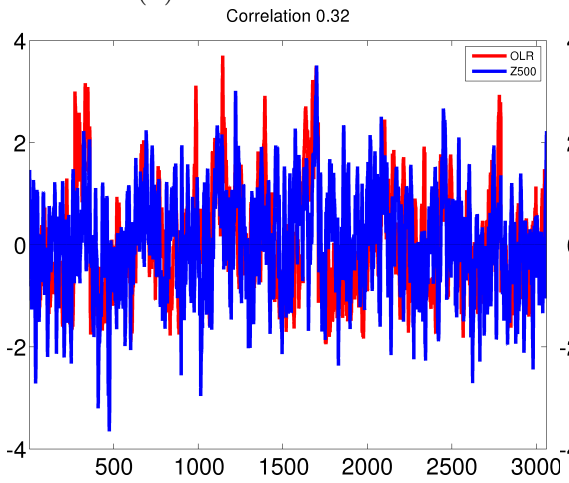
and even days because the autocorrelation of daily data makes the odd and even days samples essentially the same sample. We focus on the leading mode when comparing the previous MCA to these sub-sampled MCAs. The SCF is now separated. The correlation between the expansion coefficients of the OLR and the Z500 (0.42 and 0.35 for the subsamples)is higher than previous (0.32), indicating a stronger coupling. This might be because of the shorter time period of the subsamples. The singular vectors and regression patterns are similar. The similarity of the sub-sampled results to the previous result is because of the similar ENSO frequencies in the subsamples and the full period. As we will mention in the section 3.1.4.2, we identify 10 ENSO DJFs in this 1980 to 2013 period. Of these, 5 years are odd and 5 years are even. So the ENSO frequency is the same before and after sub-sampling. The test suggests that the results are quite robust, even though the modes are not well separated.

As another sensitivity, we compute similar correlations as in table 3.3b but the 14-days-lead OLR and the Z500 are standardized before the MCA. The correlations of OLR and Z500 mode 1 with the Niño-3.4 index is weaker, and so are the correlations of OLR and Z500 mode 2 with the NAO index. When we

(a) Squared covariance fraction




(b) Time series mode 1




(c) Time series mode 2

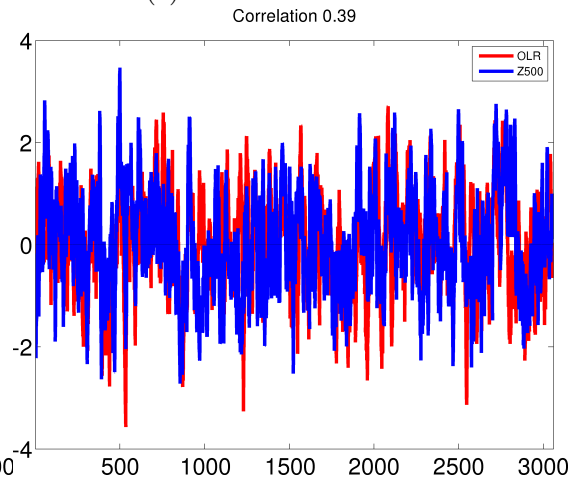



Figure 3.6: Calculated from daily data with OLR leading Z500 by 14 days, with all years used. Squared covariance fraction and the time series from the MCA between hemispheric tropical NOAA OLR and northern hemispheric extratropical NCEP2 Z500.

further remove the seasonal mean from this standardized data before the MCA, all the correlations with the Niño-3.4 and NAO indices become very weak and insignificant. We therefore keep the unstandardized data and keep the seasonal means.

#### 3.1.4.2 ENSO-neutral years

MCA is a statistical tool that requires the singular vectors of the subsequent modes to be spatially orthogonal to the leading mode. It is not clear whether the modes behind the leading mode bears any physical significances or are statistical artefacts. For example, using lead data the mode 2 OLR correlates stronger with the Niño-3.4 index (at 0.67 in table 3.3b) than with the NAO index (at -0.40). This is also seen from the mode 2 OLR regression pattern (figure 3.5c), which apart from the increased OLR over the Indian Ocean, also shows decreased OLR over the Date Line overlapping with the ENSO region in mode 1 (figure 3.5a). We further investigate this mode 2 by performing MCA only on ENSO neutral years, to take out the leading ENSO mode. We remove years with a Niño-3.4 index exceeding one standard deviation. The El-Niño years removed are 1983, 1987, 1992, 1998 and 2010; the La-Niña years removed are 1989, 1999, 2000, 2008 and 2011. Performing MCA on the lead data with these ENSO years removed, the correlation of the mode 1 OLR with the NAO index is higher (at 0.51 in table 3.3c compared to -0.40 in table 3.3b), while the mode 1 Z500 correlation with the NAO remains strong. As the mode 1 OLR now correlates stronger with the NAO index (at 0.51) than with the Niño-3.4 index (at 0.43), and also it is no longer spatially orthogonally constrained to any higher modes, we have more confidence in the physical interpretation of this mode 1 as the NAO.

Mode 2 OLR still shows strong and significant correlation with Niño-3.4 (at -0.79 in table 3.3c), suggesting it is capturing the residual ENSO variabilities within the ENSO neutral years. The mode 1 Z500 regression (figure 3.7b) resembles the mode 2 regression from the MCA when all years are included (figure 3.5d). But the mode 1 OLR regression now has a pattern a little different to that in the

previous MCA. While they both have OLR anomalies over the Indian Ocean, this new pattern has another area of OLR anomalies nearer to the Maritime Continent, compared to the previous anomalies further east over the Date Line. In terms of the SCF, mode 1 is now separated from mode 2 (figure 3.8a).

We again test the robustness of this MCA leading mode with odd and even year sub-sampling. The SCFs remain separated in the subsamples, although dropping from 0.3 to around 0.25. The correlation between the expansion coefficients of the OLR and the Z500 is again higher than previous (0.47 in both the subsamples compared to 0.42 in figure 3.8b). The singular vectors and regression patterns are similar. These give confidence to the robustness of our MCA.

To test the importance of the 14-day lead in OLR in the MCA for ENSO-neutral years, we repeat the MCA for ENSO-neutral years with concurrent OLR and Z500. Without the lead, both the leading mode OLR and Z500 regressions resemble the ENSO patterns, with an SCF well separated from the second mode. The second mode Z500 regression resembles the NAO, but the second mode OLR regression is different, with not much signal over the Indian Ocean although still with the same signal near the Maritime Continent. This change in the OLR signal may again be due to the statistical artefact of imposing spatial orthogonality from the OLR mode 1 onto the OLR mode 2. This shows that without the 14-day OLR lead time, ENSO still explains more covariance than the NAO. This also shows that the 14-day OLR lead time is important if we want to pick out the NAO and its non-artificial OLR coupling in the leading mode, and suggests a delayed link between the tropics and the extratropics with signals taking around 14 days to propagate between.

After identifying a coupling between the tropical OLR and the extratropical Z500 that resembles the NAO, we discuss its physical interpretation. Based on the OLR signals over the Indian Ocean and the Maritime Continent, we turn to the Madden-Julian Oscillation (MJO). The MJO is an eastward propagating system on the equator between the Indian Ocean and the central Pacific. It is typically decomposed into eight phases, with each phase lasting three to five days. Cassou

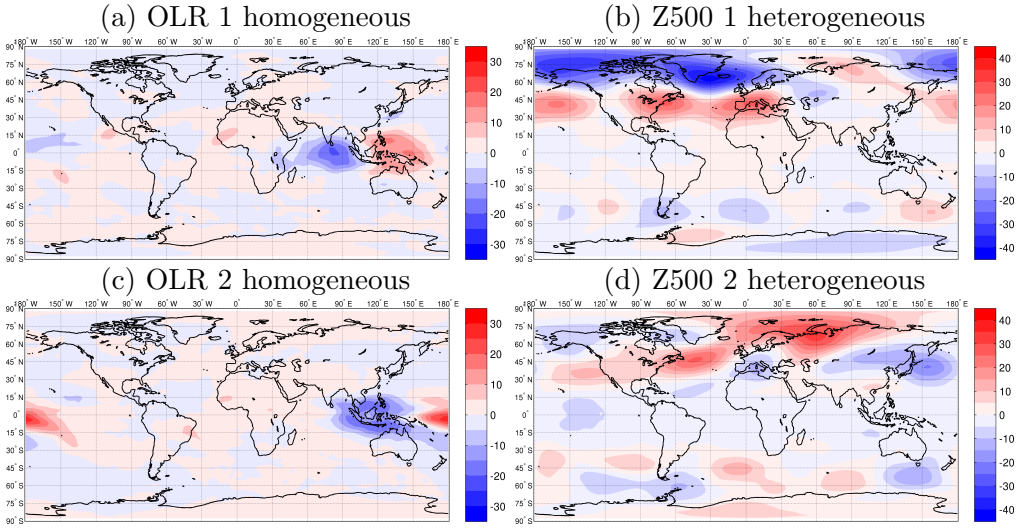
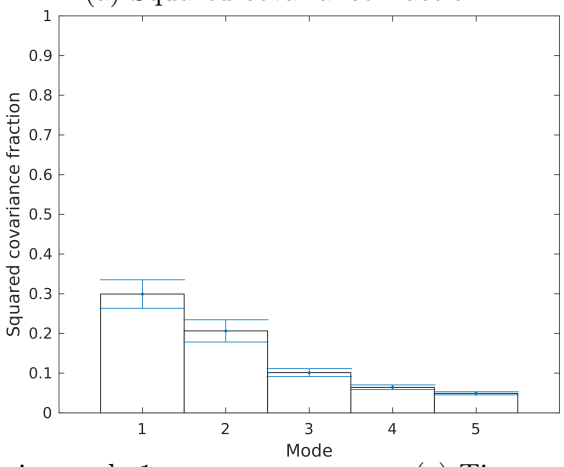



Figure 3.7: Calculated from daily data with OLR leading Z500 by 14 days, on ENSO-neutral years. First two MCA modes, with hemispheric tropical NOAA OLR homogeneously regressed ($Wm^{-2}$), and northern hemispheric extratropical NCEP2 Z500 heterogeneously regressed (m).

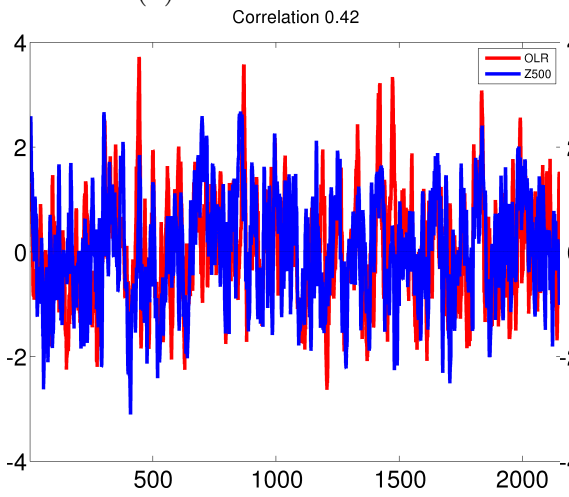
(2008) showed that phase 3 and phase 6 of the MJO are precursors of NAO+ and NAO- regimes respectively. They showed that direct MJO forcing initiates the NAO+ precursory wave train in phases 2 and 3. The OLR composites for phases 2 and 3 of the MJO (Cassou, 2008, figure 2) are consistent with our OLR leading mode for ENSO-neutral years (figure 3.7a).

The proposed teleconnections for NAO- were less straightforward. Cassou (2008) proposed two non-exclusive mechanisms between MJO phase 6 and NAO-. Their first mechanism was that the extratropical atmosphere retains information about regime occurrences over medium-range timescales, and the preferred transitions between the regimes follow the route NAO+ to Scandinavian blocking to NAO-. This is shown by Vautard (1990) using 10-day low-pass data, which shows very similar regimes as Cassou (2008). Using unfiltered daily data and similar regimes, Matsueda and Palmer (2018) showed that the preferred transition between the regimes is self-transition (i.e. persistence). The next most preferred transition from NAO+ beyond persistence is to Scandinavian blocking, and then back to NAO+ instead, with transition to NAO- being the least preferred. We suspect this discrepancy is due to non-stationarity or sampling uncertainty. Vau-

(a) Squared covariance fraction




(b) Time series mode 1




(c) Time series mode 2

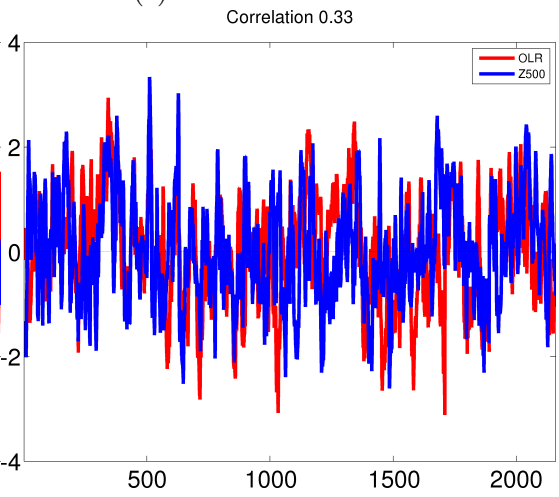



Figure 3.8: Calculated from daily data with OLR leading Z500 by 14 days, on ENSO-neutral years. Squared covariance fraction and the time series from the MCA between hemispheric tropical NOAA OLR and northern hemispheric extra-tropical NCEP2 Z500.

tard (1990) used 1974 to 1986 while Matsueda and Palmer (2018) used 1979 to 2013, and the NAO exhibits a gradual transition from NAO- dominance in 1950 to 1977, to NAO+ dominance in 1978 to 2010.

The second mechanism by Cassou (2008) was through Rossby wave propagation from the east Pacific. Their suggested MJO phase 6 is associated with tropical upper level divergence around 120° W, which generates a Rossby wave source around 20° N 110° W and initiates a wave train propagating towards Europe. The negative phase of our leading mode (NAO-) for ENSO-neutral years (figure 3.7a) shows a negative OLR signal at 15° N 110° W, which may correspond to their upper level divergence at 120° W. Although MCA is a linear statistical tool that is not expected to pick up this non-linear behaviour of the two NAO phases, our results are still consistent with the above physical mechanisms.

Cassou (2008, figure 3) also showed the lagged relationships between the eight phases of the MJO and the two phases of the NAO. The anomalous percentage occurrences of NAO+ and NAO- from climatology peaked at around 12 to 14 days after MJO phase 3 and phase 6 respectively. This agrees with our choice of 14 days lead-time for our daily OLR to Z500.

## 3.2 MOGC3 MCA

The Global Coupled configuration 3 (GC3) was introduced in 2016 as the global coupled configuration of the Met Office Unified Model (UM) (Williams et al., 2017). Soon after GC3 was released, GC3.1 was developed with a correction on anthropogenic aerosol forcing and further tuning of the sea ice. GC3.1 is important because it will be the coupled physical model upon which the UK Earth System Model version 1 (UKESM1) will be developed. Also, it is the basis of the UK's submission to the Coupled Model Intercomparison Project (CMIP) 6. The differences between GC3.0 and GC3.1, both in terms of model changes and resulting systematic errors, are relatively small and localized.

We are motivated to look at this coupled model to test how well the teleconnections we have identified in the reanalysis are represented in a state-of-the-art

model. We look at the free running control run because if there are any misrepresentations in its teleconnections, this may affect the confidence in other climate long runs from this model. For example in CMIP6, where results would be derived from taking the difference between the experimental high emission scenario run and this control run, it is useful to know the limitations of the teleconnections in the model in order to understand the uncertainty in the future projections. The control run uses forcings set to values from the year 2000, allowing fair comparison with present day reanalysis. The ocean, atmosphere and sea ice is initialized from 34 years into GC3.0 prototype runs. Our 100 years data does not contain the spin up period. This coupled climate present day control run, officially referred to as HadGEM3-GC3.0, is intended for GC3.0 assessment purposes. HadGEM (Hadley Centre Global Environmental Model) refers to the climate simulation system and the way of running the model and its initialization. GC refers to the configuration precisely defining the science settings being run, for example GC3.0 is defined by the combination of the component model scientific configurations (GA7.0, GL7.0, GO6.0, and GSI8.0) and their couplings. Hereafter, we refer to HadGEM3-GC3.0 simply as MOGC3.

### 3.2.1 Seasonal analysis

We perform the same MCA analysis on 99 DJFs from this control run. Figure 3.9 shows the regressions of the seasonal MCA between whole tropical MOGC3 OLR and whole extratropical MOGC3 Z500, to compare with the previous results from reanalysis. The Z500 homogeneous regressions are similar to the heterogeneous regressions, so only the heterogeneous regressions are shown. This is reflected by the high correlations between the expansion coefficients of OLR and Z500 (figures 3.10b, 3.10c and 3.10d). Mode 1 is well separated from mode 2 in the squared covariance fraction (figure 3.10a).

Figure 3.11 shows the difference in the MCA patterns between MOGC3 and the reanalysis. For Z500 the heterogeneously regressed patterns are used. It also shows the spatial correlations between the patterns, calculated with latitudinal

cosine weighting, and correlated over either just the tropics (15°S to 15°N) or the extratropics (40°N to 90°N). Significances in the spatial differences are tested by a two-tailed Monte Carlo method. From the 99-year MOGC3, 34 years, which corresponds to the number of years in NCEP2, is drawn randomly without replacement for each run. MCA is performed for those 34-year MOGC3, and NCEP2 MCA patterns are subtracted from each run. The sign of the MCA patterns are arbitrary, but it is important to have the same sign before any subtraction. We choose positive ENSO and negative NAO to be the reference states, and we multiply both the OLR and Z500 regression patterns by -1 whenever both the spatial correlations of the OLR and Z500 patterns are negative to these reference states. After repeating the sampling a thousand times, the significance at each grid point is deduced by where the zero value lies in the resulting distribution. For example, a grid point with a significance of 95% means that the zero lies either within the smallest 25 or the largest 25 values at the two ends of the distribution. The null hypothesis is that the difference is not statistically different from zero.

We focus on the differences in mode 1. Although both OLR and Z500 show statistically significant differences between MOGC3 and NCEP2 MCAs, the magnitude of the OLR difference is only half compared to the OLR MCAs, whereas the magnitude fo the Z500 differences is comparable to the Z500 MCAs. Therefore, for mode 1 both datasets have similar OLR but different Z500 in the MCAs. Based on the literature on tropical-extratropical teleconnections through stationary Rossby wave propagation (e.g. Hoskins and Ambrizzi, 1993; Trenberth et al., 1998), we will investigate whether this mechanism could explain the MCA differences in the next chapter.

### 3.2.2 Daily analysis

#### 3.2.2.1 All years

We also perform MCAs on daily MOGC3 data, with OLR leading Z500 by 14 days. We again remove the daily climatology and detrend the data before the MCA. Figure 3.12 shows the regressions for using all years. The leading mode OLR

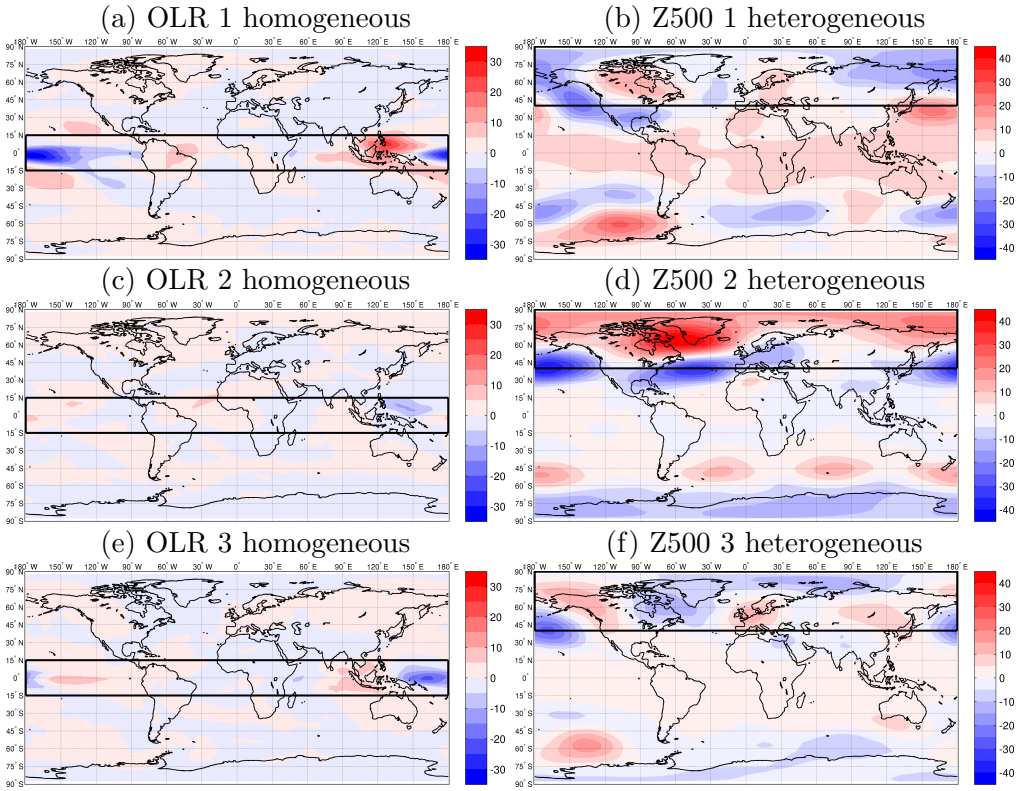
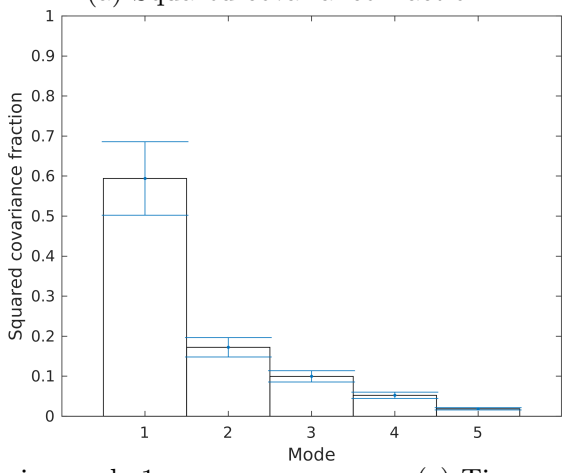
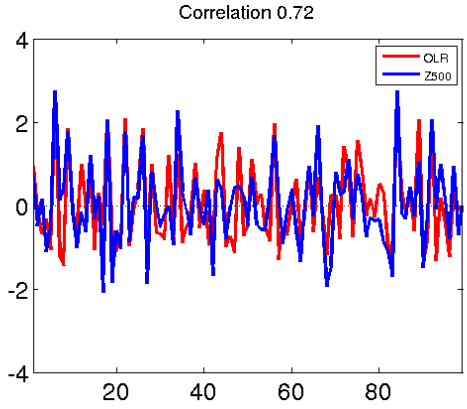



Figure 3.9: First three MCA modes, with hemispheric tropical MOGC3 OLR homogeneously regressed ($Wm^{-2}$), and northern hemispheric extratropical MOGC3 Z500 heterogeneously regressed (m). The black boxes mark the MCA regions.

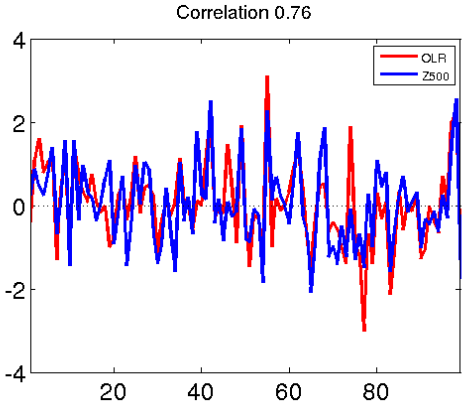
(a) Squared covariance fraction




(b) Time series mode 1




(c) Time series mode 2




(d) Time series mode 3

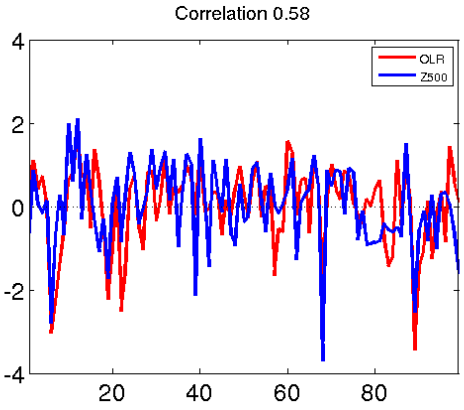



Figure 3.10: Squared covariance fraction and the time series from the MCA between hemispheric tropical MOGC3 OLR and northern hemispheric extratropical MOGC3 Z500.

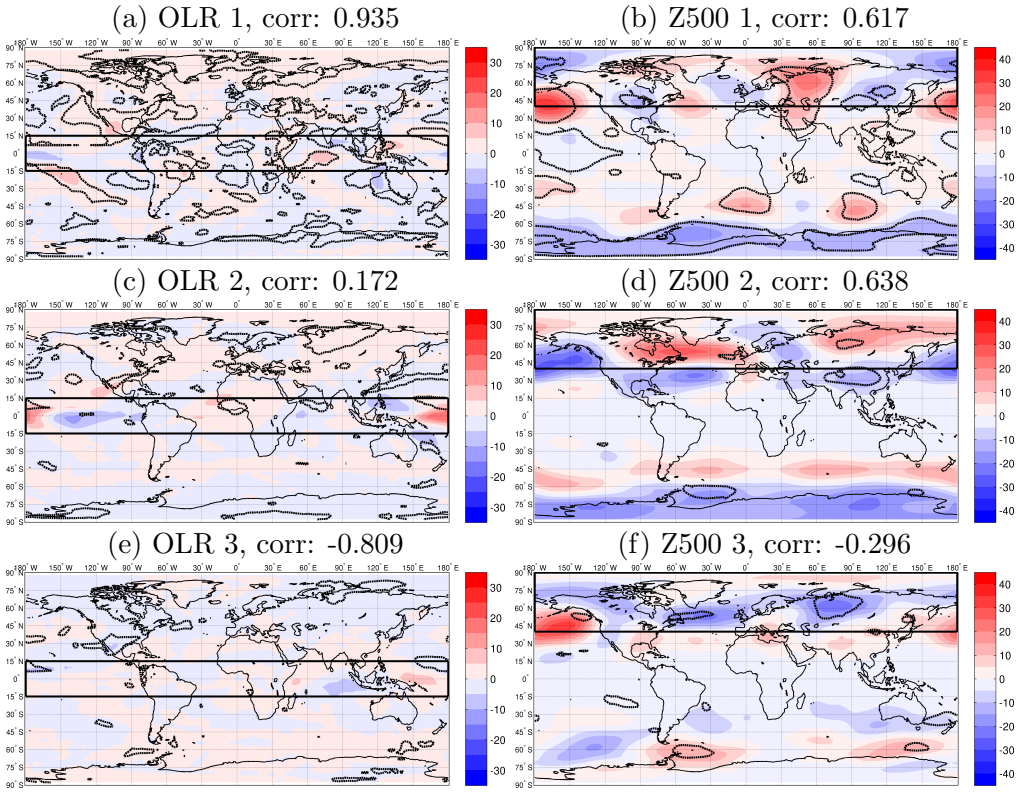



Figure 3.11: MOGC3 MCA patterns (figure 3.9) minus the NCEP2 MCA patterns (figure 3.1), for homogeneously regressed OLR ($Wm^{-2}$) and heterogeneously regressed Z500 (m), with black contouring at 95% significance. The black boxes mark the MCA regions. The spatial correlations between the MCA patterns of MOGC3 tropical OLR and NCEP2 tropical OLR, and that between the MCA patterns of MOGC3 extratropical Z500 and NCEP2 extratropical Z500, are also indicated. For mode 3, because of the anti-correlations, both MOGC3 OLR and Z500 patterns have been reversed before subtracting the mode 3 NCEP2 patterns.

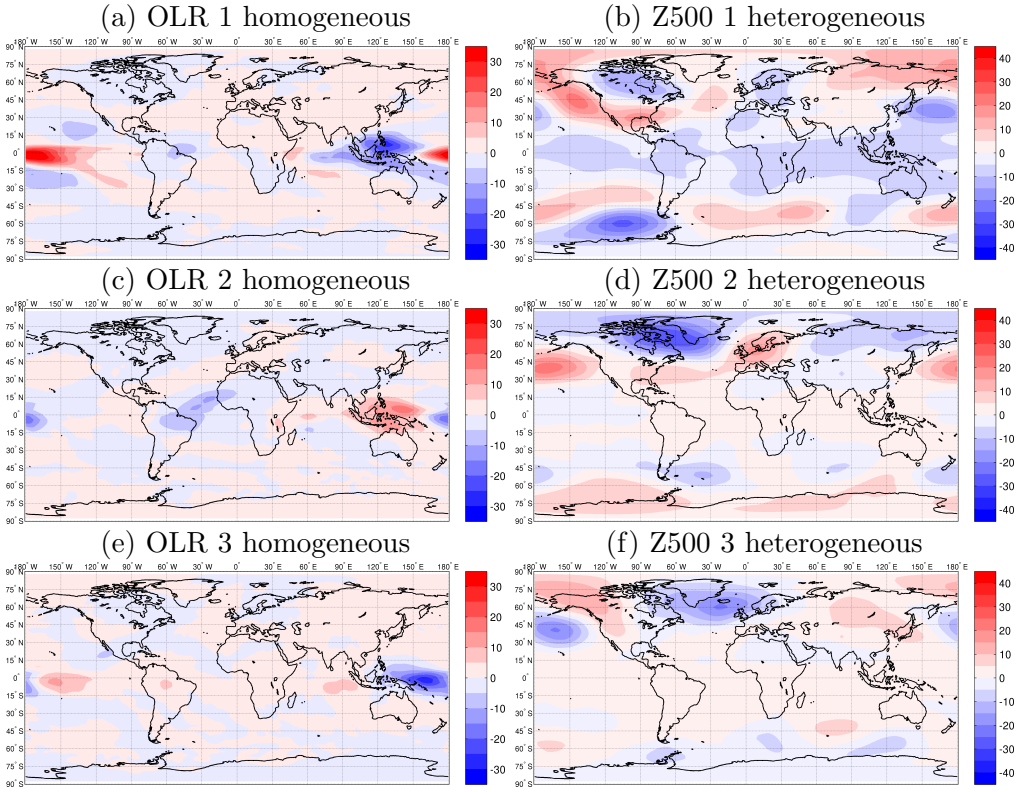



Figure 3.12: Calculated from daily data with OLR leading Z500 by 14 days, all years. First three MCA modes, with hemispheric tropical MOGC3 OLR homogeneously regressed ($Wm^{-2}$), and northern hemispheric extratropical MOGC3 Z500 heterogeneously regressed (m).

and Z500 patterns are similar to the leading mode from seasonal data. This agrees with the reanalysis MCAs between seasonal and daily data for all years, suggesting MOGC3 is capturing ENSO as the leading mode on both timescales. The leading mode also explains a fraction of squared covariance similar to the reanalysis (figures 3.13 and 3.6a respectively).

We again test the robustness of the leading mode to odd and even years subsampling. We first focus on the even years subsample. The SCF is similar and remain separated from the second mode. The correlation between the expansion coefficients of the OLR and the Z500 is again higher than previous (0.28 compared to 0.23). The singular vectors and regression patterns are similar. However, the odd years subsample result is quite different. The singular vectors and regression patterns of the leading mode in this subsample resembles the previous mode 2 in both OLR and Z500, whereas its mode 3 resembles the previous mode 1. Further

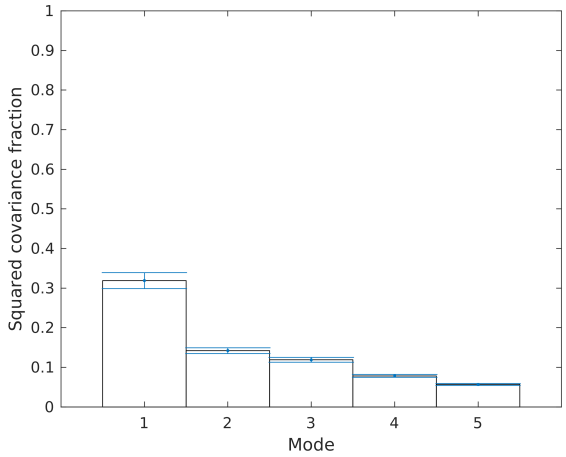



Figure 3.13: Calculated from daily data with OLR leading Z500 by 14 days, all years. Squared covariance fraction from the MCA between hemispheric tropical MOGC3 OLR and northern hemispheric extratropical MOGC3 Z500.

analysis reveals that this is due to different ENSO frequencies in the subsamples and the full period. As will be explained in section 3.2.2.2, we identify 37 ENSO winters in the 100-year period. Of these, 23 years are even and 14 years are odd. The percentage of ENSO years are 37% in the full period, 46% in the even-year subsample, and 28% in the odd-year subsample. In the full period and the even-year subsample, the MCA is picking up ENSO as the leading mode. For the odd-year subsample, because of the lower frequency of ENSO events, the MCA is picking up the NAO as the leading mode instead, and the ENSO covariability drops to the third mode. Therefore, the threshold of ENSO frequency for which MCA is picking up ENSO as the leading mode seems to be at least 37%. To summarize, if we do not consider the odd-year subsample because of its lower ENSO frequency, the full-year MCA result is robust to the sub-sampling.

#### 3.2.2.2 ENSO-neutral years

We identify ENSO-years as those where the seasonal mean of the all-years MCA mode 1 OLR daily expansion coefficient exceeds the absolute value of one standard deviation. Of the 100 years, we identify 16 El-Niño years and 21 La-Niña years. Figure 3.14 shows the MCA regressions for only using ENSO-neutral years. The leading mode is similar to that identified using reanalysis (figure 3.7), with

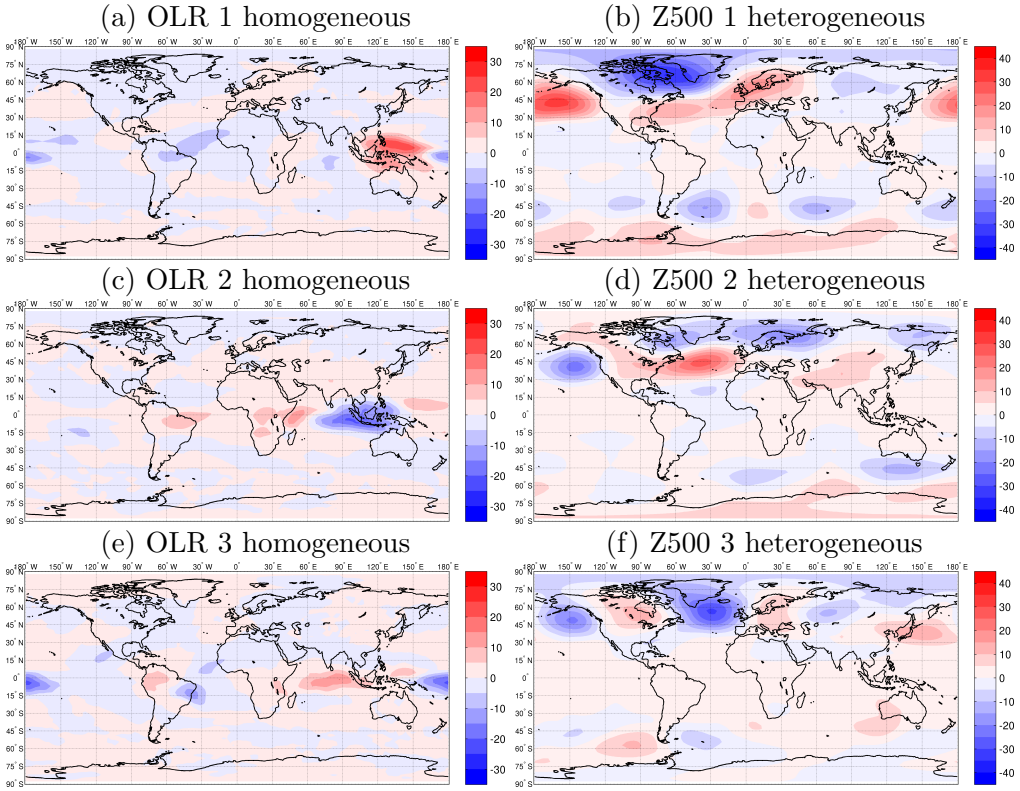



Figure 3.14: Calculated from daily data with OLR leading Z500 by 14 days, on ENSO-neutral years. First three MCA modes, with hemispheric tropical MOGC3 OLR homogeneously regressed ($Wm^{-2}$), and northern hemispheric extratropical MOGC3 Z500 heterogeneously regressed (m).

increased OLR over the Maritime Continent and an NAO-like Z500 pattern. The SCF (figure 3.15) is similar to the reanalysis and is separated from the second mode.

We again test the robustness of the leading mode to odd and even years sub-sampling. The singular vectors and regression patterns are similar. The SCF is similar in the odd-year subsample but drops to 0.2 in the even-year subsample, although both remain separated from the second mode. The correlation between the expansion coefficients of the OLR and Z500 is again higher than previous (0.41 and 0.40 compared to 0.32). We conclude that this MCA result is robust to the sub-sampling.

Finally, we look at the difference between the leading modes of MOGC3 and NCEP2 daily data with OLR leading Z500 by 14 days, for both all years (figures 3.16a and 3.16b) and only ENSO-neutral years (figures 3.16c and 3.16d). We

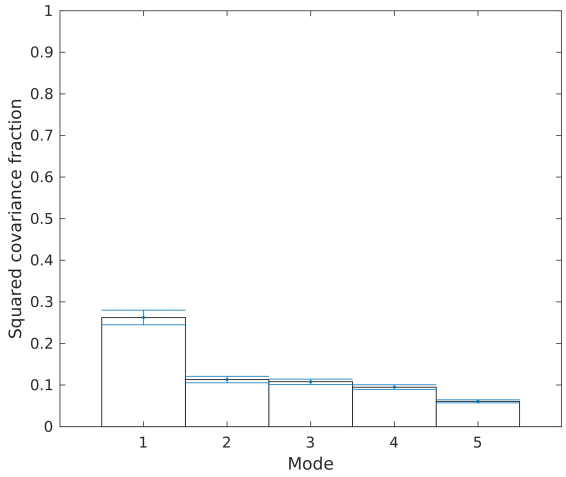



Figure 3.15: Calculated from daily data with OLR leading Z500 by 14 days, on ENSO-neutral years. Squared covariance fraction from the MCA between hemispheric tropical MOGC3 OLR and northern hemispheric extratropical MOGC3 Z500.

again make sure that the patterns are the same sign as our previously chosen reference states (El-Niño and NAO-), by reversing both OLR and Z500 patterns if necessary, before any subtraction. For the all-years MCAs, the differences in these daily patterns are similar to the seasonal data (figures 3.11a and 3.11b). Therefore, these ENSO-related MCA differences between MOGC3 and reanalysis are robust across timescales from daily to seasonal.

To further test the robustness of these differences in figure 3.16, we repeat using the aforementioned MCAs with odd or even years sub-sampling. The results are given in figure 3.17. For example, figures 3.17a and 3.17b are the even-year MCA sub-sampling of figure 3.16a and 3.16b. Comparing their similarities give us estimates on the confidence in these MCA differences maps. In particular, when considering only the even-year sub-samplings, since figures 3.16a and 3.16b compare well with figures 3.17a and 3.17b respectively, and since figures 3.16c and 3.16d compare well with figures 3.17c and 3.17d respectively, the MCA difference maps in figure 3.16 all seem to be robust when subjected to even-year sub-sampling. A similar analysis on the maps in figure 3.16a and 3.16b cannot be carried out for odd-year sub-sampling, because of the lower ENSO frequency in the odd year period explained earlier. However, a similar analysis on the maps in

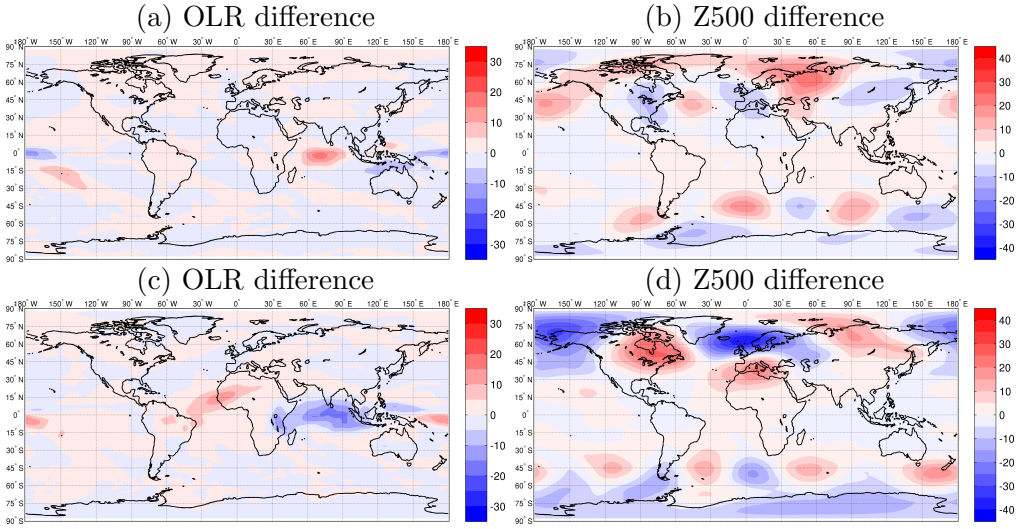



Figure 3.16: The differences in the leading mode MCAs of MOGC3 minus NCEP2 daily data, with OLR leading Z500 by 14 days, for (top row) all years and (bottom row) ENSO-neutral years. OLR is homogeneously regressed ($\mathrm{Wm}^{-2}$), and Z500 is heterogeneously regressed (m).

figure 3.16c and 3.16d carried out for odd-year sub-sampling shows quite different patterns. Comparison of the OLR in figure 3.16c to figure 3.17e shows different OLR anomalies in the Indian Ocean and the Maritime Continent. And comparison of the Z500 in figure 3.16d to figure 3.17f shows different Z500 anomalies in the east coast of the US and in northern Russia near 90°E.

To summarize, the sampling uncertainty in the daily MJO-NAO like teleconnection bias (figures 3.16c and 3.16d) is large. However, the daily ENSO-like teleconnection bias (figures 3.16a and 3.16b) is robust not just to even-year sub-sampling but also robust in the seasonal timescale (figures 3.11a and 3.11b). Therefore, in the next chapter we will focus on investigating the ENSO teleconnection bias.

## 3.3 Chapter summary

Using maximum covariance analysis, we investigate the leading modes of covariability between the tropical outgoing longwave radiation and the extratropical geopotential height. Using observed data and reanalysis, the leading mode of covariability on the seasonal timescale is associated with the El-Niño Southern

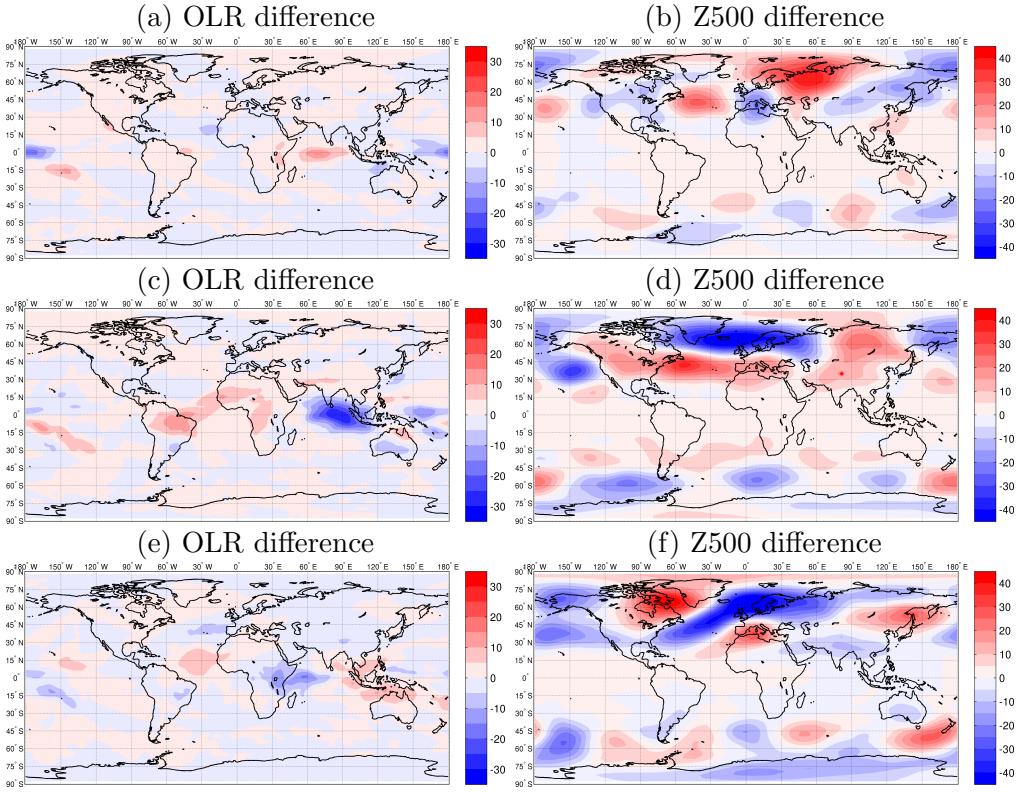



Figure 3.17: (a,b,c,d) Same as figure 3.16 but using only even years in both NCEP2 and MOGC3 datasets. (e,f) Same as (c,d) but using only odd years. The reason behind the lack of the corresponding figures of (a,b) using only odd years is addressed in the main text.

Oscillation (figures 3.1a and 3.1b). We then assess the representation of this covariability in a Met Office climate model control run. Although the leading mode is still ENSO (figures 3.9a and 3.9b), the extratropical pattern shows large differences in the North Pacific-American region that are statistically significant (figure 3.11b). This difference resembles a zonal wavenumber 3 pattern, with a phase showing higher heights in the North Pacific, western North Atlantic and western Russia, and lower heights in central North America, the UK and eastern Russia. The amplitude in the North Pacific is largest, at around 30 m.

Using reanalysis on the daily timescale, ENSO still dominates the tropical-extratropical covariability when all years are included in the analysis (figures 3.5a and 3.5b). However, when only ENSO-neutral years are used and when the tropics is leading the extratropics by 14 days, the dominant extratropical mode becomes the North Atlantic Oscillation (figure 3.7b). Associated with this is a tropical pattern resembling the Madden-Julian Oscillation (figure 3.7a). The 14-day lead is consistent with the timescale of Rossby waves propagating from the tropics into the extratropics, and other studies have also suggested similar wave propagation link from the MJO to the NAO. Although the corresponding MJO-NAO modes in the climate model show some differences to the reanalysis modes (figures 3.16c and 3.16d), these MJO-NAO differences are not as robust as the ENSO differences (figures 3.17c, 3.17d, 3.17e and 3.17f). We therefore conclude that under the maximum covariance analysis framework, the ENSO teleconnection is robustly less-well represented in the climate model compared to in the reanalysis.

# Chapter 4

# ENSO Experiments

In the last chapter, we identified the MCA leading mode in both reanalysis and MOGC3 data to be ENSO, in both seasonal and daily timescales with all years included. Comparison of the leading mode between reanalysis and MOGC3 showed similar tropical OLR patterns but less similar extratropical Z500 patterns. In this chapter we aim to explain this difference through differences in Rossby wave propagation related to the climatological upper level zonal wind bias in MOGC3.

The idea that upper level zonal wind bias could affect Rossby wave propagation in coupled models has been investigated by Dawson et al. (2011). By comparing two earlier versions of the Met Office coupled models with different horizontal resolutions in both the ocean and the atmosphere, they related the incorrect extratropical SST response to El-Niño in the lower resolution model to the upper level wind bias. They showed the possibility of these wind biases being related to different Rossby wave propagation due to subtle biases in the time-mean zonal winds in the low resolution model. In a follow-up study, Dawson et al. (2013) first performed coupled model simulations to conclude that the extratropical response to El-Niño has less bias in higher oceanic resolution simulation than in lower oceanic resolution simulation, and is independent of the atmospheric resolution. They then performed atmosphere-only simulations to show that the upper level time-mean zonal wind bias can be accounted for by the SST biases from lower oceanic resolution simulation.

In this chapter, firstly we aim to update these previous studies to the next

generation MOGC3 model which will be submitted to CMIP6. We will show that although the Met Office model has undergone development since these earlier studies, basic state biases still remain which can have significant dynamical consequences. Secondly, we aim to demonstrate the different Rossby wave propagations more explicitly, by using a hierarchy of stationary Rossby wave propagation models, from ray tracing to barotropic model to baroclinic model.

In the last chapter, we have also identified a link between the MJO and the NAO. Studies like Henderson et al. (2017) have also demonstrated the sensitivity of the MJO extratropical teleconnection to the climate model basic state. However, we have found that the 14-day lead daily MCA differences from ENSO-neutral years between reanalysis and MOGC3 are not robust to sub-sampling between odd and even years. Therefore, we do not pursuit further experiments on the MJO, which could be work in the future.

## 4.1 Jet and waveguide biases

Figure 4.1 shows the boreal wintertime climatological 250 hPa zonal wind bias of MOGC3 from the NCEP2 reanalysis. We focus on the North Pacific jet because it shows the largest bias, and also because of its proximity to the tropical ENSO region. In MOGC3 the North Pacific jet is strengthened on the equatorward flank and weakened on the poleward flank. The Hovmöller diagram shows the time evolution of the jet bias, where we have averaged the bias of each seasonal mean wind across 150°E and 240°E and plotted at all latitudes against time. It is clear this North Pacific jet bias is a robust and persistent feature across most years in MOGC3.

Stationary Rossby wave propagation depends on the background zonal wind, through the stationary wavenumber and waveguide (Hoskins and Karoly, 1981). From the previous chapter, we concluded that both the MOGC3 and NCEP2 datasets have similar tropical OLR related to ENSO but different extratropical Z500. One hypothesis is that the same tropical forcing might cause different extratropical responses through the jet bias. As the OLR centre of action is

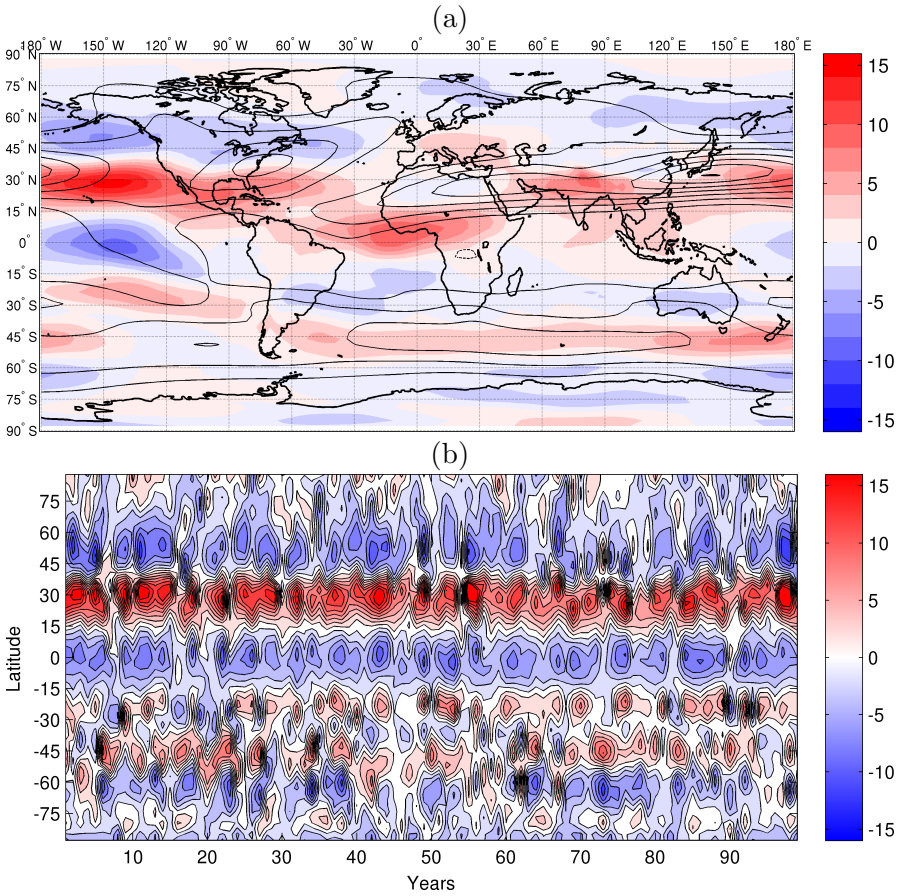



Figure 4.1: (a) DJF 250 hPa climatological zonal wind bias in MOGC3 from NCEP2 (color contour every 2 $ms^{-1}$), and the NCEP2 climatology (black contour every 10 $ms^{-1}$ from -10 to 70 $ms^{-1}$ with zero contour omitted, positive solid and negative dashed). (b) Hovmöller diagram of the North Pacific jet bias (averaged between 150°E and 240°E) of the DJF seasonal mean wind against years.

mainly in the tropical Pacific near the international Date Line, and the jet bias is mainly in the North Pacific just downstream of it, it is possible that the stationary Rossby wave triggered by the same tropical Pacific OLR source may propagate differently in the different waveguides due to the jet bias, resulting in a different extratropical response.

We first investigate how the jet bias could affect the waveguide, as revealed by analysis of the stationary wavenumber $K_s$. We test the sensitivity of the stationary wavenumber $K_s$ to different methods of calculation. We calculate $K_s$ using the DJF 250 hPa zonal wind. Figure 4.2 confirms that $K_s$ should only be calculated from the climatological wind, rather than for each DJF and then averaged interannually. This is because the turning latitudes and critical lines vary from year to year, and any averaging over interannual $K_s$ would result in large areas of the extratropics being deemed impossible for wave propagation. Figures 4.2b and 4.3b show the $K_s$ sensitivity on 60° zonal wind smoothing. A 60° smoothing is chosen following Scaife et al. (2017), under the scale separation assumption between a wave and a smoother basic state on which it propagates.

Using the climatological 250 hPa zonal wind and a 60° zonally smoothing window, figure 4.3 shows the DJF waveguides of MOGC3 and NCEP2. The mid-latitude region with the largest difference in $K_s$ extends from the Aleutian Islands to the US west coast, with a magnitude beyond -1. This region has $K_s$ between 3 and 4 in NCEP2, and has $K_s$ only between 2 and 3 in MOGC3. This negative $K_s$ bias suggests that poleward propagating waves originating from the tropical Pacific, with zonal wavenumber between 3 and 4, would encounter the $K_s$ 3 and 4 contours at a lower latitude in MOGC3 than in NCEP2. The waves might then reflect equatorward at a lower latitude. There are also big areas of differences along the equator which may affect cross-equatorial flows. These are less relevant to waves already in the mid-latitude, and only affect the critical latitudes where these waves dissipate once they have reflected equatorward from the mid-latitude. Another area with big $K_s$ difference of up to 3 in magnitude is over north-eastern Siberia, where MOGC3 shows climatological easterlies but not in NCEP2. The

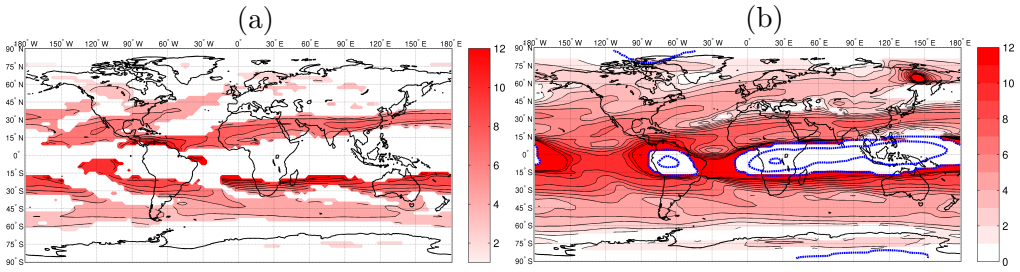



Figure 4.2: NCEP2 DJF stationary wavenumber calculated from (a) seasonal winds then averaged interannually, and from (b) climatological wind. Blue contours in (b) show the easterlies at $5\,\mathrm{ms}^{-1}$ (with the zero contour included), indicating the boundaries of the critical latitudes. White regions are boundaries of the turning latitudes for all waves, and waves cannot propagate into these regions.

zero zonal wind line between this and the westerlies around it creates a critical latitude for all waves. Such critical latitude is uncommon at high latitudes in reanalysis, and is only prevalent in the tropics.

## 4.2 Ray tracing

Here ray tracing is used to test whether the poleward propagation of stationary Rossby waves from the tropical Pacific may be different between MOGC3 and NCEP2 basic states. We specify the background zonal wind either from NCEP2 or MOGC3, the starting position of the ray, and the zonal wavenumber of the ray to be traced. We trace the rays for a maximum of 15 days, which as shown below is sufficient for the cases we are interested in.

Figure 4.4 shows the rays started from the tropical Pacific at 160°W and 15°N, using either the MOGC3 or the NCEP2 zonal winds. For each basic state, we trace rays with zonal wavenumbers (k) from 1 to 4, which represent the majority of stationary waves that could propagate from the tropics into the extratropics within this framework. We first comment on the ray paths. k1 rays propagate similarly in the two basic states, propagating north-eastward from the tropical Pacific into the Gulf of Alaska and gradually turning more zonal until finally reflecting equatorward at the eastern Beaufort Sea. k2 rays propagate similarly as the k1 rays, but because the $K_s2$ contour is slightly lower in latitude than the $K_s1$ contour, these rays propagate lower in latitude into British Columbia in Canada

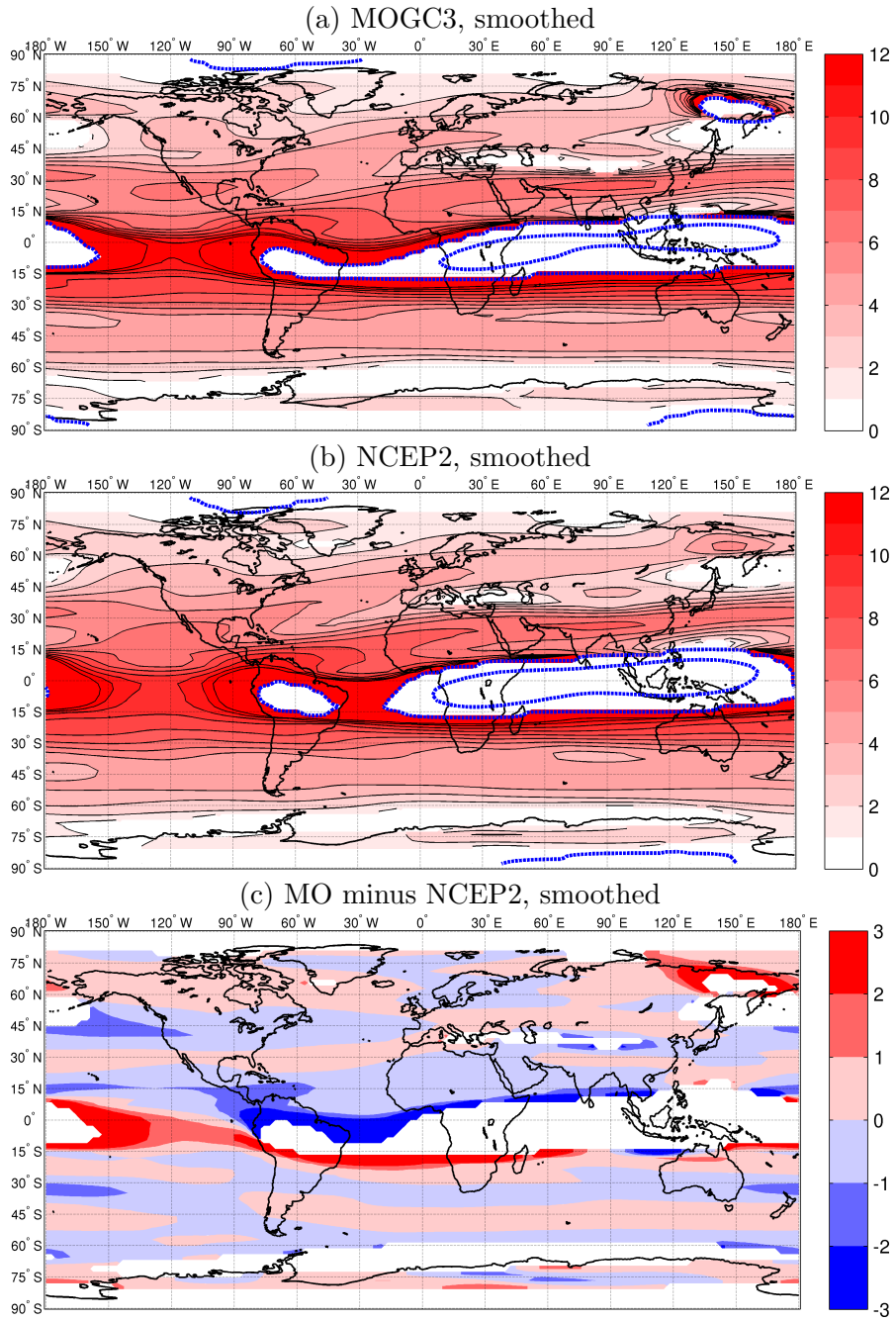



Figure 4.3: Stationary wavenumber calculated from (a) MOGC3 and (b) NCEP2, using 60° zonally smoothed climatological wind. Blue contour shows the easterlies at $5\,\mathrm{ms}^{-1}$ with the zero contour included. (c) The difference of MOGC3 minus NCEP2.

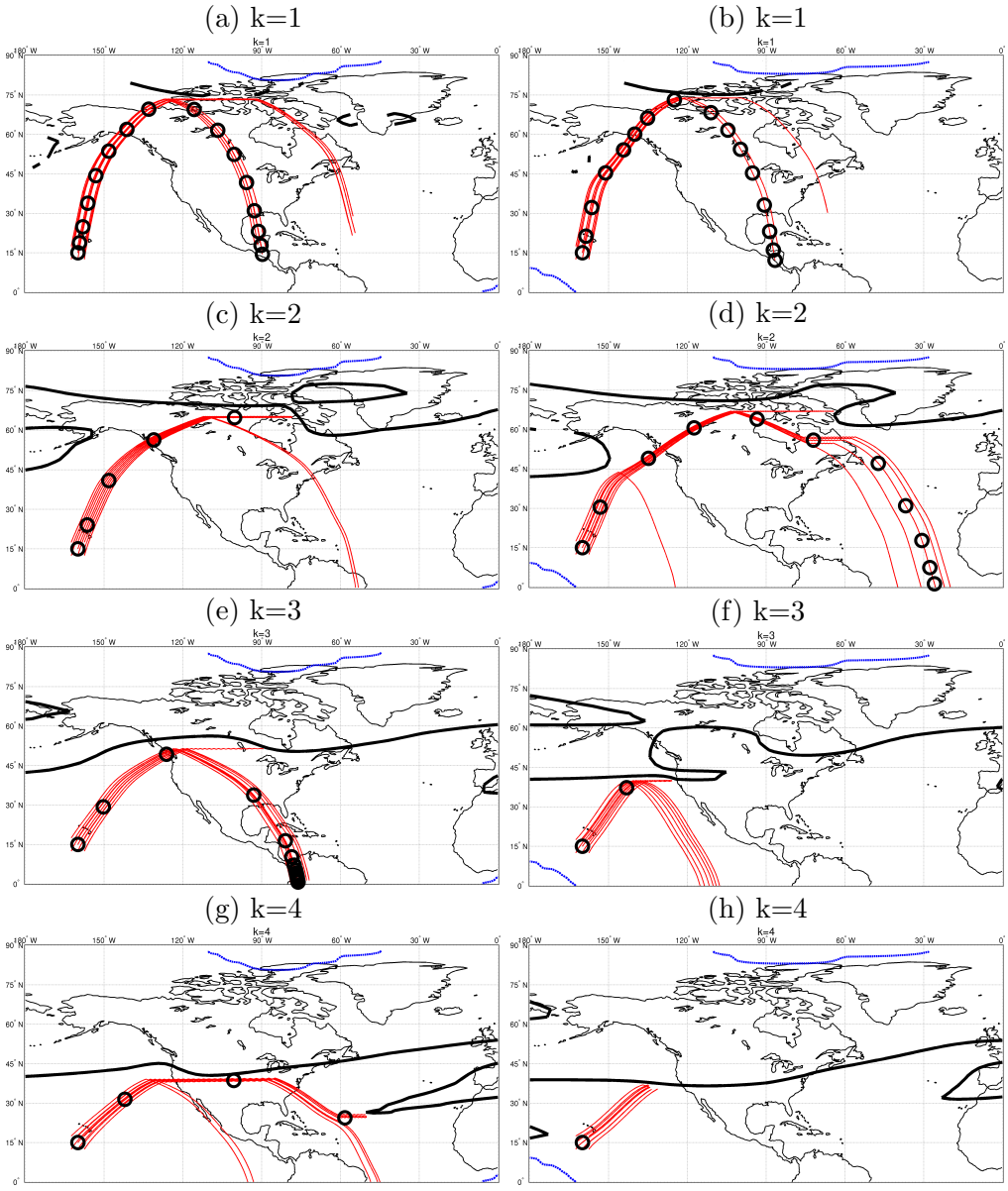



Figure 4.4: Ray tracing started at 160°W and 15°N. DJF 250 hPa zonal wind with 60° zonal smoothing are used as the basic states, for (left) NCEP2 and (right) MOGC3. Contour conventions as in figure 2.1.

and turn almost zonal near the west of Hudson Bay. The ensemble of rays split over this region in both basic states, with some continuing eastward through the north of Hudson Bay and into the Northwestern Passages, and some reflecting equatorward. Those that continue zonally finally terminate before reaching the Labrador Sea, where they intersect the $K_s2$ contour.

Although theoretically rays should reflect at these turning latitudes instead of terminating, we find that the angle between the ray path and the $K_s$ contour in this case is so sharp that one single further timestep brings the ray from a region of $K_s2.5$ or higher to a region with $K_s$ lower than 2 (for an explanation of the 0.5 threshold, please refer to the Methods section). In these regions where $K_s$ is smaller than $k$, the meridional group velocity of the ray is no longer well defined (equation 2.11), so the rays terminate. For the rays that reflect equatorward, both basic states suggest propagation arcing across North America. The NCEP2 basic state supports propagation equatorward into the east of the Leeward Islands. The MOGC3 basic state supports propagation further east into the North Atlantic before finally reaching the tropics west of North Africa.

The propagation of the k3 rays are more different between the two basic states. NCEP2 supports propagation into Vancouver before reflecting equatorward and propagating across the US from northwest to southeast, before reaching the Caribbean Sea. However, the $K_s3$ contour in MOGC3 is much lower in latitude than NCEP2, and the rays reach their turning latitude already while still in the Pacific Ocean west of the US West Coast. They reflect equatorward and propagate almost parallel to the North American coastline before reaching the equator. Finally, the $K_s4$ contour in both basic states are similar, which should support similar propagation. NCEP2 supports propagation across the central US before reflecting into the tropical Atlantic. But in MOGC3 all rays are terminated before any reflection. This is again because of the sharp angle between the ray paths and the $K_s$ contour, as explained above for the k2 rays.

Revisiting the assumption of scale separation and our 60° zonal smoothing on the zonal wind, we repeat the above ray tracing without any smoothing. The

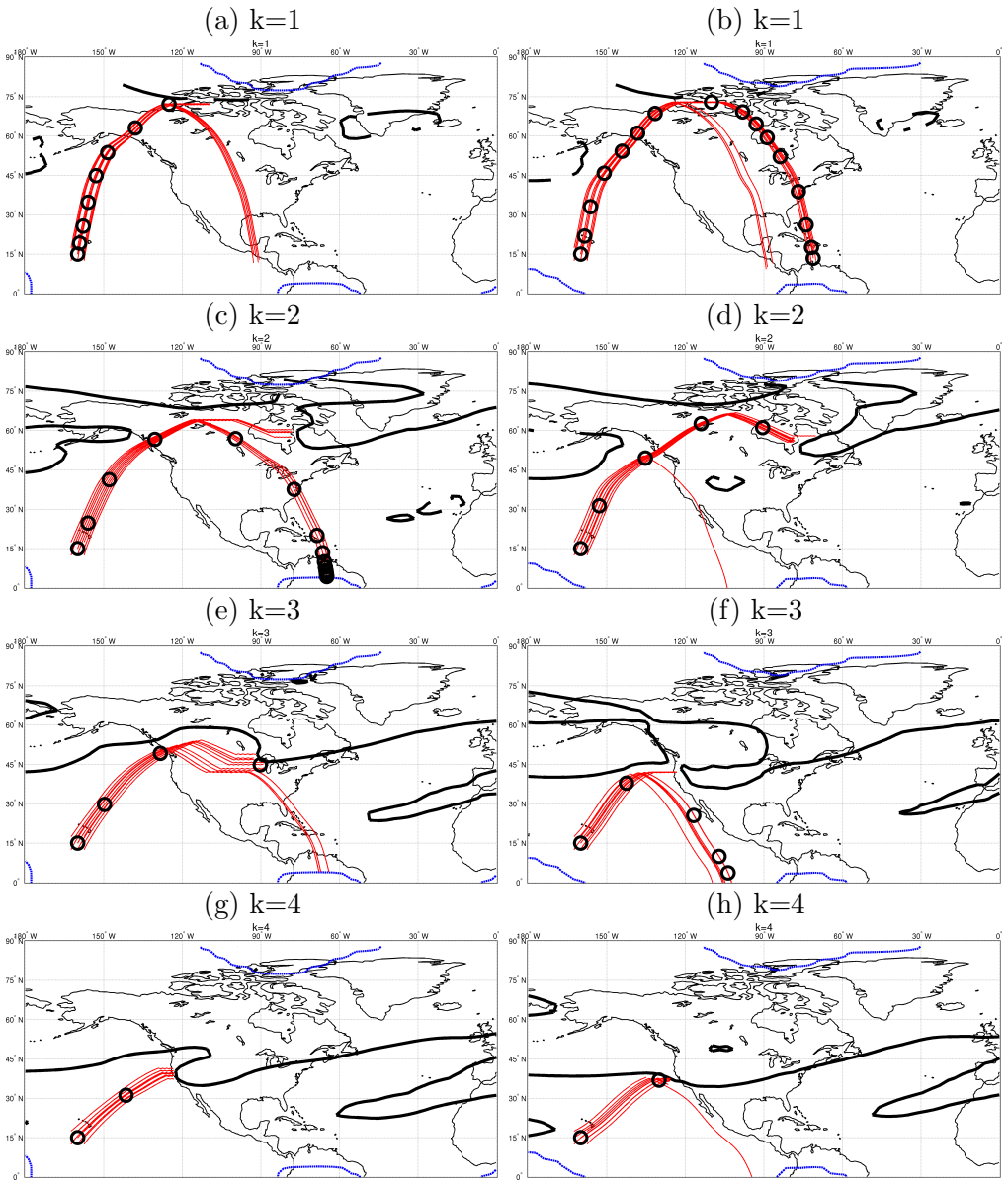



Figure 4.5: Ray tracing started at 160°W and 15°N. DJF 250 hPa zonal wind with no zonal smoothing are used as the basic states, for (left) NCEP2 and (right) MOGC3. Contour conventions as in figure 2.1.

results are qualitatively similar (figure 4.5), suggesting that at least for the North Pacific and North America, ray tracing is not too sensitive to smoothing. However, given the above sensitivities to the slight differences in orientations of the $K_s$ contours, we expect ray tracing to also be sensitive to the starting position of the rays. Although part of this has been explored by the ensemble of rays, as mentioned in the Methods section the ensemble only covers a square of 5°. We repeat the tracing further west of the above starting position by 15° (Figure 4.6). The ray paths for k1 and k3 in NCEP2 remain qualitatively unchanged apart from being shifted to the west accordingly by 15°. Interestingly, the k2 ray path remains the same over North America and is not shifted westward accordingly. The k4 rays reflect equatorward before even reaching North America, which is similar to the path of one of the ensemble members before the shift. For the MOGC3 basic state, there are big changes to the k1 and k2 ray paths. k1 rays encounter a region in the North Pacific where $K_s$ becomes zero (figure 4.3a) because the meridional gradient of the absolute vorticity becomes zero (equation 2.9). Theoretically, all rays with any values of k should reflect equatorward here. But again, the sharp angle results in ray termination. k2 rays encounter the $K_s2$ contour south of the Aleutian Islands, and reflect equatorward there instead of the previous propagation into Canada. The majority of the k4 rays immediately encounter the $K_s4$ contour and reflect equatorward or terminate due to the sharp angle. The only k4 ray that propagates out of the tropical Pacific has a similar path as the previous unshifted ensemble. Finally, the k3 rays show similar propagation as the previous ensemble apart from being shifted to the west accordingly.

Combining results from both starting positions, we conclude that the difference of ray path between NCEP2 and MOGC3 basic states is most robust for k3 rays originating from the tropical North Pacific, although k2 and k1 propagations can be different too for rays started further west towards the Date Line. To summarize, there is some evidence that waves propagating into the North Pacific should turn equatorward at a lower latitude in MOGC3. A benefit of ray tracing is its a-priori prediction from the close link to the $K_s$ theory. But the sensitivity to the starting

position of the rays highlights the limitation of the ray tracing approach.

Next we comment on the propagation speed of the rays. Rays propagate at the group velocity given by equation 2.12. The group velocity is proportional to k of the ray, with the proportionality being plotted in figure 4.7. This proportionality generally increases poleward from the tropical Pacific to the North Pacific in both NCEP2 and MOGC3, and explains why for each k ray the daily markers space out further at higher latitudes. In MOGC3 basic state however, this proportionality slightly decreases with latitude near the Gulf of Alaska. This is consistent with the daily markers of the k1 ray in MOGC3 becoming closer to each other when entering the Gulf of Alaska. And since the group velocity is proportional to k, this explains why when comparing rays with different k, the markers space out further with bigger k. The deceleration and stagnation of some rays near the equator after reflection from the mid-latitudes is because of the near zero of proportionality near the equator. Physically this can be reconciled by considering that the amplitude of the ray may already have been damped sufficiently by the time it propagates to the equator.

Finally, by counting the daily markers, the rays usually take only around 3 to 4 days to propagate from the tropics into the extratropics, in contrast to the usually quoted 7 to 14 days. This is because the ray tracing so far only shows the propagation timescale within the local sector of the North Pacific and North America, whereas the 7 to 14 days is usually for the wave pattern to set up circumglobally in the mid-latitudes as a whole. Another reason may be because in reality it takes time to set up the Rossby wave source (RWS) from tropical convection, and it takes time to set up a wave in the vicinity of the RWS before the wave can start propagating. In ray tracing the propagation is immediate.

## 4.3 Barotropic experiments

We use a barotropic model to test our ray tracing results. In our first set of experiments, we want to test if the different basic states in NCEP2 and MOGC3 can affect the stationary Rossby wave propagation from the tropics. We run our

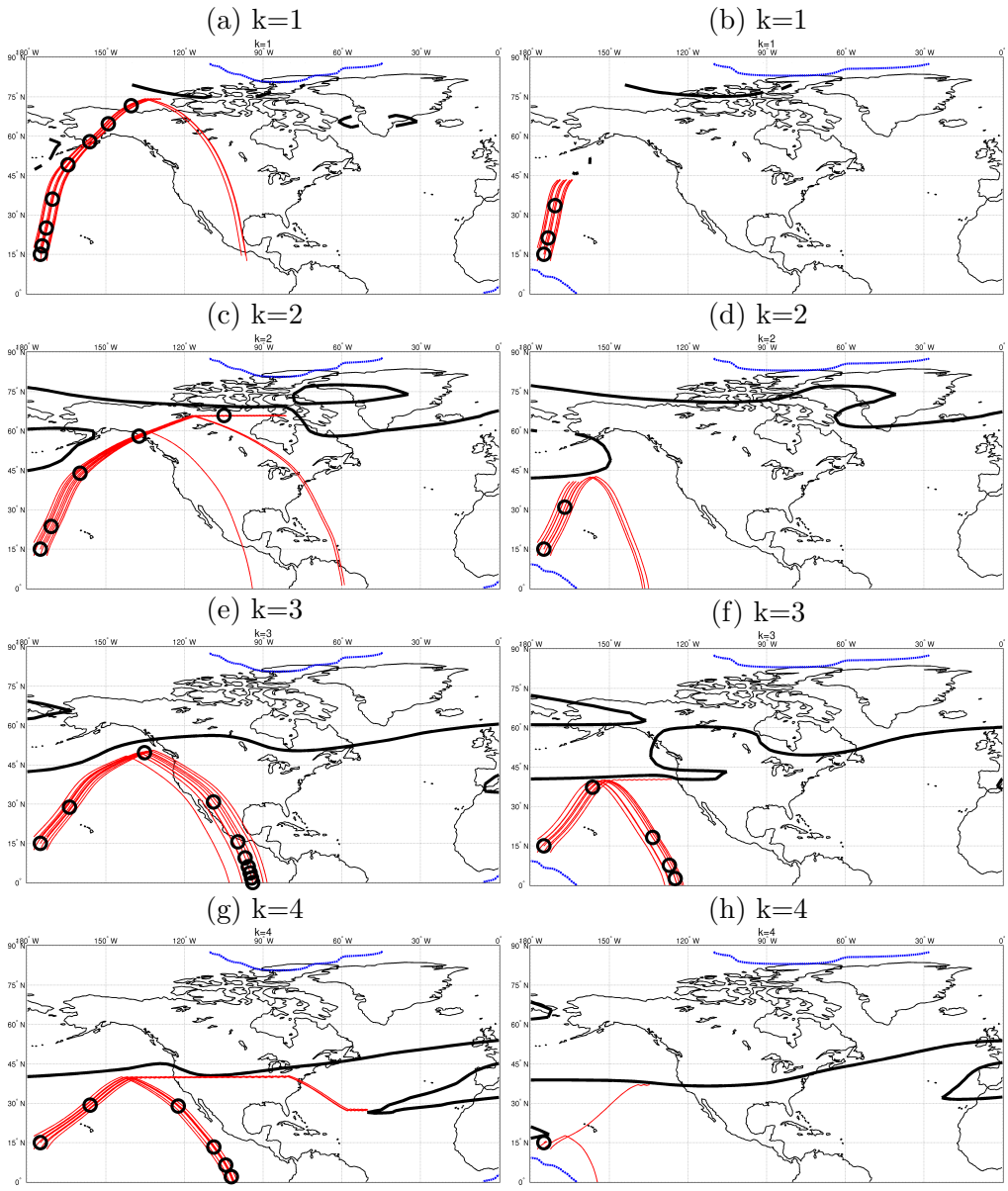



Figure 4.6: Ray tracing started at 175°W and 15°N. DJF 250 hPa zonal wind with 60° zonal smoothing are used as the basic states, for (left) NCEP2 and (right) MOGC3. Contour conventions as in figure 2.1.

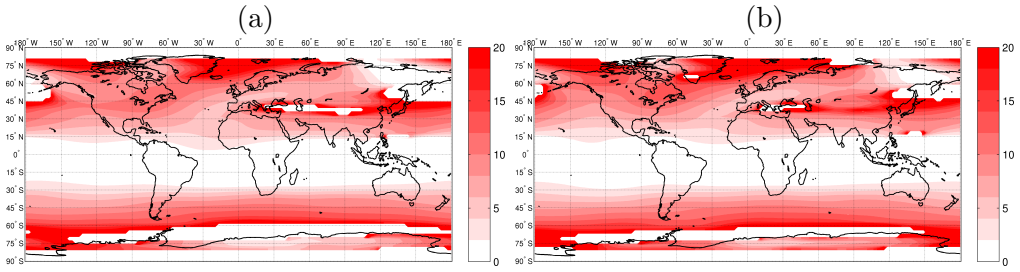



Figure 4.7: The proportionality ($\frac{\overline{u}_M}{K_s}$, equation 2.12) of the group velocity magnitude $c_g$ to the zonal wavenumber magnitude k, for (a) MOGC3 and (b) NCEP2. Units are $\mathrm{ms}^{-1}$.

model with two different basic states but the same Rossby wave source. The basic states used here are the climatological 250 hPa absolute vorticity from NCEP2 and MOGC3. Unlike in the ray tracing where scale separation has been assumed, the basic states here are not zonally smoothed in any extent.

### 4.3.1 Circumglobal tropical forcing

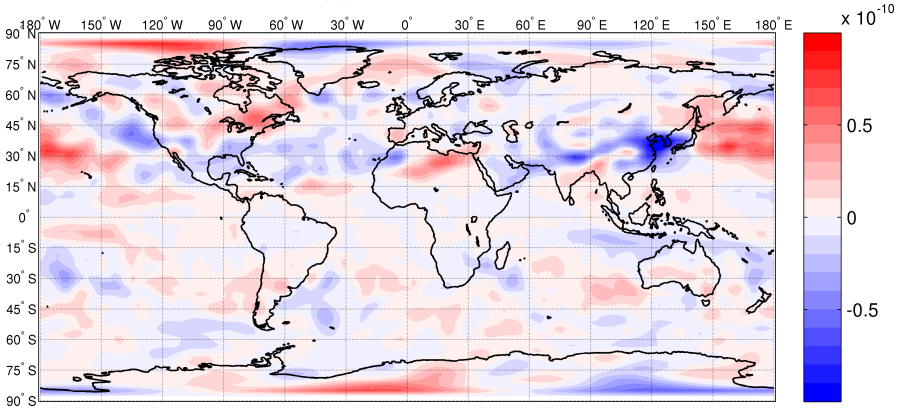
We regress the daily RWS onto the OLR expansion coefficient of the leading mode from the NCEP2 14-day-lead-OLR all-year MCA (section 3.1.4.1), with the sign reversed if necessary to ensure El-Niño. The vorticity advection term (figure 4.8b) is large over the Asian-Pacific jet and the North Atlantic jet maxima as well as near their entrances and exits, because the meridional and zonal gradients of the relative vorticity are large respectively. The vortex stretching term (figure 4.8a) dominates over most of the extratropics because the differential vertical motions from mid-latitude ageostrophic flows can generate large relative vorticity. We combine these two terms and first make a RWS forcing for our experiments using the same 15°N to 15°S latitudinal band as in our MCA OLR. However, studies like Scaife et al. (2017) and Dawson et al. (2011) have highlighted the importance of the RWS further poleward, where its magnitude is often larger than in the tropics. We make another forcing for our experiments with a wider 30°N to 30°S latitudinal band. Despite the RWS showing even larger amplitudes deeper into the extratropics, we refrain from including any RWS further poleward than 30° because our focus is on the propagation of Rossby waves from the tropics into the

extratropics, and not the in-situ generation of waves within the extratropics.

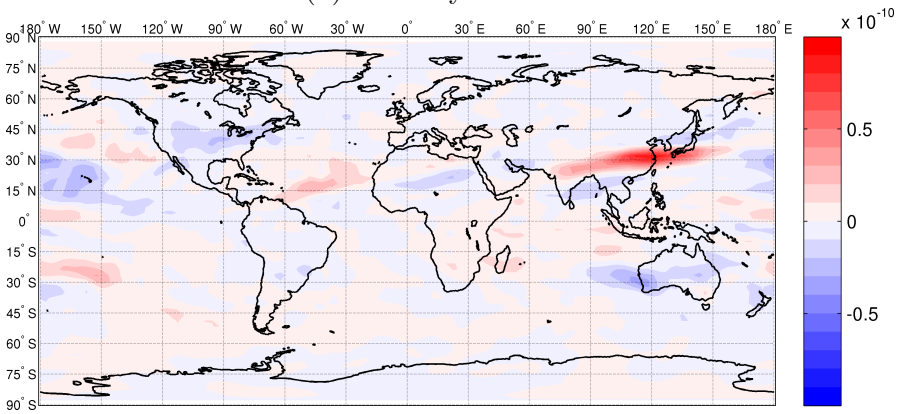
We first describe our experimental results with the meridionally narrower forcing. Under the NCEP2 basic state, the response (figure 4.9a) is similar to a k2 wave in the extratropics, unlike the seemingly k3 wave pattern in the corresponding NCEP2 MCA in figure 3.5b. The Aleutian Low projection and the high over north-eastern North America are similar however, suggesting the North Pacific extratropical response to ENSO is dominated by Rossby wave dynamics. Further downstream the patterns are much less similar, which could be just due to different propagations, or could be the importance of other mechanisms. We see strong RWAF across the North Pacific into the Gulf of Alaska. Under the MOGC3 basic state, the response (figure 4.9c) is again similar to a k2 wave with an Aleutian Low projection. However, the high is much further west over north-western North America. This disagrees with the corresponding MOGC3 MCA pattern in figure 3.12b. But as we will explain later, this does not seem to pose a major problem to our conclusion. Further downstream the pattern is similar to that of the NCEP2 basic state experiment.

The difference between the two experiments (figure 4.9e) resembles the corresponding MCA difference over the North Pacific and North American region in figure 3.16b, with the high near the Aleutian Islands and the low near the eastern North America. Further downstream, although the differences resemble the high over western Russia and the low over south-eastern Russia, we have little confidence in these given that both experiments failed to reproduce the MCA responses in these regions in the first place. The RWAF in the difference plot is computed by taking the difference between the RWAF in the two experiments rather than computed on the differences themselves, because the flux calculation is non-linear. It shows that under the MOGC3 basic state, there is more poleward propagation into Alaska near 45°N 150°W and less poleward propagation into the region off the south-west coast of USA near 30°N 120°W. To interpret the results, we recall the stationary wavenumber contours from the earlier section. $K_s$ decrease from the equator towards the pole. The ray tracing based on the NCEP2 basic state

(a) Vortex stretching




(b) Vorticity advection




(c) Total RWS

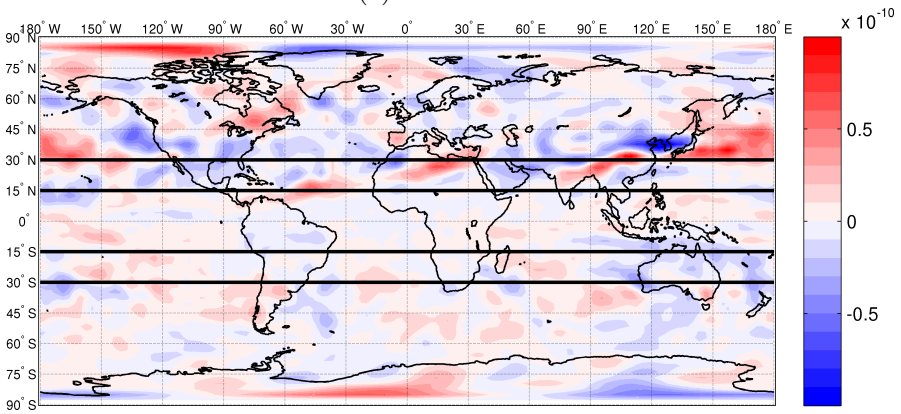



Figure 4.8: The two components of the Rossby wave source, (a) vortex stretching and (b) vorticity advection, regressed onto the NCEP2 daily 14-day-lead OLR leading mode expansion coefficient, with all years used in the MCA. (c) The total RWS (sum of a and b) with the 15° and 30° latitudes marked, used in our experiments. Contour is every $10^{-11}\mathrm{s}^{-2}$.

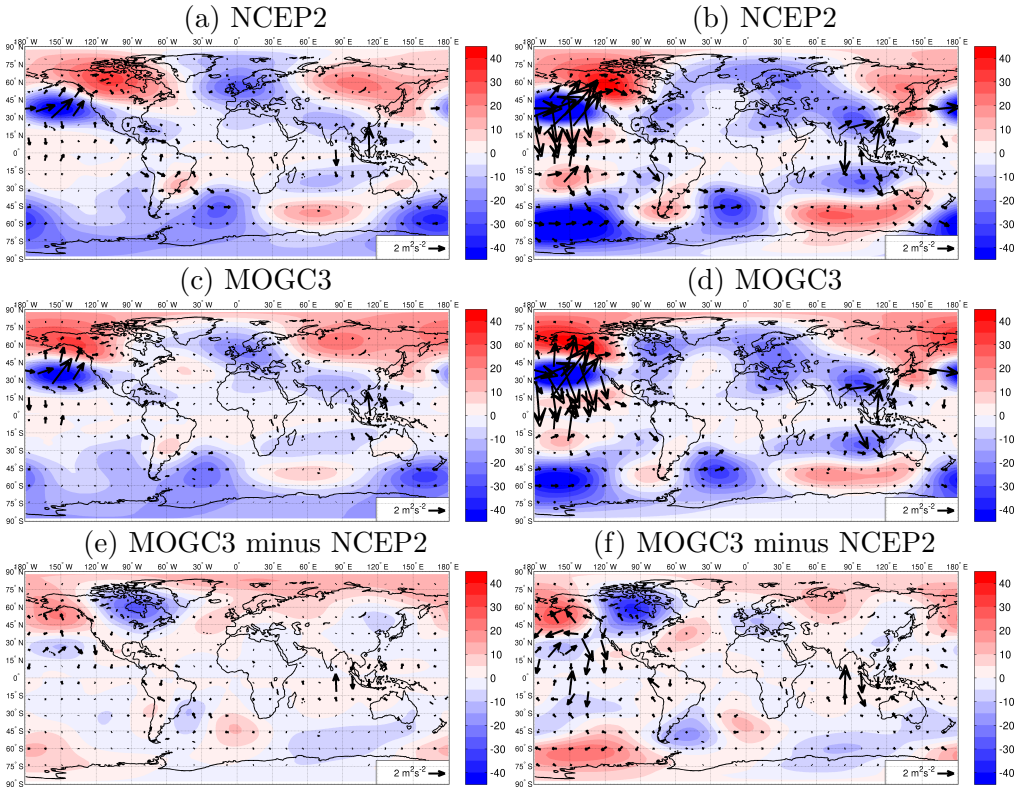



Figure 4.9: Barotropic model geopotential height response (m) using NCEP2 forcing of (left) 15°N to 15°S and (right) 30°N to 30°S. Arrow shows the Rossby wave activity flux.

suggests k1 wave propagation into the Gulf of Alaska, k2 propagation into Canada, and k3 propagation into north-western North America. The RWAF difference may be interpreted as showing more poleward k1 propagation into the Gulf of Alaska but less poleward k2 and k3 propagation into Canada and across the west coast of USA under the MOGC3 basic state. We now provide evidence to support our interpretation.

To investigate, we perform Fourier decomposition (using fast Fourier transform) on the responses from the 15°N to 15°S NCEP2 forcing experiments on the two basic states. For each day, we decompose the daily responses along each latitude circle into wavenumber amplitudes. We average these wavenumber amplitudes between days 7 and 10, and plot against the latitudes. In the NCEP2 plot (figure 4.10a), in accordance with $K_s$ theory, the k1 amplitude is largest at higher latitudes between 50°N and 75°N. This is followed at lower latitudes by the peak in k2 amplitude between 30°N and 65°N, and finally by the peak in k3 amplitude between 25°N and 50°N. The amplitudes of higher wavenumbers are even smaller and we restrict our attention to these lower wavenumbers.

Looking at the distribution of wavenumber amplitudes in the MOGC3 basic state (figure 4.10c), the k1 peak remains at the same latitude band as NCEP2 but has a larger amplitude, suggesting stronger k1 propagation into the Gulf of Alaska. The k2 peak has a smaller amplitude from 45°N to 75°N, suggesting weaker k2 propagation into Canada. The k3 amplitude shows two distinct changes. While its amplitude in the 25°N to 40°N band decreases, it shows a new peak between 50°N and 70°N which is not present in NCEP2. There is distinctly almost zero amplitude between 40°N and 50°N.

Figure 4.10e shows the difference in wavenumber amplitude. This Fourier analysis on the barotropic experiments concludes that under the MOGC3 basic state, there is indeed smaller k2 and k3 amplitude along 45°N. This agrees with our ray tracing results and supports our RWAF interpretation of less poleward propagation of k2 and k3 waves off the south-west coast of USA. It also shows larger k1 amplitude along 60°N, supporting our RWAF interpretation of more

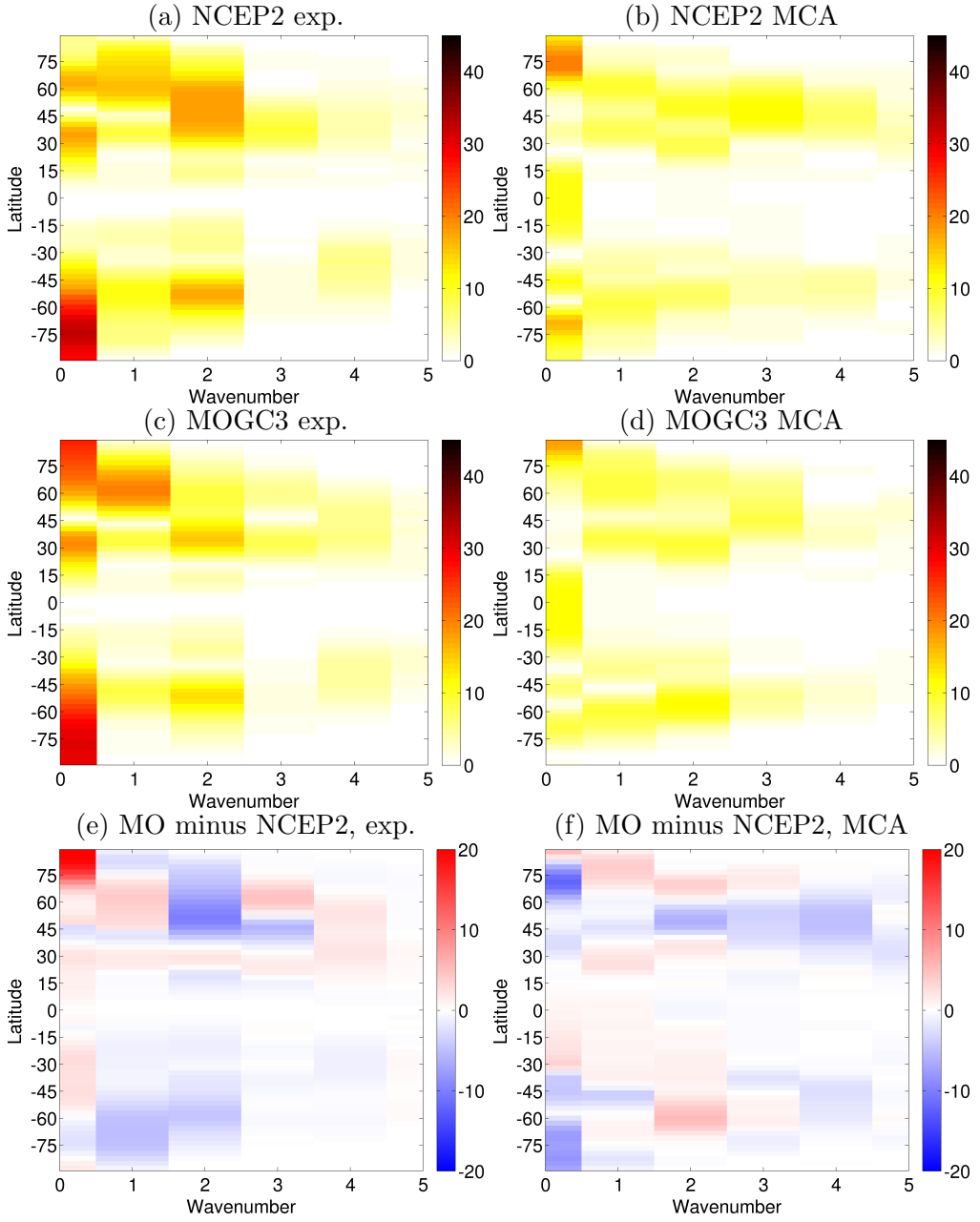



Figure 4.10: Amplitudes (m) of the Fourier decomposition into wavenumbers of (left column) the responses from the 15°N to 15°S NCEP2 forcing experiments in figure 4.9, with the two basic states; and (right column) the heterogeneously regressed Z500 maps from the 14-day-OLR-lead MCAs from NCEP2 and MOGC3 with all years used.

poleward propagation of k1 waves into the Gulf of Alaska.

We perform similar Fourier decomposition on the corresponding 14-day-OLR-lead MCAs from NCEP2 and MOGC3 using all years. For example, figure 4.10b is the decomposition of figure 3.5b, and figure 4.10d is the decomposition of figure 3.12b. Reversing the signs of these patterns to ensure the ENSO-positive state is found to have no effect on the Fourier amplitudes, because the amplitudes are absolute values. Whereas the amplitudes of k1 and k2 are much larger than k3 in both experiments, the amplitudes of k1, k2 and k3 are more similar to each other in both MCAs. This is consistent with the aforementioned mismatch between the k2-like response in both experiments and the k3-like pattern in both MCAs. Comparing the Fourier amplitude differences from the two experiments (figure 4.10e) to the two MCAs (figure 4.10f), despite failing to reproduce the k0 and k1 amplitude differences, the barotropic experiments can explain the reduction in k2 and k3 amplitudes along 45°N.

By using Fourier decomposition and amplitude of zonal wavenumbers at each latitude, we have attempted to link the barotropic model responses and the MCA differences to the turning latitudes of the waves in ray tracing. However, figure 4.10 shows the amplitude of each zonal wavenumber across an entire latitude belt, whereas ray tracings show ray paths with turning latitudes for rays initiated at a particular longitude, namely from the Pacific. If the ray path was initiated at other longitudes, the turning latitudes would not be the same as the turning latitudes in the North Pacific, as we have been interested in the longitudinal variation of $K_s$ and its difference between reanalysis and MOGC3 climate. To reconcile the global zonal average nature of the Fourier decomposition with the local nature of the turning latitude from ray tracing, we calculate a local amplitude of the zonal waves that is averaged over the Pacific longitudes (figure 4.11).

To prepare figures 4.11a and 4.11c, from the barotropic model response on MOGC3 basic state, which we refer to as the global response, we isolate the response over the Pacific longitudes, which we refer to as the Pacific response, and we refer to the response outside of the Pacific longitudes as the outside-Pacific

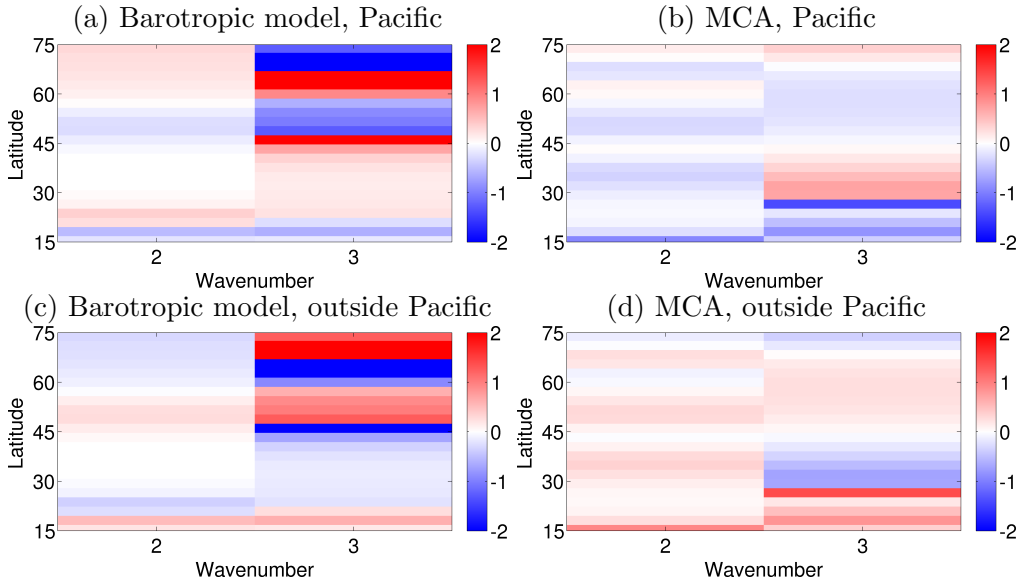



Figure 4.11: (a) Differences in the normalized projection amplitudes (no unit) between barotropic model responses isolated over the Pacific and the k2 and k3 Fourier components of such responses, on MOGC3 basic state and on reanalysis basic state. (c) Similar to (a) but for the responses isolated outside the Pacific. (b,d) Similar to (a,c) but for the MCA patterns instead of the barotropic model responses.

response. At each latitude, we calculate the dot product between the Pacific response and the k2 and k3 components of the Fourier decomposed global response. We then normalize this projection, by dividing by the dot product between the global response and the k2 and k3 components of the Fourier decomposed global response, to get a Pacific projection of the zonal k2 and k3 waves on the MOGC3 basic state. We repeat the procedure for the outside-Pacific response. Our normalization is chosen such that the Pacific projection and the outside-Pacific projection add up to one at each latitude and wavenumber.

We repeat the procedure for the barotropic model response on the reanalysis basic state. Figure 4.11a is obtained by subtracting the Pacific projection of the zonal k2 and k3 waves on the reanalysis basic state from the Pacific projection of the zonal k2 and k3 waves on the MOGC3 basic state. Figure 4.11c is obtained by subtracting the outside-Pacific projection of the zonal k2 and k3 waves on the reanalysis basic state from the outside-Pacific projection of the zonal k2 and k3 waves on the MOGC3 basic state. Because of our aforementioned normalization,

figures 4.11a and 4.11c add up to zero at each latitude and wavenumber. These two figures show that the zonal-averaged reduction in k2 and k3 amplitude near 45°N in figure 4.10e comes mainly from the Pacific. Figures 4.11b and 4.11d are similar to these two figures but for the MCA patterns instead of the barotropic model responses. Again, the MCAs show large contributions to the global k2 and k3 reduction from the local Pacific sector. Therefore, our global Fourier results in figure 4.10 can be reconciled with the local nature of the turning latitudes from ray tracing. We conclude that the k2 and k3 components in the MCA differences can be explained by ray tracing and barotropic model experiments through different basic states altering the propagation of these waves in the Pacific sector.

However, there are still some unaddressed questions. Firstly, the mechanism behind the larger k1 amplitude at high latitudes centered at 60°N under the MOGC3 basic state in the barotropic experiment, which leads to the aforementioned disagreement with the corresponding MOGC3 MCA pattern, is not clear. This mechanism may explain the similar larger k1 amplitude in the MCA Fourier analysis at 75°N. But this does not affect our conclusion drawn for the k2 and k3 propagations. Secondly, the newly emerged k3 peak at 60°N in the barotropic experiment under the MOGC3 basic state is difficult to understand. If we compare the k3 amplitude at 60°N in the NCEP2 basic state experiment with the NCEP2 MCA, we might conclude from the absence of any amplitude in the experiment and the presence of some amplitude in the MCA that the mechanism which generates k3 at such high latitude is something other than Rossby wave dynamics, such as eddy-feedback. But the presence of such k3 amplitude at 60°N in the MOGC3 basic state experiment suggests otherwise, because Rossby wave propagation is the only mechanism in the barotropic model. Still, according to $K_s$ theory, k3 propagation into such high latitudes should be unlikely.

In addition to the complication caused by different wavenumbers, the RWAF is further complicated by the simultaneous propagation of waves from the tropics at different longitudes. The two experiments show strongest poleward propagations from the tropics over the Maritime Continent as well as over the central Pacific,

and this superposition of waves from different starting longitudes may complicate the interpretation of the RWAF. We perform regional forcing experiments later to address this issue. However, in conclusion, given the similarity between the individual experiment response and the corresponding MCA pattern over the North Pacific and North America, we have confidence that the MCA differences over these regions could be explained by the difference in wave propagation due to the different basic states.

For the meridionally wider forcing experiments, the model responses for both basic state show a k3 wave. This is probably because the subtropical forcings, being closer in latitude to the extratropical wave, contain more information about the k3 wave from the MCA regression, and so forces an extratropical k3 wave. However, again the model responses are more different to the MCA patterns downstream of North America, with the phase of the k3 wave shifted to the west over the Euro-Atlantic region, although the phase is similar again with the low over western Russia and the high over south-eastern Russia. Over the North Pacific and North America regions, the same conclusions can be drawn as for the meridionally narrower forcing experiments. One notable difference to the narrower forcing experiments is in the difference plot. This difference pattern agrees remarkably well with the MCA difference pattern not just over the North Pacific and North America but almost circumglobally, with the high off the US East Coast, the low over western Europe and the high over western Russia.

In an attempt to explain the annular model response beyond around day 15, we rerun the experiments with the zonal mean of the RWS removed. The zonal mean of the RWS is almost zero in our latitude band, except at a latitude in the southern hemisphere where there is a stronger zonal mean. This approach does not solve the annular response beyond 15 days. And over our period of 7 to 10 days, the responses in the northern hemisphere are similar as before, but the southern hemisphere response is more wavelike. This is probably because of the aforementioned strong zonal mean band in the SH.

#### 4.3.1.1 Sensitivity to MOGC3 forcing

So far, we have been forcing the experiments with the same RWS from NCEP2, and testing the sensitivity to the basic states. Although we showed in the previous chapter that the differences in the OLRs between NCEP2 and MOGC3 are small, we have arbitrarily chosen to use the NCEP2 forcings so far. Here, we investigate the sensitivity by using the MOGC3 RWS. Figure 4.12 shows the responses from using RWS regressed onto the corresponding MOGC3 MCA OLR expansion coefficient, with the sign reversed if necessary again to ensure it is representing El-Niño. Comparison with figure 4.9 shows similarity in the 15°N to 15°S forcing experiments. This is because the RWS differences within 15°N and 15°S are small. However, results using 30°N to 30°S forcing show larger differences, for example the opposite responses over Europe and western Russia in the difference plots. This is because the RWS differences between 15°N and 30°N are large. Williams et al. (2017) showed that a variety of MOGC3 performance measures for ENSO compares well with observations. This explains why the MOGC3 RWS related to ENSO within the deeper tropics collocated with the ENSO SST latitudinal band shows little difference to that from NCEP2. Further away from the deep tropics, the extratropical responses to ENSO start to interfere more with the RWS. Given there are biases in the MOGC3 ENSO extratropical response, this explains why the MOGC3 RWS shows larger differences to that from NCEP2 closer to 30°N.

Figure 4.13 shows the barotropic model response differences between experiments using the same basic state but either MOGC3 forcing or NCEP2 forcing. In the experiments using 15°N to 15°S forcing, the difference in response in the northern hemisphere has a smaller amplitude and also a different pattern than figures 4.9e and 4.12f. This is also true for figure 4.13c using MOGC3 basic state. This suggests that for the meridionally narrower forcing experiments, changing the forcing has a smaller effect on the barotropic experiment response than changing the basic state. In the experiments using 15°N to 15°S forcing, the amplitudes are now comparable to figures 4.9f and 4.12g, showing that for the meridionally wider forcing experiments, changing the forcing has as big an effect as changing

the basic state. However the patterns are different especially over the North Pacific and North America. So changing the forcing does not explain the difference in the extratropical response.

Finally, figures 4.13e and 4.13f show the difference in response using MOGC3 forcing on MOGC3 basic state, and using NCEP2 forcing on NCEP2 basic state. Consistent with our descriptions above, the difference in response over the North Pacific and North America is dominated by the change in basic state in the narrowing forcing experiment, while it is dominated by the change in forcing in the wider forcing experiment. These sensitivity experiments conclude that all our results with the same forcing but different basic state are not too sensitive to whether we choose arbitrarily NCEP2 or MOGC3 forcings, as long as we restrict the RWS to within 15°N and 15°S.

### 4.3.2 Regional tropical forcing

In the circumglobal forcing experiments, we noted that the RWAF differences in the North Pacific are quite inhomogeneous. We suggested that under the MOGC3 basic state, there is more propagation into the Gulf of Alaska, but less propagation into north-west of the US. We suggested that the inhomogeneous RWAF differences was due to a combination of waves propagating from different longitudes simultaneously. Here, we investigate this by separating the circumglobal forcing into three regions, namely the Indian Ocean, the tropical Pacific and the tropical Atlantic.

Figure 4.14 and 4.15 (left column) shows the model response using NCEP2 15°N to 15°S forcings for the three tropical regions. Linearity of the three basin experiments is verified by the sum of the regional experiment responses being equal to the circumglobal experiment response. We first discuss the responses with the NCEP2 basic state. The Indian Ocean experiment produces a clear wavelike response from the forcing region, with a low over southern Asia, a high over eastern Russia, a low over the Aleutian Islands, and a high over northern Canada. This interpretation of wave propagation is supported by the RWAF.

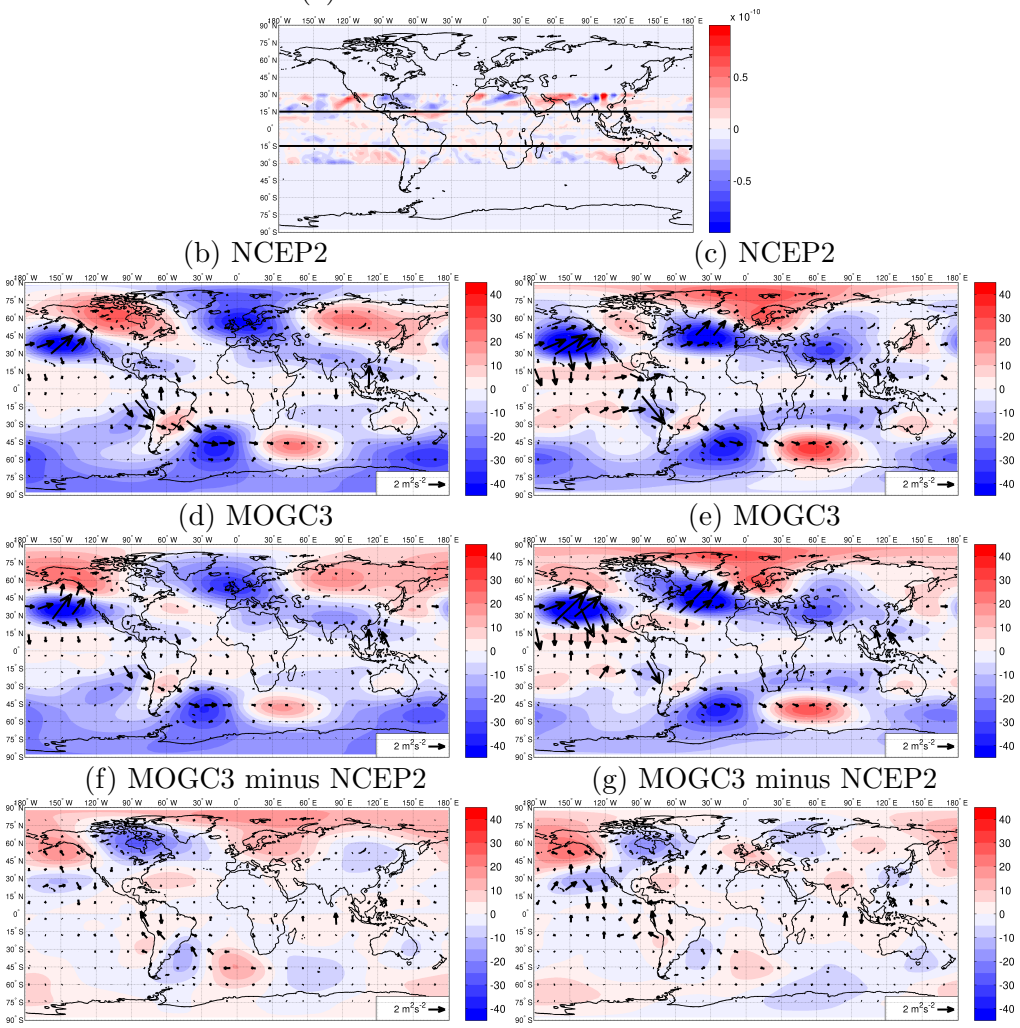



Figure 4.12: (Top) RWS difference of MOGC3 minus NCEP2. (Below top) Barotropic model geopotential height response (m) using MOGC3 forcing of (left) 15°N to 15°S and (right) 30°N to 30°S. Arrow shows the Rossby wave activity flux.

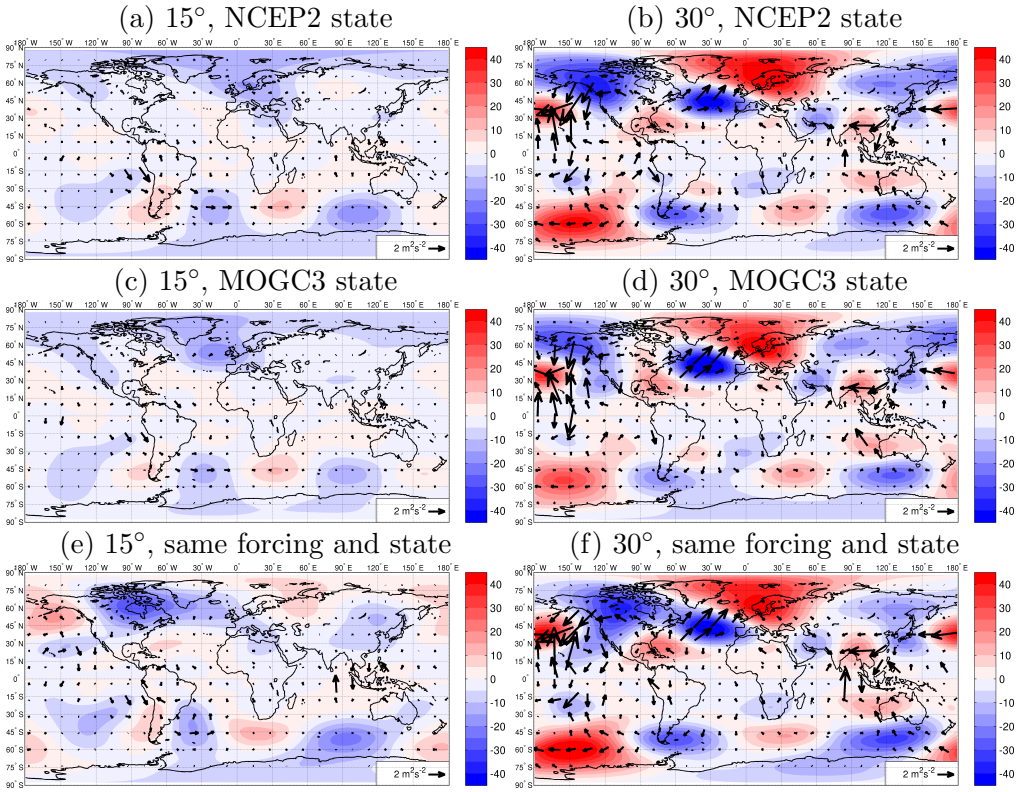



Figure 4.13: (a) Difference in barotropic model geopotential height response (m) using 15°N to 15°S MOGC3 forcing on NCEP2 basic state minus using 15°N to 15°S NCEP2 forcing on NCEP2 basic state. (b) Same as (a) but using 30°N to 30°S forcings. (c,d) Same as (a,b) but using MOGC3 basic states. (e) Difference in barotropic model geopotential height response (m) using 15°N to 15°S MOGC3 forcing on MOGC3 basic state minus using 15°N to 15°S NCEP2 forcing on NCEP2 basic state. (f) Same as (e) but using 30°N to 30°S forcings. Arrow shows the differences in Rossby wave activity flux.

This is in agreement with Simmons et al. (1983), where they showed using a barotropic model that large perturbations over the Pacific are most easily excited by forcing over southeast Asia and the tropical northwest Pacific.

Under the NCEP2 basic state, the tropical Pacific experiment reproduces the low over the Aleutian Islands and the high over northern Canada. The tropical Atlantic experiment reproduces the low over the UK. Despite both experiments showing wavelike propagation in the vicinity northeast of their forcing regions, both responses are quite zonal in the rest of the extratropics, with circumglobal high pressure in the tropical Pacific experiment and circumglobal low pressure in the tropical Atlantic experiment. This may be understood physically that these two forcings probably do not occur in isolation. These two basins, and to some extent also the Indian Ocean, are coupled together by the Walker circulation. The Walker circulation during neutral ENSO consists of ascent over the Maritime Continent and northern South America, and descent over the eastern Pacific Ocean. The Walker Circulation weakens or even reverses in El-Niño, while it strengthens in La-Niña. The coupling between the tropical Pacific and Atlantic suggests that these seemingly zonal responses should be considered together rather than in isolation, mostly cancelling each other apart from in their largest response regions.

This is seen in the experiment with the combined forcings from the tropical Pacific and the tropical Atlantic (figure 4.15 right column). The combined response is a wave across the North Pacific and North America into Europe and Russia. The circumglobal forcing response is a combination of two waves with the same phase but with different major centers of action, with the Indian Ocean forcing response contributing to large amplitudes from southern Asia to the North Pacific, and with the tropical Pacific and Atlantic forcing response contributing to large amplitudes from the North Pacific across North America into Europe.

Under the MOGC3 basic state, in the Indian Ocean experiment although the wave propagation is similar to the NCEP2 basic state, with a low over southern Asia, a high over eastern Russia and a low over the Aleutian Islands, the high over northern Canada is absent. This agrees with the RWAF being weaker propagating

into northern Canada. In the tropical Pacific experiment, the high over northeastern North America is shifted westward over Alaska. The larger amplitude is consistent with stronger RWAF into the Gulf of Alaska. The tropical Atlantic experiment shows a similar response in the MOGC3 state compared to NCEP2, with wave propagation from northern South America into the North Atlantic.

Looking at the difference in responses between the two basic states, both the Indian Ocean experiment and the combined tropical Pacific and Atlantic experiment show differences similar to the circumglobal forcing experiment, with the high over the Aleutian Islands and the low over northeastern North America (figures 4.15g and 4.15h). But now the RWAF differences in the North Pacific are more homogeneous and clear. The Indian Ocean experiment shows RWAF differences pointing southwestward, and the combined tropical Pacific and Atlantic experiment pointing northeastward. This suggests that in the North Pacific, the waves from different forcing regions propagate differently. In the North Pacific, waves from the Indian Ocean propagate less poleward in the MOGC3 state than in NCEP2, while waves from the tropical Pacific propagate more poleward in MOGC3 than in NCEP2. To understand this, we again look at the wavenumber amplitudes (figure 4.16).

Under the NCEP2 state along 45°N, waves driven by the Indian Ocean forcing have largest amplitudes in k2 and k3, whereas waves driven by the combined tropical Pacific and Atlantic forcing have largest amplitudes in k0 and k1 but much less in k3. So we expect the Indian Ocean experiment to be affected more by the $K_s3$ bias and to show less poleward propagation in the North Pacific in MOGC3. This is confirmed by the large reduction in k3 amplitude between 30°N and 45°N in the Indian Ocean MOGC3 experiment. In the tropical Pacific and Atlantic experiment, the more poleward propagation in MOGC3 seems to come from a zonal mean k0 response poleward of 60°N, which is much larger than in NCEP2. Although there is again reduction in k2 and k3 amplitudes at 45°N in MOGC3, the more poleward propagating k0 response seems to have dominated over the less poleward propagating k2 and k3 waves in the RWAF, thus showing

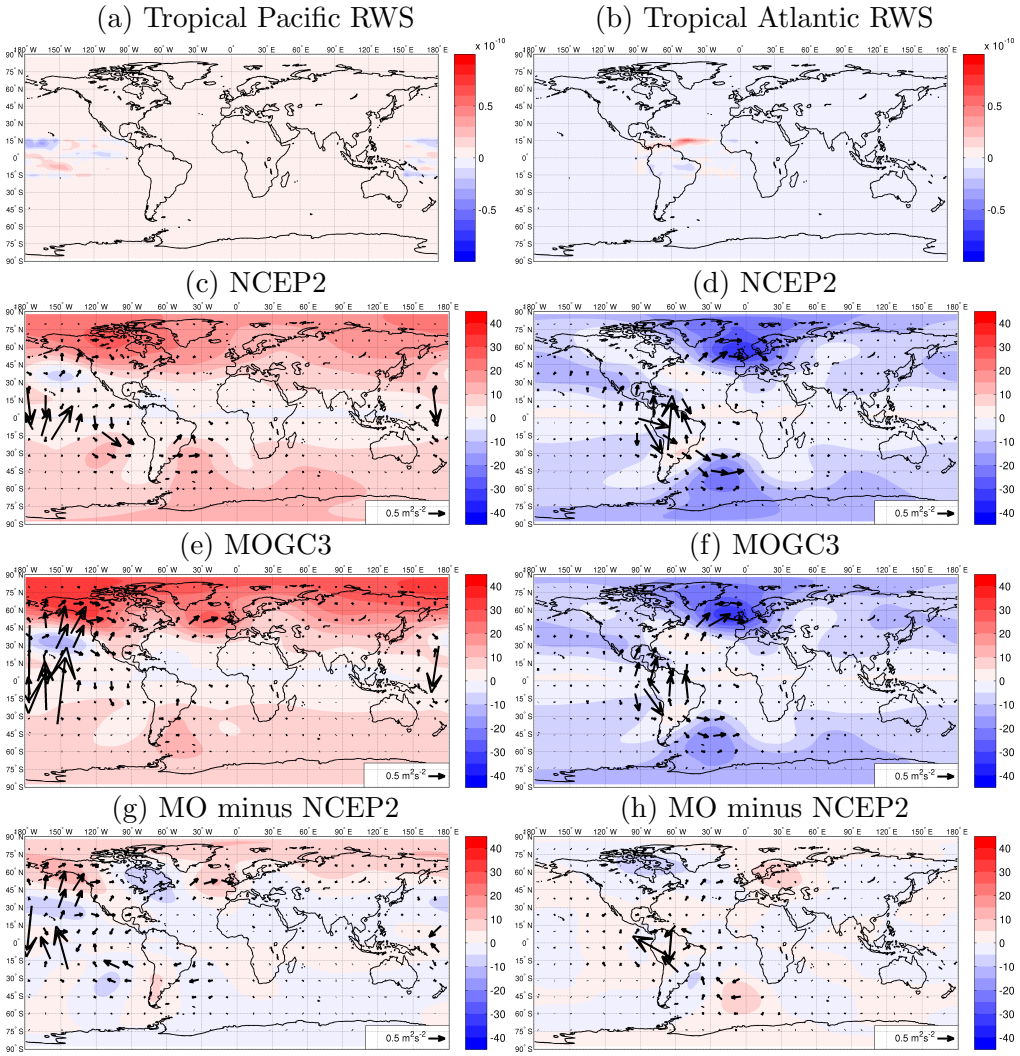



Figure 4.14: Barotropic model geopotential height response (m) using NCEP2 15°N to 15°S forcings for (left) tropical Pacific and (right) tropical Atlantic forcing regions. Arrow shows the Rossby wave activity flux.

an overall enhanced poleward propagation in RWAF.

### 4.3.3 RWS mean bias and jet bias

So far, we have been looking at the sensitivity of wave propagation to the basic state. Apart from the difference in the climatological basic state between NCEP2 and MOGC3, there is also a difference in the climatological RWS between them. Under the same wave propagation framework, we address to what extent can this mean RWS bias contribute to the mean North Pacific jet bias. Figure 4.17 shows the climatological RWS bias and the 250 hPa zonal wind response, averaged

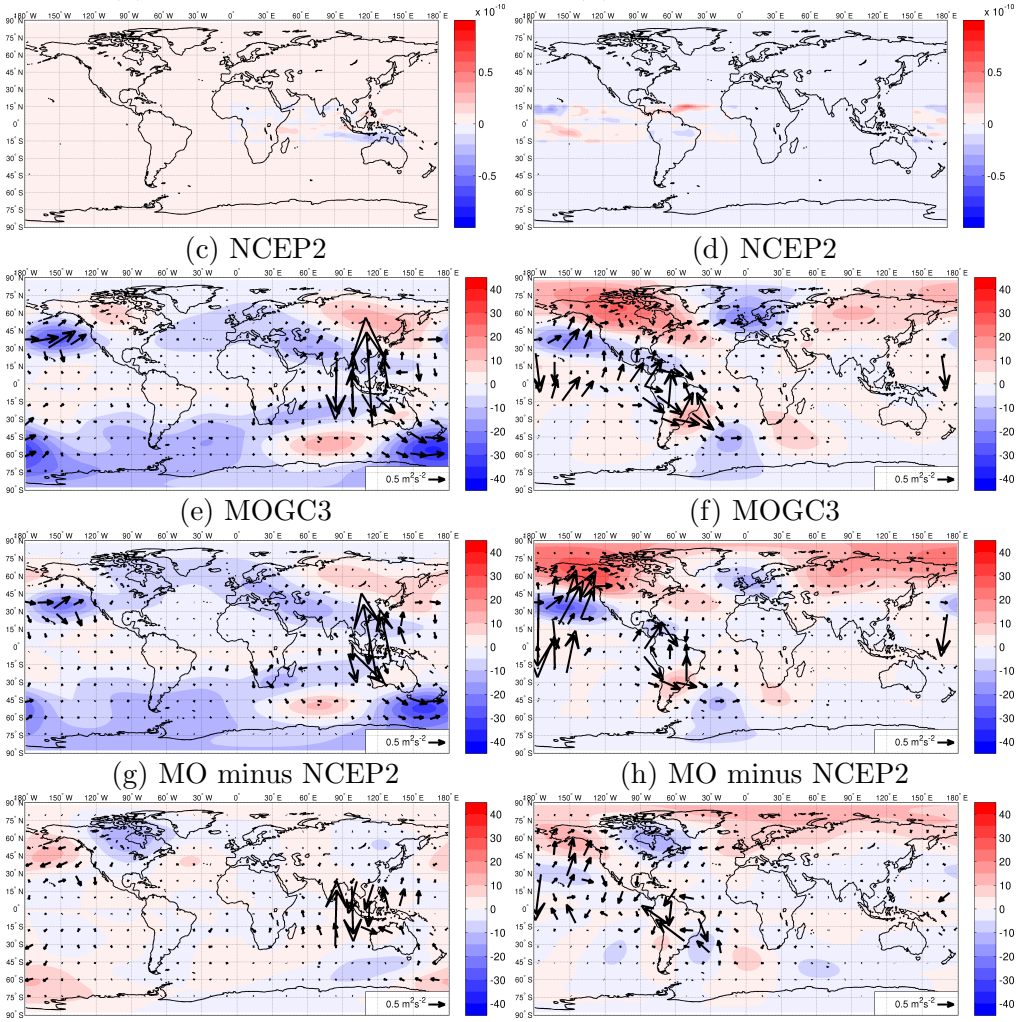



Figure 4.15: Barotropic model geopotential height response (m) using NCEP2 15°N to 15°S forcings for (left) Indian Ocean and (right) the sum of tropical Pacific and tropical Atlantic forcing regions. Arrow shows the Rossby wave activity flux.

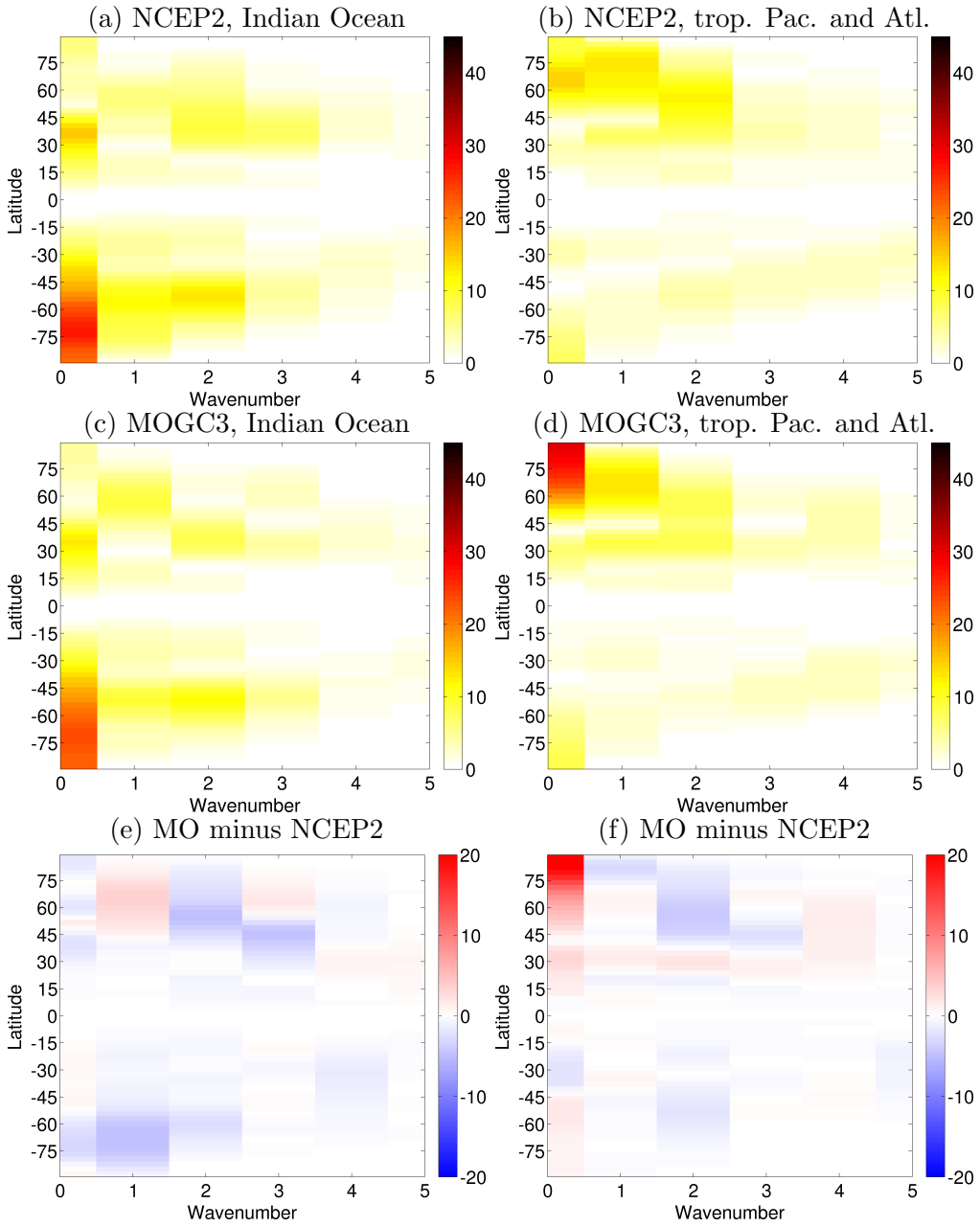



Figure 4.16: Amplitudes (m) of the Fourier decomposition into wavenumbers of the responses from the 15°N to 15°S NCEP2 forcing experiment with the two basic states, with (left) Indian Ocean forcing and (right) tropical Pacific and Atlantic forcing.

between days 7 and 10. We only consider the bias between 15°N and 15°S. In the North Pacific, the response of stronger zonal wind between 15°N and 30°N and weaker zonal wind near the Aleutian Islands resembles the jet bias, although the stronger band should be more poleward along 30°N. However, downstream of the North Pacific the model response wind bias is not as zonal as the observed jet bias. Therefore, the RWS bias can only explain some of the jet bias in the North Pacific but not elsewhere.

The North Pacific jet bias seems to be a coupled bias that has developed in the free-running climate model. We therefore do not expect the bias to be as severe in seasonal forecasts, which does not have enough time for the bias to develop. Indeed, the North Pacific jet bias is not as severe in the seasonal hindcasts from the same model used in MOGC3. We average over the ensemble mean of the 200 hPa zonal wind from the MOGC3 model hindcasts (seasonal forecast system GloSea5-GC3), for each of the 20 winters from 1992/3 to 2011/12. Figure 4.18 shows the 200 hPa zonal wind bias from NCEP2 and the stationary wavenumber bias. The bias over the North Pacific is largely reduced, and consequently so is the stationary wavenumber bias. This is because the hindcasts are initialized near the beginning of each season, and there may not be enough time for a coupled jet bias to develop within the season.

Dawson et al. (2013) showed that a coupled model with lower oceanic horizontal resolution cannot resolve small-scale processes and produces a less realistic oceanic mean state, which allows the atmospheric model component to be forced less realistically, producing a similar mean state bias. It is possible that the climatological RWS bias in MOGC3 may have come from the oceanic component. Figure 4.17c shows the climatological sea surface temperature bias of MOGC3 from the International Comprehensive Ocean-Atmosphere Data Set (ICOADS) Release 3.0 enhanced data (Freeman et al., 2017). This is similar to the MOGC3 SST bias reported in Williams et al. (2017, figure 2 top right), and shows tropical SST biases of up to 2 K. This may lead to a tropical convection bias and RWS bias, with the North Pacific jet bias arising as a forced response. The negative

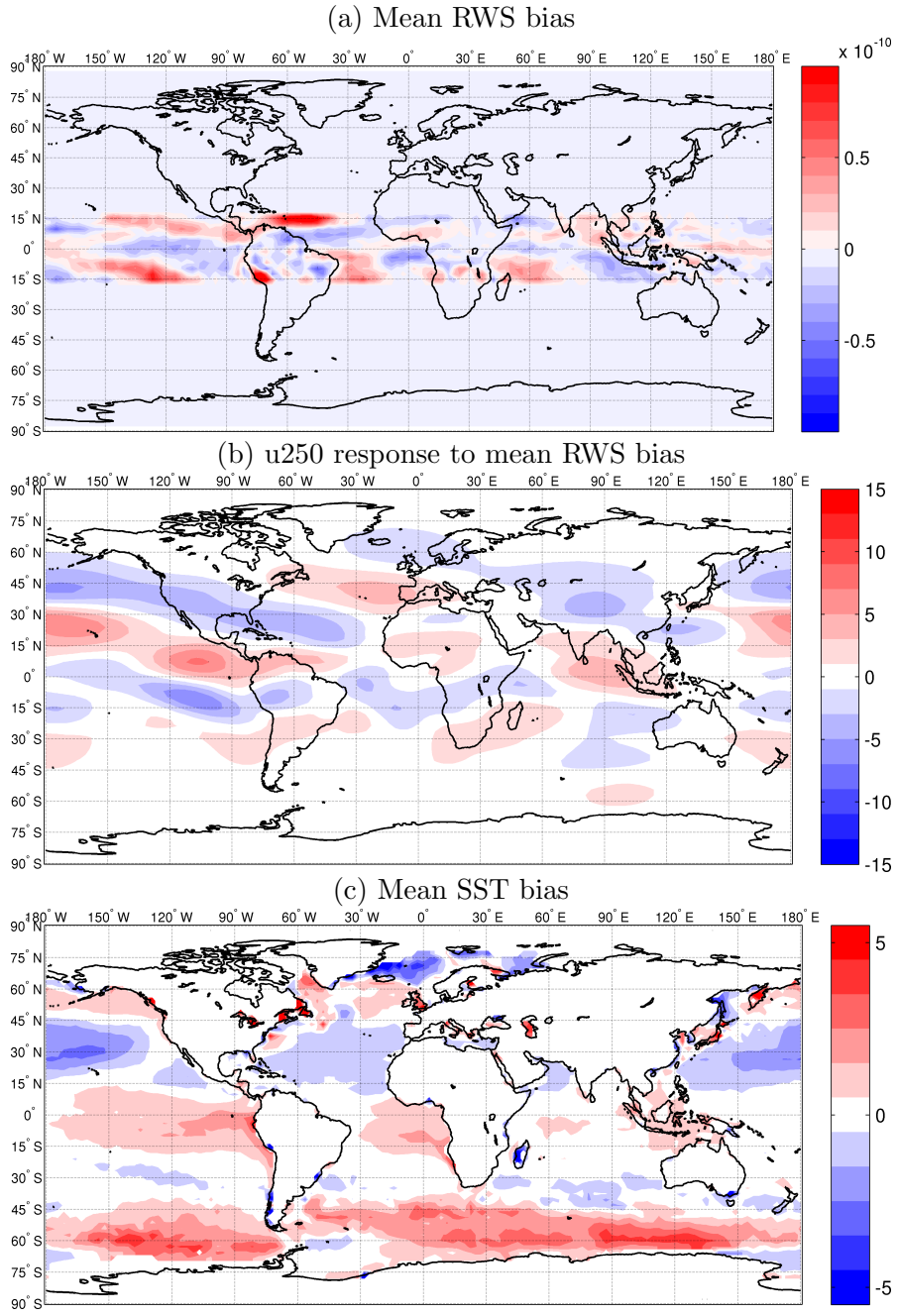



Figure 4.17: (a) The climatological RWS bias of MOGC3 from NCEP2, for the region 15°N to 15°S. Contour is every $10^{-11}$s$^{-2}$. (b) 250 hPa zonal wind response from this forcing on NCEP2 basic state. Interval is every 2ms$^{-1}$. (c) The climatological sea surface temperature bias of MOGC3 from ICOADS observations. Contour is every 1 K.

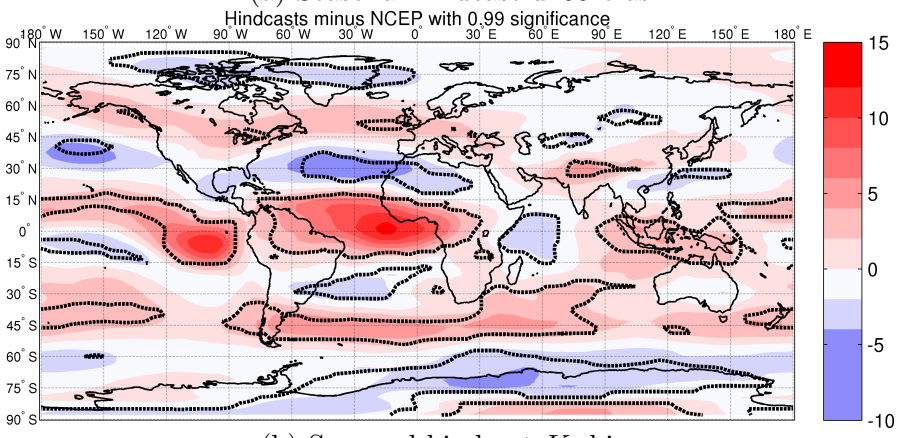
SST bias in the North Pacific in figure 4.17c coincides in latitude with the positive upper-level jet bias. Associated with the increase in speed of the upper-level North Pacific jet at 30°N is an increase in surface wind speed at 30°N through the equivalent barotropic eddy-driven jet. This is in line with the bulk aerodynamic formula used for heat fluxes in the boundary layer (Hartmann, 2016), which relates the heat flux to the temperature difference and also the mean wind speed. Increased surface winds therefore results in the negative SST bias in the North Pacific. Finally, the atmosphere-only run of the same Met Office climate model provides another piece of evidence that the jet bias is a coupled bias. When sea surface temperatures are prescribed, the North Pacific jet bias is reduced (figure 4.18c).

## 4.4 Baroclinic model experiments

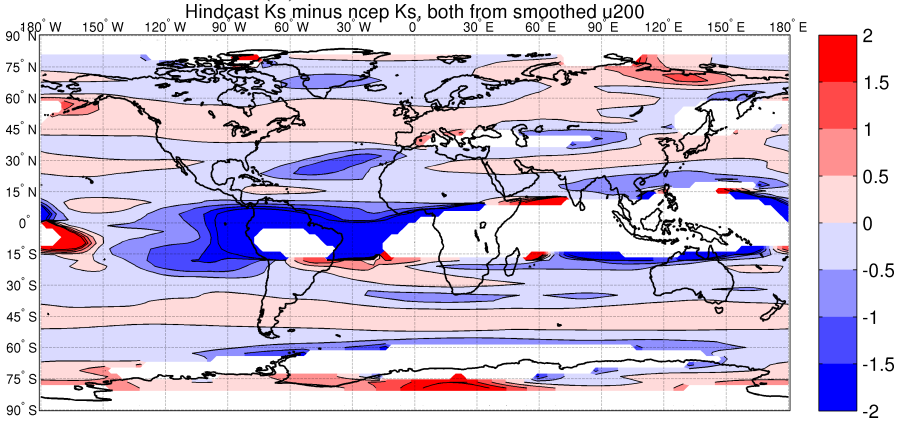
A clear limitation of the barotropic model is that there is only one level. So far we have been running experiments on the 250 hPa level. Another limitation of the barotropic model is the necessity to specify the RWS, which so far has been obtained by regression and may contain some consequences from the wave itself. To further investigate wave propagation beyond these two limitations, we use a baroclinic model.

The baroclinic model requires the specification of diabatic heating. The diabatic heating is described in equation 2.29. As concluded from the last chapter, ENSO closely resembles the leading covariability mode in the seasonal timescale, as well as in the daily timescale when all years are used. Here we choose to focus on the seasonal timescale, partly because the difference in the MCA patterns between MOGC3 and NCEP2 has been more rigorously tested for the seasonal timescale (figure 3.11b) than the daily timescale, and also partly because our diabatic heating is of a seasonal timescale. We regress the diabatic heating onto the standardized time series of the seasonal OLR MCA leading mode, to obtain the related diabatic heating (figure 4.19a). Consistent with the OLR anomalies, this mode shows diabatic heating in the eastern tropical Pacific and diabatic cooling in the western tropical Pacific. Although there are small areas of diabatic cooling

(a) Seasonal hindcast u200 bias




(b) Seasonal hindcast $K_s$ bias




(c) Atmosphere-only run u200 bias

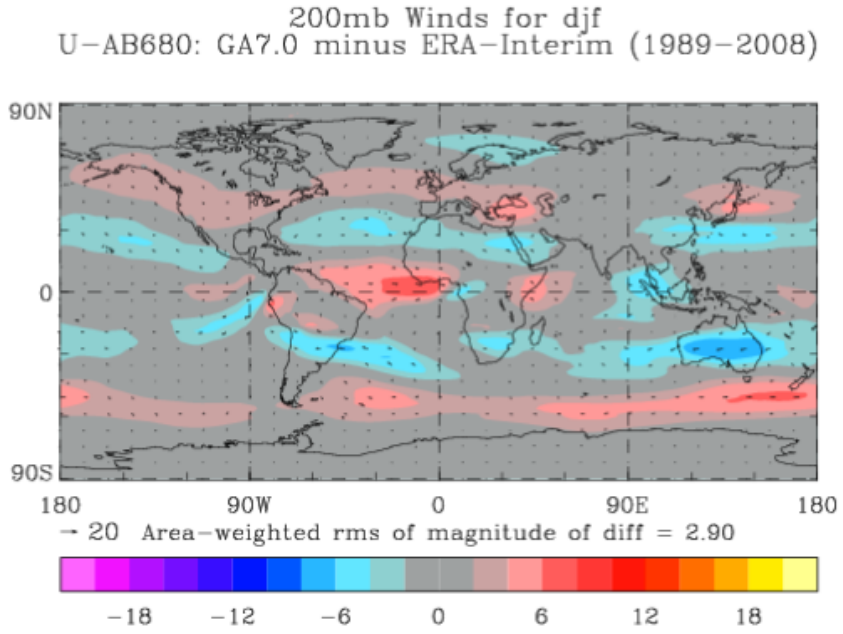



Figure 4.18: MOGC3 seasonal hindcast biases from NCEP2 in (a) 200 hPa zonal wind with 99% significances in black contour, and in (b) stationary wavenumber. (c) shows the atmosphere-only run 200 hPa zonal wind bias.

also observed in the tropical Atlantic, we focus on the larger areas of forcings in the tropical Pacific. We approximate the heating area to be a zonally elongated ellipse centered at 140°W 0°N so that its centre coincides with the centre of the much more zonally elongated heating observed (figure 4.19b), and approximate the cooling area to be a circle centered at 130°E 7°N (figure 4.19c). Using the radiative-convective equilibrium assumption (section 2.4), we convert the heating maximum from around 100 $\mathrm{Wm}^{-2}$ to 0.83 $\mathrm{K\,day}^{-1}$, and the cooling maximum from around -50 $\mathrm{Wm}^{-2}$ to -0.42 $\mathrm{K\,day}^{-1}$.

### 4.4.1 On the reanalysis basic state

Figure 4.20 shows the responses to the diabatic forcing in figure 4.19b, using the ERA-Interim basic state (section 2.4). Although the heating area is quite large, the atmospheric mass in the model is still conserved until day 25 (figure A.7a), showing that the model is running stably for this period. The extratropical response is a wave that has an equivalent barotropic structure (figure 4.20c) and is stationary in time (figure 4.20d). The wave on the 250 hPa level (figure 4.20a) is very similar to the wave from the barotropic model experiment on the 250 hPa level using NCEP2 basic state and NCEP2 observed RWS forcing between 15°N and 15°S (figure 4.9a). The low pressure near the Aleutian Islands, high pressure over Canada, and low pressure over Iceland and the UK are reproduced, suggesting the very idealized heating in the eastern tropical Pacific can already capture most of the barotropic model response in this region. The 500 hPa level response (figure 4.20b) compares well with the corresponding NCEP2 MCA (figure 3.1b) with the low near the Aleutian Islands and the high over Canada, although the high in the baroclinic model is positioned a bit further west than the MCA. This gives confidence that the baroclinic model is capturing the observed pattern at least over the North Pacific-North America sector.

Whereas the Rossby wave source in the barotropic model is specified, the baroclinic model generates the RWS from the diabatic forcing. Figure 4.21 shows the RWS response averaged between days 10 and 14, calculated from the zonal and

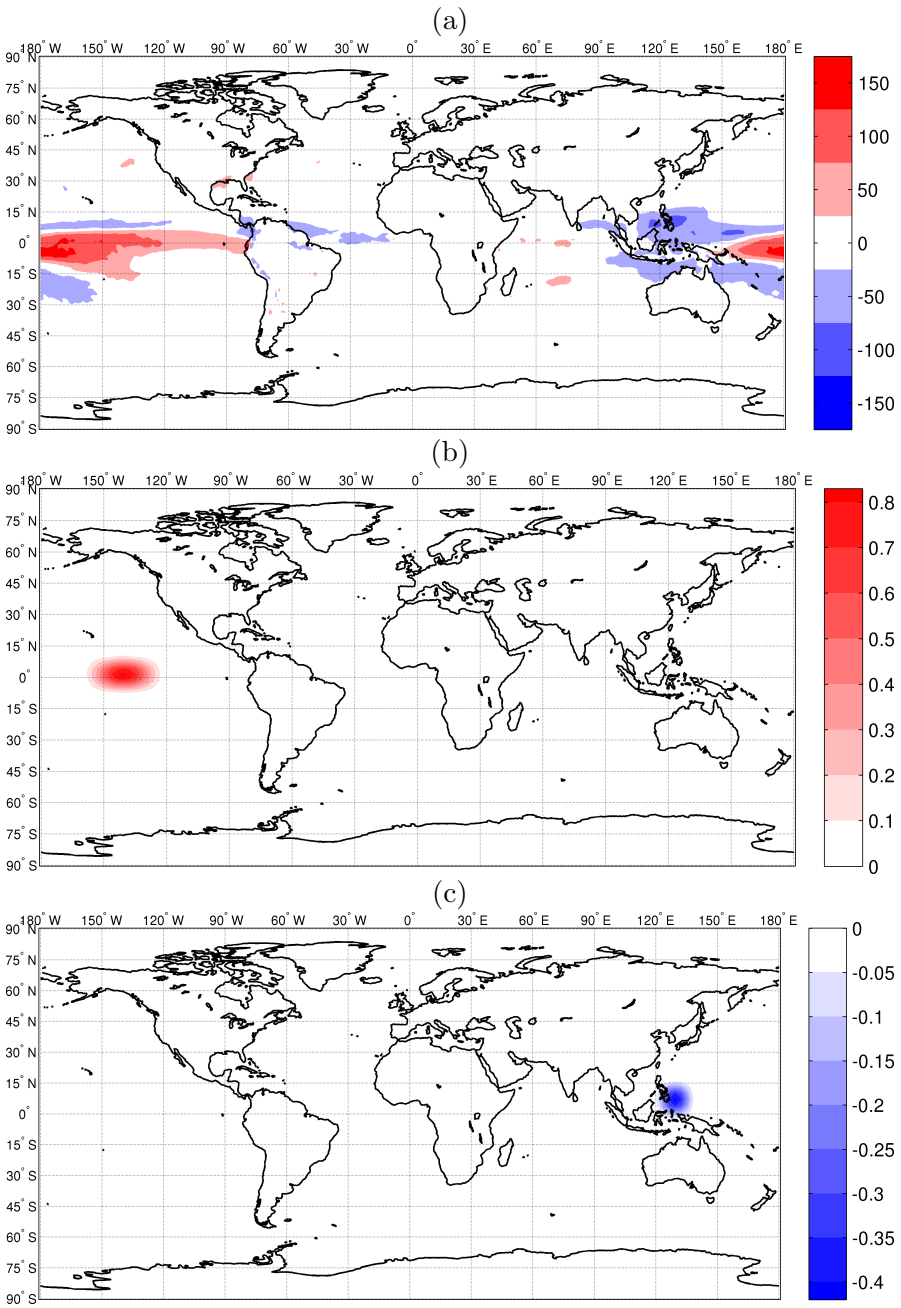



Figure 4.19: (a) Diabatic heating ($\mathrm{Wm}^{-2}$) regressed onto the standardized time series of the seasonal MCA OLR leading mode (ENSO). (b) The idealized diabatic heating in the eastern tropical Pacific ($\mathrm{K\,day}^{-1}$). (c) The idealized diabatic cooling in the western tropical Pacific ($\mathrm{K\,day}^{-1}$).

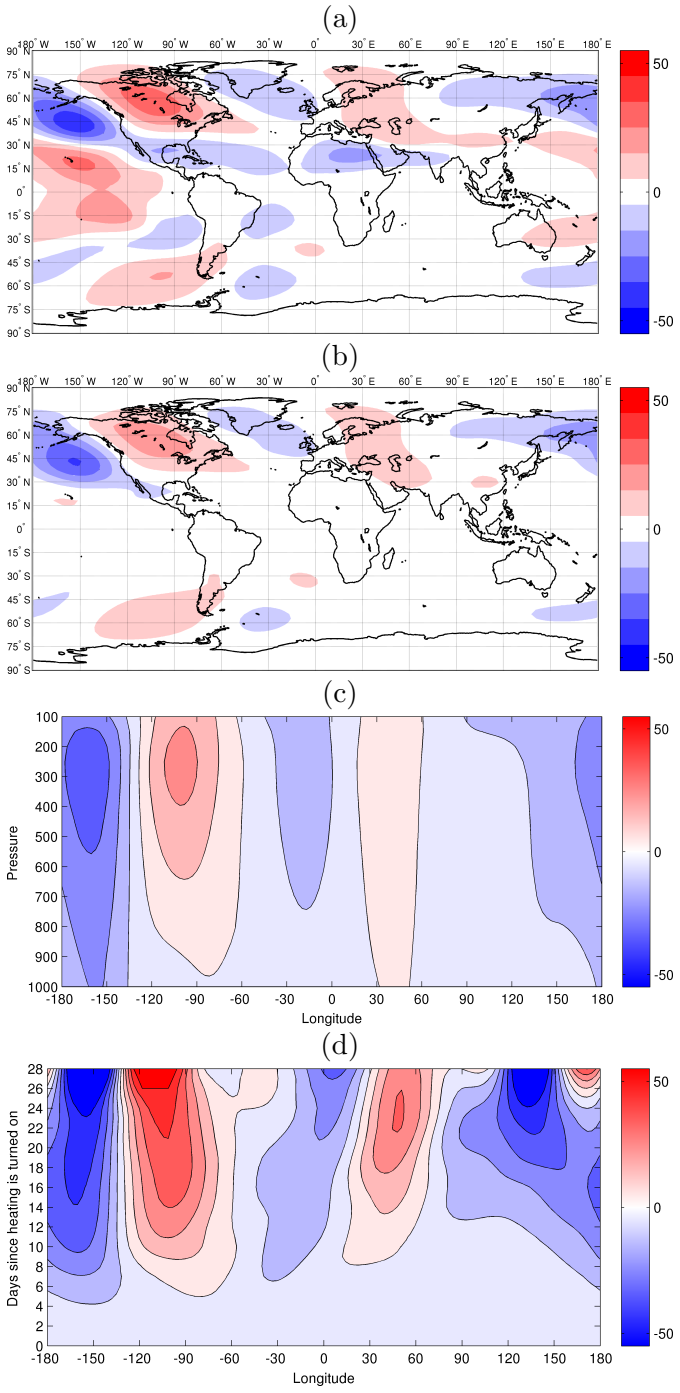



Figure 4.20: Geopotential height responses (m) to the diabatic forcing in figure 4.19b, on ERA-I basic state, averaged between days 10 and 14, for (a) 250 hPa, (b) 500 hPa, (c) vertical cross section average between 45°N and 60°N, and (d) Hovmöller diagram on 250 hPa.

meridional wind responses in the baroclinic model. The diabatic heating in the eastern tropical Pacific generates a RWS response in the central tropical Pacific (figure 4.21c) that matches well with the observed (figure 4.8c), with the north-south dipole near the Date Line with zonally elongated positive RWS near 0°N and zonally elongated negative RWS near 15°N. The contribution is mostly from the vorticity advection term (figure 4.21b), which dominates in the tropics whereas the vortex stretching (figure 4.21a) dominates in the subtropics (15°N to 30°N). Physically, the diabatic forcing sets up local heating (figure A.8a) and generates large divergences at the upper level (figure A.8b) near the vicinity above the forcing maximum at 400 hPa (section 2.4). The associated anomalous divergent wind acts on the climatological gradient of relative vorticity and generates the vorticity advection term (equation 2.17). Focusing on the tropics, the observed vorticity advection (figure 4.8b) is strongest in the tropical Pacific. But in the baroclinic model, there are also large vorticity advection contributions near the west coast of South America and in North Africa. These may be artefacts of our model related to the orographic effects of the Andes and the Ethiopian Highlands respectively, since we have applied a very strong constraint on the inverse initial tendency (section 2.4).

We also look at the RWS response at an earlier period. Figure 4.22 shows the RWS response averaged between days 5 to 9. In the subtropics, the vortex stretching (figure 4.22a) is less noisy than from days 10 to 14, probably due to the consequence of the developed wave at the later period. But the large scale structures of the vortex stretching, as well as the vorticity advection in the tropics (figure 4.22b), are similar to the later period. This shows that at least under the linear framework of our experiment, the development of the extratropical wave does not significantly modify the RWS in the tropics.

To summarize, we find that although the heating is restricted in the eastern tropical Pacific, the diagnosed RWS can extend around the globe. The baroclinic model also supports the findings from the barotropic model, as the RWS is reproduced in the regions used for the barotropic experiments, and the wave responses

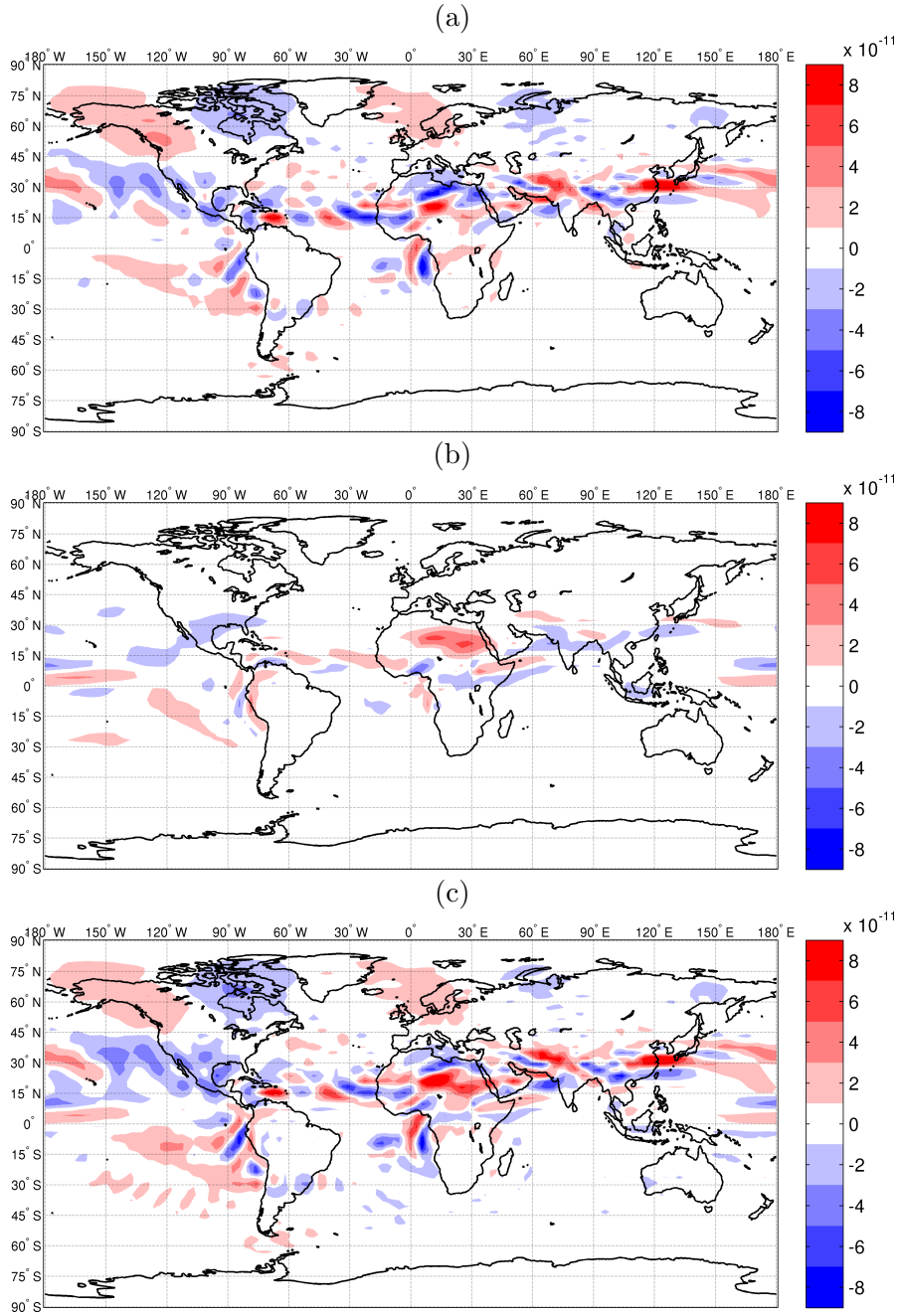



Figure 4.21: 250 hPa Rossby wave source responses ($s^{-2}$) to the diabatic forcing in figure 4.19b, on ERA-I basic state, averaged between days 10 and 14, for (a) vortex stretching, (b) vorticity advection and (c) the total.

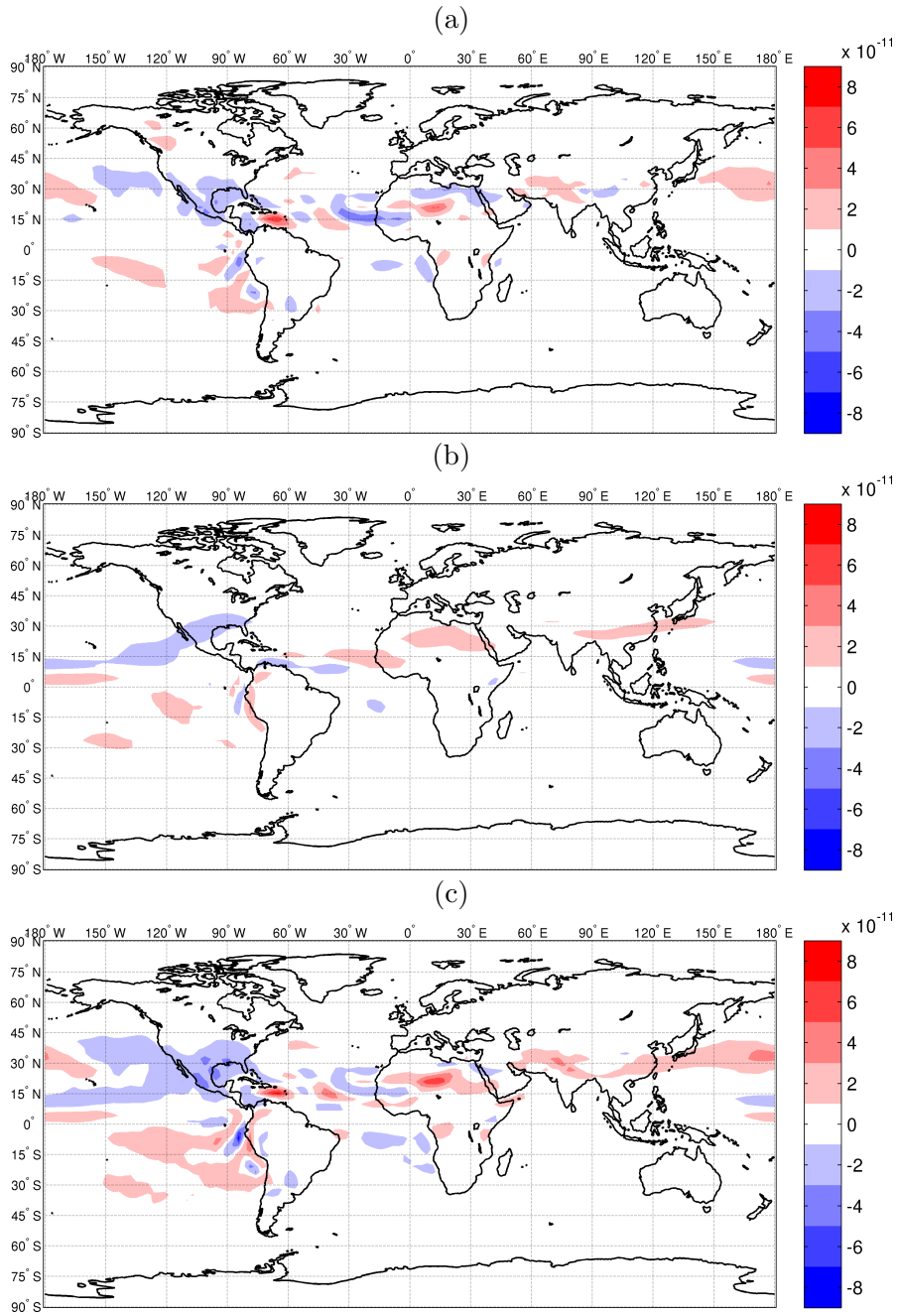



Figure 4.22: Similar to figure 4.21. 250 hPa Rossby wave source responses ($s^{-2}$) to the diabatic forcing in figure 4.19b, on ERA-I basic state, averaged between days 5 and 9, for (a) vortex stretching, (b) vorticity advection and (c) the total.

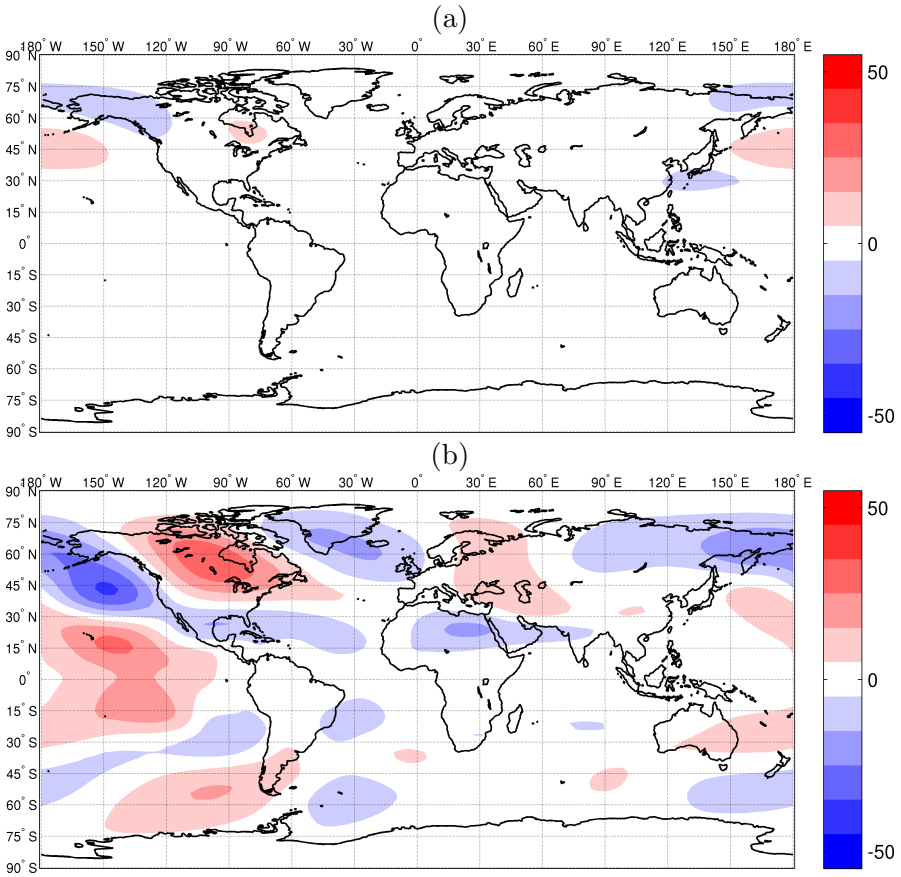



Figure 4.23: (a) 250 hPa geopotential height response (m) to the diabatic forcing in figure 4.19c, on ERA-I basic state, averaged between days 10 and 14. (b) The sum of the 250 hPa geopotential height responses from the eastern tropical Pacific heating (figure 4.20a) and the response in (a).

are very similar.

For the experiment with the diabatic cooling (figure 4.19c) in western tropical Pacific, the response (figure 4.23a) is a wave from the Maritime Continent, with a low over Japan, a high near the Aleutian Islands, a low over Alaska and a high over eastern Canada. However, the response is much weaker than the response from the diabatic heating, because the cooling region is smaller in size and also smaller in amplitude. Since the experiments are linear, we can add the responses of the heating and the cooling together. The full geopotential height response (figure 4.23b) is dominated by the heating response. Also, the RWS response to the cooling is weak (figure A.9). Therefore, we focus on the diabatic heating in the eastern tropical Pacific from now on.

### 4.4.2 On the MOGC3 basic state

Similar to our approach in the barotropic model, we test the sensitivity of the baroclinic model response to the MOGC3 basic state. As noted in section 2.4, we have used the ERA-Interim climatology instead of the NCEP2 climatology as the reanalysis basic state. Figure A.10 shows the zonal wind bias on 250 hPa of MOGC3 minus ERA-I. This is very similar to the bias of MOGC3 minus NCEP2 in figure 4.1a. Hence, we do not expect much differences by changing the reanalysis basic state from NCEP2 to ERA-I. Figure 4.24 shows the geopotential height responses to the diabatic heating in the eastern tropical Pacific using the MOGC3 basic state. Comparing the response on 250 hPa (figure 4.24a) to the barotropic model response using NCEP2 15°N to 15°S circumglobal RWS (figure 4.9c), they match well with the low heights near the Aleutian Islands and near Iceland. However, the baroclinic model response shows a more zonal wave across North America, unlike the more meridional propagation into Alaska in the barotropic model. The baroclinic model response on 500 hPa (figure 4.24b) matches better than the barotropic model to the MOGC3 seasonal MCA leading mode in 500 hPa geopotential height (figure 3.9b). The low height near the Aleutian Islands, high height over Canada, low height near Iceland and high height over Scandinavia and eastern Europe are all reproduced. This suggests that using the MOGC3 basic state, to capture the more zonal wave propagation pattern from the North Pacific across North America into the North Atlantic more similar to the observed, the vertical structure of the basic state or of the diabatic forcing may be important.

Figure 4.25 shows the RWS response to the heating in MOGC3 basic state. The total RWS is similar to the RWS in the NCEP2 basic state (figure 4.21c), for example the aforementioned dipole near the Date Line is again generated. We also compute the differences in the RWS between using the ERA-I basic state and the MOGC3 basic state (figure 4.26). Over the tropical Pacific, the difference is mainly originated from the vorticity advection term. If we assume the same divergent winds from the same heating in both basic states, this difference in vorticity

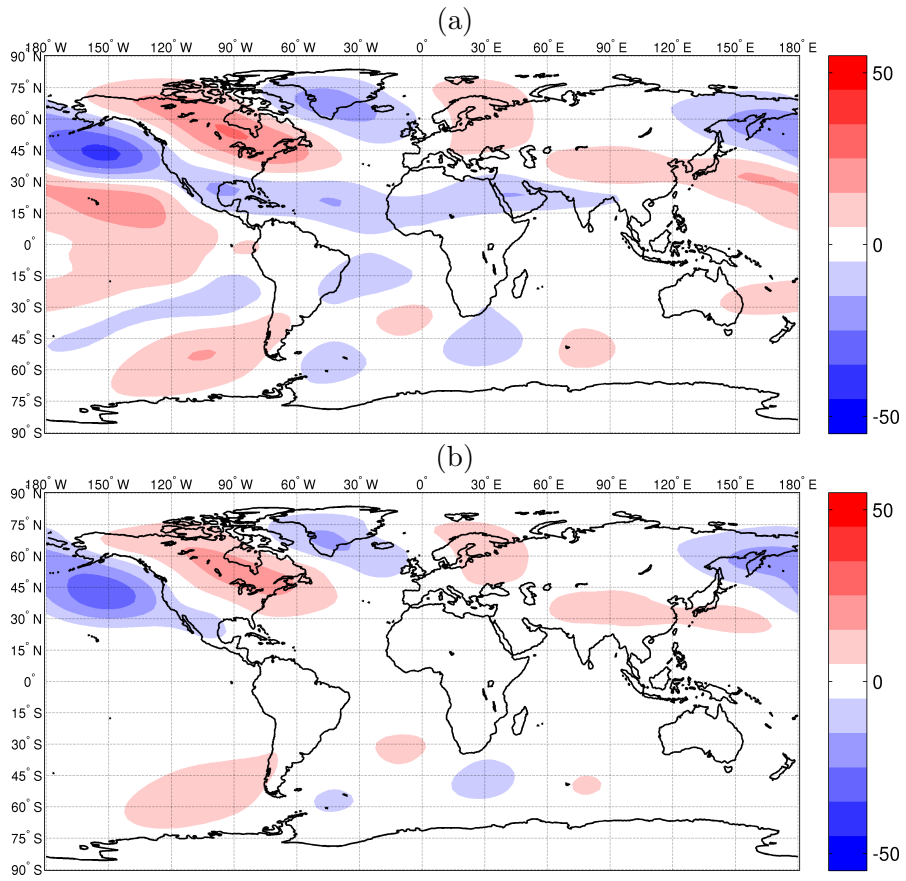



Figure 4.24: Geopotential height responses (m) to the diabatic forcing in figure 4.19b, on MOGC3 basic state, averaged between days 10 and 14, for (a) 250 hPa and (b) 500 hPa.

advection must come from the bias in the climatological vorticity gradient associate with the North Pacific jet bias further north. We compare this baroclinic model RWS difference with the RWS difference between NCEP2 MCA mode 1 RWS and MOGC3 MCA mode 1 RWS (figure 4.12a, which we reproduce in figure 4.26d). By comparing figures 4.26c and 4.26d, the baroclinic model seems to reproduce this difference at the tropical Date Line well, with the positive difference at around 10°N and the negative difference at around 15°N. There are some small-scale ripple-like structures in other parts of the tropics in figure 4.25c, for example at northwestern South America, northeastern Africa and the northeast of India. These may again be orographic artefacts from the Andes, the Ethiopian Highlands and the Himalayas respectively.

### 4.4.3 Difference between the two basic states

Finally, we look at the difference in the geopotential height response due to the change in the basic state. Figure 4.27 shows the difference in the response from using the MOGC3 basic state (figure 4.24) minus the response from using the ERA-I basic state (figure 4.20). The pattern shows an equivalent barotropic structure, in line with the suggestion that the difference is due to a different response in barotropic stationary Rossby waves. Over the regions of the North Pacific, the North America and the North Atlantic where the individual baroclinic experiments match well with the MCAs, the difference in the baroclinic response is similar to the MCA difference (figure 3.11b). This difference mainly results from the wave amplitude being weaker over these regions under MOGC3 basic state than ERA-I basic state, in agreement with the conclusion from the barotropic experiments that the wave propagation is affected by the basic state through the North Pacific jet bias. There are some notable differences however, with the high heights south of the Aleutian Islands in the MCA difference being further north over Alaska in the baroclinic difference. Also the low and high heights at 90°W and 45°W respectively in the MCA difference are now shifted westward by around 15° in the baroclinic difference. These can be due to the limitation of our idealized heating

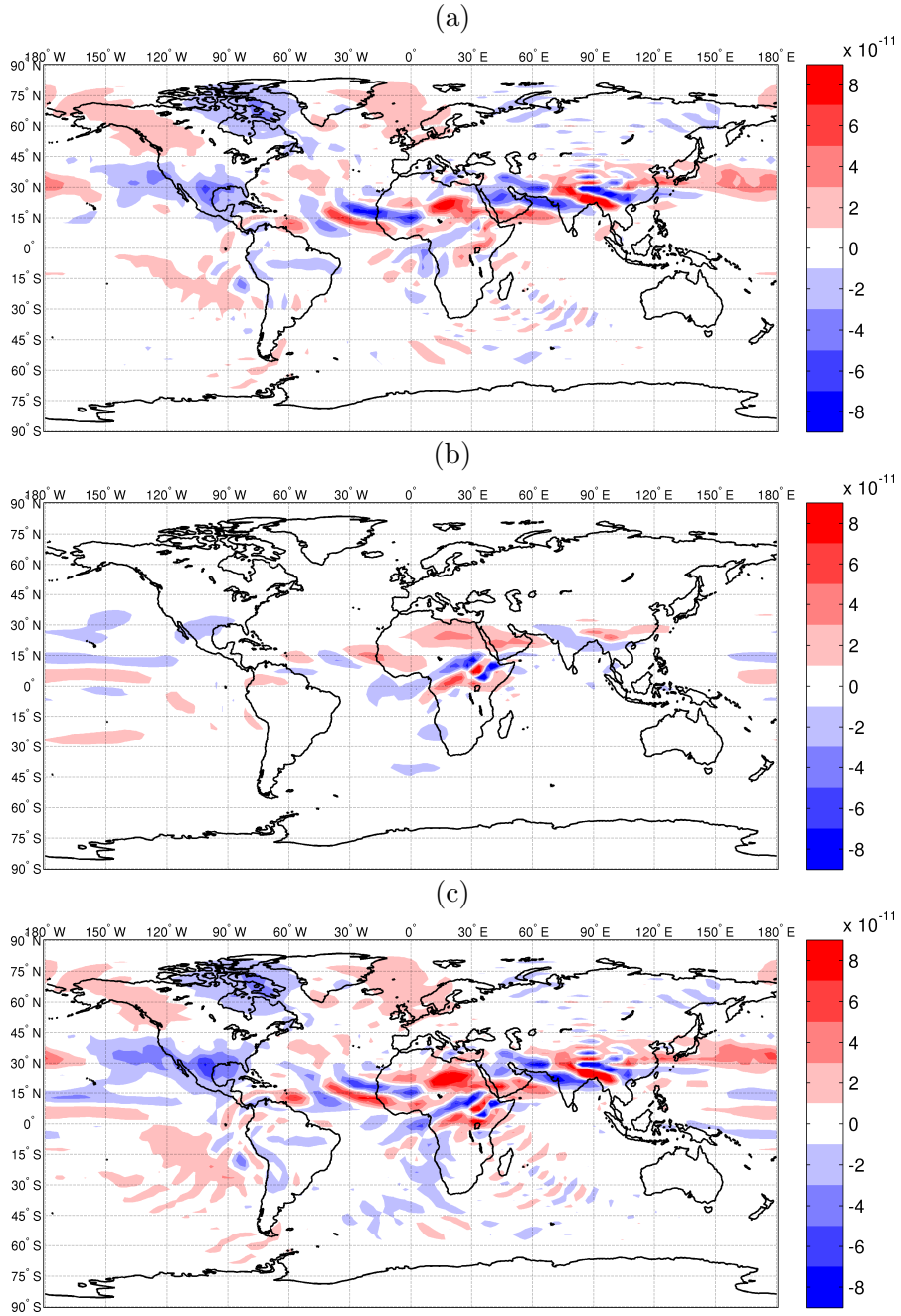



Figure 4.25: 250 hPa Rossby wave source responses ($s^{-2}$) to the diabatic forcing in figure 4.19b, on MOGC3 basic state, averaged between days 10 and 14, for (a) vortex stretching, (b) vorticity advection and (c) the total.

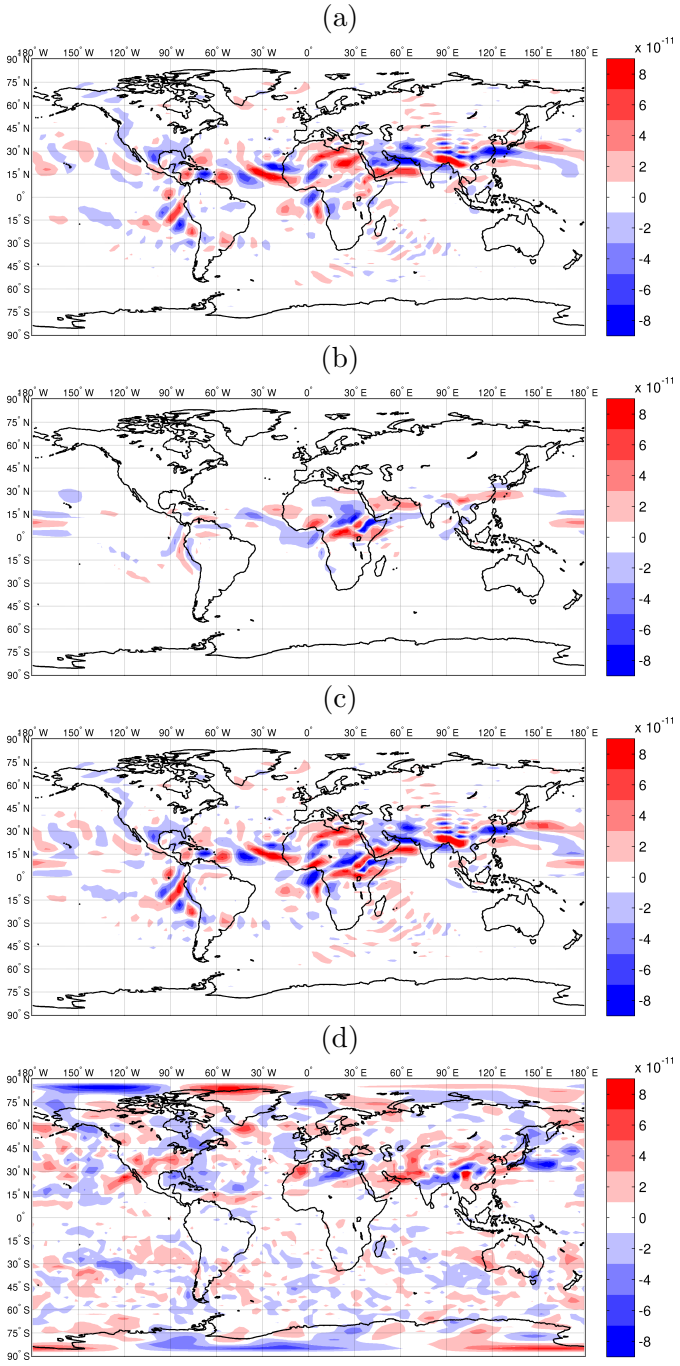



Figure 4.26: Differences in 250 hPa Rossby wave source responses ($s^{-2}$) to the diabatic forcing in figure 4.19b, of the response on MOGC3 basic state minus the response on ERA-I basic state, averaged between days 10 and 14, for (a) vortex stretching, (b) vorticity advection and (c) the total. (d) A reproduction of the RWS difference between MOGC3 MCA mode 1 and NCEP2 MCA mode 1 from figure 4.12a.

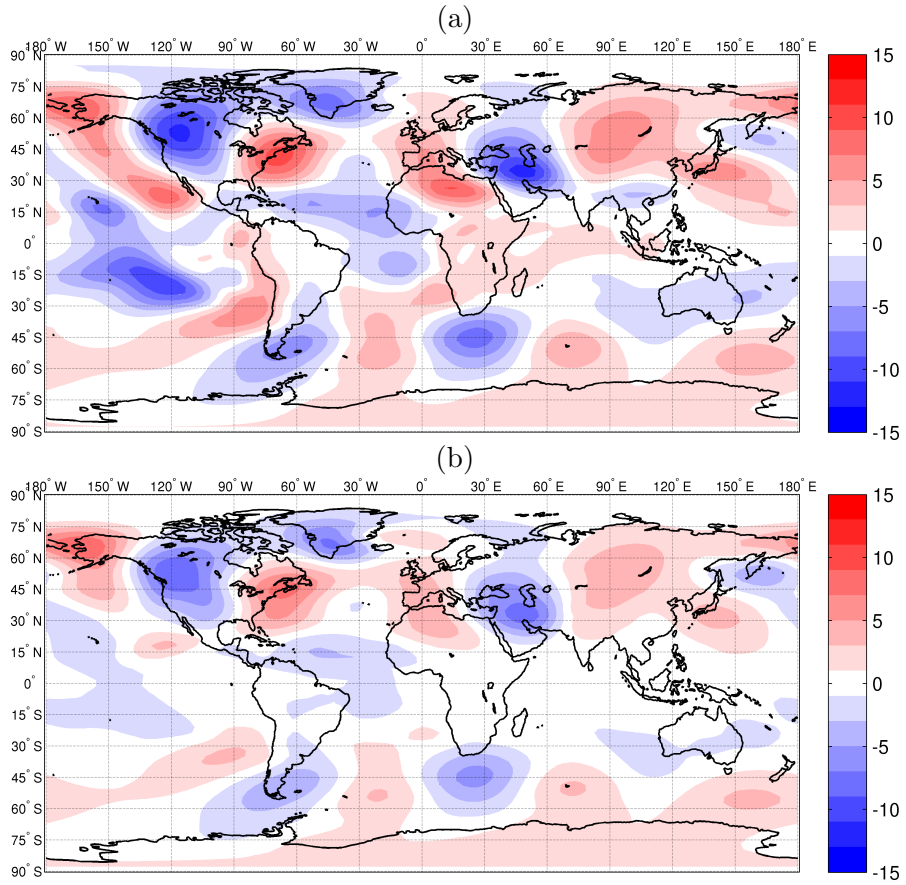



Figure 4.27: The differences in geopotential height responses (m) to the diabatic forcing in figure 4.19b, on MOGC3 basic state (figure 4.24) minus the response on ERA-I basic state (figure 4.20), averaged between days 10 and 14, for (a) 250 hPa and (b) 500 hPa.

in the eastern tropical Pacific, or due to the omission of other diabatic forcing regions from figure 4.19a. But to conclude, the qualitatively different propagation over North America from the North Pacific into the North Atlantic, of a wave with zonal wavenumber of around 2 to 3, agrees with our results from ray tracing and from barotropic model experiments. This further suggests the importance of the basic state in the ENSO tropical-extratropical teleconnection in this region.

## 4.5 Chapter discussion and summary

Figure 4.28 shows the schematic diagram summarizing the sensitivity of the ENSO tropical-extratropical teleconnection to the basic state. Following on from chapter 3 where we have shown that the tropical-extratropical leading mode of covari-

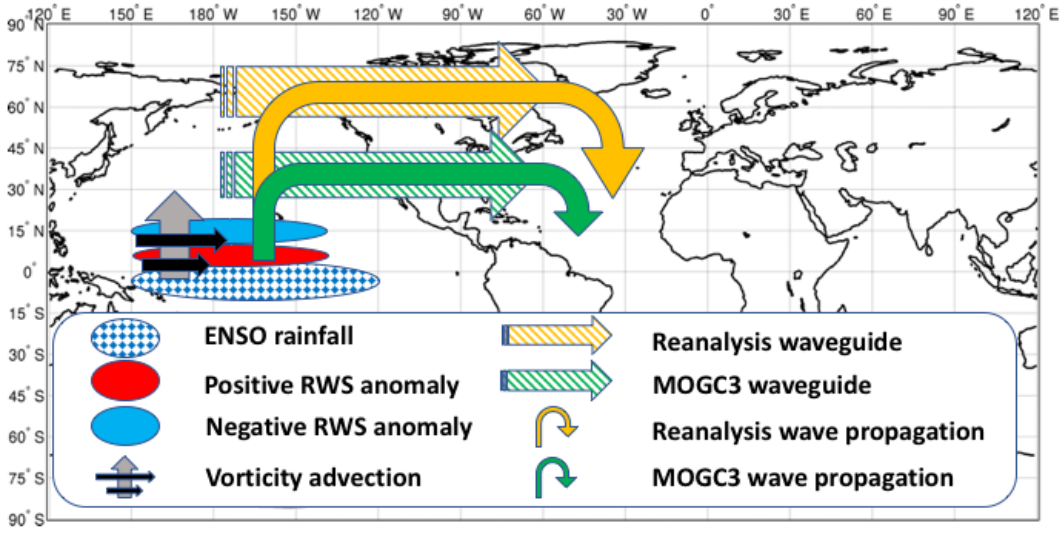



Figure 4.28: Summary schematic linking the important features of the ENSO tropical forcings to the different extratropical wave propagations between the Met Office climate model and the reanalysis, through differences in the climate model basic state.

ability which was the ENSO pattern was different between the climate model and the reanalysis (figure 3.11b), we began in this chapter by showing that the climate model had a large North Pacific jet bias (figure 4.1a). This led to a bias in the North Pacific Rossby wave waveguide, with the turning latitudes being lower in the climate model than in the reanalysis for waves with zonal wavenumbers 2 and 3. Ray tracing showed that this bias resulted in different propagations of waves that were propagating polewards from the tropical Pacific ENSO region into the North Pacific (figure 4.6).

We performed barotropic model experiments forced with the same ENSO tropical Rossby wave sources from the reanalysis (figure 4.8c), but linearized upon the different basic states of the climate model and the reanalysis. The largest differences in the responses were in the North Pacific and North American region (figure 4.9e), and mostly agreed with the differences identified in chapter 3. The zonal wavenumbers 2 and 3 propagated differently, with these waves reflecting equatorward at a lower latitude in the climate model basic state (figure 4.10).

Calculation of a local amplitude of the zonal waves revealed that the Pacific sector contributed to the difference in the global zonal average nature of the Fourier decomposition (figure 4.11), in agreement with the local nature of the turning latitude differences in the North Pacific from ray tracings.

Baroclinic model experiments forced with heating in the tropical Pacific generated the meridional dipole of Rossby wave sources along the Date Line observed in the reanalysis ENSO, with a positive source near the equator and a negative source to the north (figure 4.21c). These were generated mainly through vorticity advection (figure 4.21b) by the upper level divergences associated with the enhanced tropical Pacific rainfall during El-Niño. The extratropical responses also agreed with the barotropic model responses in the North Pacific and North American region (figure 4.27a).

Finally, for discussion in a wider context of climate modelling, our findings may contribute to resolving the signal-to-noise paradox in climate predictions. The paradox refers to a widespread inconsistency between the low strength of predictable signals in climate models and the relatively high level of agreement they exhibit with observed variability of the atmospheric circulation (Eade et al., 2014; Scaife and Smith, 2018). Although it is clearest in the Atlantic basin, for example in NAO ensemble seasonal predictions (Scaife et al., 2014), it also occurs in parts of the Pacific, and on longer timescales in both interannual and decadal predictions (Eade et al., 2014). There is also growing evidence that this is common across different climate models and common across a range of timescales. It has been suggested that the amplitude of predictable signals may be much too weak. Although our North Pacific jet bias is not as severe in the seasonal hindcasts from the same climate model, our findings may still contribute to understanding the signal-to-noise paradox in some longer timescale climate model predictions, where there is sufficient time for a coupled jet bias to develop. For example, our jet bias leads to teleconnection errors and weaker extratropical waves, and can result in a weaker amplitude of predictable signals in the climate model.

# Chapter 5

# Atmospheric drivers of European drought events

After looking at the circumglobal tropical-extratropical teleconnections in the previous chapters, in this chapter we focus on European precipitation and its possible teleconnection from the tropics. Many studies have looked at recent wet European winters, but not many studies have looked at recent dry winters. As we will show in this chapter, the seasonal anomalies between European dry and wet winters are almost linear. This motivates us to look at these European heavy precipitation events and meteorological drought events together in a linear framework.

Knight et al. (2017) performed seasonal-length relaxation experiments using numerical ocean-atmosphere models, and found that the extratropical pattern associated with the record UK rainfall of winter 2013-14 could be partly reproduced by relaxing over the tropics, especially over the tropical Atlantic. They then looked at observational data of tropical Rossby wave sources and tropical rainfall, and suggested that enhanced Amazonian convection could be an atmospheric driver of the extratropical Rossby wave. This extreme UK rainfall season was also part of a larger high rainfall pattern spanning across Portugal, France, Ireland, southern Scandinavia, northern Italy and the Alps. So, their analysis might suggest similar atmospheric drivers contributing to extreme rainfall events across neighbouring regions in the North Atlantic-European sector.

Apart from stationary Rossby waves, there are other mechanisms for European precipitation events. For example, Huntingford et al. (2014) showed that

the UK's floods of winter 2013-14 were associated with a very strong Atlantic jet and many intense storms. Intense Indonesian rainfall can lead to stronger Atlantic jet through a stratospheric pathway. The mechanism is similar to the ENSO stratospheric pathway to the North Atlantic (Ineson and Scaife, 2008), as we have already described in section 3.1.3 but with the opposite sign. The Indonesian rainfall can also cause strong temperature gradients between North America and the tropical Atlantic. This can increase baroclinic instability, through the mechanism in Eady's model (Eady, 1949), and can increase the storm development in the east Pacific near the entrance of the Atlantic jet. Another stratospheric pathway is through the strong westerly phase of the Quasi-Biennial Oscillation (QBO) in the tropical stratosphere during that winter. The QBO has been shown to affect the extratropical stratosphere (Watson and Gray, 2014), and the signal can eventually propagate downward to affect the North Atlantic surface climate (Marshall and Scaife, 2009).

In this chapter, we only focus on the influence through the propagation of stationary tropospheric Rossby waves from the tropics, using methods already employed in the previous chapters including ray tracing, barotropic model and baroclinic model. We emphasize that we do not expect Rossby wave propagation from the tropics into the extratropics to be the complete mechanism of these events. However, there are evidences that recurring low frequency atmospheric circulation anomalies organize storm track anomalies (Branstator, 1995). These low frequency anomalies are also partly maintained by anomalous transient fluxes (Branstator, 1992). We focus on the setting up of these low frequency anomalies from the tropics.

## 5.1 Observational analysis

We use the CRU monthly precipitation data (Harris et al., 2014). The advantage of this dataset is the long period of data availability, but the disadvantage is that this data is only available over land surfaces and excluding Antarctica. We define our European area of interest to be 0°E to 20°E and 45°N to 55°N. We choose

this because firstly, it is mainly over land to capture as much available land data as possible. Secondly, our box is around 1400 km in longitude and 1000 km in latitude, which is not too big when compared with the predominant synoptic scale of 1000 km of cyclones and anticyclones in the mid-latitude atmosphere, given by the Rossby deformation radius where the rotational effect becomes as important as the buoyancy effect.

We average the precipitation for the DJF seasons from 1902 to 2010 (figure 5.1a). There is a small positive trend in our European precipitation. We assess its significance by a re-sampling test. We reshuffle the 109 seasons 20000 times and calculate the trend in each to build up a distribution, and compare the observed trend to this distribution using a two-tailed test. For example, if the observed trend lies within the 2.5% percentile of either tail of the distribution, it is significant at the 0.05 p-value. From this calculation, the observed trend is not significant. We therefore do not detrend the data in our subsequent analysis. We also note that the twenty driest and twenty wettest seasons are qualitatively evenly distributed across the 109 years, consistent with the insignificant trend.

We regress the global precipitation on land surface onto the standardized European precipitation time series (figure 5.1b). The precipitation is concentrated in the southern flank of our box. It also shows that our European precipitation is positively correlated with precipitation over the Iberian Peninsula, the UK, southern Sweden and western Russia, but anti-correlated with precipitation over Norway and southern Greenland. The above correlations still hold qualitatively with the twenty driest and twenty wettest seasonal composites (figure A.11), suggesting linearity between the dry and wet seasons. Therefore, instead of just focusing on the European meteorological drought events, we investigate both dry and wet seasons together.

To relate our European precipitation to the preferred patterns of large scale atmospheric dynamics, we perform EOF analysis on the 500 hPa geopotential height (Z500) over the North Atlantic-European region (90°W-90°E, 20°N-90°N) (figures 5.2a and 5.2c). We use the ERA-20C reanalysis (Poli et al., 2016) to match

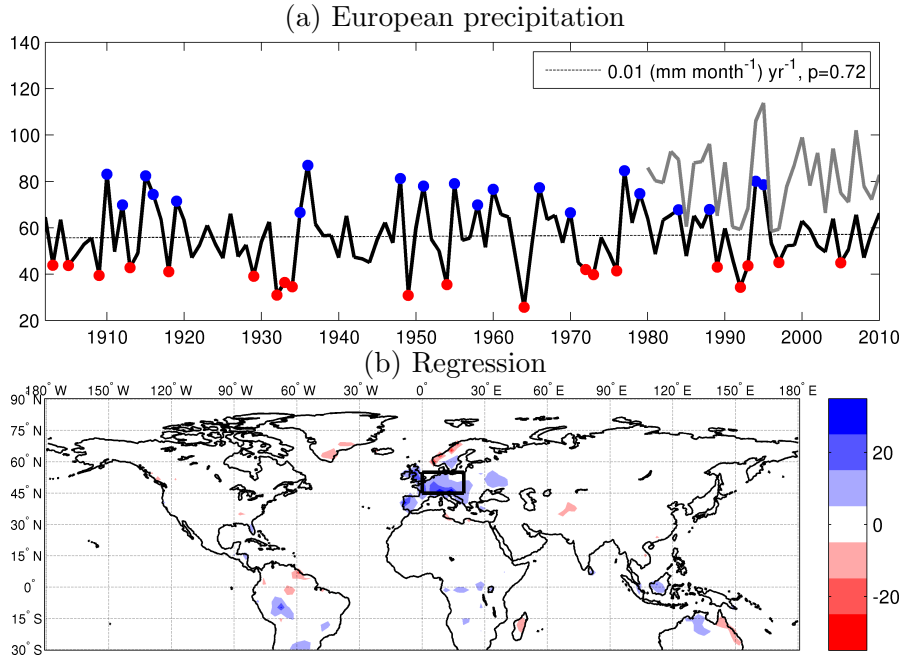



Figure 5.1: (a) Time series of DJF seasonal mean of monthly CRU land precipitation over our European box (thick black line), with the twenty driest and twenty wettest seasons marked in red and blue respectively. Legend shows the interannual trend (thin black line) and the corresponding p-value. Also shown is the GPCP precipitation (gray line) from 1980 to 2010, which correlates with CRU over the same period at 0.84. (b) Global CRU precipitation regressed onto the standardized CRU European land precipitation time series. All units are in mm per month.

the long CRU land precipitation period. The first mode (EOF1) resembles the positive phase of the North Atlantic Oscillation (NAO+) and explains 30% variance in Z500. EOF2 resembles the positive phase of the East Atlantic pattern (EA+) and explains 15% variance. Our European box precipitation time series correlates in this period of 1902 to 2010 with the NAO at -0.44, and with the EA at 0.20, suggesting neither EOFs capture much of its variability. This is also seen from the regression of the CRU land precipitation onto the standardized principal components of the EOFs. The land precipitation associated with NAO+ (figure 5.2b)shows a meridional dipole, with increased precipitation over Scotland and Norway, and decreased precipitation over the Iberian Peninsula and the southern flank of Europe along the Mediterranean Sea. This is different to the coherent pattern across our European region and into the UK and the Iberian Peninsula. The land precipitation associated with EA+ (figure 5.2d) shows a more coherent pattern across the Iberian Peninsula and the UK. However, the EA+ precipitation signal is weaker over most of our European region. To summarize, by choosing a box to include both the positive and negative NAO-related precipitation anomalies, we have limited the influence of the NAO.

So far, we have been looking at the period 1902 to 2010 covered by the CRU land precipitation dataset. One disadvantage of CRU is the unavailability of precipitation data in massive areas in the tropics over the oceans, which we want to look at when investigating tropical-extratropical teleconnections. Therefore, we now use the GPCP combined surface precipitation dataset (Adler et al., 2003), for the period 1980 to 2010. It combines satellite observations and makes precipitation data available even on ocean surfaces. In the extratropics, GPCP also allows EOF analysis on a much larger region than just the European land area. Figure 5.3 shows the EOFs of GPCP over the same North Atlantic-European region used in the previous EOFs. For EOF1, GPCP is similar to CRU regressed onto Z500 EOF1, with increased precipitation over the UK and northeastern South America, and reduced precipitation along the northern flank of the Mediterranean Sea and in central tropical Africa. The similarity suggests that the GPCP EOF1 is associated

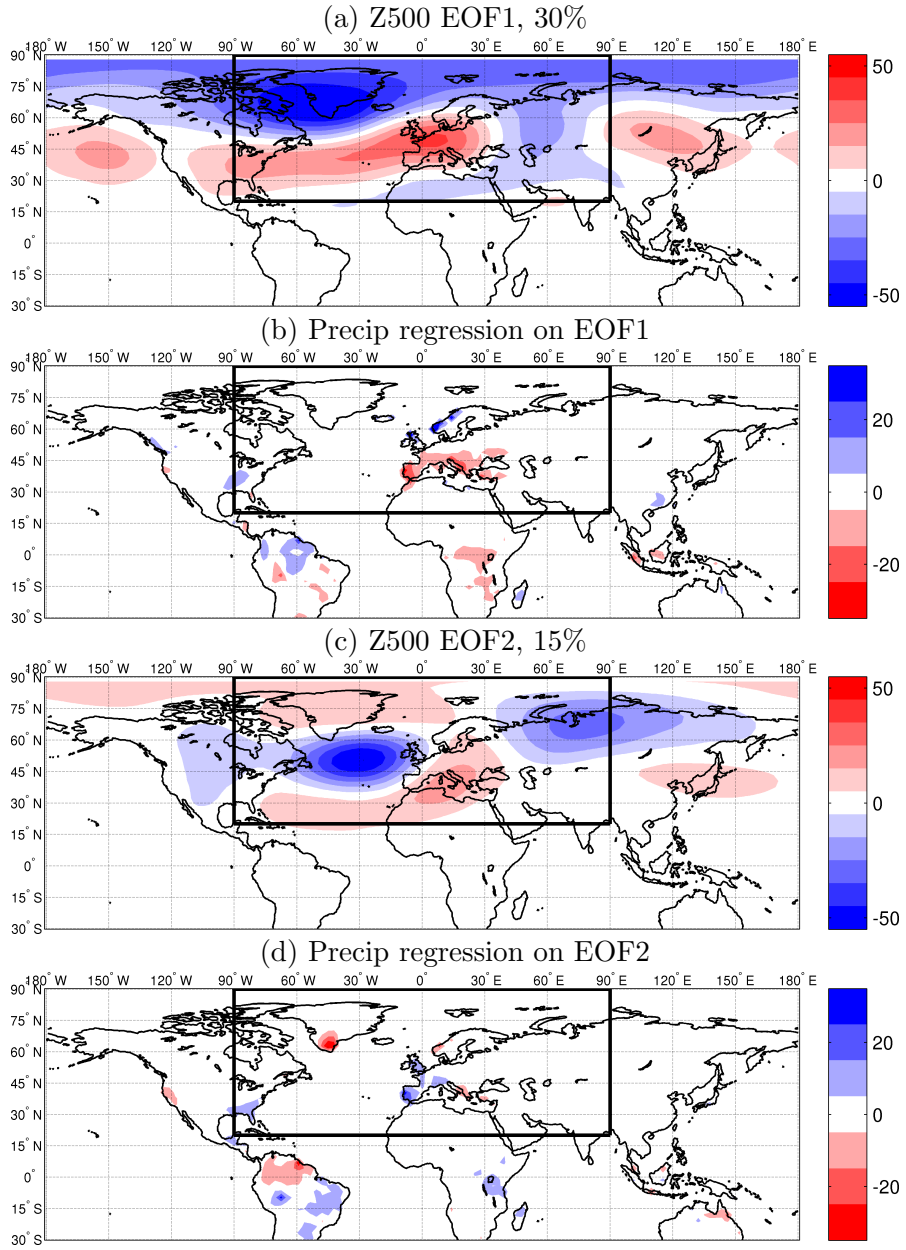



Figure 5.2: (a) EOF mode 1 of the North Atlantic-European region (black box) 500 hPa geopotential height (m), and the percentage of variance explained. (b) Precipitation regressed onto the principal component of EOF1 (mm per month). (c,d) Same as (a,b) but for EOF2. These are for the period 1902 to 2010.

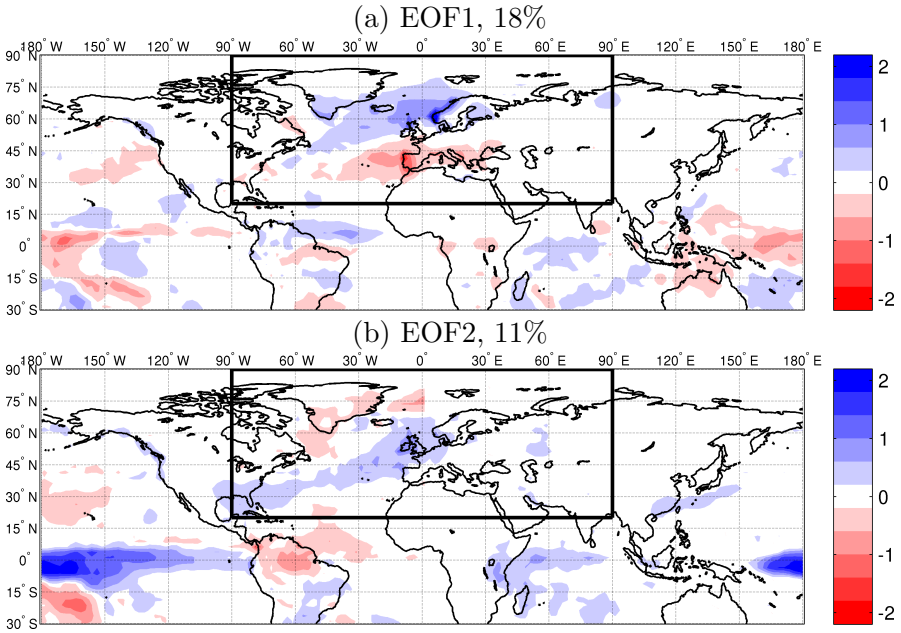



Figure 5.3: GPCP precipitation (mm day$^{-1}$) regressed onto the standardized principal components of the EOFs of the GPCP precipitation in the North Atlantic-European region (black box).

with NAO+ again. For EOF2, GPCP is similar to CRU regressed onto Z500 EOF2, with increased precipitation in the UK, the Iberian Peninsula, Florida, eastern tropical South America and eastern tropical Africa, and reduced precipitation in the southern tip of Greenland. The similarity suggests that the GPCP EOF2 is associated with EA+ again. Figure 5.1a shows that the GPCP time series averaged over our European box correlates at 0.84 with CRU over their overlapping period of 1980 to 2010, despite a slight systematic offset between their two means with GPCP being higher. This, and together with the EOFs, show the agreement between GPCP and CRU, and justify our use of GPCP for looking at tropical precipitation anomalies over oceans that are not provided by CRU.

Figure 5.4 shows some key variables regressed onto the standardized European precipitation time series based on GPCP for the period 1980 to 2010. The 250 hPa zonal wind shows an equatorward shift in the North Atlantic jet exit and a poleward shift in the Asian jet entrance. This reflects the aforementioned partial correlation with the NAO. The 250 hPa geopotential height is suggestive of two waves linking areas of statistical significances. The first one is a high in the

subtropical eastern Pacific, low in central North America, high in northeastern North America, low in the UK and high in western Asia. The second is a high in northwestern Africa, low in the UK and again high in western Asia. By choosing our box to include both the positive and negative NAO-related precipitation anomalies, we have found a more wave-like pattern that might be forced from the tropics. The result is similar if using ERA-20C 250 hPa heights for the longer period of 1902 to 2010, suggesting its robustness and stationarity across different periods. Further inspection using 500 hPa height shows an equivalent barotropic structure (figure A.13). The 250 hPa Rossby wave source shows statistically significant anomalies in the tropical Atlantic below 15°N. There are also significant RWS anomalies in the tropical eastern Pacific crossing into the subtropics into the Gulf of California. Dry and wet composites for the geopotential heights and RWS suggest linearity of these anomalies (figure A.12).

Figure 5.4d shows the GPCP precipitation regression. The Intertropical Convergence Zone (ITCZ) strengthens over the tropical Pacific and Indian Ocean. The strengthening in the tropical eastern Pacific is statistically significant. In the tropical Atlantic, the ITCZ shifts southward, with reduced precipitation just north of the equator and increased precipitation just south of the equator. This shift is also statistically significant. The relationship between the increased precipitation in the tropical Atlantic just south of the equator and the positive region of RWS along 15°N from 60°W to 30°W has also been reported in a seasonal forecast model study (Scaife et al., 2017, figure 7d). Figure 5.4e shows the vertically integrated diabatic heating (section 2.4), with a similar structure in the tropics to the GPCP precipitation because precipitation dominates the heating in the tropics. The precipitation of around 0.4 mm day$^{-1}$ in the tropical Atlantic in figure 5.4d corresponds to around 10 Wm$^{-2}$ of diabatic heating in figure 5.4e, in good agreement with the radiative-convective equilibrium mentioned in section 2.4.

We have so far been focusing on anomalies in the seasonal timescale. To briefly look into the daily timescale circulations, we regress the seasonal mean of the daily blocking index (section 2.5) onto the standardized European precipitation

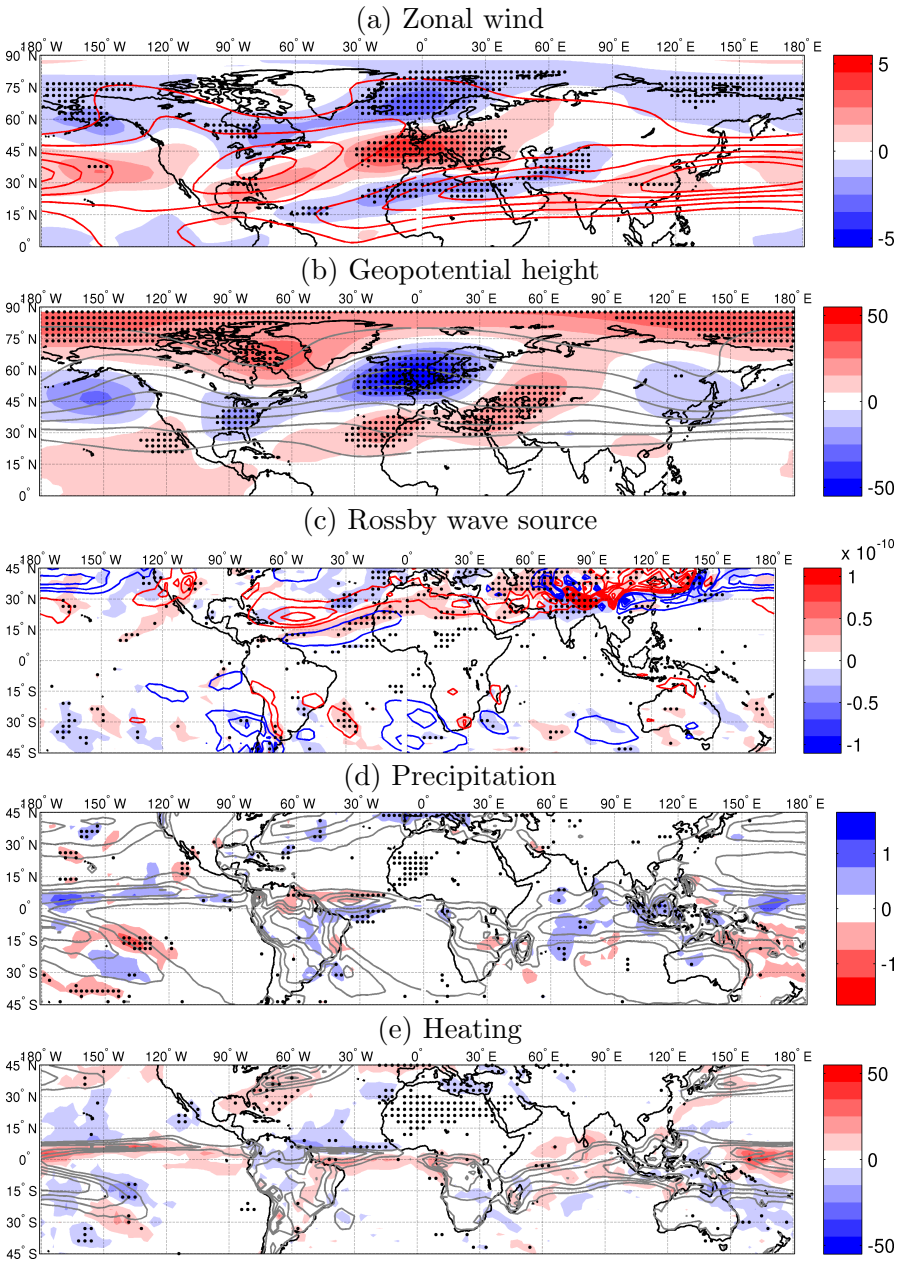



Figure 5.4: Color shading shows the regressions onto the standardized European precipitation time series between 1980 and 2010, for (a) 250 hPa zonal wind ($\mathrm{ms}^{-1}$), (b) 250 hPa geopotential height (m), (c) 250 hPa RWS ($\mathrm{s}^{-2}$), (d) precipitation ($\mathrm{mm\,day}^{-1}$) and (e) vertically integrated heating ($\mathrm{Wm}^{-2}$). Black dotting demonstrates a 95% significant linear regression relationship. Solid contour shows the climatologies, with contouring every (a) $10\,\mathrm{ms}^{-1}$ from $10\,\mathrm{ms}^{-1}$, (b) 200 m from 9600 m, (c) $1\times10^{-10}\,\mathrm{s}^{-2}$ from zero with positive red and negative blue and zero omitted, (d) $2\,\mathrm{mm\,day}^{-1}$ from $2\,\mathrm{mm\,day}^{-1}$ and (e) $50\,\mathrm{Wm}^{-2}$ from $50\,\mathrm{Wm}^{-2}$.

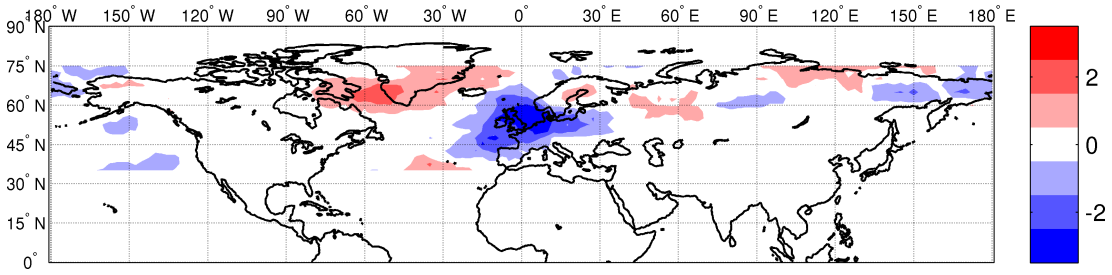



Figure 5.5: Blocking frequency computed from 500 hPa geopotential height, regressed onto the standardized European precipitation time series. Unit is percentage of blocked days to the total number of days per season.

time series. Figure 5.5 shows that the blocking frequency increases over southern Greenland and reduces over the UK and northern Europe. Increase in Greenland blocking has been associated with NAO- events (Woollings et al., 2008), and this agrees with our European precipitation events correlating with the NAO at -0.44. The reduction in blocking over the UK is also consistent with the increased frequency of cyclones passing the UK and Europe. This pattern is also similar to the blocking frequency composite maps for daily NAO+ and NAO- in Scherrer et al. (2006), but the amplitude in percentage change is smaller than theirs. This is possibly because the European precipitation time series only correlates with the NAO at 0.44. In the rest of this chapter, we will return our focus onto the seasonal mean anomalies, although in the future, examination of events within the season may provide additional insight into the higher frequency drivers of European precipitation events.

To summarize, we have identified a large scale wave pattern associated with seasonal European precipitation events, which is linear with respect to the dry and wet events. We have also identified anomalous tropical precipitation, and strengthening in precipitation in the tropical eastern Pacific and the southward shift in the tropical Atlantic are both statistically significant. In the following sections, we drive waves from the tropics in a barotropic and a baroclinic model, as well as ray tracing, to test the tropical-extratropical teleconnections.

## 5.2 Barotropic model experiments

### 5.2.1 Circumglobal patch forcings

In this section, we perform firstly barotropic model idealized patch experiments and secondly realistic circumglobal forcing experiments, to investigate potential tropical drivers of European precipitation events.

Figure 5.6 shows the results from the barotropic model patch experiment. The linear combination of the patch forcing experiments 250 hPa response (figure 5.6a) is able to match the observed 250 hPa pattern well, with the low over the UK, the high over western Russia, the low south of the Aleutian Islands and the high over the Hudson Bay. However, a perfect match to the observed pattern is beyond the capability of our barotropic patch experiment. Still, we shall investigate the extent to which Rossby wave propagations can contribute to the observed dynamical pattern associated with our European precipitation events.

The linear combination of the patch forcings shows a northwest-southeast tilted banded structure in RWS over the tropics and the subtropics (figure 5.6b), from the Pacific Ocean to the Atlantic Ocean. This tilt is consistent with the phase tilt of Rossby waves propagating northeastward from the tropics into the extratropics. These show the theoretical forcings that can generate the target geopotential height response. We compare this theoretical forcing pattern to the observed RWS to isolate regions where both agree in the sign of the forcing. In the tropics up to 15°N, regions with the same sign (figure 5.6c) include the positive source in the tropical western Atlantic (304°E, 15°N) and the negative source in the tropical eastern Atlantic (338°E, 10°N). In the subtropics above 15°N, regions with the same sign include the positive source in the subtropical eastern Pacific over the Gulf of California (248°E, 27°N) and the negative source in the subtropical eastern Atlantic (326°E, 32°N).

Although there are many regions where the observed forcing generates a response with a negative projection onto the observed wave (black dots in figure 5.6c), many of these responses are only very weakly negative in the projection,

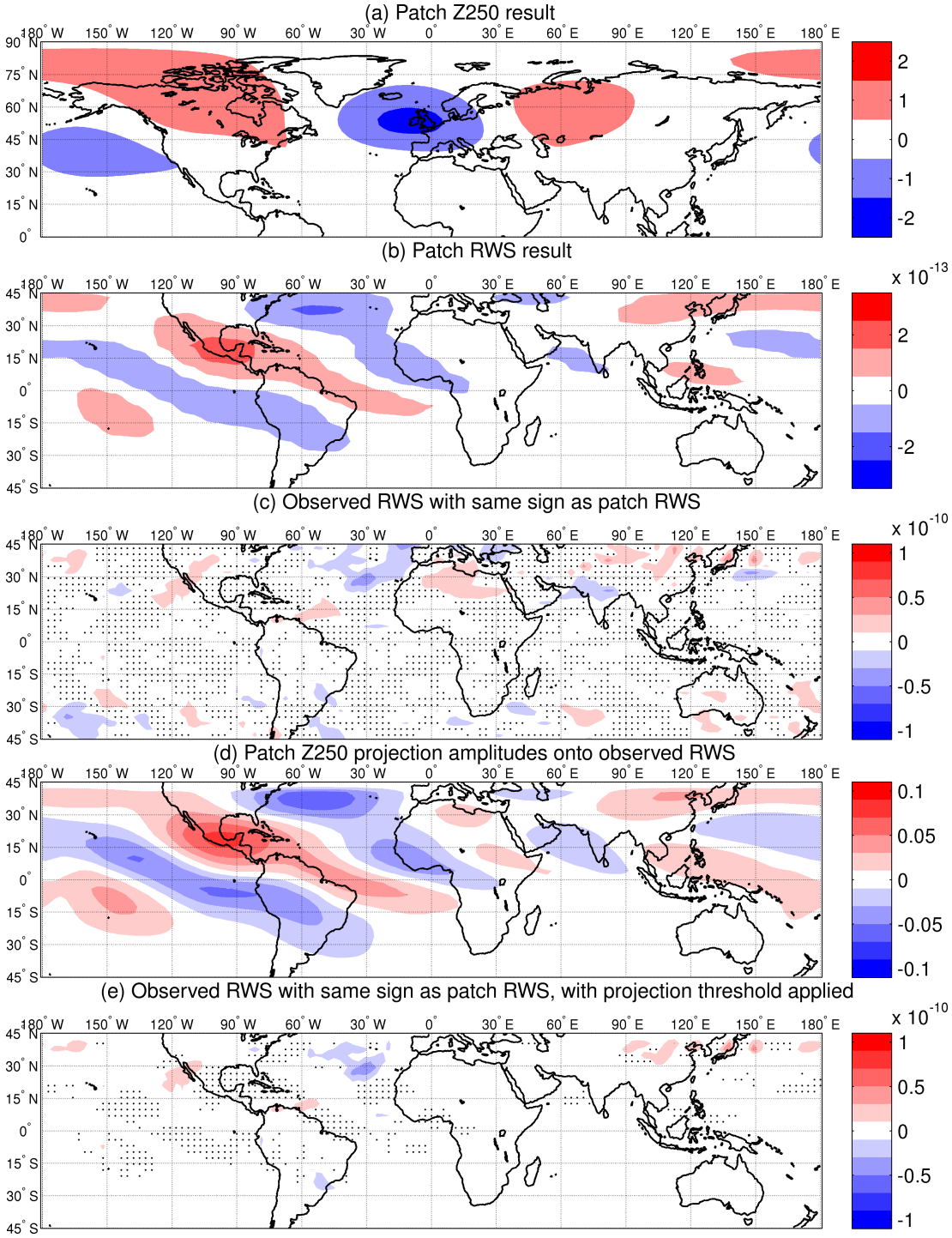



Figure 5.6: (a) 250 hPa geopotential height result from barotropic model patch experiment (m). (b) Rossby wave source result from barotropic model patch experiment ($s^{-2}$). (c) Regions of observed Rossby wave source that are the same sign as the Rossby wave source result from barotropic model patch experiment ($s^{-2}$). Regions where the signs do not agree are set to zero and are dotted. (d) Normalized projection amplitudes between the patch forcing experiment responses and the observed wave. (e) Same as (c) but with a projection threshold applied to filter out weak projections.

and are negligible. Figure 5.6d shows the normalized projection of the response from each forcing onto the observed wave. It is calculated as the dot product of each patch forcing response with the observed wave, and normalized by the dot product of the observed wave with itself. Hence, the normalized projection can range from -1 to 1. It is similar to the patch RWS result in figure 5.6b because it is used to weight the individual patch forcings. The projection values in figure 5.6d are smaller than the range from -1 to 1. The observed forcings have much larger spatial area than each of the individual patch forcings, which may explain why the projection values are smaller than the allowed range.

There are many regions where the normalized projection is weak. To focus on regions where the normalized projection is strong, we apply a projection threshold in figure 5.6c to produce figure 5.6e. We arbitrarily choose a threshold of 0.02 in absolute value, and define strong projections as having an absolute value in projection of above 0.02, and define a projection as weak otherwise. In figure 5.6e, the red and blue regions show the same-sign forcings with strong projections, the black dotted regions show the opposite-sign forcings with strong projections, and the white regions show the weak projections with either same-sign or opposite-sign forcings. Compared to the original in figure 5.6c, a lot of the black dotted regions have been filtered out. As the threshold is applied as an absolute value to act on both positive and negative projections, some of the red and blue regions in figure 5.6c are also filtered out. However, the main sources in the tropical western and eastern Atlantic, in the subtropical eastern Atlantic and in the subtropical eastern Pacific are still present, further supporting their importance as potential drivers of European precipitation events.

Using the observed RWS (figure 5.4c) isolated over the tropics and subtropics, we run the barotropic experiment. Using the observed forcing from 15°N to 15°S produces a very weak extratropical response (figure 5.7a). This is because the RWS is relatively small in amplitude within 15°N circumglobally. Using the wider 30°N to 30°S forcing produces a stronger extratropical wave pattern (figure 5.7b). A Hovmöller diagram (figure A.14b) shows the wave pattern developing circum-

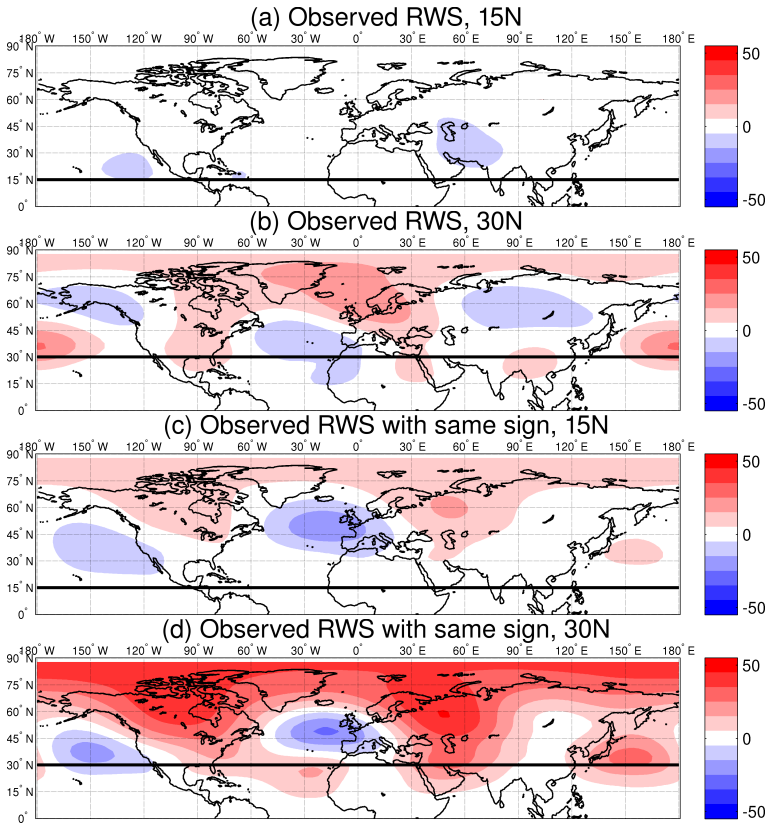



Figure 5.7: Barotropic model responses to observed forcings. 250 hPa geopotential height responses from barotropic experiments (m), using (a,b) the observed Rossby wave source and (c,d) the observed Rossby wave source where the sign agrees with the patch result. Forcings up to 15°N are used in (a,c), and 30°N in (b,d).

globally almost simultaneously, because at 30°N, forcings with large amplitude are present at almost all longitudes. Although this reproduces part of the observed pattern, such as the high over Baffin Bay and the low over eastern Russia, the pattern is different especially over the North Atlantic, where the pattern now is more of a north-south dipole than the observed east-west dipole. Using all the observed RWS cannot reproduce the observed pattern associated with our European precipitation, especially over the North Atlantic region. There are two possible reasons.

Firstly, the observed RWS includes large regions in the eastern tropical Pacific and tropical Atlantic where the signs are opposite and the projections are strong (black dots in figure 5.6e). A possible reason is that some of these anomalies are consequences rather than causes of the waves. The waves can generate anoma-

lous vorticities ($\zeta'$) and divergent winds ($\mathbf{V}'_\chi$), which can affect the RWS (equation 2.17). Such consequence of the wave does not have to be confined within the extratropics. The wave can affect the basic state and change the propagation characteristics of higher frequency waves, which then can propagate into the tropics and affect the RWS. An observational study of the MJO has suggested similar mechanism (Matthews and Kiladis, 1999). Our experiments cannot capture this mechanism because our model does not have propagations of high frequency waves. In an attempt to separate the effect of the wave on the RWS, O'Reilly et al. (2018) ignored terms due to anomalous vorticities in their RWS because these corresponded to the circulation response they were assessing. However, we think the wave can still affect the RWS through anomalous divergent winds by modifying the clouds and affecting convection. A second possibility is that the observed RWS is obtained from regression, which does not imply causality. Other atmospheric processes that are correlated with our European precipitation time series are captured in the regression, but may have no causality in either direction.

Next, we run the model with the RWS in figure 5.6e where we set the RWS to zero over regions where the sign of the observed RWS disagrees with the sign of the patch RWS result. Although using the patch RWS result (figure 5.6b) should produce the best-match extratropical response to the observed (figure 5.6a), by only retaining regions where the sign of the RWS agrees with observation (figure 5.6e), it is not guaranteed how much of the best-match response will be retained. In the end, using only up to 15°N of this forcing is capable of reproducing most of the best-match response pattern (figure 5.7c). The sources with the largest amplitude for this 15°N case are over the tropical Atlantic. This agrees with the corresponding Hovmöller diagram (figure A.14c) which shows the response first developing in the North Atlantic region on day 4. However, the response amplitude is only around half of the observed. This underestimation may be partly due to the forcing being restricted to within 15°N. Extending the forcing region to 30°N does not change the response pattern much, and only increases the amplitude (figure 5.7d). The amplitude of the low near the UK is comparable to the

observed, but the two highs over Canada and western Russia are too strong. This may be because some of the higher latitude observed RWS is generated by the observed extratropical wave pattern rather than generating it. Including these as forcings in the barotropic model increases the response amplitude. For the 30°N case, the forcings with large amplitude are no longer restricted in the Atlantic, so the Hovmöller diagram shows the wave pattern developing circumglobally almost simultaneously (figure A.14d). Finally, the Hovmöller diagrams (figure A.14) also show that the extratropical responses, averaged between 45°N and 60°N, are indeed quasi-stationary over our averaging period of 7 to 10 days.

### 5.2.2 Individual patch forcings

To further investigate the importance of the tropical and subtropical RWS in the Atlantic and the Pacific, figure 5.8 shows the responses from individual idealized patch forcings selected from figure 5.6e where the aforementioned signs agree. The four idealized RWS forcings include the tropical western Atlantic (304°E, 15°N) with amplitude $8\times10^{-11}\,s^{-2}$, the tropical eastern Atlantic (338°E, 10°N) with amplitude -$8\times10^{-11}\,s^{-2}$, the subtropical eastern Atlantic (326°E, 32°N) with amplitude -$16\times10^{-11}\,s^{-2}$ and the subtropical eastern Pacific (248°E, 27°N) with amplitude $8\times10^{-11}\,s^{-2}$. The amplitudes are chosen to match the observed amplitudes in figure 5.6e. For example, averaging over the 2D cosine-squared patch in the tropical western Atlantic gives an average amplitude of $2\times10^{-11}\,s^{-2}$ that matches the observed.

Figure 5.8a shows a wave emanating from the forcing in the tropical western Atlantic, crossing the North Atlantic into Europe and Scandinavia. Although this response captures the low over our European box, it does not capture the high downstream in western Russia or upstream in Baffin Bay. Figure 5.8b shows a wave emanating from the forcing in the tropical eastern Atlantic. It crosses the Mediterranean Sea and into western Russia. In addition to capturing the low over Europe, this response captures the downstream high over western Russia. Combining both forcings (figure 5.8e) gives a pattern more similar to the observed

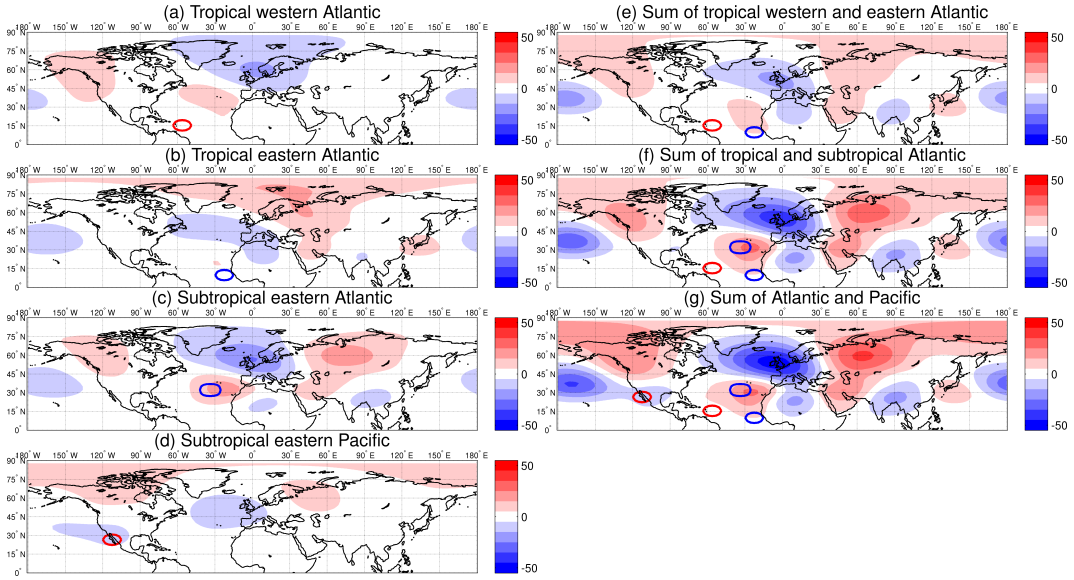



Figure 5.8: Barotropic model responses from selected individual patch forcings. Color shadings show the 250 hPa geopotential height response from barotropic experiment (m), using idealized forcing in (a) tropical western Atlantic with amplitude $8\times10^{-11}\,s^{-2}$, (b) tropical eastern Atlantic with amplitude $-8\times10^{-11}\,s^{-2}$, (c) subtropical eastern Atlantic with amplitude $-16\times10^{-11}\,s^{-2}$, (d) subtropical eastern Pacific with amplitude $8\times10^{-11}\,s^{-2}$. (e) Sum of (a,b). (f) Sum of (a,b,c). (g) Sum of (a,b,c,d). Vorticity forcings are contoured in solid at $\pm2\times10^{-11}\,s^{-2}$, with positive in red and negative in blue.

than from each forcing individually. This suggests that when considering RWS below 15°N, these two forcings in the tropical Atlantic can together contribute to the observed pattern over Europe and western Russia. There is another region of large amplitude forcing in the subtropical eastern Atlantic. The response from this forcing (figure 5.8c) is similar to that of the previous two forcings within 15°N. This suggests that this forcing at higher latitude can reinforce the response of the forcings at lower latitude in the tropical Atlantic. In the subtropical eastern Pacific, figure 5.8d shows a wave propagating from the Gulf of California across North America into the North Atlantic. It captures the low over Europe and the highs in northwestern Russia and northern Canada. This response is weaker than the combined responses from the three Atlantic forcings in figure 5.8f. The RWS at these four regions are linear in sign with respect to the wet and dry European composites (figures A.12b and A.12d).

Finally, figure 5.8g shows the combined response from all four forcings. It

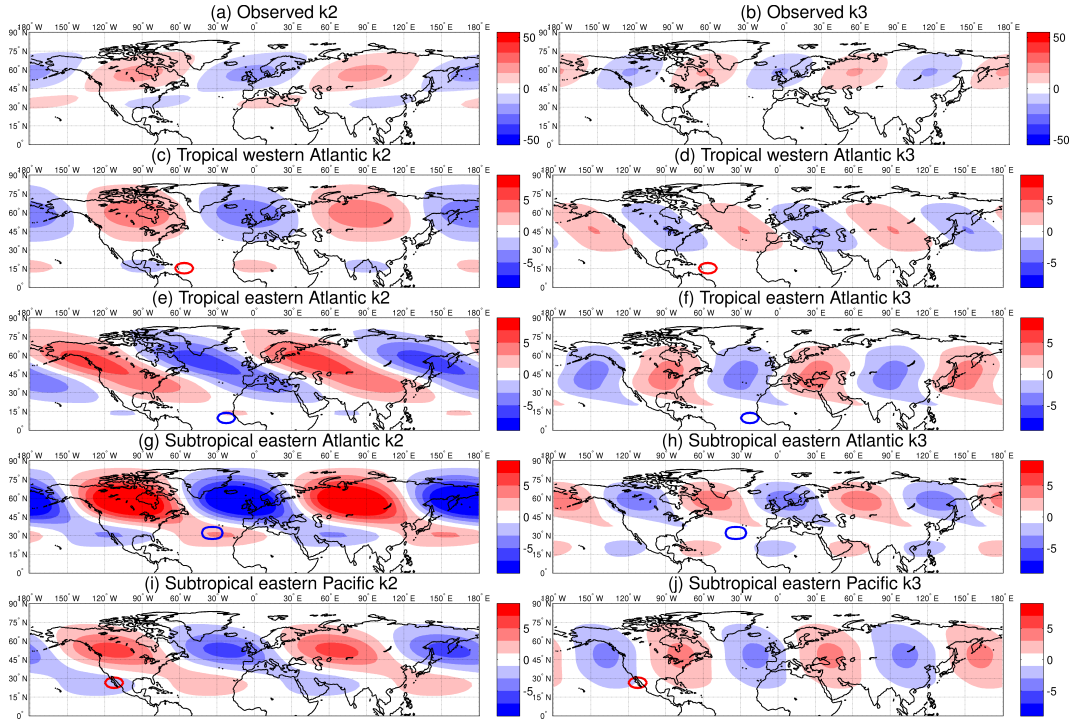



Figure 5.9: Fourier analysis of the barotropic model responses from selected individual patch forcings. Color shadings show the zonal wavenumbers 2 and 3 components of 250 hPa geopotential height (m), of (a,b) the observed pattern, and barotropic model responses to idealized forcings at (c,d) tropical western Atlantic, (e,f) tropical eastern Atlantic (g,h) subtropical eastern Atlantic and (i,j) subtropical eastern Pacific. Vorticity forcings are contoured in solid at $\pm 2\times10^{-11}\,\mathrm{s}^{-2}$, with positive in red and negative in blue. Note the different colourbars for observed and model.

resembles figure 5.7d and shows that our four idealized forcings already capture most of the important same-sign forcings in figure 5.6e. The amplitude of the UK low response also matches closely that of the observed. To summarize, RWS anomalies in the tropical Atlantic (lower than 15°N) can trigger the observed extratropical wave. Anomalies in the subtropical Atlantic and Pacific (between 15°N and 30°N) can enhance the wave, but it is not clear how much of these are just part of the response of the wave itself, given that the latitude is much closer to the extratropics.

As the observed pattern is quite zonal, we might learn more by looking at the contribution from each zonal wavenumber (k) of its decomposition. Also, Fourier decomposition allows us to compare with the ray tracing results in the

next section, which are performed for each wavenumber separately. Figure 5.9 shows the k2 and k3 components of the observed pattern, and of the barotropic model responses to individual idealized forcings from figure 5.8. Only k2 and k3 are shown because these are found to be the dominant components in the mid-latitudes. The barotropic model with forcings in the tropical western Atlantic (figure 5.9c,d) and the subtropical eastern Atlantic (figure 5.9g,h) produce very similar k2 and k3 patterns to the observed. The tropical eastern Atlantic forcing produces a k2 wave (figure 5.9e) that is slightly less similar to the observed, but it produces a k3 wave (figure 5.9f) with a phase more different to the observed.

### 5.2.3 Barotropic results discussion

As mentioned earlier, in the patch experiments we have arbitrarily chosen a projection threshold of 0.02 to filter out the weak projections from figure 5.6c to obtain figure 5.6e. To demonstrate a case where an originally black-dotted region is filtered out, we consider the forcing at 15°N 315°E (figure 5.10a) that is in the black-dotted region in figure 5.6c. As this forcing is just to the east of the western tropical Atlantic forcing considered in figures 5.8a, their responses are slightly similar (compare figure 5.10b with figure 5.8a). However, by shifting the forcing to the east, the response is also shifted and is almost in quadrature with the observed wave, resulting in a normalized projection of -0.0158 from figure 5.6d. Although the projection is negative, the projection is very weak and is negligible. So this forcing is only marked by black dot in figure 5.6c but is filtered out in figure 5.6e after the threshold is applied. This example also shows that these forcing locations can give strong extratropical responses, but they just do not project well onto our particular pattern. In section 5.4, we will investigate the causality of the RWS from tropical heating. However, further investigations into whether some of the observed RWS are feedbacks or are correlated processes without causality are beyond the scope of this study.

To summarize, barotropic experiments suggest four regions in the tropical and subtropical Atlantic and Pacific which force Rossby waves that can contribute to

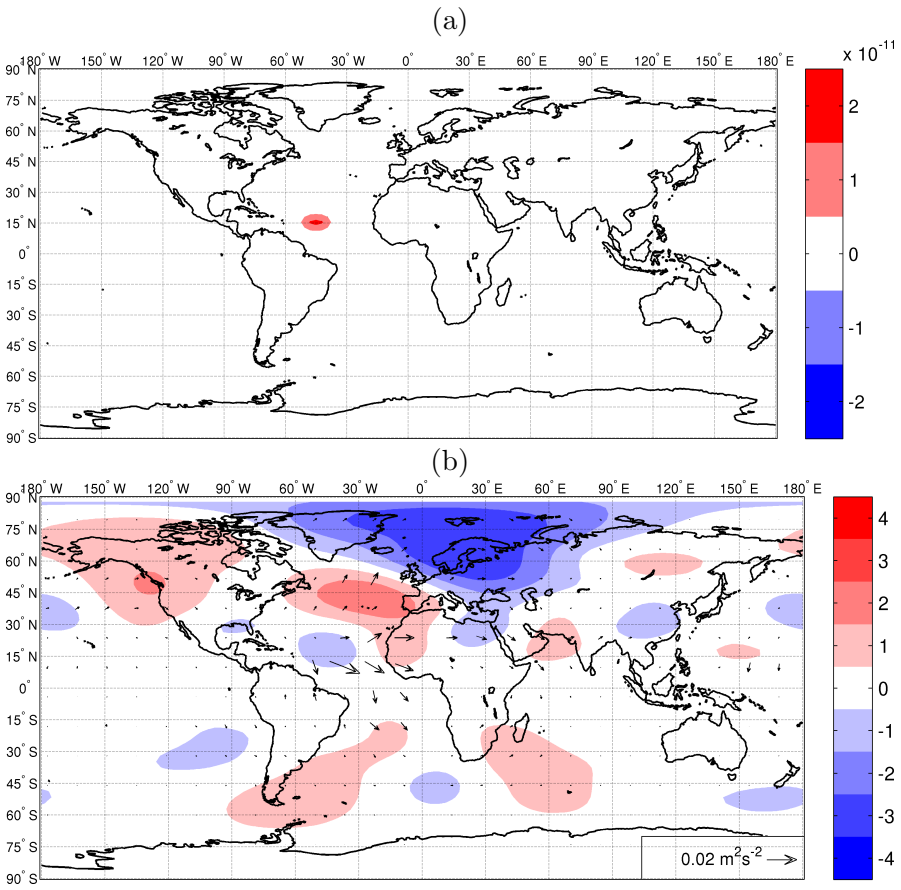



Figure 5.10: (a) Vorticity forcing ($s^{-2}$) at 315°E 15°N. (b) Response in 250 hPa geopotential height (m) averaged between days 7 and 10. Arrows show the Rossby wave activity fluxes.

European precipitation and drought events, and the k2 and k3 components seem particularly important. The importance of the k2 component from the tropical Atlantic is also mentioned in Knight et al. (2017). Their ray tracing from the western tropical Atlantic shows a ray path across the North Atlantic into the UK through the centres of action of the streamfunction wave anomalies during the extreme UK rainfall of winter 2013-14. However, although the barotropic model has shown that the observed wave can be forced from the tropical Atlantic, there is not enough evidence that this has definitely occurred, since the wave also correlates with other RWS features which we think could be consequences of the wave. This is an important caveat of our barotropic experiments.

## 5.3 Ray tracing

To further investigate these forcings, we perform ray tracing for the four forcing locations from the barotropic model section. Ray traced from the tropical western Atlantic (figure 5.11a,b) can propagate across Europe for both k2 and k3, although the propagation is less robust for the k2 ensemble. Ray traced from the tropical eastern Atlantic can propagate across Europe robustly for k2. Ray traced from the subtropical eastern Atlantic can propagate across Europe robustly for both k2 and k3. These are in agreement with the barotropic model k2 and k3 responses resembling the observed, and suggest that the observed pattern can be explained by waves forced from these regions.

The k3 ray traced from the tropical eastern Atlantic cannot propagate across Europe, and this result is robust across all ensemble members. This may be consistent with the aforementioned phase difference in the barotropic k3 response compared to the observed, and suggests that k3 wave propagation from this region cannot robustly match the observed. Finally, all rays traced from the subtropical eastern Pacific do not reach Europe, suggesting that the Pacific forcing teleconnection to Europe is not as robust as the Atlantic forcings.

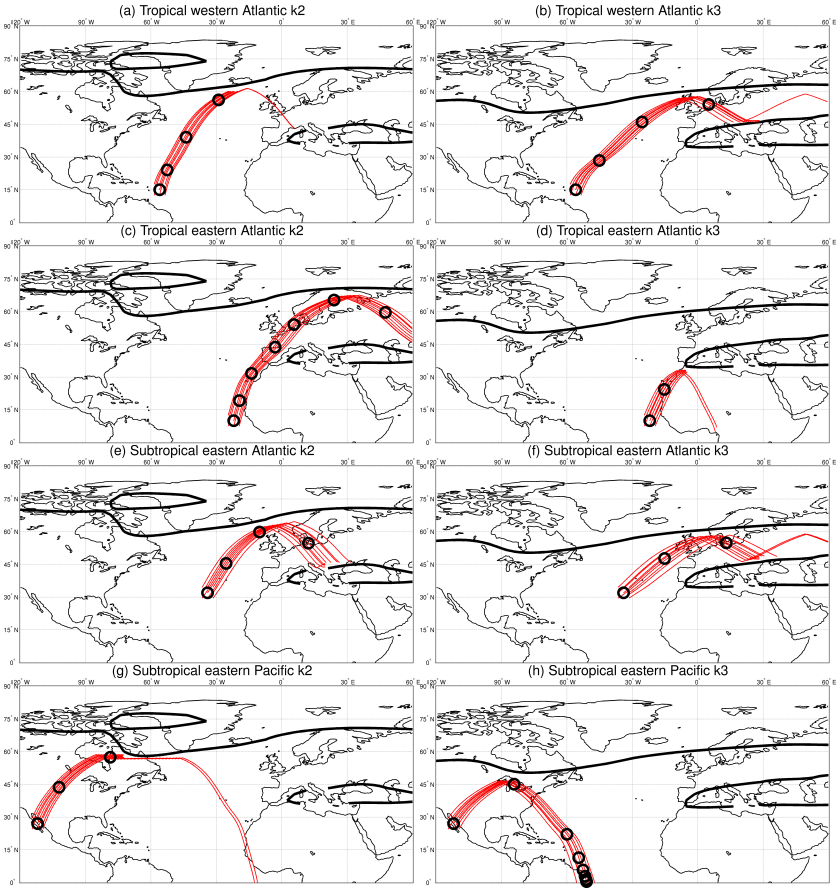



Figure 5.11: Ray tracings from the Atlantic and the Pacific. Ray tracing on 250 hPa climatological winds for zonal wavenumbers 2 (left) and 3 (right), initiated from (a,b) tropical western Atlantic, (c,d) tropical eastern Atlantic, (e,f) subtropical eastern Atlantic and (g,h) subtropical eastern Pacific. For each wavenumber traced, the corresponding stationary wavenumber contour is in black. Each ensemble ray is in red, and black circles are superimposed daily on the central ray.

## 5.4 Baroclinic model experiments

### 5.4.1 Tropical Atlantic forcings

In this section, we present baroclinic model responses to tropical diabatic heating. Following from our conclusion with the barotropic model, we focus on the tropical Atlantic as a potential atmospheric driver of European precipitation events. From the diabatic heating observed with the European precipitation events (figure 5.4e), we pick out the region of diabatic cooling in the tropical Atlantic just north of the equator associated with reduced precipitation, to match one of the prominent regions in the observed diabatic forcing. Figure 5.12 shows the ideal-

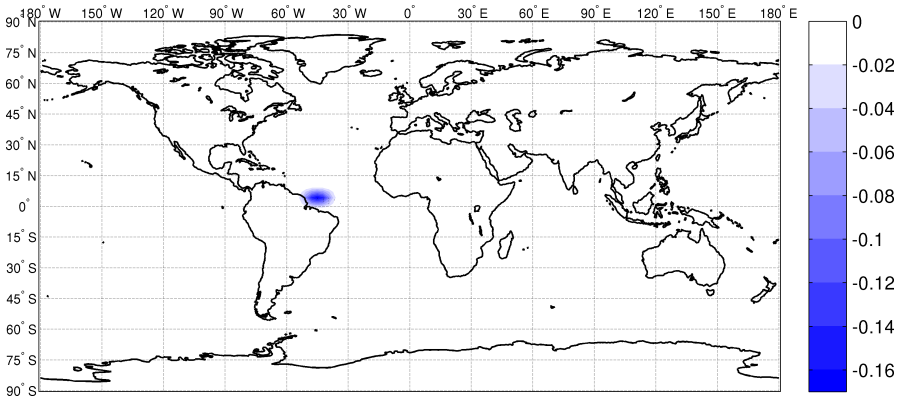



Figure 5.12: Diabatic cooling at 45°W 5°N ($\mathrm{K\,day^{-1}}$).

ized elliptical diabatic forcing in the model. We use the approximation mentioned in section 2.4 to convert the diabatic cooling amplitude from around -20 $\mathrm{Wm^{-2}}$ in the observation to -0.17 $\mathrm{K\,day^{-1}}$ in the model.

Figure 5.13 shows the responses to this forcing. On the 250 hPa level, a Rossby wave propagates from the tropical diabatic cooling region, with a low in the subtropical Atlantic. This branches into two waves. The first wave propagates along the Asian jet from northeastern Africa to southeast China. The second wave propagates into the higher latitudes, with a high in the central-eastern North Atlantic, a low across the UK and Iceland, and a high in northwestern Russia. This wave pattern shows some similarity to the observed (figure 5.4b), with low height near the south of the Aleutian Islands, high height near northern North America, low height near the UK, and high height near northwestern Russia. But it is not an exact match, since especially the wave response in the subtropical and central North Atlantic is not seen in the observed. Also, the model response is about ten times weaker than the observed. A possible reason for both of these is because we have only included one small region of diabatic forcing. There are horizontal differences between the total observed forcing and our single idealized forcing. Still, this idealized tropical Atlantic forcing experiment already shows promising results.

In the extratropics, the wave shows an equivalent barotropic structure (figure 5.13b). The Hovmöller diagram (figure 5.13c) shows eastward group propaga-

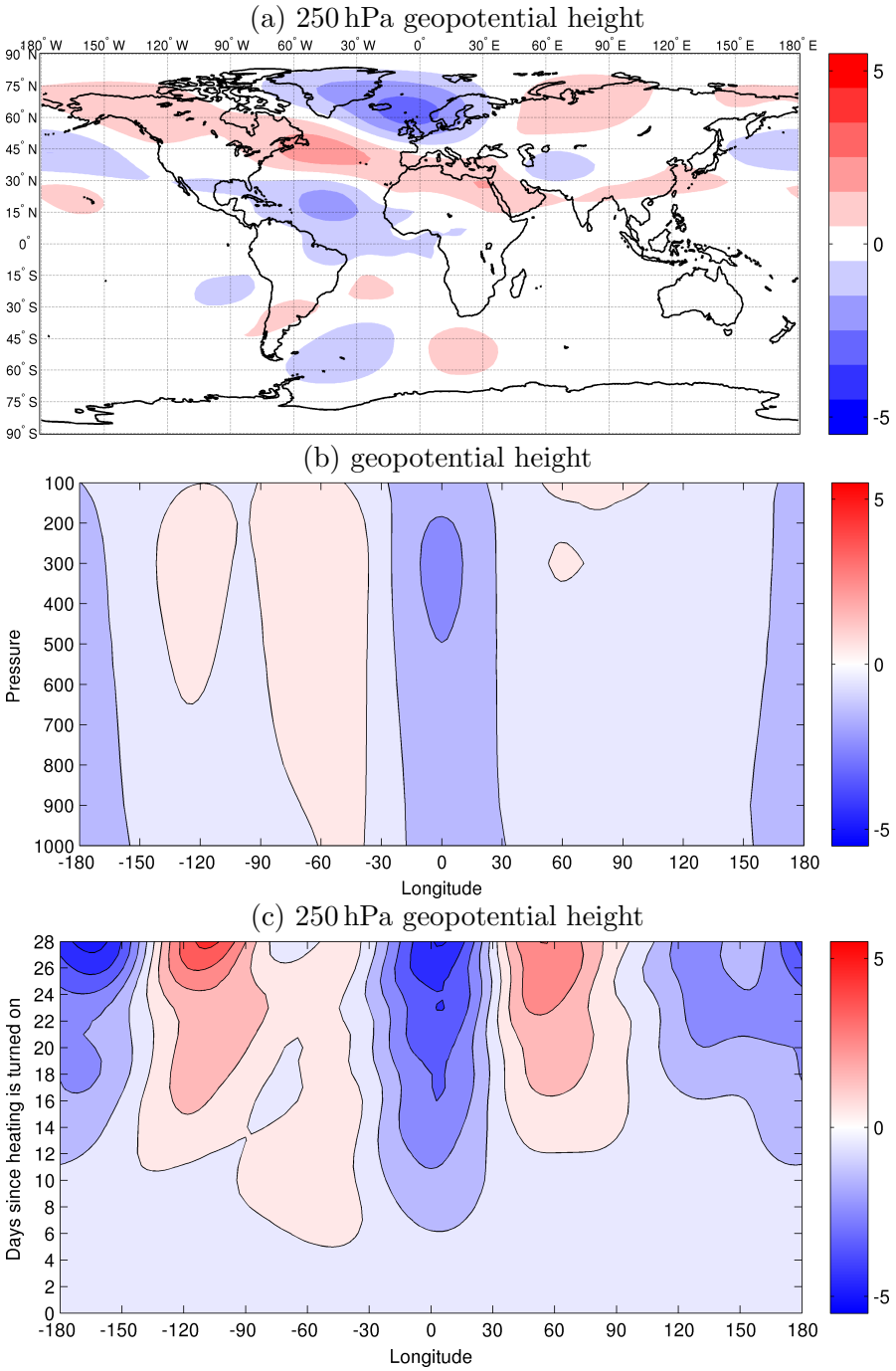


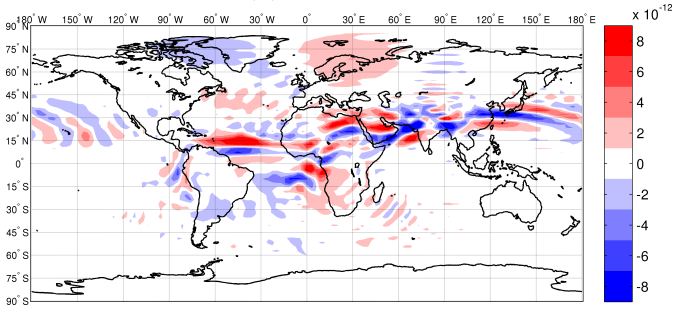

Figure 5.13: Model responses in geopotential height (m) to the cooling in figure 5.12, averaged between days 10 and 14, for (a) 250 hPa level, and (b) the vertical cross section. (c) Hovmöller diagram of 250 hPa geopotential height (m). Both (b) and (c) are averaged meridionally between 45°N and 60°N.

tion from the forcing longitude from day 5, which indicates the time it takes for the disturbance to first enter the extratropics from the tropics. By day 10, the wave has propagated circumglobally once. No eastward phase speed is observed within the integration period, suggesting baroclinic instability does not develop during the integration. Finally, the total atmospheric mass in the model is well conserved in this experiment (figure A.15), confirming our run is stable.

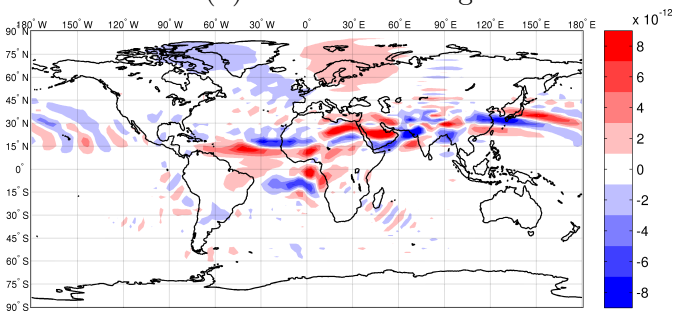
Whereas the RWS in the barotropic model is specified, the baroclinic model generates the RWS from the diabatic forcing. Figures 5.14a to 5.14c show the RWS response averaged between days 10 to 14, calculated from the zonal and meridional wind responses. In the subtropics (15°N to 30°N), vortex stretching dominates the total RWS. In the tropical Atlantic, although vortex stretching is still present, the amplitude of vorticity advection is larger. Physically, the diabatic cooling generates large convergences at the upper level (figure 5.14d) above the forcing maximum at 400 hPa (section 2.4). The associated anomalous convergent wind acts on the climatological gradient of relative vorticity and generates the vorticity advection term (equation 2.17). This meridionally banded structure in vorticity advection between 60°W and 30°W, with positive source along 15°N and negative source along 7°N, which also dominates in the total RWS, agrees well with the positive source observed (figure 5.4c), and also partly agrees with the negative source near 7°N 30°W. These two regions also include the two same-sign forcing regions in the tropical Atlantic from the barotropic model patch experiment (figure 5.6e). In the barotropic model patch experiments, we have concluded that combining both of these sources (figure 5.8e) gives a more similar wave pattern together to the observed than from each source individually (figures 5.8a,b). This agrees with our baroclinic model result, which suggests that both of these sources are generated together from the same region of cooling.

However, another same-sign forcing region identified in the subtropical Atlantic (at 326°E 32°N in figure 5.6e) is not present in the baroclinic model RWS, although there is a similarly negative RWS just to the southwest of this region. It is possible that this observed negative region is generated by other regions of diabatic forcing

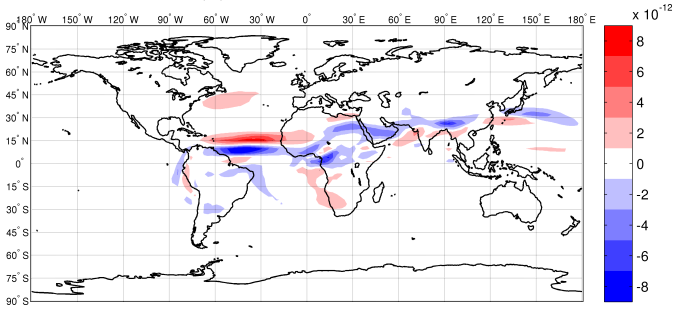
(a) Total RWS




(b) Vortex stretching




(c) Vorticity advection




(d) Divergence

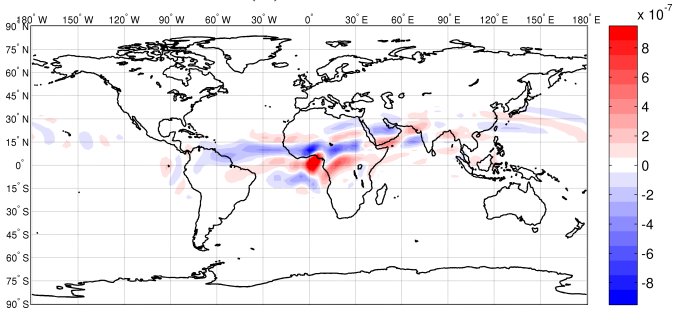



Figure 5.14: 250 hPa model responses, averaged between days 10 and 14, in (a) total Rossby wave source ($s^{-2}$), (b) vortex stretching ($s^{-2}$), (c) vorticity advection ($s^{-2}$), (d) divergence ($s^{-1}$), to the diabatic forcing in figure 5.12 .

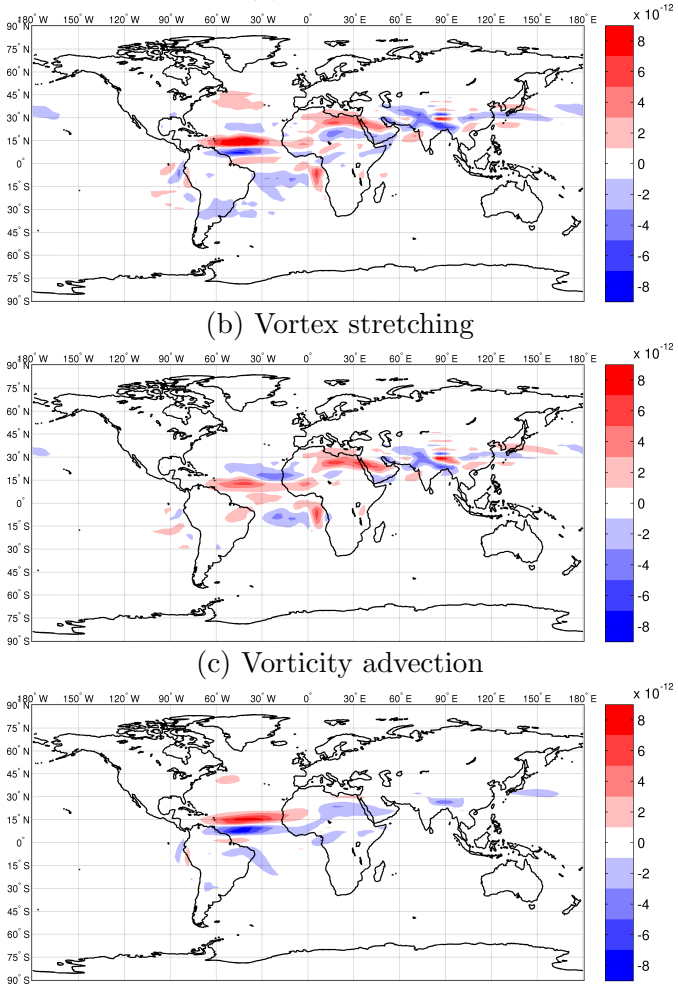
outside of our idealized tropical Atlantic cooling. It can also be a consequence of the wave itself, since it is in the subtropics and close to the extratropics. To further investigate, we look at the RWS response at an earlier period. Figure 5.15 shows the RWS response averaged between days 5 to 9. The pattern is similar to that averaged between days 10 to 14, showing that the development of the extratropical wave does not significantly modify the RWS. Our model diabatic forcing has been scaled down and should not include any non-linear terms between perturbation-perturbation interactions. We conclude that the observed RWS at 326°E 32°N is at least not a linear consequence of the wave. It still can be a non-linear consequence of the wave, which is not captured by our linear experiment.

Finally, the RWS shows some small-scale ripple-like structures, for example near 30°N 90°E and near 30°S 60°E. We suspect these to be associated with the nearby orographic features, namely the Himalayas in northern India and the Drakensbery mountain range in South Africa. For example, in the past we have seen similar ripples when examining the RWS on sigma 0.2 level from reanalysis. These RWS ripples seen in our responses could be artefacts of our model, since we have applied a very strong constraint on the inverse initial tendency (section 2.4).

We also perform an experiment using the region of diabatic heating just south of the equator. Figure 5.16 shows the forcing and the response. As this diabatic heating is close to the previous region of diabatic cooling and is opposite in sign, the response is a similar wave but with the opposite phase. However, the two waves do not cancel out completely (figure 5.17), especially the low over the UK and Iceland, because the region of diabatic heating is narrower meridionally and also has a smaller absolute amplitude on average spatially. A similar conclusion can also be drawn for the RWS and divergence associated with this diabatic heating (figure A.16).

To summarize, the idealized diabatic cooling in the tropical Atlantic from observation produces an extratropical wave pattern similar to the observed. It also produces Rossby wave sources in the tropical eastern Atlantic and tropical western Atlantic in line with observation and with the barotropic model patch

(a) Total RWS




(b) Vortex stretching




(c) Vorticity advection




Figure 5.15: Similar to figure 5.14. 250 hPa model responses, averaged between days 5 and 9, in (a) total Rossby wave source ($s^{-2}$), (b) vortex stretching ($s^{-2}$), and (c) vorticity advection ($s^{-2}$), to the diabatic forcing in figure 5.12 .

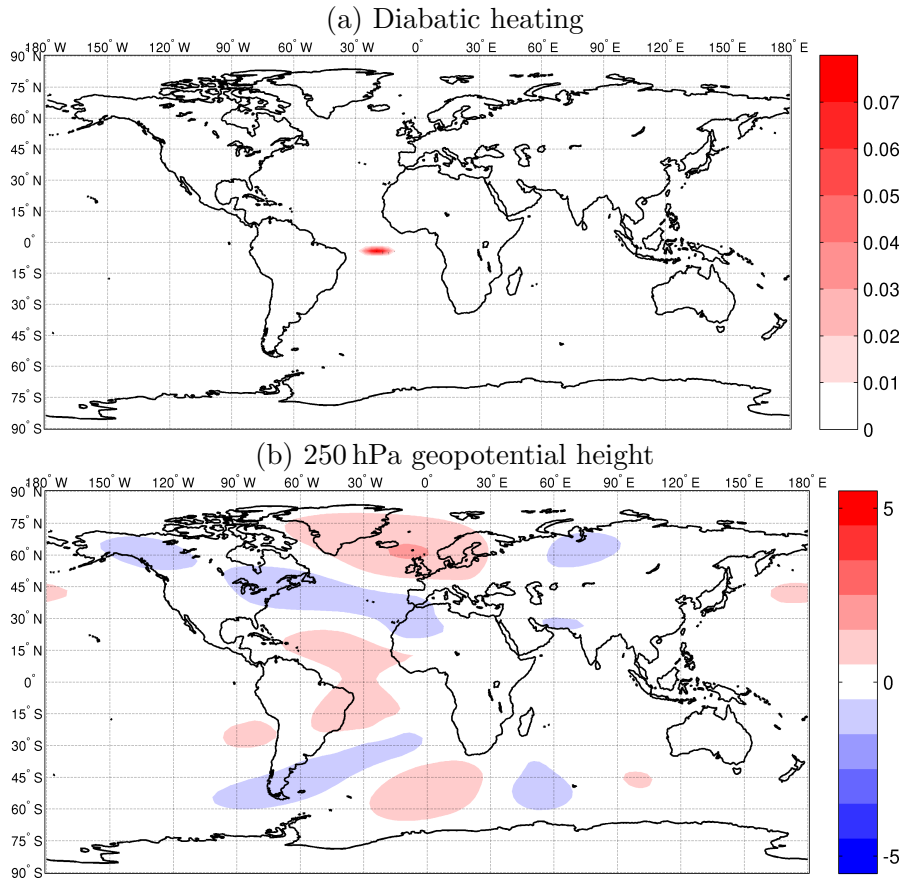



Figure 5.16: (a) Diabatic heating at 20°W 3°S (K day$^{-1}$). (b) 250 hPa geopotential height (m) response to this forcing, averaged between days 10 and 14.

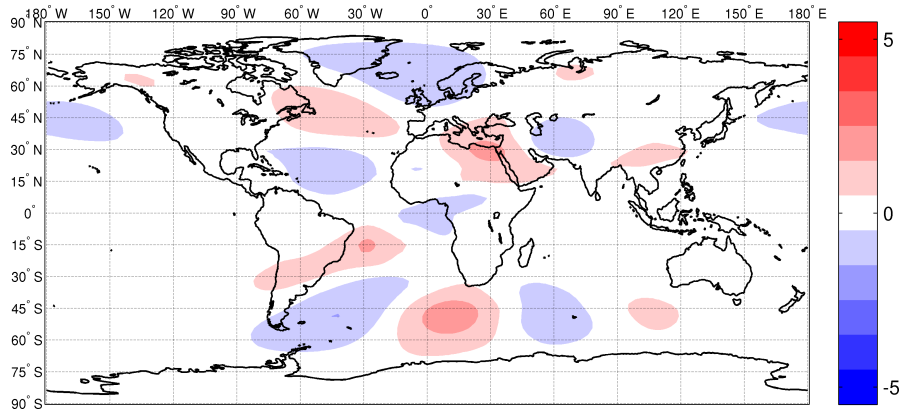



Figure 5.17: The sum of the 250 hPa geopotential height (m) responses to the diabatic cooling (figure 5.13a) and the diabatic heating (figure 5.16a) in the tropical Atlantic.

experiment results.

### 5.4.2 Forcings in other basins

In this section, we investigate the responses to the diabatic forcings in basins other than the tropical Atlantic. Figure 5.18a shows the idealized heating designed to match the observed anomalous heating in the Indian Ocean (figure 5.4e), associated with a strengthening of the ITCZ in this basin (figure 5.4d). The geopotential height response (figure 5.18b) is a wave propagating across southeast Asia and into the North Pacific, with a low across Japan and central Russia which is near the observed low in eastern Russia. It then splits into two waves, with one path propagating back into the tropics and the other path into Canada and eastern North America. Over the North Atlantic and European sector, the signal is very weak. The heating generates a negative source over northern India (figure 5.18c), which matches with the observation (figure 5.4c). It also matches with the same-sign barotropic model patch experiment result before the projection threshold is applied (figure 5.6c), but it is filtered out in figure 5.6e as having a weak projection onto the observed wave pattern. To summarize, this experiment suggests a minor contribution from the Indian Ocean in driving European precipitation events.

Figure 5.19a shows the idealized heating designed to match the anomalous heating in the tropical western Pacific (figure 5.4e), associated with a strengthening of the ITCZ in this basin (figure 5.4d). The geopotential height response (figure 5.19b) is a wave propagating into the North Pacific, with a low near the Aleutian Islands which is similar to the observed. While one wave then propagates into the tropics, another wave propagates across North America and into the North Atlantic-European sector. However, this does not match the observed pattern there. The generated RWS (figure 5.19c) also does not match well with the observed. Therefore, this experiment does not support the tropical western Pacific as a driver of European precipitation events.

Next, we present experiments for the tropical eastern Pacific. Figure 5.20a shows the idealized heating designed to match the anomalous heating in the trop-

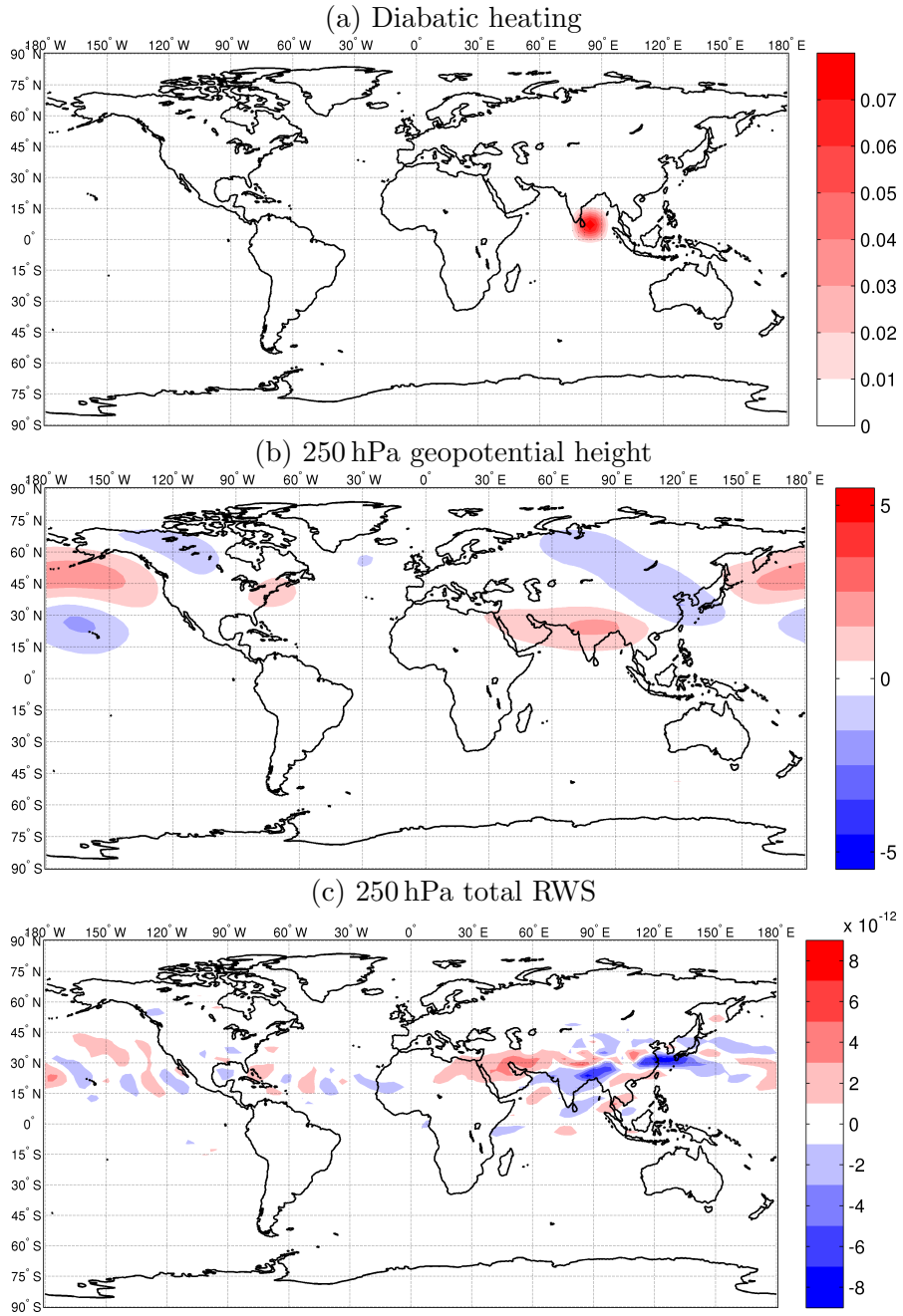



Figure 5.18: (a) Diabatic heating at 85°E 7°N ($\mathrm{K\,day^{-1}}$). The responses on 250 hPa to this diabatic forcing, averaged between days 10 and 14, in (b) geopotential height (m) and (c) total RWS ($\mathrm{s^{-2}}$).

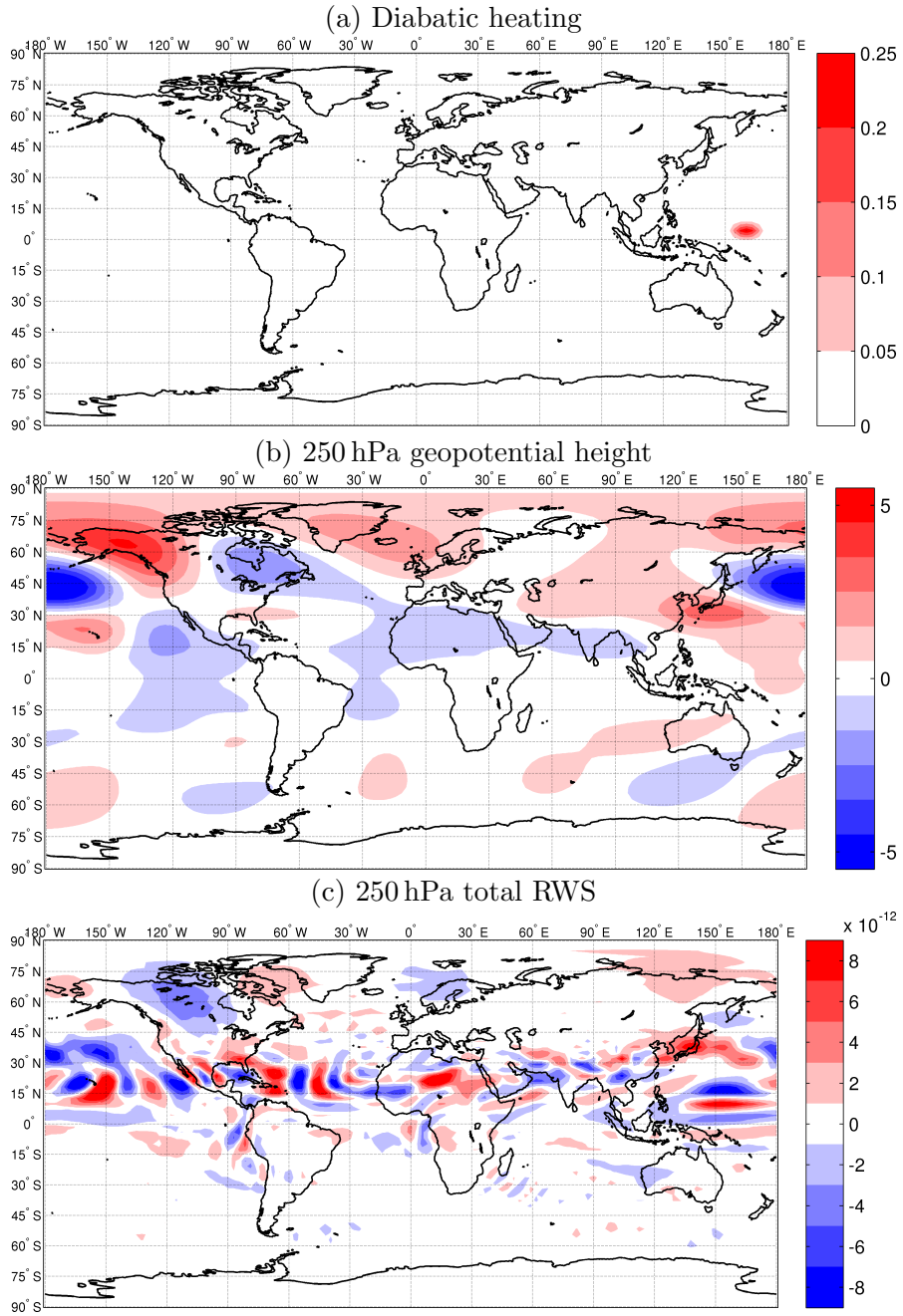



Figure 5.19: (a) Diabatic heating at 160°E 3°N (K day$^{-1}$). The responses on 250 hPa to this diabatic forcing, averaged between days 10 and 14, in (b) geopotential height (m) and (c) total RWS (s$^{-2}$).

ical eastern Pacific in figure 5.4e, associated with a strengthening of the ITCZ in this basin (figure 5.4d). The geopotential height response (figure 5.20b) is a wave propagating into the North Pacific, with a low near the Aleutian Islands which is similar to the observed, a high over northeastern North America, a low over Iceland, and a high near the Mediterranean Sea. Over the North Atlantic-European sector, the response is similar to the observed but with the low over Iceland and the high near the Mediterranean Sea shifted westward by about 30°. When the heating is moved eastward by 30° (figure 5.21a), the response matches better with the observation over the North Atlantic-European sector. The heating generates positive RWS over the Gulf of California (figure 5.21c). This matches with the observation (figure 5.4c) and with the same-sign barotropic model patch experiment result with strong projection (figure 5.6e). Therefore, in addition to the tropical Atlantic cooling discussed in section 5.4.1, baroclinic experiments also suggest the tropical eastern Pacific heating as a driver of European precipitation events.

Finally, we have only looked at several idealized forcings in our baroclinic experiments so far. But these already provided promising results for the tropical Atlantic and tropical eastern Pacific. For a more comprehensive analysis perhaps in the future, we can systematically test all the different forcings, as we have done with the barotropic model patch experiments.

## 5.5 Chapter discussion and summary

Figure 5.22 shows a summary schematic linking the important features of tropical forcings and extratropical responses during European precipitation events. From observations, we have identified a wave-like pattern associated with European precipitation events (figure 5.4b), which has limited influence from the North Atlantic leading modes of variability, namely the North Atlantic Oscillation and the East Atlantic pattern. We have identified a southward shift in the tropical Atlantic precipitation and a strengthening of the tropical eastern Pacific precipitation (figure 5.4d). The result is linear with respect to the precipitation and drought events, allowing us to investigate both types of events in a linear framework.

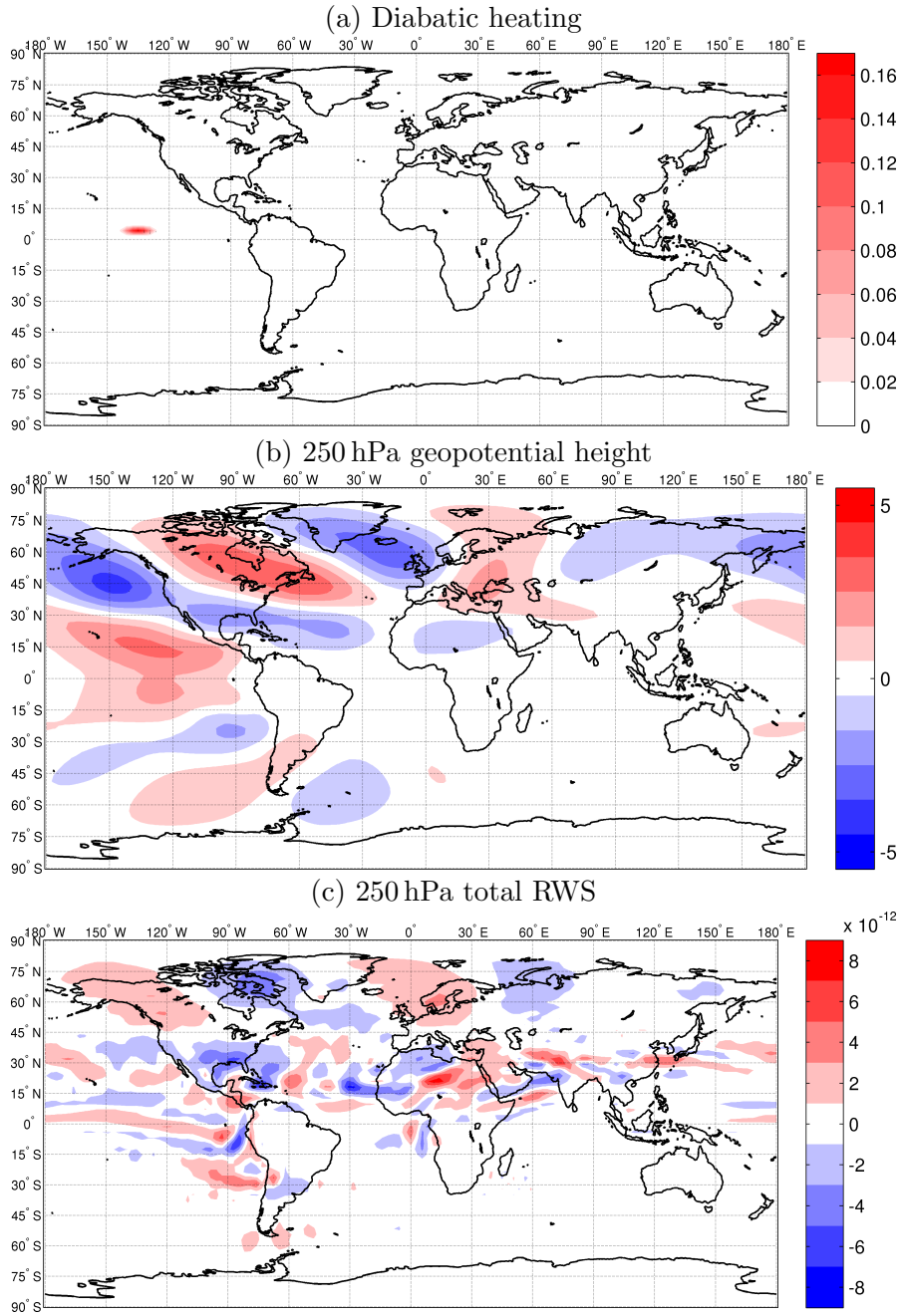



Figure 5.20: (a) Diabatic heating at 135°W 5°N (K day$^{-1}$). The responses on 250 hPa to this diabatic forcing, averaged between days 10 and 14, in (b) geopotential height (m) and (c) total RWS (s$^{-2}$).

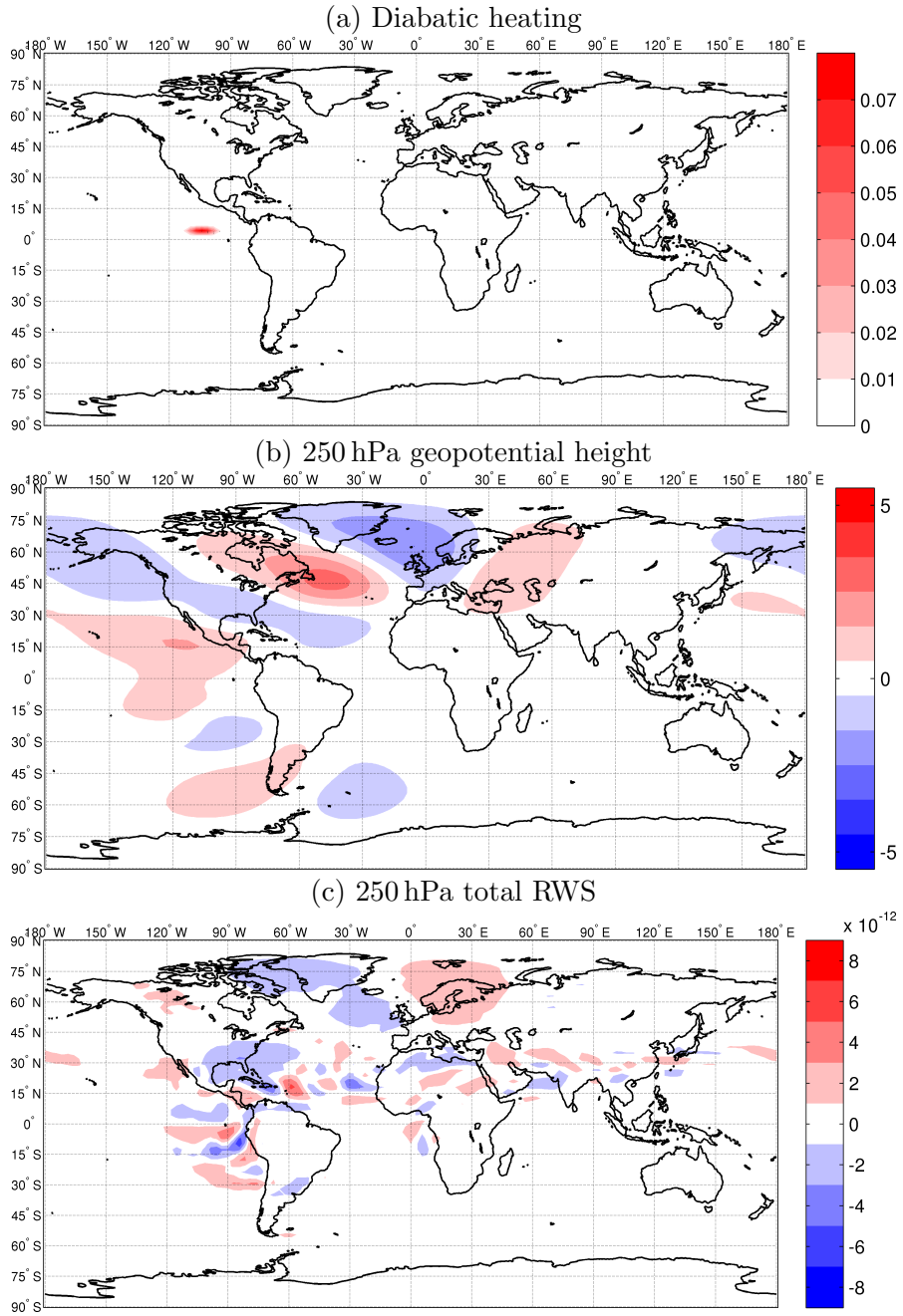



Figure 5.21: (a) Diabatic heating at 105°W 3°N ($\mathrm{K\,day^{-1}}$). The responses on 250 hPa to this diabatic forcing, averaged between days 10 and 14, in (b) geopotential height (m) and (c) total RWS ($\mathrm{s^{-2}}$).

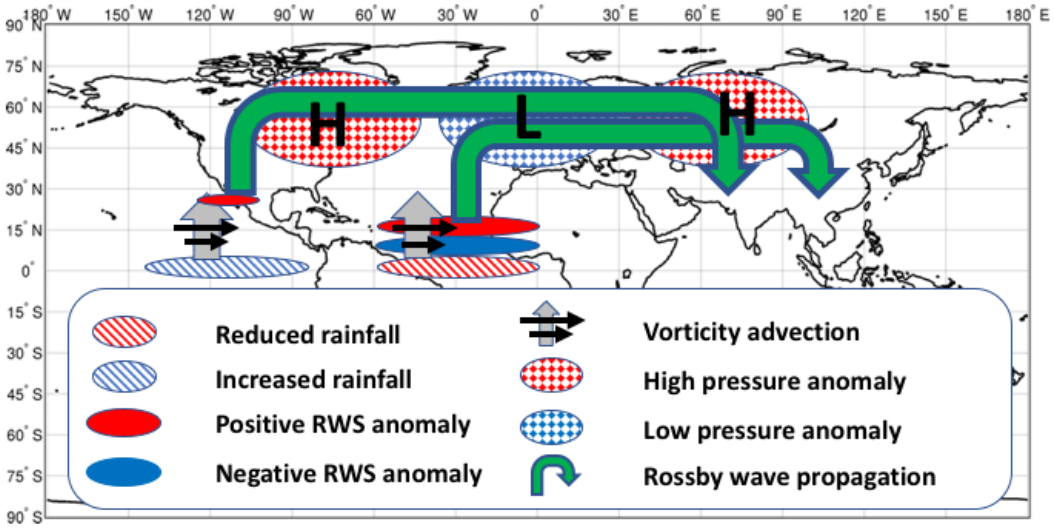



Figure 5.22: Summary schematic linking the important features of tropical forcings and extratropical responses during European precipitation events.

Barotropic model patch experiment picks out several regions of the observed Rossby wave source that can force the observed extratropical pattern (figure 5.6e). These include the positive source in the tropical western Atlantic, the negative source in the tropical eastern Atlantic, the negative source in the subtropical eastern Atlantic and the positive source in the subtropical eastern Pacific (figure 5.8). The zonal wavenumbers 2 and 3 are particularly important (figure 5.9), and this is further supported by ray tracing (figure 5.11).

Baroclinic model experiments show that the cooling in the tropical Atlantic just north of the equator associated with the southward shift in the climatological precipitation generates the positive and negative Rossby wave sources in the tropical Atlantic, mainly through vorticity advection (figure 5.14c). These tropical sources are not affected by the linear development of the extratropical wave (figures 5.14a and 5.15a). It drives a wave with a high over northeastern North America, a low over the UK and a high over northwestern Asia. The heating in the tropical eastern Pacific associated with the strengthening of the climatological precipitation generates the positive source in the subtropical eastern Pacific (figure 5.21c). The wave it drives also contributes to the low over the UK and the

high over northwestern Asia.

Rossby wave propagation is affected by both the forcing and the basic state on which it propagates. In this chapter, we have only looked at the effect of the anomalous tropical forcings. The basic state is also important because the zonal winds affect the waveguides. For example, in chapter 4 we found that a correct representation of the North Pacific tropospheric jet is needed to capture ENSO teleconnections through wave propagations. Associated with our European precipitation events is a North Atlantic jet shift (figure 5.4a). When we repeat the ray tracings with the regressed wind anomalies included in the basic state, we find only subtle differences in the waveguides and the rays traced. Ray tracing results using the basic state composited for the twenty wettest years are also similar. We therefore conclude that the basic state anomalies are less important than the tropical forcing anomalies during these European precipitation events.

We have been focusing on the mean of the wettest and the mean of the driest events. To demonstrate the teleconnection more directly, we present a closer analysis of specific wettest and driest years, and address what fraction of these years were significantly influenced by our tropical forcings.

Since the identified tropical anomalies include part of the tropical Pacific ENSO region, we first investigate the contribution of ENSO to our European precipitation events. Figure 5.23a shows the GPCP precipitation regressed onto the standardized Niño-3.4 index. It shows an increase in precipitation in the tropical central to eastern Pacific, and decreases in the tropical western Pacific and the tropical Atlantic. However, it has no precipitation signal in Europe. The correlation between Niño-3.4 and the European precipitation time series is 0.18 and is statistically insignificant at the 95% level (p=0.34), indicating ENSO has little association with our events. Next, we show the precipitation regressed onto the NAO (figure 5.23b). This is similar to figure 5.2b earlier, but here using GPCP global data for the period 1980 to 2010 instead of CRU land data. The tropical anomalies of the NAO are very similar to the opposite phase of the European precipitation tropical anomalies in figure 5.4d, which we reproduce in figure 5.23c. This is

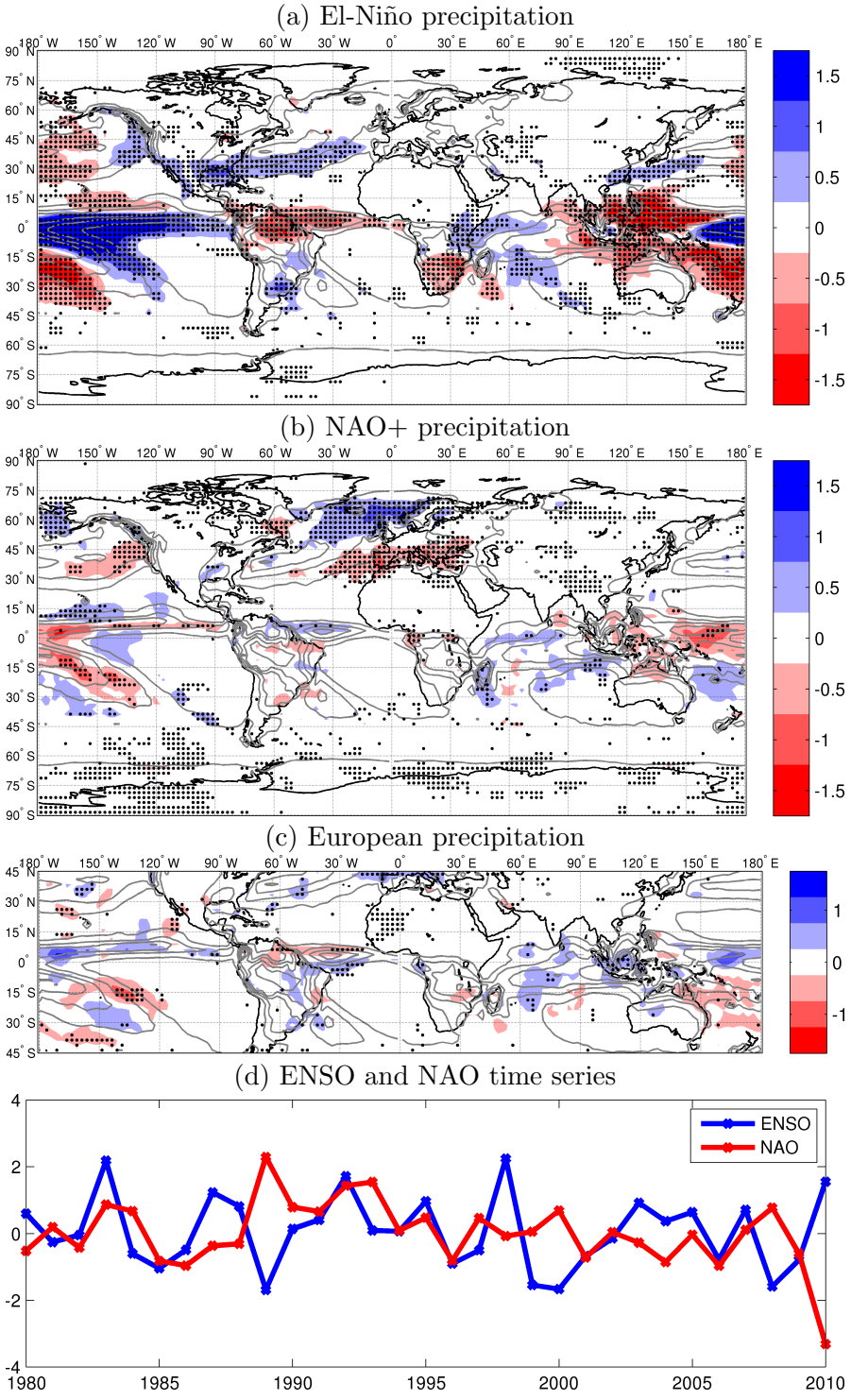



Figure 5.23: GPCP precipitation regressed onto the standardized (a) ENSO (b) NAO and (c) European precipitation time series, for 1980 to 2010. Hatching demonstrates a 95% significant linear regression relationship. (d) The time series of ENSO and NAO.

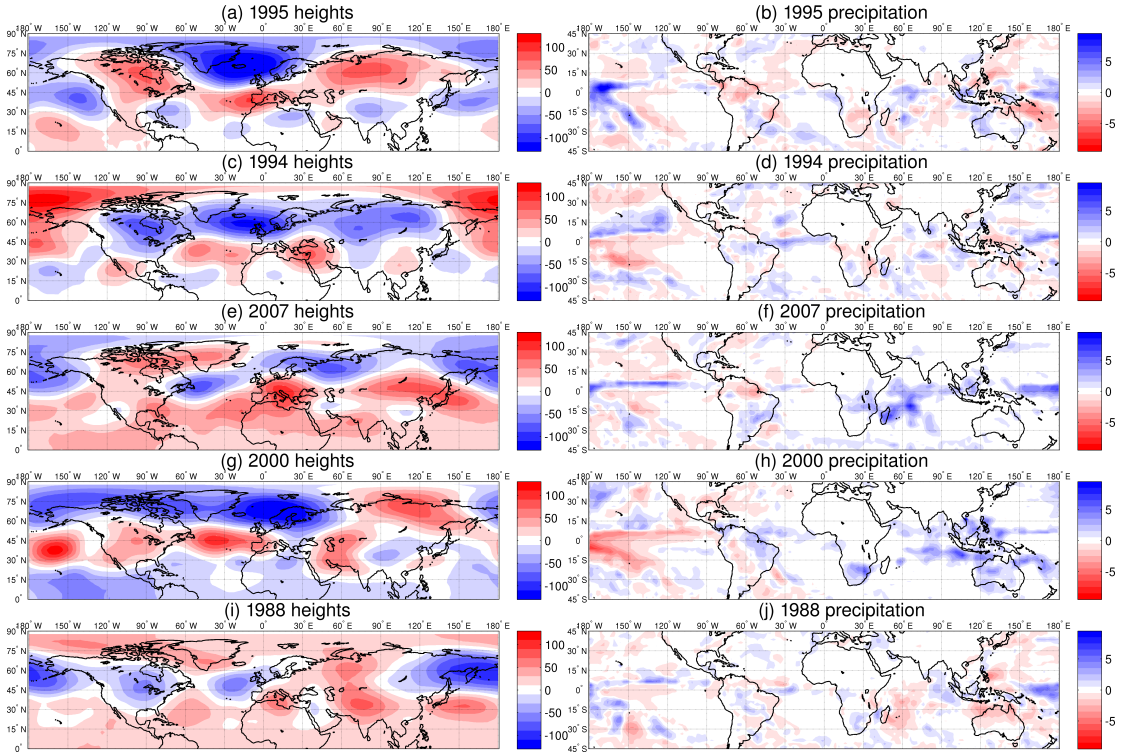



Figure 5.24: (Left) Geopotential height anomalies (m) and (right) tropical precipitation anomalies (mm day$^{-1}$) on 250 hPa for the five wettest years in our European region, in descending order with the wettest year on the top row.

consistent with the NAO correlating with European precipitation at -0.34 for the period 1980 to 2010, although it is marginally statistically insignificant (p=0.06). In particular, the tropical Atlantic and tropical eastern Pacific anomalies are statistically significant in both figures 5.23b and 5.23c. Therefore, the NAO has more association than ENSO with our events, although the NAO still does not fully capture the variability of our events. Finally, the correlation between ENSO and NAO is only -0.14 and is statistically insignificant (p=0.44).

Figure 5.24 shows the geopotential height anomalies and tropical precipitation anomalies for the five wettest winters between 1980 and 2010. The wettest year of 1995 exhibited both our tropical Atlantic and tropical eastern Pacific anomalies. Years 2007 and 1988 also exhibited both precipitation anomalies, while year 1994 exhibited the tropical Atlantic anomaly only. However, year 2000 exhibited anomalies of the opposite signs in both the tropical Atlantic and tropical eastern Pacific. This year had the second strongest La-Niña in this period (fig-

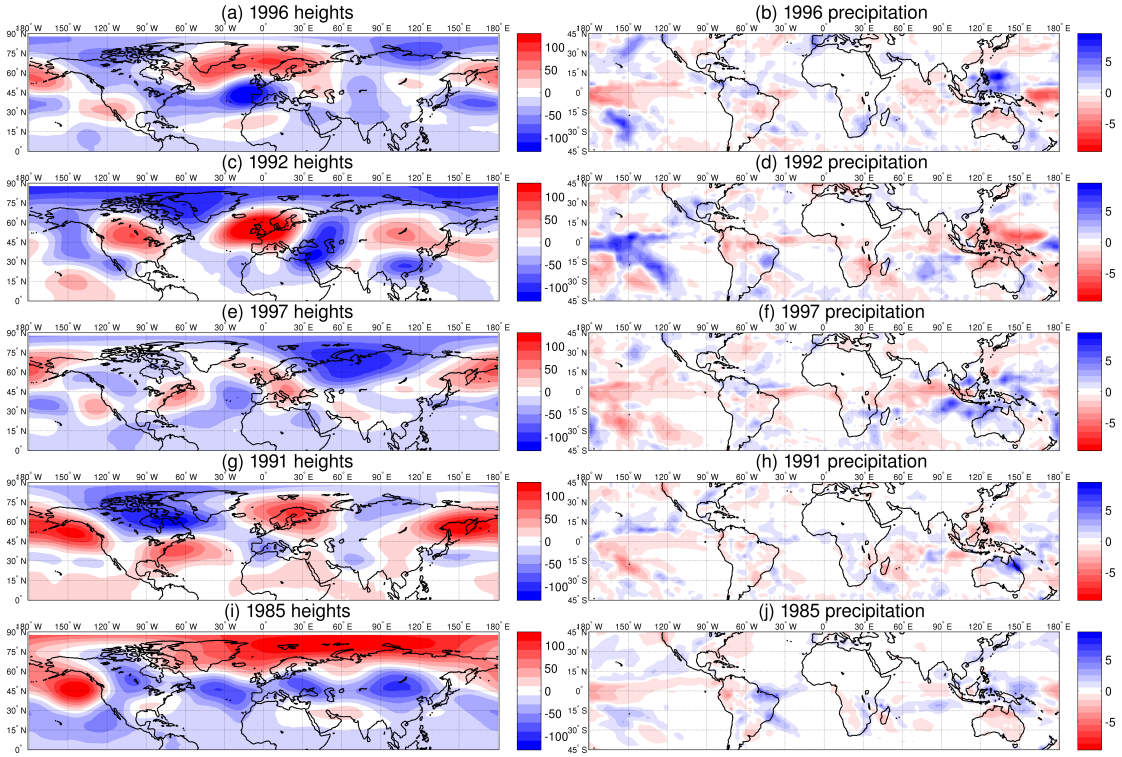



Figure 5.25: (Left) Geopotential height anomalies (m) and (right) tropical precipitation anomalies (mm day$^{-1}$) on 250 hPa for the five driest years in our European region, in descending order with the driest year on the top row.

ure 5.23d). Hardiman et al. (2019) showed that the dominant teleconnection pathway to the North Atlantic is stratospheric for strong La-Niña events. The height anomalies were also very zonal and different to the more wave-like observed mean. This is consistent with the signal propagating from the stratosphere into the troposphere being more zonal. Therefore, four out of the five wettest events were significantly influenced by our tropical forcings. The fraction is seven out of ten if we extend our analysis to the ten wettest events.

Figure 5.25 shows the anomalies for the five driest winters. All these years exhibited reduced precipitation in the tropical eastern Pacific except 1992, which had the third strongest El-Niño. The dominant pathway to the North Atlantic in strong El-Niño is through the troposphere (Toniazzo and Scaife, 2006; Hardiman et al., 2019), but the specific locations of the tropical forcings and the specific waves are different to ours. Therefore, the higher heights observed over the UK in 1992 were not forced from our tropical forcings. In the tropical Atlantic, all years exhibited a northward shift from the climatology except 1985, which only showed a strengthening of the climatology. This year had the fifth strongest La-Niña. The more zonal height anomalies in 1985 is again consistent with a dominant stratospheric pathway in strong La-Niña years. Therefore, three out of the five driest events were significantly influenced by our tropical forcings. The fraction is five out of ten if we extend our analysis to the ten driest events.

To summarize, our closer analysis of individual years reveals that about 60% of the European precipitation and drought events were significantly influenced by our tropical forcings. While our results show more connection to the NAO than to ENSO, the NAO cannot fully capture the variability. Occasional large ENSO events can also lead to European precipitation and drought events through different forcings and mechanisms than ours.

To discuss our results in a wider context of climate modelling, although we have not looked at our teleconnections in seasonal hindcasts, we comment on the prediction of our tropical precipitation in the seasonal forecast models. Using the Met Office GloSea5 prediction system, Scaife et al. (2017, figure 2) showed

skilful prediction in seasonal tropical rainfall. Correlations between predicted and observed rainfall showed correlation skill in excess of 0.6 in many regions, and even exceeded 0.8 in the tropical Pacific due to the high predictability of ENSO coming from the slowly varying large-scale ocean temperatures. Although the prediction was not as skilful in the tropical Atlantic, the correlation was still around 0.6. A follow-up study looking at fourteen climate forecast systems showed similar prediction skills too (Scaife et al., 2019, figure 2). However, the teleconnections between different tropical ocean basins due to ENSO appeared to be responsible for much of the prediction skill. As our European precipitation events had little association with ENSO, without actually looking at the seasonal hindcasts it is not clear how well our tropical-extratropical teleconnections for these events are represented in seasonal forecast systems. This can be an interesting topic for future work.

# Chapter 6

# Conclusion

## 6.1 Chapter summaries

### 6.1.1 Ch1: Motivation

Atmospheric dynamics are important in the seasonal timescale, and seasonal forecasts for Europe remains especially challenging. Large uncertainties in climate projections can be reduced through improving the representation of atmospheric dynamics in climate models. As the projection of future climate response onto the modes of natural variability can be strong, further understanding of the errors in present-day model dynamics can reduce the dynamical uncertainty in future projections. Therefore, we have motivations from both seasonal forecasts and from climate projections to study atmospheric dynamics in more detail, for example the tropical-extratropical teleconnections.

### 6.1.2 Ch2: Methods

Firstly, we introduce the statistical tool of maximum covariance analysis. We then introduced the theories and applications of ray tracing, barotropic model and baroclinic model for stationary Rossby wave propagation experiments. We reproduce some literature results to illustrate the model applications and to show that our models are properly set up. Finally, we introduce the diagnostic tools of the Rossby wave activity flux and the blocking index.

### 6.1.3 Ch3: Tropical-extratropical teleconnections

We apply maximum covariance analysis on geophysical data to detect patterns of covariability. We investigate the teleconnection patterns between the whole tropics and the whole northern hemisphere extratropics, on both seasonal and daily timescales.

In the seasonal timescale analysis, the leading mode of covariability is associated with the El-Niño Southern Oscillation. The second mode of covariability is associated with the North Atlantic Oscillation. We find that these patterns are not sensitive to the exact regions chosen, suggesting that they are capturing hemispheric large-scale patterns. They are also not sensitive to choosing a different geopotential height level, suggesting an equivalent barotropic structure. And they are not too sensitive to whether the data are standardized or not, before the computation of the maximum covariance analysis.

In the daily timescale analysis, the El-Niño Southern Oscillation pattern remains the leading mode when all years are used, and are not sensitive to lead-lag. We show that this is in agreement with the El-Niño Southern Oscillation having larger interannual variability than intraseasonal variability. When only the years with neutral El-Niño Southern Oscillation index are used and with the tropics leading the extratropics by 14 days, the leading extratropical mode becomes the North Atlantic Oscillation, and the leading tropical mode resembles the Madden-Julian Oscillation. This result is sensitive to the lead, suggesting a delayed link between the tropics and the extratropics with a timescale consistent with Rossby wave propagation.

We further investigate whether such teleconnection is represented in a climate model. Although the leading tropical pattern in the climate model is similar to the El-Niño Southern Oscillation tropical pattern in reanalysis, we find large areas of statistically significant differences in the North Pacific and North America, between the climate model extratropical pattern and that of the reanalysis. This suggests that the climate model is not fully capturing the El-Niño Southern Oscillation extratropical teleconnection, especially over the North Pacific and North

America.

### 6.1.4 Ch4: ENSO experiments

This chapter follows up on explaining the differences in ENSO extratropical teleconnection, especially over the North Pacific and North America, between reanalysis and the climate model MOGC3. A strong North Pacific jet bias exists in the MOGC3 climatology. Ray tracing shows that this jet bias affects the propagation of stationary Rossby waves from the tropical Pacific into the North Pacific, with largest effects on zonal wavenumber 2 and 3 waves.

This motivates us to use a barotropic model linearized about the climatological basic state, to study the sensitivity of stationary Rossby wave propagation on the two different basic states. The largest differences in the response are in the North Pacific and North America, and agree with the MCA differences. Fourier analysis shows that the difference is mainly a reduction in zonal wavenumber 2 and 3 waves in the mid-latitude, in agreement with ray tracing. Finally, the climatological tropical Rossby wave source bias in MOGC3 can explain some of the North Pacific jet bias.

We also use a baroclinic model to study the wave propagation. Using the reanalysis basic state, the extratropical response to tropical diabatic heating in the baroclinic model is very similar to the patterns from the barotropic model and from the MCA. The diabatic forcing in the tropical eastern Pacific dominates the extratropical response when compared to a forcing in the Maritime Continent. Although the diabatic forcing is local, it generates Rossby wave sources almost circumglobally.

Using the MOGC3 basic state, the baroclinic model response matches better than the barotropic model response to the MCA. This shows the importance of the vertical structure in more realistically capturing wave propagations on the MOGC3 basic state. The difference between the responses on the two basic states matches with the difference in the MCA patterns between reanalysis and MOGC3, confirming the important effect of the jet bias on wave propagation. Our finding

may also contribute to resolving the signal-to-noise paradox in some climate predictions.

### 6.1.5 Ch5: Atmospheric drivers of European drought events

We turn our focus to Europe, and investigate the tropical contributions in driving European precipitation and drought events on the seasonal timescale. We focus on a European region that is only weakly correlated to the NAO, and identify a more wave-like pattern that may be forced from the tropics. Associate with European precipitation events, we identify a southward shift in tropical Atlantic precipitation and a strengthening of tropical eastern Pacific precipitation, which may be the sources of the extratropical wave anomaly. The result is linear with respect to the precipitation and drought events, allowing us to investigate both types of events in a linear framework.

Using barotropic patch experiments, among all the observed Rossby wave source anomalies, we isolate source anomalies in the tropical Atlantic, subtropical Atlantic and subtropical Pacific that can drive waves similar to the observation. Fourier analysis of the responses from these tropical sources shows the importance of zonal wavenumbers 2 and 3. These wavenumbers agree with ray tracing results from the tropical Atlantic and Pacific.

Using a baroclinic model, we show that the cooling in the tropical Atlantic associated with the shifted tropical precipitation not only generates similar anomalous wave patterns to the observation, but also generates Rossby wave sources in the tropical Atlantic that match with those identified in the barotropic patch experiments. Heating in the tropical eastern Pacific associated with the strengthened tropical precipitation also generates the observed wave pattern, and generates the Rossby wave sources in the subtropical Pacific that match with the patch experiments. Looking at individual seasons, about 60% of our European precipitation and drought events are significantly affected by our tropical forcings.

## 6.2 On the usefulness of our methods

An advantage of the maximum covariance analysis is its straightforward application in looking for patterns of covariability between two data. A disadvantage is that the expansion coefficients associated with different modes are not guaranteed to be uncorrelated. Therefore, extra care is needed to compare any regression onto the expansion coefficient with the singular vector pattern, to see if they are similar. If not, the regression may be contaminated by the singular vector of another mode that correlates with this mode.

An advantage of ray tracing is its a-priori prediction from its close link to theory. It allows for quick investigations into the propagation of individual zonal wavenumber waves. It is also useful to compare the Fourier filtered signals from observations or from barotropic or baroclinic model to the results of ray tracing for each of the individual wavenumbers. A disadvantage is that ray tracing is based on many assumptions and is very simplified, and can result in unrealistic ray paths in some cases.

The barotropic model has the advantage of fewer assumptions than ray tracing. For example, it does not assume scale separation. It is also straightforward to use as there is only one equation. By only having to specify the basic state and forcings on one level, the barotropic model can already give realistic wave propagations. A disadvantage is the need to specify the Rossby wave source, which can be affected by the extratropical wave itself for example in observations. Another disadvantage is that it is not always possible to capture realistic wave propagating using one level. For example, the vertical structure of the basic state may be important.

The baroclinic model has the advantage of providing the vertical structure, which in some cases as we have shown can produce more realistic propagations than the barotropic model. It requires the specification of diabatic heating rather than the Rossby wave source, which although can still be affected by the extratropical response, suffers less from the extratropical influence than the Rossby wave source. A disadvantage is that there are more equations and parameter settings, which may complicate the interpretation of some results. The higher number of vertical

levels can also complicate the set up of some basic states. For example, we once had difficulty in setting up the MOGC3 basic state because the model stability was sensitive to the details of extrapolating pressure levels below orography. Finally, our baroclinic model for stationary waves does not provide any insight into the important interaction of the waves with mid-latitude transients,

## 6.3 Implications and future work

We begin by discussing the relevance of the Met Office climate model problem for other climate models. Through the Primavera project, we obtain 64-year-long free-running atmosphere-only and coupled runs of the ECMWF IFS model (Roberts et al., 2018). We look at the lower resolution IFS runs which have closer resolutions to the Met Office model than the higher resolution IFS runs. There are six lower resolution ensemble runs initialized from the same initial conditions, but the ensemble members differ in stochastic physics, with different seeds to the stochastically perturbed parametrization tendency scheme. Figure A.17 shows the DJF 250 hPa zonal wind biases. The ensemble mean for the coupled runs shows an equatorward shifted North Pacific jet bias of up to $7\,\mathrm{ms}^{-1}$. This may affect the ENSO extratropical teleconnections in this model. The atmosphere-only runs are forced by daily sea surface temperature and sea-ice concentration data, and the ensemble mean North Pacific bias for these runs is reduced. This is in agreement with our comparison of the Met Office coupled and atmosphere-only runs in section 4.3.3, further suggesting the equatorward shifted North Pacific jet bias is a coupled bias and the bias is also present in the ECMWF model.

The North Pacific jet bias is not limited to the Met Office model and the ECMWF model. In the CMIP5 historical runs, the North Pacific jet annual mean latitude shows large differences across models (Barnes and Polvani, 2013, table 1). The model latitudes range from 38.9°N to 45.9°N with the latitude from reanalysis at 42.5°N (Barnes and Polvani, 2013, figure 2c). Although this study focuses on the annual mean rather than DJF, it shows that the North Pacific jet biases in climate models are not limited to shifting equatorward like in the Met Office and

ECMWF models, but can shift poleward in other models. It further shows that jet biases in climate models are not limited to the North Pacific, and are present in the North Atlantic and the Southern Hemisphere. Focusing on the Southern Hemisphere in CMIP5 runs, Bracegirdle et al. (2013) analyzed atmosphere-only and coupled runs and found that 28% of the zonal mean jet latitude bias came from coupling of the ocean and ice models to the atmosphere, quantifying the contribution of the coupling to jet biases. To summarize, coupled jet biases are quite common across different models and different basins. Our results for the Met Office model may therefore have wider implications than just for the Met Office model.

To discuss the implications of our results in seasonal prediction, although there is not enough time for the coupled bias to develop in seasonal forecasts, there are increasing interests in 1 to 2 year forecasts. If the timescale of the coupled jet bias development is shorter than 1 to 2 years, our ENSO results may have implications for these forecasts. Meanwhile, our results on the tropical drivers of European precipitation and drought events can be very useful to improving seasonal forecast models. The models can be assessed on how well they predict our specific locations of tropical precipitation in the tropical Atlantic and tropical eastern Pacific. and on how well they capture the extratropical wave response over Europe.

to see if there is .

This thesis already opens up some future work. Firstly, given the success of the barotropic patch experiments in helping us identify potential tropical drivers that are consistent between observations and the idealized models, baroclinic patch experiments can be carried out to make our analysis more comprehensive. Secondly, we can extend the idealized nature of the current baroclinic model diabatic forcing, by including more realistic horizontal and vertical heating profiles. Thirdly, so far we have only been using the climatology as the basic state. Individual extreme seasons however may show a zonal mean anomaly. Assuming scale separation, we can include the zonal mean anomaly from some extreme seasons in the basic state, and compare with our current result with the climatological basic state. This can

assess whether the seasonal zonal mean anomaly is important in affecting wave propagation. Lastly, although our idealized models suggest links from the tropics to European precipitation and drought events, these links are not very strong in observations. It is possible that in reality there is much more noise and also other pathways to such events, for example through the stratosphere. More complex models can be used to further test our links.

Finally, we can also look at the summertime. One motivation is that recent studies like Petoukhov et al. (2013) have linked northern hemisphere summer weather extremes to the quasi-resonance between transient synoptic waves and the stationary planetary waves. When free synoptic waves are latitudinally trapped within the mid-latitude waveguides, the usually weak responses of these waves to quasi-stationary thermal and orographic sources and sinks may be strongly amplified through quasi-resonance. Our model set up with an imposed basic state can help test the sensitivity of the trapped waves to the basic state, although it is not immediately clear how our stationary wave model can be modified to allow for transient wave investigations.

# Appendix A

# Additional figures

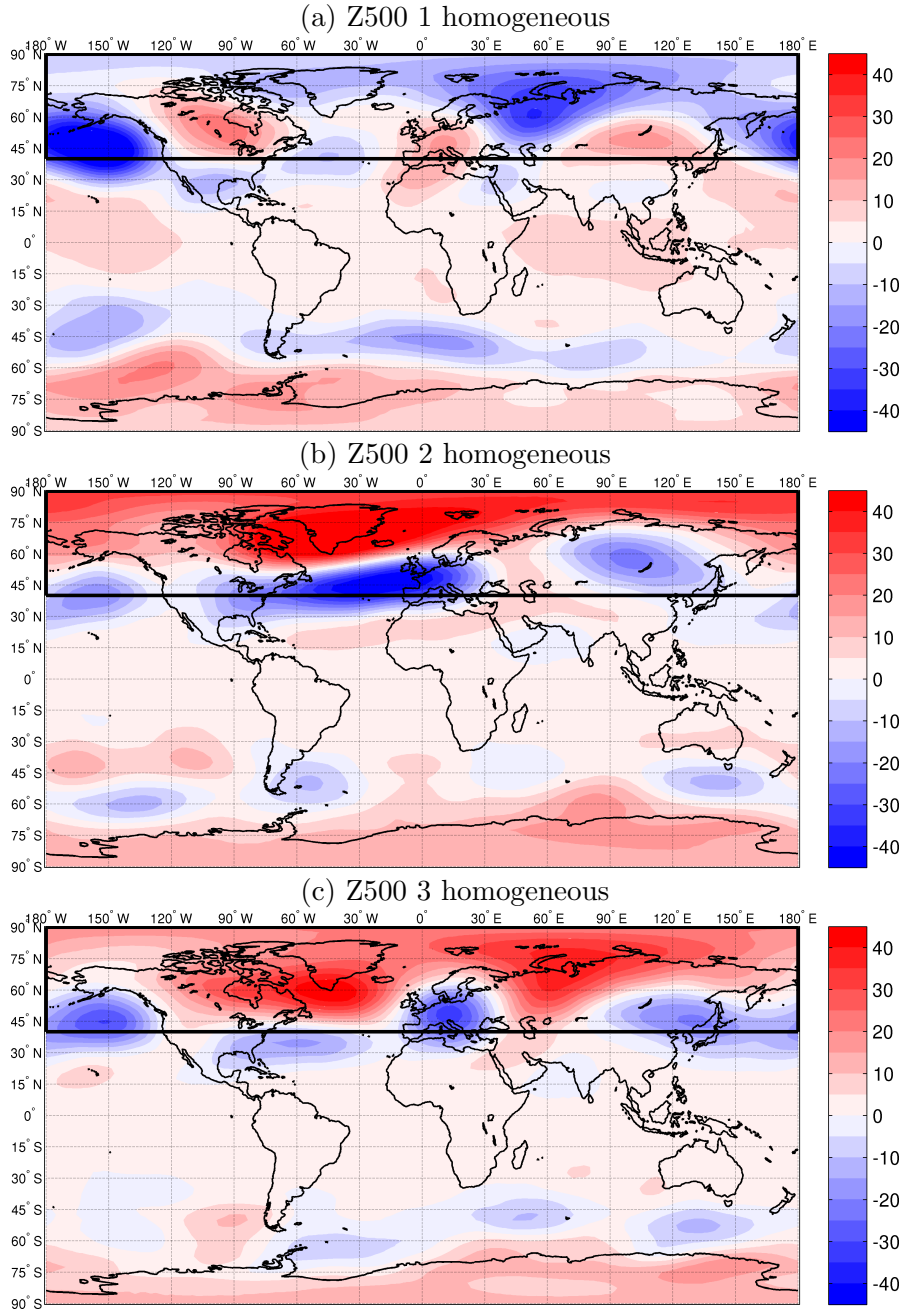



Figure A.1: Supplement to figure 3.1. First three MCA modes, with northern hemispheric extratropical NCEP2 Z500 homogeneously regressed (m). The black box marks the MCA region.

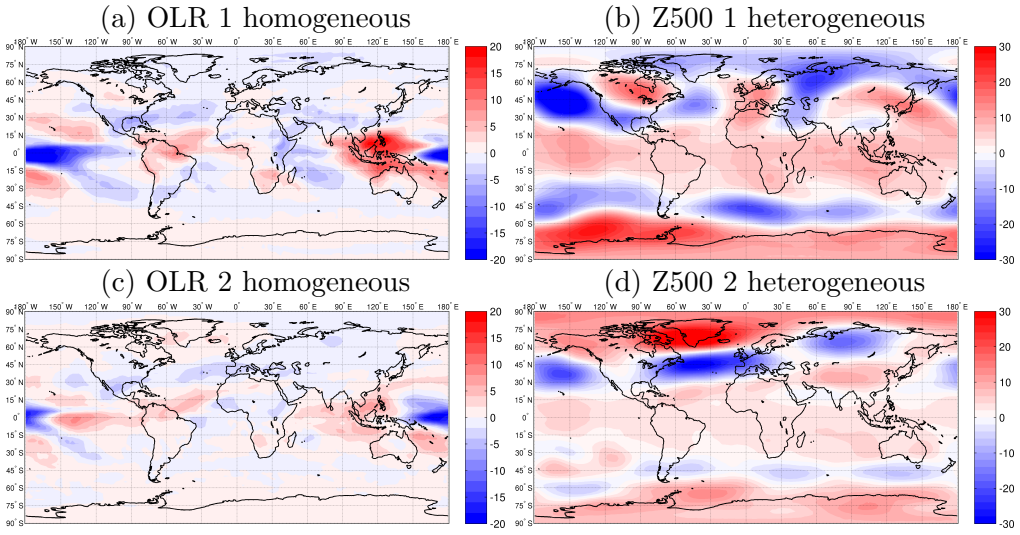



Figure A.2: First two MCA modes, with whole tropical NOAA OLR homogeneously regressed ($Wm^{-2}$), and North Atlantic NCEP2 Z500 heterogeneously regressed (m).

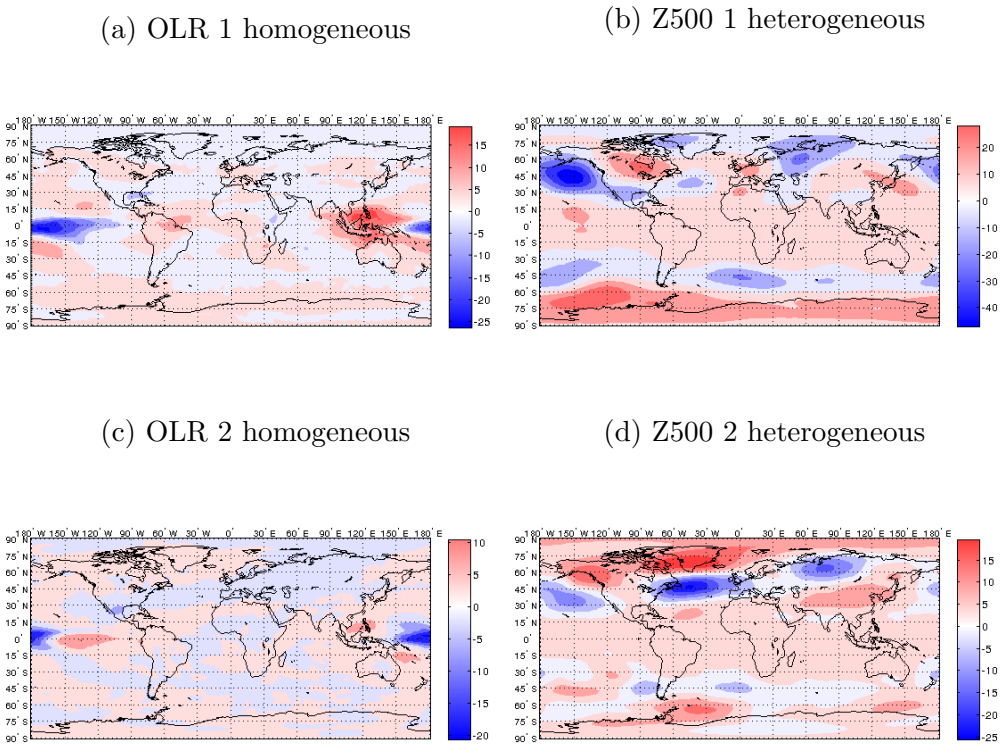



Figure A.3: First two MCA modes, with tropical east Pacific NOAA OLR homogeneously regressed ($Wm^{-2}$), and North Atlantic NCEP2 Z500 heterogeneously regressed (m),

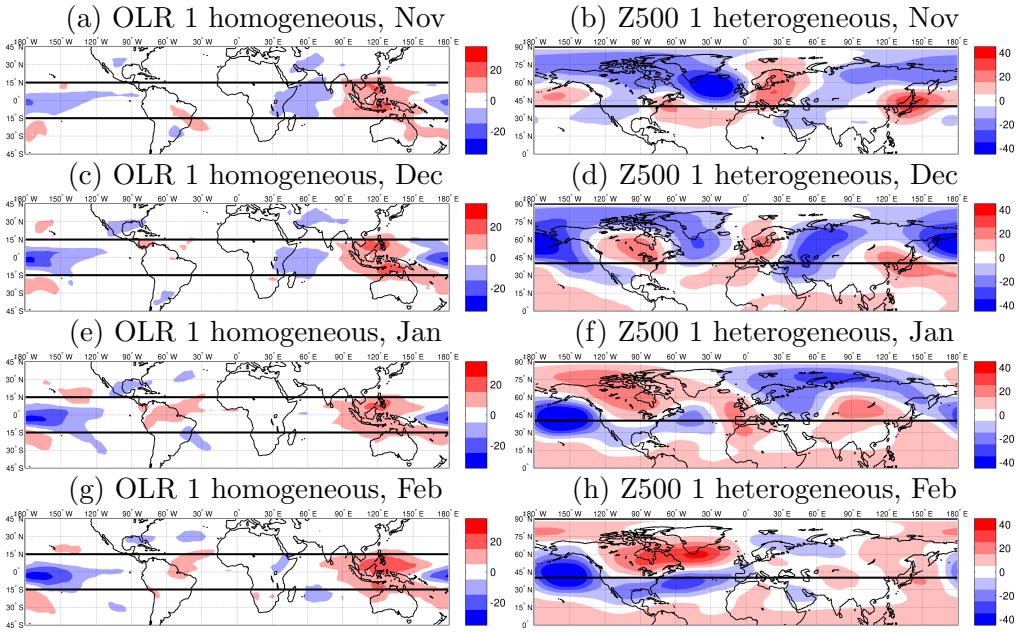
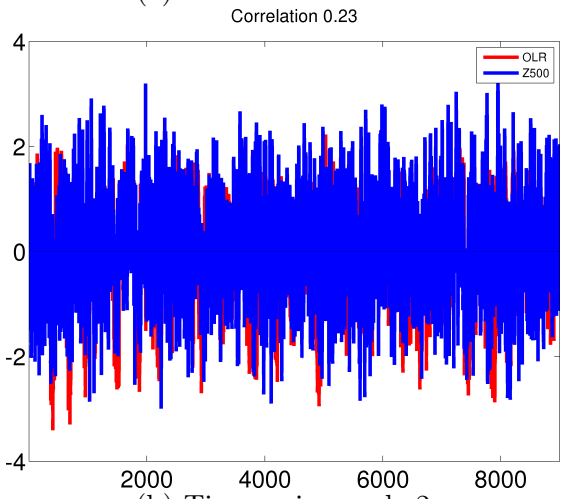
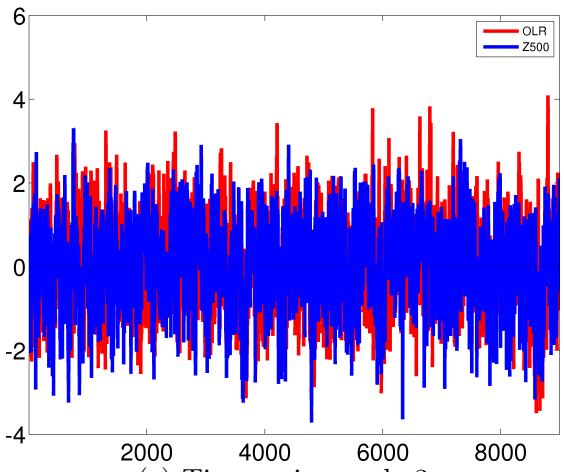



Figure A.4: The leading MCA mode for November, December, January and February, with hemispheric tropical NOAA OLR homogeneously regressed ($\mathrm{Wm}^{-2}$), and northern hemispheric extratropical NCEP2 Z500 heterogeneously regressed (m). The black boxes mark the MCA regions.

(a) Time series mode 1




(b) Time series mode 2




(c) Time series mode 3

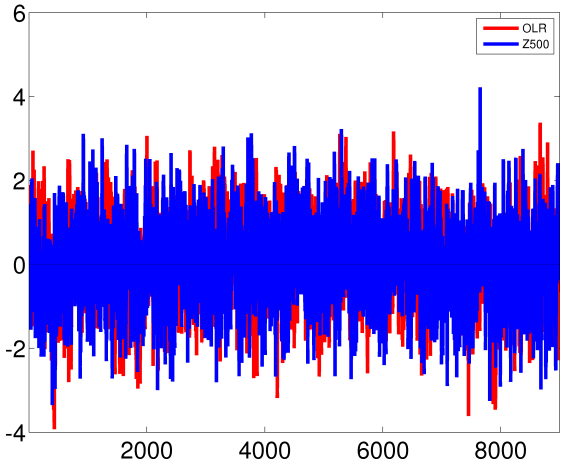
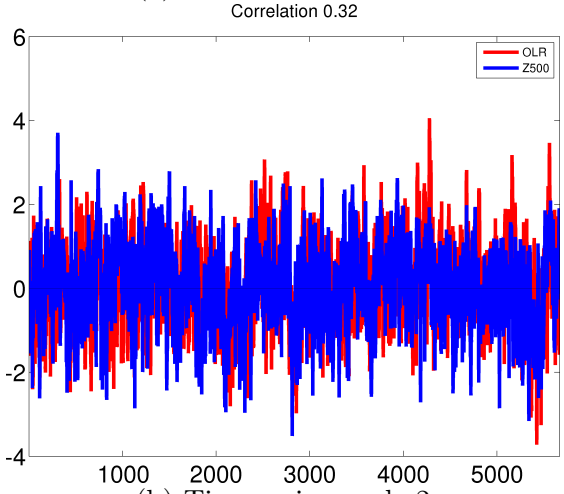
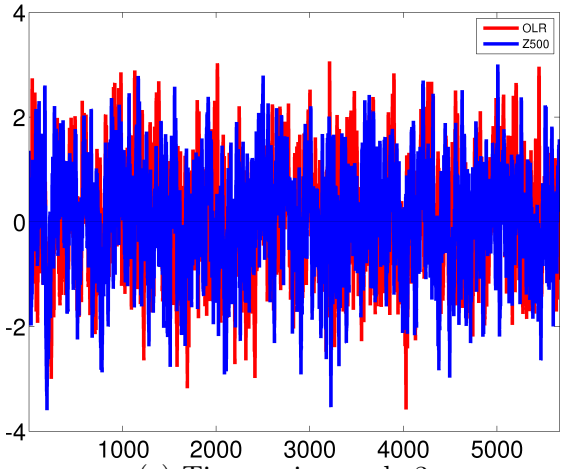



Figure A.5: Calculated from daily data with OLR leading Z500 by 14 days, all years. Time series from the MCA between hemispheric tropical MOGC3 OLR and northern hemispheric extratropical MOGC3 Z500.

(a) Time series mode 1




(b) Time series mode 2




(c) Time series mode 3

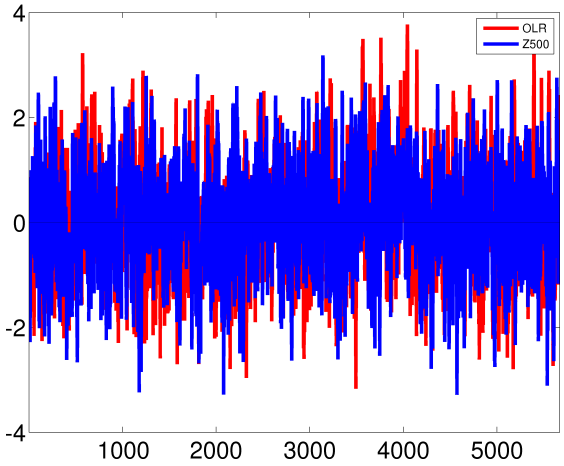



Figure A.6: Calculated from daily data with OLR leading Z500 by 14 days, on ENSO-neutral years. Time series from the MCA between hemispheric tropical MOGC3 OLR and northern hemispheric extratropical MOGC3 Z500.

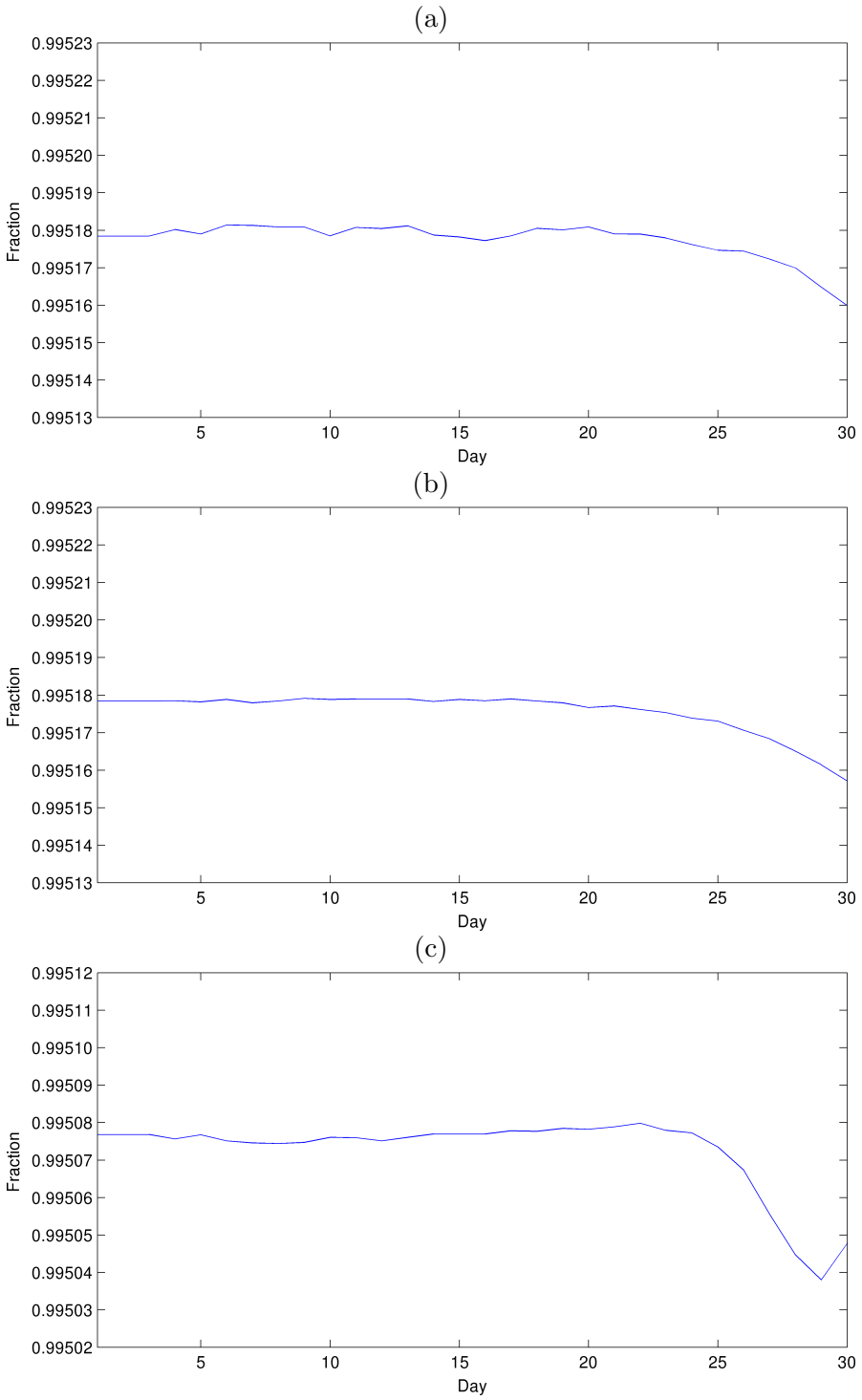



Figure A.7: Total atmospheric mass evolution, as a percentage of the observed mass, in the baroclinic model experiment using (a) the diabatic heating in figure 4.19b with the ERA-I basic state, (b) the diabatic cooling in figure 4.19c with the ERA-I basic state, and (c) the same diabatic heating as (a) but with the MOGC3 basic state.

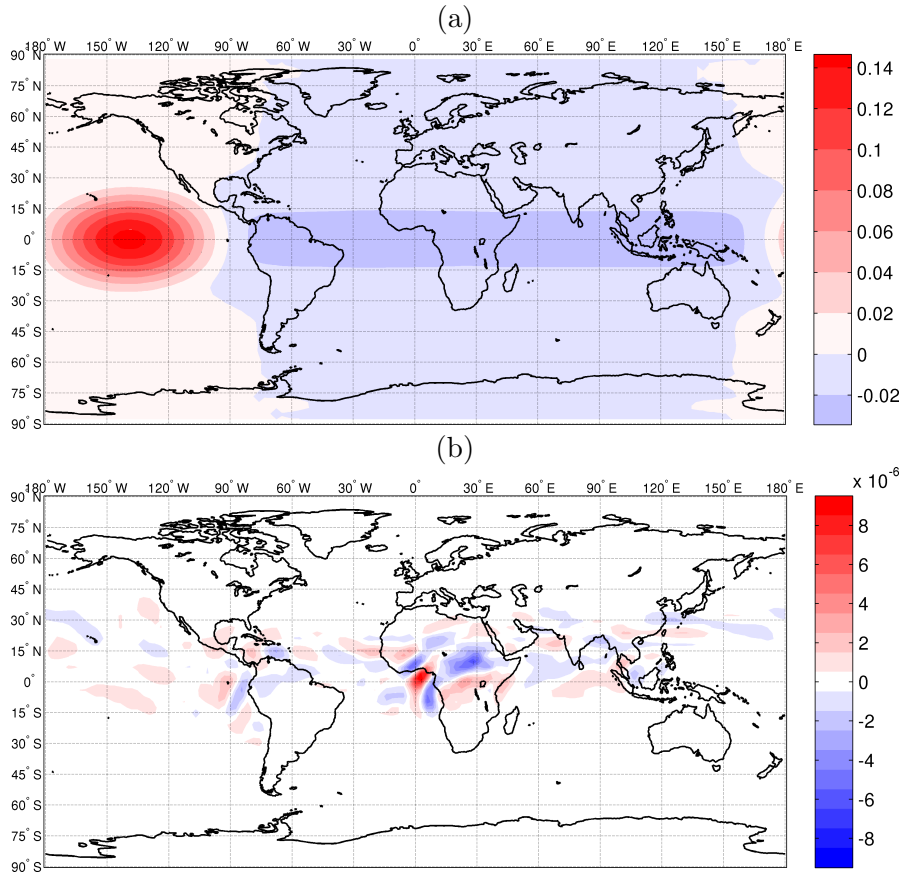



Figure A.8: Responses to the diabatic forcing in figure 4.19b, on ERA-I basic state, (a) 400 hPa temperature (K) at day 0.25, and (b) 250 hPa divergence ($s^{-1}$) averaged between days 10 and 14.

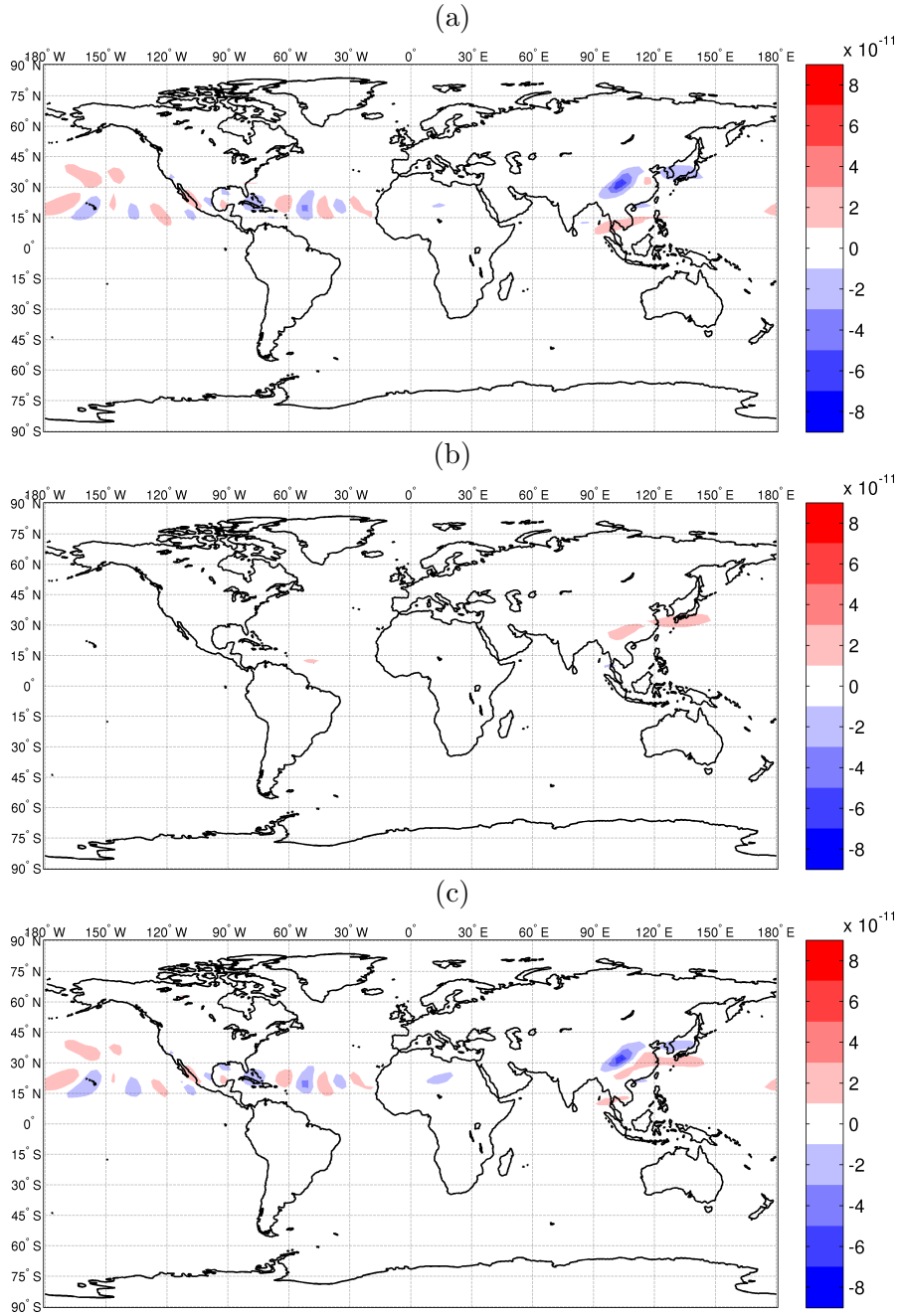



Figure A.9: 250 hPa Rossby wave source responses ($s^{-2}$) to the diabatic forcing in figure 4.19c, on ERA-I basic state, averaged between days 10 and 14, for (a) vortex stretching, (b) vorticity advection and (c) the total.

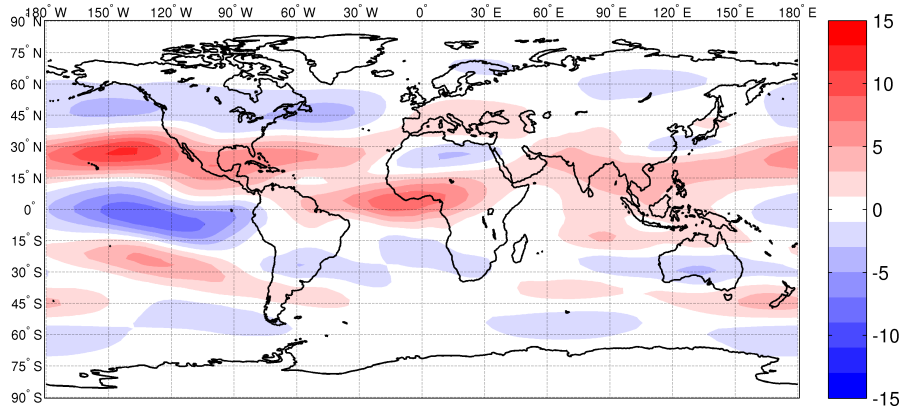



Figure A.10: 250 hPa DJF climatological zonal wind of MOGC3 minus ERA-I ($ms^{-1}$). This can be compared with that of MOGC3 minus NCEP2 (figure 4.1a).

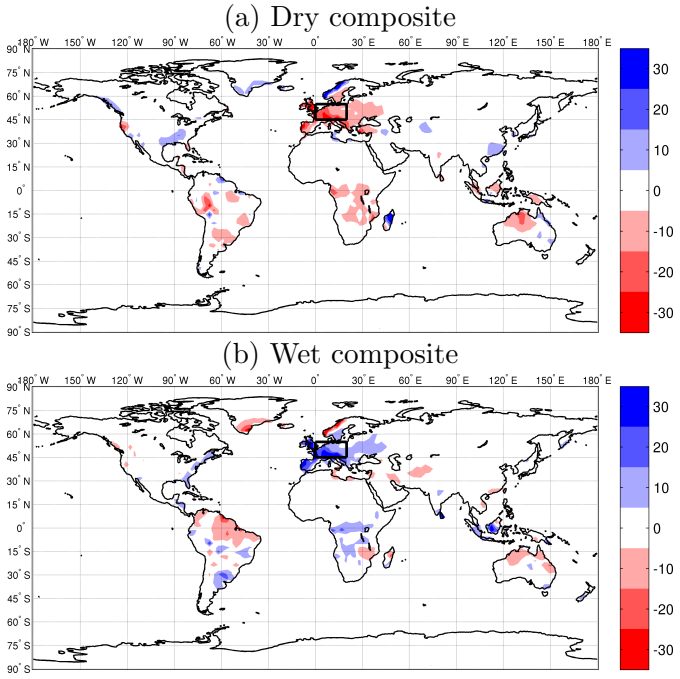



Figure A.11: CRU land surface precipitation composites of the twenty (a) driest and (b) wettest European DJF, with our European region marked in black box. All units are in mm per month.

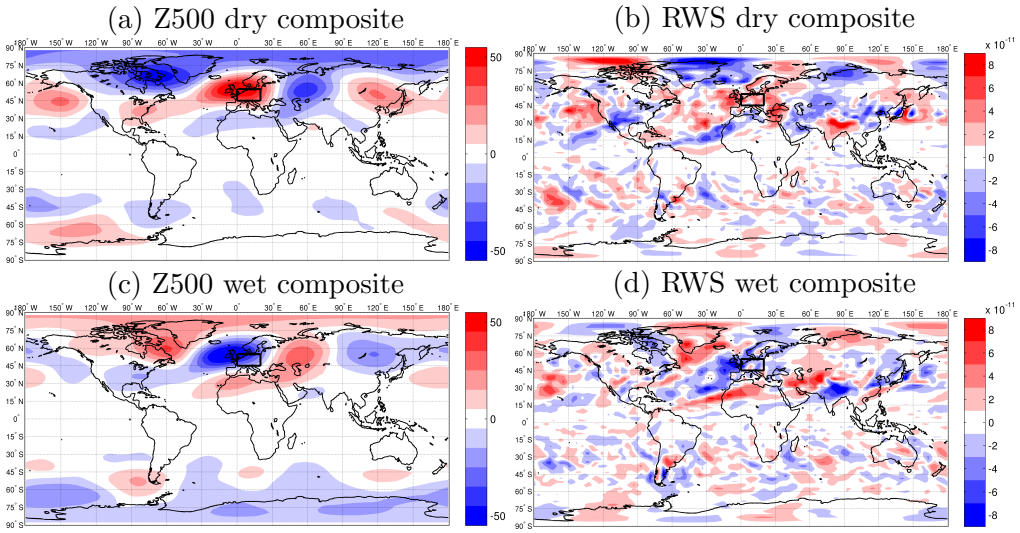



Figure A.12: Z500 (m) and RWS ($s^{-2}$) composited for the twenty driest and wettest DJFs.

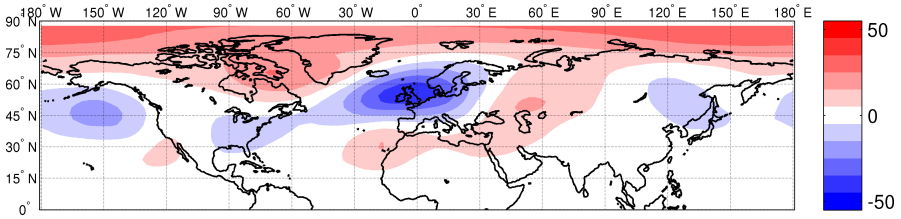



Figure A.13: NCEP2 500 hPa geopotential height (m) regression onto the standardized CRU European region precipitation time series between 1980 and 2010.

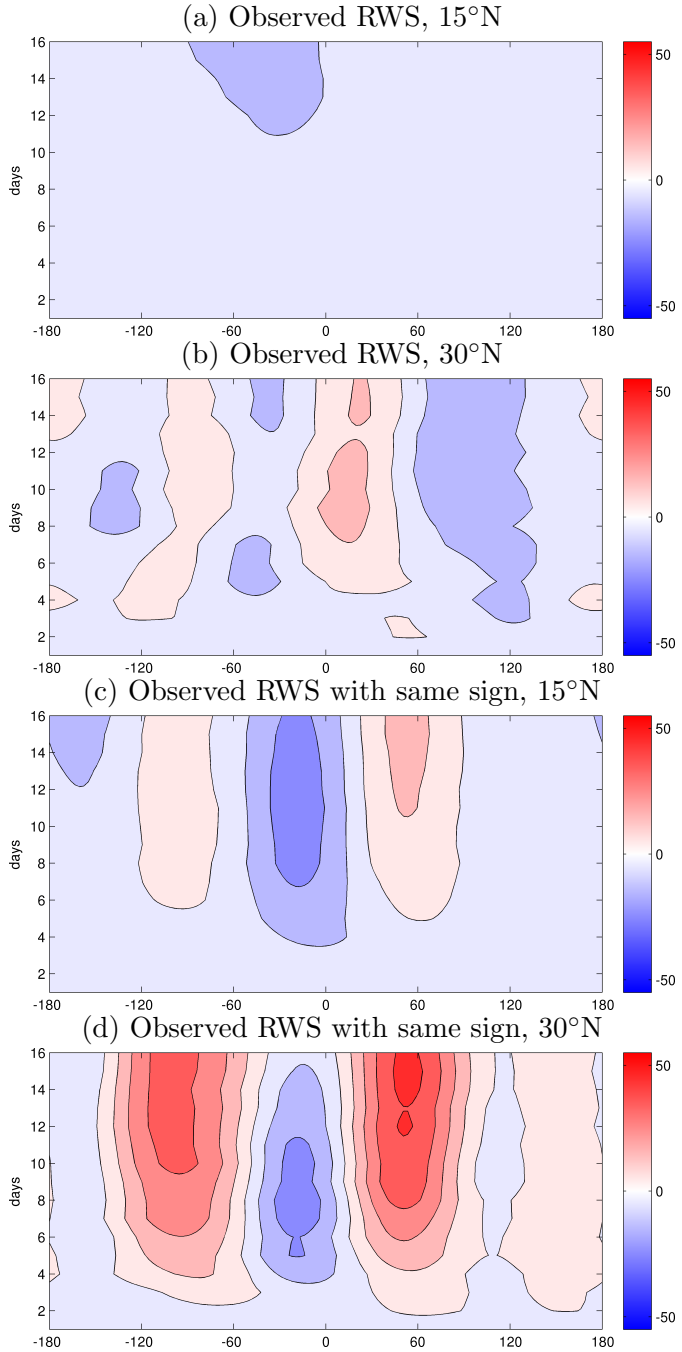



Figure A.14: Hovmöller diagrams, averaged between 45°N and 60°N, of the 250 hPa geopotential height responses (m) from barotropic experiment (figure 5.7), using (a,b) the observed RWS and (c,d) the observed RWS where the sign agrees with the patch result. Units are in m.

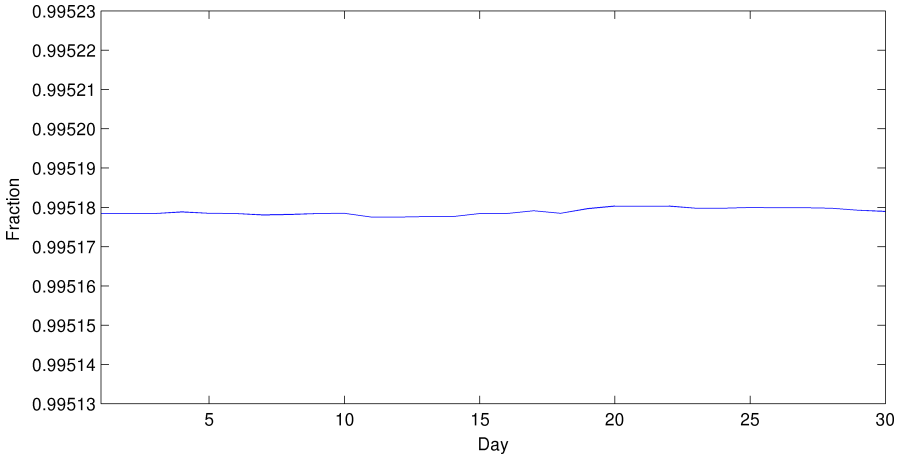
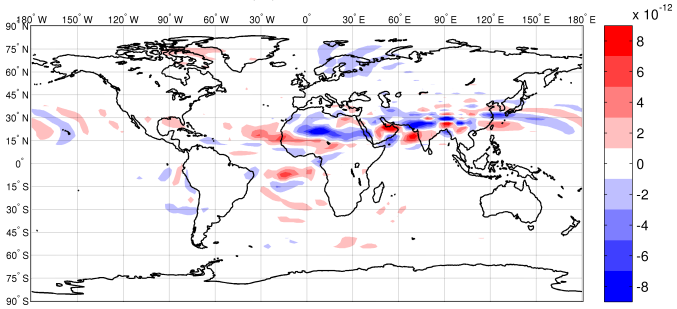
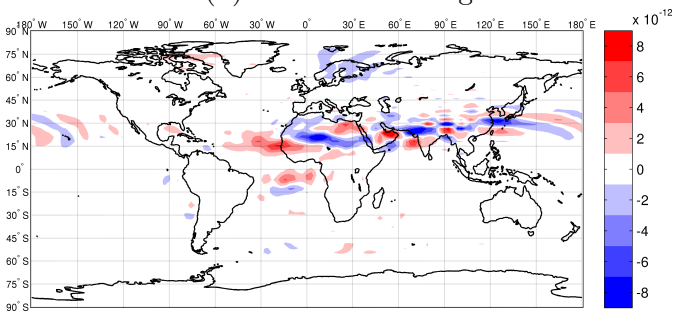



Figure A.15: Total atmospheric mass evolution in the baroclinic model experiment using the diabatic forcing in figure 5.12, as a percentage of the observed mass.

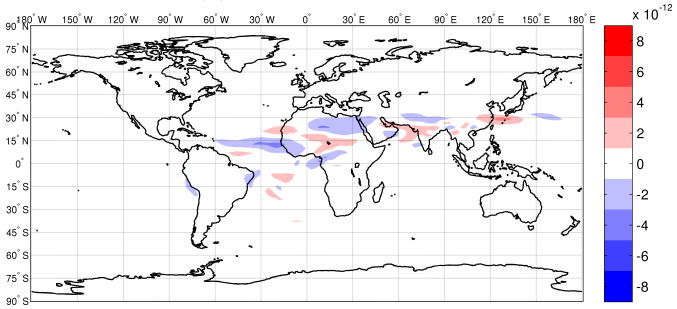
(a) Total RWS




(b) Vortex stretching




(c) Vorticity advection




(d) Divergence

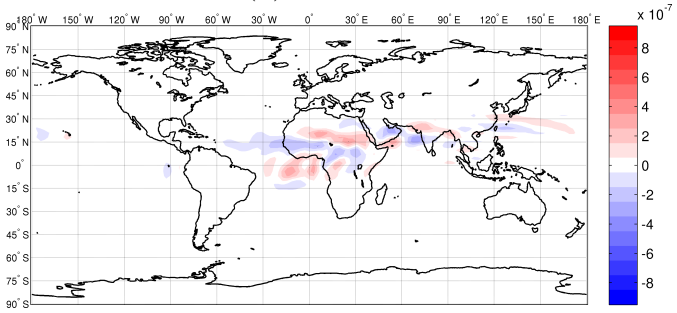



Figure A.16: 250 hPa model responses, averaged between days 10 and 14, in (a) total Rossby wave source ($s^{-2}$), (b) vortex stretching ($s^{-2}$), (c) vorticity advection ($s^{-2}$), (d) divergence ($s^{-1}$), to the diabatic forcing in figure 5.16a .

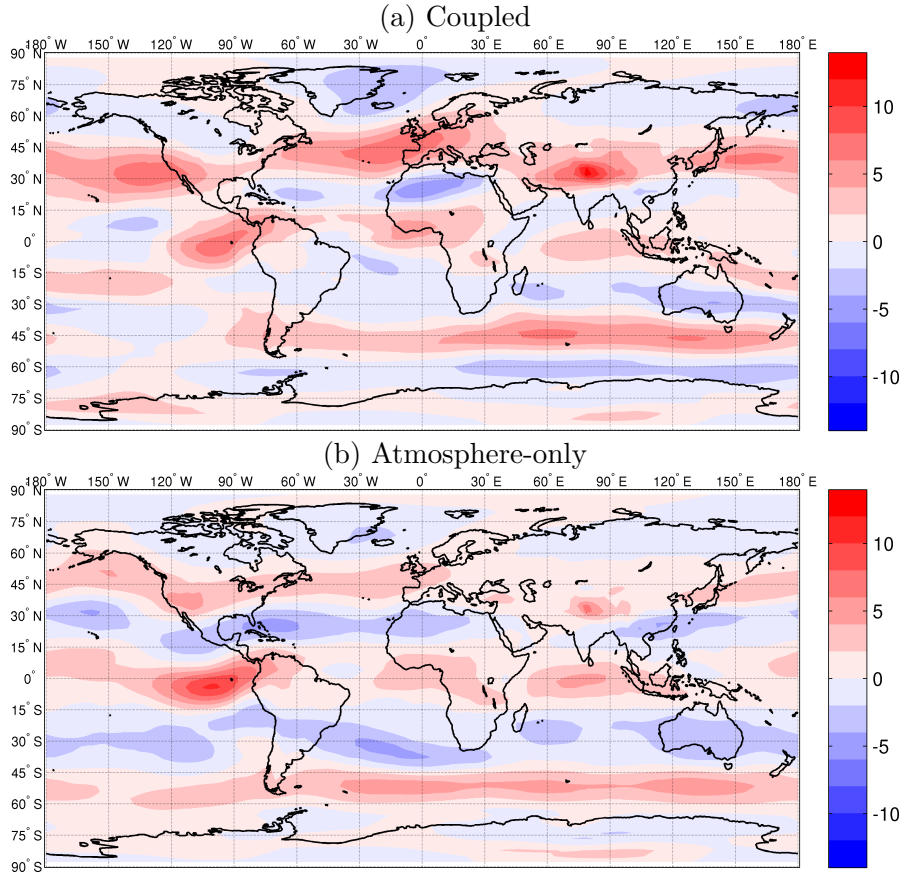



Figure A.17: IFS lower resolution runs ensemble mean bias from NCEP2 reanalysis, of DJF mean 250 hPa zonal wind ($ms^{-1}$), for (a) coupled runs and (b) atmosphere-only runs.

# Bibliography

Adler, R. F., Huffman, G. J., Chang, A., Ferraro, R., Xie, P.-P., Janowiak, J., Rudolf, B., Schneider, U., Curtis, S., Bolvin, D., Gruber, A., Susskind, J., Arkin, P., and Nelkin, E. (2003). The Version-2 Global Precipitation Climatology Project (GPCP) Monthly Precipitation Analysis (1979-Present). *Journal of Hydrometeorology*, 4(6):1147–1167.

Alexander, M. A., Bladé, I., Newman, M., Lanzante, J. R., Lau, N.-C., and Scott, J. D. (2002). The Atmospheric Bridge: The Influence of ENSO Teleconnections on Air-Sea Interaction over the Global Oceans. *Journal of Climate*, 15(16):2205–2231.

Ambaum, M. H. P., Hoskins, B. J., and Stephenson, D. B. (2001). Arctic Oscillation or North Atlantic Oscillation? *Journal of Climate*, 14(16):3495–3507.

Ambrizzi, T. and Hoskins, B. J. (1997). Stationary rossby-wave propagation in a baroclinic atmosphere. *Quarterly Journal of the Royal Meteorological Society*, 123(540):919–928.

Andrews, D. G. (2010). *An Introduction to Atmospheric Physics*. Cambridge University Press, 2 edition.

Andrews, D. G. and McIntyre, M. E. (1976). Planetary Waves in Horizontal and Vertical Shear: The Generalized Eliassen-Palm Relation and the Mean Zonal Acceleration. *Journal of the Atmospheric Sciences*, 33(11):2031–2048.

Ayarzagüena, B., Ineson, S., Dunstone, N. J., Baldwin, M. P., and Scaife, A. A. (2018). Intraseasonal Effects of El Niño-Southern Oscillation on North Atlantic Climate. *Journal of Climate*, 31(21):8861–8873.

Barnes, E. A. and Polvani, L. (2013). Response of the Midlatitude Jets, and of Their Variability, to Increased Greenhouse Gases in the CMIP5 Models. *Journal of Climate*, 26(18):7117–7135.

Barsugli, J. J. and Sardeshmukh, P. D. (2002). Global Atmospheric Sensitivity to Tropical SST Anomalies throughout the Indo-Pacific Basin. *Journal of Climate*, 15(23):3427–3442.

Bell, C. J., Gray, L. J., Charlton-Perez, A. J., Joshi, M. M., and Scaife, A. A. (2009). Stratospheric Communication of El Niño Teleconnections to European Winter. *Journal of Climate*, 22(15):4083–4096.

Benedict, J. J., Lee, S., and Feldstein, S. B. (2004). Synoptic View of the North Atlantic Oscillation. *Journal of the Atmospheric Sciences*, 61(2):121–144.

Blackmon, M. L., Lee, Y.-H., and Wallace, J. M. (1984a). Horizontal Structure of 500 mb Height Fluctuations with Long, Intermediate and Short Time Scales. *Journal of the Atmospheric Sciences*, 41(6):961–980.

Blackmon, M. L., Lee, Y.-H., Wallace, J. M., and Hsu, H.-H. (1984b). Time Variation of 500 mb Height Fluctuations with Long, Intermediate and Short Time Scales as Deduced from Lag-Correlation Statistics. *Journal of the Atmospheric Sciences*, 41(6):981–991.

Bracegirdle, T. J., Shuckburgh, E., Sallee, J.-B., Wang, Z., Meijers, A. J. S., Bruneau, N., Phillips, T., and Wilcox, L. J. (2013). Assessment of surface winds over the Atlantic, Indian, and Pacific Ocean sectors of the Southern Ocean in CMIP5 models: historical bias, forcing response, and state dependence. *Journal of Geophysical Research: Atmospheres*, 118(2):547–562.

Branstator, G. (1983). Horizontal Energy propagation in a Barotropic Atmosphere with Meridional and Zonal Structure. *Journal of the Atmospheric Sciences*, 40(7):1689–1708.

Branstator, G. (1992). The Maintenance of Low-Frequency Atmospheric Anomalies. *Journal of the Atmospheric Sciences*, 49(20):1924–1946.

Branstator, G. (1995). Organization of Storm Track Anomalies by Recurring Low-Frequency Circulation Anomalies. *Journal of the Atmospheric Sciences*, 52(2):207–226.

Branstator, G. (2002). Circumglobal Teleconnections, the Jet Stream Waveguide, and the North Atlantic Oscillation. *Journal of Climate*, 15(14):1893–1910.

Bretherton, C. S., Smith, C., and Wallace, J. M. (1992). An Intercomparison of Methods for Finding Coupled Patterns in Climate Data. *Journal of Climate*, 5(6):541–560.

Bretherton, C. S., Widmann, M., Dymnikov, V. P., Wallace, J. M., and Bladé, I. (1999). The Effective Number of Spatial Degrees of Freedom of a Time-Varying Field. *Journal of Climate*, 12(7):1990–2009.

Brönnimann, S. (2007). Impact of El Niño-Southern Oscillation on European climate. *Reviews of Geophysics*, 45(3).

Cassou, C. (2008). Intraseasonal interaction between the Madden-Julian Oscillation and the North Atlantic Oscillation. *Nature*, 455:523 EP –.

Charney, J. G. and Drazin, P. G. (1961). Propagation of planetary-scale disturbances from the lower into the upper atmosphere. *Journal of Geophysical Research*, 66(1):83–109.

Collins, M., Knutti, R., Arblaster, J., Dufresne, J.-L., Fichefet, T., Friedlingstein, P., Gao, X., Gutowski, W., Johns, T., Krinner, G., Shongwe, M., Tebaldi, C., Weaver, A., and Wehner, M. (2013). Chapter 12 - Long-term climate change: Projections, commitments and irreversibility. In IPCC, editor, *Climate Change 2013: The Physical Science Basis. IPCC Working Group I Contribution to AR5.* Cambridge University Press, Cambridge.

Dai, A. and Wigley, T. M. L. (2000). Global patterns of ENSO-induced precipitation. *Geophysical Research Letters*, 27(9):1283–1286.

Dawson, A., Matthews, A. J., and Stevens, D. P. (2011). Rossby wave dynamics of the North Pacific extra-tropical response to El Niño: importance of the basic state in coupled GCMs. *Climate Dynamics*, 37(1):391–405.

Dawson, A., Matthews, A. J., Stevens, D. P., Roberts, M. J., and Vidale, P. L. (2013). Importance of oceanic resolution and mean state on the extra-tropical response to El Niño in a matrix of coupled models. *Climate Dynamics*, 41(5):1439–1452.

Dee, D. P., Uppala, S. M., Simmons, A. J., Berrisford, P., Poli, P., Kobayashi, S., Andrae, U., Balmaseda, M. A., Balsamo, G., Bauer, P., Bechtold, P., Beljaars, A. C. M., van de Berg, L., Bidlot, J., Bormann, N., Delsol, C., Dragani, R., Fuentes, M., Geer, A. J., Haimberger, L., Healy, S. B., Hersbach, H., Hólm, E. V., Isaksen, L., Kāllberg, P., Köhler, M., Matricardi, M., McNally, A. P., Monge-Sanz, B. M., Morcrette, J.-J., Park, B.-K., Peubey, C., de Rosnay, P., Tavolato, C., Thépaut, J.-N., and Vitart, F. (2011). The ERA-Interim reanalysis: configuration and performance of the data assimilation system. *Quarterly Journal of the Royal Meteorological Society*, 137(656):553–597.

Derome, J., Lin, H., and Brunet, G. (2005). Seasonal Forecasting with a Simple General Circulation Model: Predictive Skill in the AO and PNA. *Journal of Climate*, 18(4):597–609.

Deser, C., Magnusdottir, G., Saravanan, R., and Phillips, A. (2004). The Effects of North Atlantic SST and Sea Ice Anomalies on the Winter Circulation in CCM3. Part II: Direct and Indirect Components of the Response. *Journal of Climate*, 17(5):877–889.

Ding, Q., Wang, B., M. Wallace, J., and Branstator, G. (2011). Tropical-Extratropical Teleconnections in Boreal Summer: Observed Interannual Variability. 24:1878–1896.

Drouard, M., Rivire, G., and Arbogast, P. (2013). The North Atlantic Oscillation Response to Large-Scale Atmospheric Anomalies in the Northeastern Pacific. *Journal of the Atmospheric Sciences*, 70(9):2854–2874.

Drouard, M., Rivire, G., and Arbogast, P. (2015). The Link between the North Pacific Climate Variability and the North Atlantic Oscillation via Downstream Propagation of Synoptic Waves. *Journal of Climate*, 28(10):3957–3976.

Duchon, C. E. (1979). Lanczos Filtering in One and Two Dimensions. *Journal of Applied Meteorology*, 18(8):1016–1022.

Eade, R., Smith, D., Scaife, A., Wallace, E., Dunstone, N., Hermanson, L., and Robinson, N. (2014). Do seasonal-to-decadal climate predictions underestimate the predictability of the real world? *Geophysical Research Letters*, 41(15):5620–5628.

Eady, E. T. (1949). Long Waves and Cyclone Waves. *Tellus*, 1(3):33–52.

Feldstein, S. B. (2003). The dynamics of NAO teleconnection pattern growth and decay. *Quarterly Journal of the Royal Meteorological Society*, 129(589):901–924.

Fereday, D., Chadwick, R., Knight, J., and Scaife, A. A. (2018). Atmospheric Dynamics is the Largest Source of Uncertainty in Future Winter European Rainfall. *Journal of Climate*, 31(3):963–977.

Freeman, E., Woodruff, S. D., Worley, S. J., Lubker, S. J., Kent, E. C., Angel, W. E., Berry, D. I., Brohan, P., Eastman, R., Gates, L., Gloeden, W., Ji, Z., Lawrimore, J., Rayner, N. A., Rosenhagen, G., and Smith, S. R. (2017). ICOADS Release 3.0: a major update to the historical marine climate record. *International Journal of Climatology*, 37(5):2211–2232.

Greatbatch, R. J., Lin, H., Lu, J., Peterson, K. A., and Derome, J. (2003). Tropical/Extratropical forcing of the AO/NAO: A corrigendum. *Geophysical Research Letters*, 30(14).

Hannachi, A., Jolliffe, I. T., and Stephenson, D. B. (2007). Empirical orthogonal functions and related techniques in atmospheric science: A review. *International Journal of Climatology*, 27(9):1119–1152.

Hardiman, S. C., Dunstone, N. J., Scaife, A. A., Smith, D. M., Ineson, S., Lim, J., and Fereday, D. (2019). The Impact of Strong El Niño and La Niña Events on the North Atlantic. *Geophysical Research Letters*, 0(0).

Harris, I., Jones, P., Osborn, T., and Lister, D. (2014). Updated high-resolution grids of monthly climatic observations - the CRU TS3.10 Dataset. *International Journal of Climatology*, 34(3):623–642.

Hartmann, D. L. (2016). Chapter 4 - The Energy Balance of the Surface. In Hartmann, D. L., editor, *Global Physical Climatology (Second Edition)*, pages 95 – 130. Elsevier, Boston, second edition.

Hawkins, E. and Sutton, R. (2011). The potential to narrow uncertainty in projections of regional precipitation change. *Climate Dynamics*, 37(1):407–418.

Henderson, S. A., Maloney, E. D., and Barnes, E. A. (2016). The Influence of the Madden-Julian Oscillation on Northern Hemisphere Winter Blocking. *Journal of Climate*, 29(12):4597–4616.

Henderson, S. A., Maloney, E. D., and Son, S.-W. (2017). Madden-Julian Oscillation Pacific Teleconnections: The Impact of the Basic State and MJO Representation in General Circulation Models. *Journal of Climate*, 30(12):4567–4587.

Hoerling, M. P., Kumar, A., and Zhong, M. (1997). El Niño, La Niña, and the Nonlinearity of Their Teleconnections. *Journal of Climate*, 10(8):1769–1786.

Hoskins, B. J. and Ambrizzi, T. (1993). Rossby Wave Propagation on a Realistic Longitudinally Varying Flow. *Journal of the Atmospheric Sciences*, 50(12):1661–1671.

Hoskins, B. J. and James, I. (2016). Chapter 6 - Alternative vertical coordinates. In *Fluid Dynamics of the Midlatitude Atmosphere*, pages 97–108. Wiley-Blackwell, first edition.

Hoskins, B. J. and Karoly, D. J. (1981). The Steady Linear Response of a Spherical Atmosphere to Thermal and Orographic Forcing. *Journal of the Atmospheric Sciences*, 38(6):1179–1196.

Hoskins, B. J. and Simmons, A. J. (1975). A multi-layer spectral model and the semi-implicit method. *Quarterly Journal of the Royal Meteorological Society*, 101(429):637–655.

Huang, B., Banzon, V. F., Freeman, E., Lawrimore, J., Liu, W., Peterson, T. C., Smith, T. M., Thorne, P. W., Woodruff, S. D., and Zhang, H.-M. (2015). Extended Reconstructed Sea Surface Temperature Version 4 (ERSST.v4). Part I: Upgrades and Intercomparisons. *Journal of Climate*, 28(3):911–930.

Huntingford, C., Marsh, T., Scaife, A. A., Kendon, E. J., Hannaford, J., Kay, A. L., Lockwood, M., Prudhomme, C., Reynard, N. S., Parry, S., Lowe, J. A., Screen, J. A., Ward, H. C., Roberts, M., Stott, P. A., Bell, V. A., Bailey, M., Jenkins, A., Legg, T., Otto, F. E. L., Massey, N., Schaller, N., Slingo, J., and Allen, M. R. (2014). Potential influences on the United Kingdom's floods of winter 2013/14. *Nature Climate Change*, 4:769 EP –. Perspective.

Hurrell, J. W., Kushnir, Y., Ottersen, G., and Visbeck, M. (2013). *An Overview of the North Atlantic Oscillation*, pages 1–35. American Geophysical Union (AGU).

Ineson, S. and Scaife, A. A. (2008). The role of the stratosphere in the European climate response to El Niño. *Nature Geoscience*, 2:32 EP –.

Jin, E. K., Kinter, J. L., Wang, B., Park, C.-K., Kang, I.-S., Kirtman, B. P., Kug, J.-S., Kumar, A., Luo, J.-J., Schemm, J., Shukla, J., and Yamagata, T. (2008). Current status of ENSO prediction skill in coupled ocean–atmosphere models. *Climate Dynamics*, 31(6):647–664.

Jin, F. and Hoskins, B. J. (1995). The Direct Response to Tropical Heating in a Baroclinic Atmosphere. *Journal of the Atmospheric Sciences*, 52(3):307–319.

Kallberg, P., Berrisford, P., J. Hoskins, B., Simmons, S., Uppala, S., and Hine, R. (2005). ERA-40 atlas.

Kalnay, E., Kanamitsu, M., Kistler, R., Collins, W., Deaven, D., Gandin, L., Iredell, M., Saha, S., White, G., Woollen, J., Zhu, Y., Chelliah, M., Ebisuzaki, W., Higgins, W., Janowiak, J., Mo, K. C., Ropelewski, C., Wang, J., Leetmaa, A., Reynolds, R., Jenne, R., and Joseph, D. (1996). The NCEP/NCAR 40-Year Reanalysis Project. *Bulletin of the American Meteorological Society*, 77(3):437–472.

Karoly, D. J. (1983). Rossby wave propagation in a barotropic atmosphere. *Dynamics of Atmospheres and Oceans*, 7(2):111 – 125.

Kiladis, G. N. and Feldstein, S. B. (1994). Rossby wave propagation into the tropics in two GFDL general circulation models. *Climate Dynamics*, 9(4):245–252.

Kiladis, G. N. and Weickmann, K. M. (1992). Extratropical Forcing of Tropical Pacific Convection during Northern Winter. *Monthly Weather Review*, 120(9):1924–1939.

King, M. P., Herceg-Buli, I., Bladé, I., Garca-Serrano, J., Keenlyside, N., Kucharski, F., Li, C., and Sobolowski, S. (2018). Importance of late fall ENSO teleconnection in the Euro-Atlantic sector. *Bulletin of the American Meteorological Society*, 0(0):null.

Knight, J. R., Maidens, A., Watson, P. A. G., Andrews, M., Belcher, S., Brunet, G., Fereday, D., Folland, C. K., Scaife, A. A., and Slingo, J. (2017). Global meteorological influences on the record UK rainfall of winter 2013-14. *Environmental Research Letters*, 12(7):074001.

Li, C. and Wettstein, J. J. (2012). Thermally Driven and Eddy-Driven Jet Variability in Reanalysis. *Journal of Climate*, 25(5):1587–1596.

Liebmann, B. and Hartmann, D. L. (1984). An Observational Study of Tropical-Midlatitude Interaction on Intraseasonal Time Scales during Winter. *Journal of the Atmospheric Sciences*, 41(23):3333–3350.

Lin, H., Derome, J., Greatbatch, R. J., Andrew Peterson, K., and Lu, J. (2002). Tropical links of the Arctic Oscillation. *Geophysical Research Letters*, 29(20):4–1–4–4.

Liu, Y., Hoskins, B., and Blackburn, M. (2007). Impact of Tibetan Orography and Heating on the Summer Flow over Asia. *Journal of the Meteorological Society of Japan. Ser. II*, 85B:1–19.

Madden, R. A. and Julian, P. R. (1972). Description of Global-Scale Circulation Cells in the Tropics with a 40-50 Day Period. *Journal of the Atmospheric Sciences*, 29(6):1109–1123.

Marshall, A. G. and Scaife, A. A. (2009). Impact of the QBO on surface winter climate. *Journal of Geophysical Research: Atmospheres*, 114(D18).

Matsueda, M. and Palmer, T. N. (2018). Estimates of flow-dependent predictability of wintertime Euro-Atlantic weather regimes in medium-range forecasts. *Quarterly Journal of the Royal Meteorological Society*, 144(713):1012–1027.

Matthews, A. J., Hoskins, B. J., and Masutani, M. (2004). The global response to tropical heating in the Madden-Julian oscillation during the northern winter. *Quarterly Journal of the Royal Meteorological Society*, 130(601):1991–2011.

Matthews, A. J. and Kiladis, G. N. (1999). The Tropical-Extratropical Interaction between High-Frequency Transients and the Madden-Julian Oscillation. *Monthly Weather Review*, 127(5):661–677.

Müller, W. A., Appenzeller, C., and Schär, C. (2005). Probabilistic seasonal prediction of the winter North Atlantic Oscillation and its impact on near surface temperature. *Climate Dynamics*, 24(2):213–226.

Newman, M. and Sardeshmukh, P. D. (2008). Tropical and Stratospheric Influences on Extratropical Short-Term Climate Variability. *Journal of Climate*, 21(17):4326–4347.

North, G. R., Bell, T. L., Cahalan, R. F., and Moeng, F. J. (1982). Sampling Errors in the Estimation of Empirical Orthogonal Functions. *Monthly Weather Review*, 110(7):699–706.

O'Reilly, C. H., Woollings, T., Zanna, L., and Weisheimer, A. (2018). The Impact of Tropical Precipitation on Summertime Euro-Atlantic Circulation via a Circumglobal Wave Train. *Journal of Climate*, 31(16):6481–6504.

Palmer, T. N. (1999). A Nonlinear Dynamical Perspective on Climate Prediction. *Journal of Climate*, 12(2):575–591.

Pelly, J. L. and Hoskins, B. J. (2003). A New Perspective on Blocking. *Journal of the Atmospheric Sciences*, 60(5):743–755.

Petoukhov, V., Rahmstorf, S., Petri, S., and Schellnhuber, H. (2013). Quasiresonant amplification of planetary waves and recent Northern Hemisphere weather extremes. 110.

Poli, P., Hersbach, H., Dee, D. P., Berrisford, P., Simmons, A. J., Vitart, F., Laloyaux, P., Tan, D. G. H., Peubey, C., Thépaut, J.-N., Trémolet, Y., Hólm, E. V., Bonavita, M., Isaksen, L., and Fisher, M. (2016). ERA-20C: An Atmospheric Reanalysis of the Twentieth Century. *Journal of Climate*, 29(11):4083–4097.

Rennert, K. J. and Wallace, J. M. (2009). Cross-Frequency Coupling, Skewness, and Blocking in the Northern Hemisphere Winter Circulation. *Journal of Climate*, 22(21):5650–5666.

Roberts, C. D., Senan, R., Molteni, F., Boussetta, S., Mayer, M., and Keeley, S. P. E. (2018). Climate model configurations of the ECMWF Integrated Forecasting System (ECMWF-IFS cycle 43r1) for HighResMIP. *Geoscientific Model Development*, 11(9):3681–3712.

Rodrigues, R. R., Campos, E. J. D., and Haarsma, R. (2015). The Impact of ENSO on the South Atlantic Subtropical Dipole Mode. *Journal of Climate*, 28(7):2691–2705.

Rodrigues, R. R. and Woollings, T. (2017). Impact of Atmospheric Blocking on South America in Austral Summer. *Journal of Climate*, 30(5):1821–1837.

Santos, J. A., Woollings, T., and Pinto, J. G. (2013). Are the Winters 2010 and 2012 Archetypes Exhibiting Extreme Opposite Behavior of the North Atlantic Jet Stream? *Monthly Weather Review*, 141(10):3626–3640.

Sardeshmukh, P. D. and Hoskins, B. J. (1988). The Generation of Global Rotational Flow by Steady Idealized Tropical Divergence. *Journal of Atmospheric Sciences*, 45:1228–1251.

Scaife, A. A., Arribas, A., Blockley, E., Brookshaw, A., Clark, R. T., Dunstone, N., Eade, R., Fereday, D., Folland, C. K., Gordon, M., Hermanson, L., Knight, J. R., Lea, D. J., MacLachlan, C., Maidens, A., Martin, M., Peterson, A. K., Smith, D., Vellinga, M., Wallace, E., Waters, J., and Williams, A. (2014). Skillful long-range prediction of European and North American winters. *Geophysical Research Letters*, 41(7):2514–2519.

Scaife, A. A., Comer, R. E., Dunstone, N. J., Knight, J. R., Smith, D. M., MacLachlan, C., Martin, N., Peterson, K. A., Rowlands, D., Carroll, E. B., Belcher, S., and Slingo, J. (2017). Tropical rainfall, Rossby waves and regional winter climate predictions. *Quarterly Journal of the Royal Meteorological Society*, 143(702):1–11.

Scaife, A. A., Ferranti, L., Alves, O., Athanasiadis, P., Baehr, J., Dequé, M., Dippe, T., Dunstone, N., Fereday, D., Gudgel, R. G., Greatbatch, R. J., Hermanson, L., Imada, Y., Jain, S., Kumar, A., MacLachlan, C., Merryfield, W., Müller, W. A., Ren, H.-L., Smith, D., Takaya, Y., Vecchi, G., and Yang, X. (2019). Tropical rainfall predictions from multiple seasonal forecast systems. *International Journal of Climatology*, 39(2):974–988.

Scaife, A. A. and Smith, D. (2018). A signal-to-noise paradox in climate science. *npj Climate and Atmospheric Science*, 1(1):28.

Scherrer, S. C., Croci-Maspoli, M., Schwierz, C., and Appenzeller, C. (2006). Two-dimensional indices of atmospheric blocking and their statistical relationship with winter climate patterns in the Euro-Atlantic region. *International Journal of Climatology*, 26(2):233–249.

Shepherd, T. G. (2014). Atmospheric circulation as a source of uncertainty in climate change projections. *Nature Geoscience*, 7:703 EP –. Perspective.

Simmons, A. J. (1982). The forcing of stationary wave motion by tropical diabatic heating. *Quarterly Journal of the Royal Meteorological Society*, 108(457):503–534.

Simmons, A. J., Wallace, J. M., and Branstator, G. W. (1983). Barotropic Wave Propagation and Instability, and Atmospheric Teleconnection Patterns. *Journal of the Atmospheric Sciences*, 40(6):1363–1392.

Smith, D. M., Scaife, A. A., Eade, R., and Knight, J. R. (2016). Seasonal to decadal prediction of the winter North Atlantic Oscillation: emerging capability and future prospects. *Quarterly Journal of the Royal Meteorological Society*, 142(695):611–617.

Smith, D. M., Scaife, A. A., and Kirtman, B. P. (2012). What is the current state of scientific knowledge with regard to seasonal and decadal forecasting? *Environmental Research Letters*, 7(1):015602.

Stan, C., Straus, D. M., Frederiksen, J. S., Lin, H., Maloney, E. D., and Schumacher, C. (2017). Review of Tropical-Extratropical Teleconnections on Intraseasonal Time Scales. *Reviews of Geophysics*, 55(4):902–937.

Stott, P. A., Tett, S. F. B., Jones, G. S., Allen, M. R., Mitchell, J. F. B., and Jenkins, G. J. (2000). External Control of 20th Century Temperature by Natural and Anthropogenic Forcings. *Science*, 290(5499):2133–2137.

Takaya, K. and Nakamura, H. (1997). A formulation of a wave-activity flux for stationary Rossby waves on a zonally varying basic flow. *Geophysical Research Letters*, 24(23):2985–2988.

Takaya, K. and Nakamura, H. (2001). A Formulation of a Phase-Independent Wave-Activity Flux for Stationary and Migratory Quasigeostrophic Eddies on a Zonally Varying Basic Flow. *Journal of the Atmospheric Sciences*, 58(6):608–627.

Tibaldi, S. and Molteni, F. (1990). On the operational predictability of blocking. *Tellus A*, 42(3):343–365.

Ting, M. and Sardeshmukh, P. D. (1993). Factors Determining the Extratropical Response to Equatorial Diabatic Heating Anomalies. *Journal of the Atmospheric Sciences*, 50(6):907–918.

Toniazzo, T. and Scaife, A. A. (2006). The influence of ENSO on winter North Atlantic climate. *Geophysical Research Letters*, 33(24).

Trenberth, K. E., Branstator, G. W., Karoly, D., Kumar, A., Lau, N.-C., and Ropelewski, C. (1998). Progress during TOGA in understanding and modeling global teleconnections associated with tropical sea surface temperatures. *Journal of Geophysical Research: Oceans*, 103(C7):14291–14324.

Vautard, R. (1990). Multiple Weather Regimes over the North Atlantic: Analysis of Precursors and Successors. *Monthly Weather Review*, 118(10):2056–2081.

Wallace, J. M. and Gutzler, D. S. (1981). Teleconnections in the Geopotential Height Field during the Northern Hemisphere Winter. *Monthly Weather Review*, 109(4):784–812.

Wallace, J. M., Smith, C., and Bretherton, C. S. (1992). Singular Value Decomposition of Wintertime Sea Surface Temperature and 500-mb Height Anomalies. *Journal of Climate*, 5(6):561–576.

Wanner, H., Brönnimann, S., Casty, C., Gyalistras, D., Luterbacher, J., Schmutz, C., Stephenson, D. B., and Xoplaki, E. (2001). North Atlantic Oscillation – Concepts And Studies. *Surveys in Geophysics*, 22(4):321–381.

Watson, P. A. G. and Gray, L. J. (2014). How Does the Quasi-Biennial Oscillation Affect the Stratospheric Polar Vortex? *Journal of the Atmospheric Sciences*, 71(1):391–409.

Weisheimer, A. and Palmer, T. N. (2014). On the reliability of seasonal climate forecasts. *Journal of The Royal Society Interface*, 11(96).

Weisheimer, A., Schaller, N., O'Reilly, C., MacLeod, D. A., and Palmer, T. (2017). Atmospheric seasonal forecasts of the twentieth century: multi-decadal variability in predictive skill of the winter North Atlantic Oscillation (NAO) and their potential value for extreme event attribution. *Quarterly Journal of the Royal Meteorological Society*, 143(703):917–926.

Wilks, D. (2011a). Chapter 12 - Principal Component (EOF) Analysis. In Wilks, D. S., editor, *Statistical Methods in the Atmospheric Sciences*, volume 100 of *International Geophysics*, pages 519 – 562. Academic Press.

Wilks, D. (2011b). Chapter 13 - Canonical Correlation Analysis (CCA). In Wilks, D. S., editor, *Statistical Methods in the Atmospheric Sciences*, volume 100 of *International Geophysics*, pages 563 – 582. Academic Press.

Williams, K. D., Copsey, D., Blockley, E. W., Bodas-Salcedo, A., Calvert, D., Comer, R., Davis, P., Graham, T., Hewitt, H. T., Hill, R., Hyder, P., Ineson,

S., Johns, T. C., Keen, A. B., Lee, R. W., Megann, A., Milton, S. F., Rae, J. G. L., Roberts, M. J., Scaife, A. A., Schiemann, R., Storkey, D., Thorpe, L., Watterson, I. G., Walters, D. N., West, A., Wood, R. A., Woollings, T., and Xavier, P. K. (2017). The Met Office Global Coupled Model 3.0 and 3.1 (GC3.0 and GC3.1) Configurations. *Journal of Advances in Modeling Earth Systems*, 10(2):357–380.

Woollings, T. (2010). Dynamical influences on European climate: an uncertain future. *Philosophical Transactions of the Royal Society of London A: Mathematical, Physical and Engineering Sciences*, 368(1924):3733–3756.

Woollings, T., Hannachi, A., and Hoskins, B. (2010). Variability of the North Atlantic eddy-driven jet stream. *Quarterly Journal of the Royal Meteorological Society*, 136(649):856–868.

Woollings, T., Hoskins, B., Blackburn, M., and Berrisford, P. (2008). A New Rossby Wave–Breaking Interpretation of the North Atlantic Oscillation. *Journal of the Atmospheric Sciences*, 65(2):609–626.

Yang, S., Lau, K.-M., and Kim, K.-M. (2002). Variations of the East Asian Jet Stream and Asian-Pacific-American Winter Climate Anomalies. *Journal of Climate*, 15(3):306–325.

Yao, Y. and Luo, D. (2015). Do European blocking events precede North Atlantic Oscillation events? *Advances in Atmospheric Sciences*, 32(8):1106–1118.

Zappa, G., Hoskins, B. J., and Shepherd, T. G. (2015). The dependence of wintertime Mediterranean precipitation on the atmospheric circulation response to climate change. *Environmental Research Letters*, 10(10):104012.

Zhang, Y.-C. and Rossow, W. B. (1997). Estimating Meridional Energy Transports by the Atmospheric and Oceanic General Circulations Using Boundary Fluxes. *Journal of Climate*, 10(9):2358–2373.